CHALMERS UNIVERSITY OF TECHNOLOGY
Gothenburg, Sweden
www.chalmers.se

PHD THESIS

Imagine being able to cause an inflammation-like state in a tumor, by raising its temperature just a few degrees centigrade above the baseline for a prolonged time. Even by this tiny amount, a cascade of biological responses is triggered in the body: blood rushes to the affected area, in an effort to counteract the extra heat; capillaries dilate to increase the exchange of oxygen and metabolites with the local tissues; the immune system, normally unaware of the threat posed by the altered cancer material, becomes more alert, and the white cells begin seeking for anomalies; the tumor enters a state of frenetic activity to restore its balance.
But we have prepared two deadly traps: the blood stream carries a poison with it, chemical agents with the ability to tamper with and kill the cancer cells. From the outside, incoming high energy gamma rays bomb the tumor's DNA causing breaks in the nucleotide chain. The tumor struggles to stem the damage, its internal repair mechanisms being inhibited by the exerted rise in temperature. Eventually, the fight reaches a tipping point and the tumor retreats.
This epic tale is regularly played out in patients afflicted by tumors in the pelvis, in the abdomen, in the breast, in the neck, and in the extremities, with remarkable results. The boost in survival rates speaks clearly: hyperthermia works. But a whole group of people has been left out by this advancement, namely brain cancer patients. The main reason behind this is the difficulty in implementing a controlled heat delivery inside the head with high enough accuracy for the treatment to be safe and effective.
In the present work, we devise new techniques for the non-invasive thermal treatment of tumors in the brain. We devote particular attention to young patients, where the incidence of such diseases is the highest, and where the long-lasting side effects of traditional therapies severely degrade the quality of life of survivors. Thanks to improvements in the control of the thermal dose delivery by means of innovative system designs and sophisticated steering tools, we show that it is possible to achieve therapeutic temperatures even in the nastiest of tumors. The wish is for microwave hyperthermia to become a regular modality in brain cancer treatment, and finally exploit the benefits of this technique in younger sufferers.

CHALMERS
UNIVERSITY OF TECHNOLOGY

MASSIMILIANO ZANOLI • Ultra wideband microwave hyperthermia for brain cancer treatment • 2022

Ultra wideband microwave hyperthermia for brain cancer treatment

From treatment planning to applicator design

MASSIMILIANO ZANOLI

DEPARTMENT OF ELECTRICAL ENGINEERING
CHALMERS UNIVERSITY OF TECHNOLOGY
Gothenburg, Sweden 2022
www.chalmers.se

THESIS FOR THE DEGREE OF DOCTOR OF PHILOSOPHY

Ultra wideband microwave hyperthermia for brain cancer treatment

Massimiliano Zanoli

Department of Electrical Engineering
Chalmers University of Technology
Gothenburg, Sweden, 2022

Ultra wideband microwave hyperthermia for brain cancer treatment

Massimiliano Zanoli

This thesis has been prepared using LaTeX.

Department of Electrical Engineering
Chalmers University of Technology
SE-412 96 Gothenburg, Sweden
Phone: +46 (0)31 772 1000
www.chalmers.se

Printed by Chalmers Reproservice
Gothenburg, Sweden, November 2022

Abstract

Despite numerous clinical trials demonstrating that microwave hyperthermia is a powerful adjuvant modality in the treatment of cancers, there have been few instances where this method has been applied to brain tumors. The reason is a combination of anatomical and physiological factors in this site that require an extra degree of accuracy and precision in the thermal dose delivery. Current clinical applicators are not able to provide such control, partly because they are designed to operate at a single fixed frequency. In terms of treatment planning, the use of a single frequency is limiting as the size of the focal spot cannot be modified to accommodate the specific tumor volume and location. The introduction of ultra wide-band (UWB) systems opens up an opportunity to overcome these limitations, as they convey the possibility of adapting the focal spot and obtaining different power deposition patterns to reduce the heating of healthy tissues.

In this thesis, we explore whether the current SAR-based treatment planning methods can be meaningfully translated to the UWB setting and propose new solutions for deep UWB microwave hyperthermia. We analyze the most commonly used cost functions for treatment planning optimization and discuss their suitability for use with UWB systems. Then, we propose a novel SAR-based cost function (HCQ) for UWB optimization that exhibits a high correlation with the resulting tumor temperature. To solve for the HCQ, we describe a novel, time-reversal-based, iterative scheme for a rapid and efficient optimization of UWB treatment plans. Next, we investigate the design possibilities of UWB brain applicators and introduce a fast E-field approximation scheme to quickly explore a large number of array configurations. The method determines the best antenna arrangement around the head with respect to the multiple objectives and requirements of clinical hyperthermia. Together, the proposed solutions manage to achieve the level of tumor coverage and hot-spot suppression that is necessary for a successful treatment. Finally, we investigate the benefit of integrating hyperthermia delivered by an optimized UWB applicator into the radiation therapy plan for a pediatric medulloblastoma patient. The results suggest that UWB microwave hyperthermia for brain cancer treatment is feasible and motivate efforts for further development of UWB applicators and systems.

Keywords: microwave hyperthermia, treatment planning, brain cancer.

List of Publications

This thesis is based on the following publications:

[A] **Massimiliano Zanoli**, Hana Dobšíček Trefná, "Suitability of eigenvalue beamforming for discrete multi-frequency hyperthermia treatment planning". *Medical Physics*, 2021.

[B] **Massimiliano Zanoli**, Hana Dobšíček Trefná, "The hot-to-cold spot quotient for SAR-based treatment planning in deep microwave hyperthermia". *Submitted to the International Journal of Hyperthermia*, 2022.

[C] **Massimiliano Zanoli**, Hana Dobšíček Trefná, "Iterative time-reversal for multi-frequency hyperthermia". *Physics in Medicine & Biology*, 2020.

[D] **Massimiliano Zanoli**, Hana Dobšíček Trefná, "Antenna arrangement in UWB helmet brain applicators for deep microwave hyperthermia". *Submitted to Cancers*, 2022.

[E] Morteza Ghaderi Aram, **Massimiliano Zanoli**, Håkan Nordström, Iuliana Toma-Dasu, Klas Blomgren, Hana Dobšíček Trefná, "Radiobiological Evaluation of Combined Gamma Knife Radiosurgery and Hyperthermia for Pediatric Neuro-Oncology". *Cancers*, 2021.

Other publications by the author, not included in this thesis, are:

[F] **Massimiliano Zanoli**, Mikael Persson and Hana Dobšıcek Trefná, "Self-calibration algorithms for microwave hyperthermia antenna arrays". *12th European Conference on Antennas and Propagation*, 2018.

[G] **Massimiliano Zanoli** and Hana Dobšıcek Trefná, "Optimization of microwave hyperthermia array applicators using field interpolation". *2019 IEEE International Symposium on Antennas and Propagation and USNC-URSI Radio Science Meeting*, 2019.

Acknowledgments

Thank you for thoroughly reading this thesis.

Contents

E **E1**

Part I

Overview

CHAPTER 1

Introduction

Cancer represents the second leading cause of death worldwide [1]. While the survival rates for most types of cancer have seen a steady improvement over the past decades, certain tumor types seem to have been excluded from this positive trend. For instance, cancers of the central nervous system, the pancreas, the bowel, and the lungs [2]. The brain in particular remains one of the most challenging sites to treat, as expressed by an extremely low 5-year survival rate of 22% in the 20-44 age group [3]. Together with short life expectancy, currently available brain cancer therapies are also associated with potentially severe, long-lasting side effects. Survivors often experience seizures, walking difficulties, speech problems, and a wide range of other disorders for the rest of their lives [4]. The situation is worse in pediatric patients, where brain tumors are the second most common form of cancer after leukemia. Modern therapies can cure more than 75% of all children struck with cancer [5], but they entail severe acute and long-lasting side effects. Even low doses of ionizing radiation to the brain can cause cognitive impairment as well as growth disorders [6]–[8]. Therefore, there is a strong need for complementary therapies with low toxicity that can reduce the amount of radiation administered to the patient without compromising the treatment outcome.

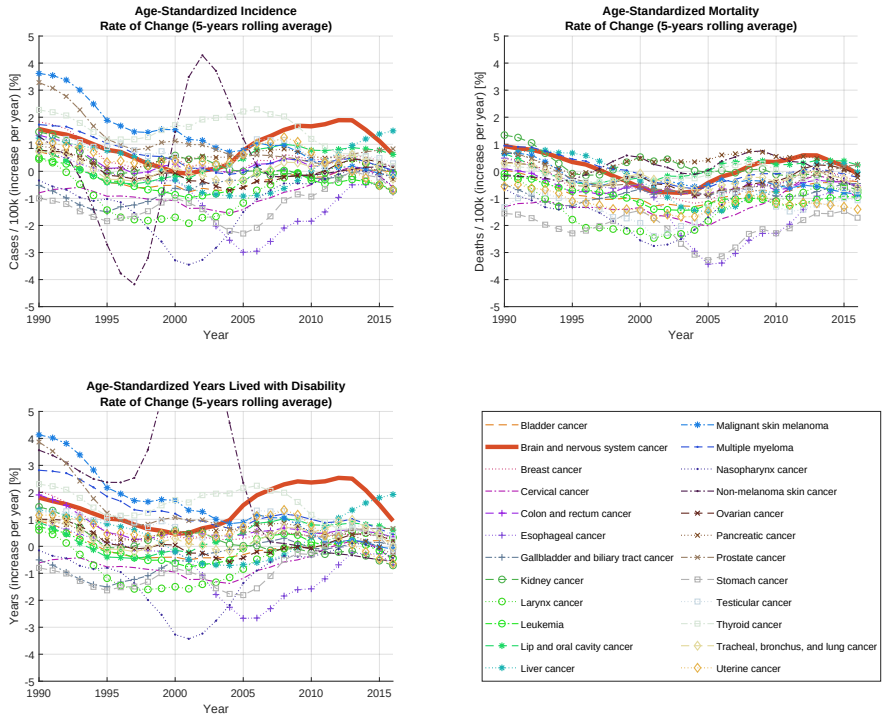

Figure 1.1: Overall age-standardized rate of change of the cancer-related incidence, mortality, and amount of years lived with a disability considering patients all over the world over the past 30 years. The trend for brain and nervous system cancers is highlighted in solid **red**. While the absolute incidence of these cancers is lower compared to other types, the relative figures indicate that this measure is increasing for brain cancers. In particular, the quality of life of brain cancer survivors, unlike most other patients, has never really improved over the last decades, as shown by the bottom left figure.

Hyperthermia appears to be an ideal candidate for this purpose. After a number of results below expectations in the 1980s, followed by a period of skepticism [9], caused mostly by technological limitations and lack of knowledge over the complex, temperature-dependent biological mechanisms in the human body, this form of thermal therapy has seen a major revival in the past decade [10]. Recent meta-analyses and reviews have managed to collect an impressive amount of evidence documenting its positive adjuvant effects when applied in combination with radio- or chemo-therapy [11]–[14]. These analyses have demonstrated a significant increase in tumor control probability and even survival rate in some cases with no added toxicity [15], [16]. Yet, to date, only few clinical trials have seen the application of microwave hyperthermia as a treatment modality for brain tumors, albeit with encouraging results [17]–[19]. The reason behind this lack of confidence is the imperfect technology used to accurately deliver the prescribed thermal dose in the proximity of critical organs. For instance, in the glioblastoma study [19], despite the improved clinical outcome, homogeneous therapeutic temperatures were difficult to achieve with the interstitial methods used. Thanks to the exponential growth of computational capabilities and the development of microwave technology for communication purposes, we are now able to simulate with far greater accuracy the scattering of high-frequency electromagnetic waves inside the body and provide better control of the radiation during treatment. This enables the design of external antenna arrays capable of focusing the heat selectively into the tumor, thus achieving thermal therapy in its most sophisticated form: deep microwave hyperthermia for brain cancer treatment.

1.1 Thesis concept

Intracranial heating is a demanding task. In order to achieve high thermal doses and complete tumor coverage in such a delicate area, microwave hyperthermia systems have to be refined in all their parts to reach the necessary accuracy and precision. Today's loco-regional systems, which are successfully employed in the treatment of abdomen, extremities, and neck cancers, rely on a single and fixed operating frequency. This choice comes with many benefits, such as the possibility of being implemented via a simple and robust RF design, but it also involves some limitations. The main constraint of single-frequency systems is the inability to adapt the size of the focal spot to the

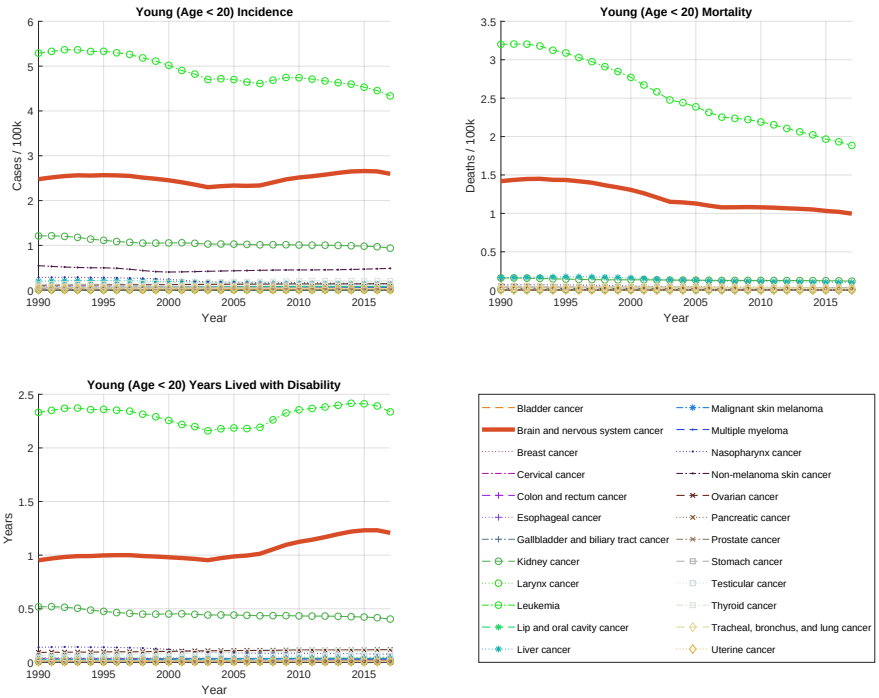

Figure 1.2: Cancer-related incidence, mortality, and amount of years lived with a disability, considering young patients all over the world over the past 30 years. The trend for brain and nervous system cancers is highlighted in solid **red**. Brain tumors are the most common solid-type cancers in children, but unlike leukemia, their incidence has not been decreasing over the past decades. A slight improvement in mortality rates has however led to a huge increase in the number of years spent with disabilities for these patients, indicating a strong need for therapies with lower toxicities and fewer after-treatment complications.

particular tumor size and location. We strongly believe that UWB systems are necessary to fulfill the rigorous requirements of microwave hyperthermia treatments in the brain, since they introduce a new degree of freedom in the formation of the power deposition pattern inside the body. The shift towards USB systems is however not trivial, and it implies a revision of hyperthermia treatment planning algorithms, together with a careful redesign of the RF steering systems. A second limitation comes from the antenna array applicators, which nowadays are meant to target a body region rather than a particular tumor. In our opinion, a generic applicator will always struggle to reach optimal heating patterns in brain cancer patients, due to the added difficulties in the treatment of this site. A paradigm shift in the applicator design is thus necessary: from regional applicator arrays to target-specific ones. Exploring possible array designs and validating them for each case, however, is a burdensome task. Fast array simulation techniques and treatment planning methods are necessary to let us survey all the possible combinations of antennas and frequencies for a specific patient. In this thesis, we focus on the development of fast UWB treatment planning algorithms and on the design of (patient) specific (brain) applicators, which will help address these questions.

1.2 Thesis outline

This thesis is organized as follows. In Chapter 2, the concept of hyperthermia therapy is introduced along with a brief summary of the main challenges faced and current clinical implementations. The scope is then narrowed down to the application of microwave hyperthermia (MW-HT) for deep-seated tumors. The implications of moving towards a UWB setting on the applicator design and treatment planning optimization are subsequently explained, and the potential benefits of UWB treatments for brain cancer are discussed.

Chapter 3 begins with an overview of the challenges faced in electromagnetic and thermal modeling. The treatment planning (TP) phase of MW-HT, which is extensively based on computer simulations, is described, and several approaches to this problem are discussed. The author's novel contributions of a temperature-correlated cost function and an iterative time-reversal scheme for SAR-based TP optimization are reported and compared to the clinical standards.

The investigations carried out on how to put together an optimal antenna array applicator for MW-HT are reported in Chapter 4. Here, the design of the array is discussed from the UWB perspective. A field interpolation technique to quickly evaluate many potential array configurations is described and utilized to propose a nearly-optimal applicator design for a specific patient and tumor anatomy. The method is applied to the specific case of a pediatric medulloblastoma patient, and the clinical benefit of integrating hyperthermia into the radiation therapy plan is demonstrated.

Chapter 5 includes a discussion on the hardware needed to implement such a helmet applicator and describes the ongoing efforts in manufacturing a robust MW-HT system for head, neck, and brain cancer treatment. The chapter ends with general remarks about the remaining technological challenges in hyperthermia and suggestions on how to address these. The author's paper contributions are summarized thereafter and reported at the end of the thesis.

CHAPTER 2

(Microwave) Hyperthermia

Thermal therapy has been known to humankind as a way to treat diseases ever since ancient times. In many examples throughout history, physicians attempted, often successfully, to cure diseases by means of induced fever or burn malignancies with incandescent sticks or blades [20]. Heat is also a fundamental component of the body's natural self-defense mechanisms. Local and systemic responses, triggered by the presence of pathogens, are often associated with inflammation or fever, implying a temperature increase in the tissue or body, respectively. In the past, the temperature rise was seen as a mere consequence of the increased metabolic activity necessary for the fight, but nowadays, this is no longer the general view among immunologists. In fact, it has become more and more evident that the elevated temperature has a role in itself, enhancing the activity and efficacy of our immune system, even in the absence of pathogens [21].

With time, researchers have unveiled a number of microscopic and macroscopic, local and systemic, biological and physiological effects of heat and elevated temperature on the body [22], [23]. These mechanisms point toward a strong therapeutic potential of artificial temperature elevation in the treatment of cancers and other diseases. Treatment methods relying on the external

administration of heat are nowadays divided into two categories: thermal ablation and *hyperthermia*. The aim of the first is to kill the tumor cells by literally burning them, which requires temperatures > 45 °C. The method is highly localized and carried out by means of invasive procedures [24]. Modern mild hyperthermia for cancer treatment, on the other hand, is defined as the elevation of the tumor temperature to $40 \sim 44$ °C [25]. This range of temperatures has been shown to trigger a number of mechanisms at a molecular and tissular level that considerably improve the tumor response to traditional cancer therapies such as radio- and chemotherapy [26], [27], Fig. 2.1. Hyperthermia is thus seen today as a potent adjuvant modality to these two main practices, and its inclusion has been shown to enhance survival rate and tumor control probability for a number of cancer types [10]–[13], [16].

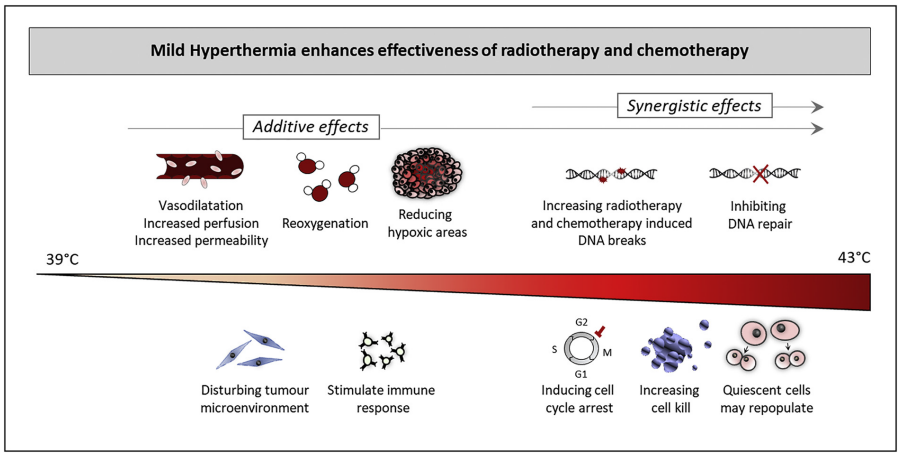

Figure 2.1: Summary of the additive and synergistic effects of mild hyperthermia on radiotherapy and chemotherapy, from [28]. Vasodilation increases blood perfusion resulting in deeper penetration of chemotherapeutic agents; increased oxygenation enhances the induction of DNA breaks by radiotherapy; disturbances in the tumor micro-environment stimulate the immune responses; inhibition of the DNA repair mechanisms enhances the damage provoked by radio- and chemotherapy.

Unfortunately, the optimal temperature of 43 °C, as suggested by biological studies [28], [29], is usually not achieved inside the target in clinical practice [30]. The reason behind this is the imperfect technology utilized in delivering

the prescribed thermal dose to the target volume [31]. From a biomedical engineering perspective, the task of reaching a predefined and controlled temperature distribution in a biological tissue *in-vivo* is indeed a challenging task. The ability of living organisms to maintain homeostasis is extraordinary, and the body will use all its means to counteract the artificially administered heat. As soon as the local temperature deviates from the set level of 37 °C, blood perfusion and sweating increase to remove the excess heat. This response is non-linear and can vary significantly from patient to patient. This renders external heat delivery a demanding technique whose implementation requires careful and robust design. On top of this, the monitoring of the actual temperature distribution inside the patient during treatment, necessary for the assessment of the thermal dose, is by no means a trivial task [32]. All these aspects have to be taken into account and addressed when designing a reliable system for hyperthermia treatments.

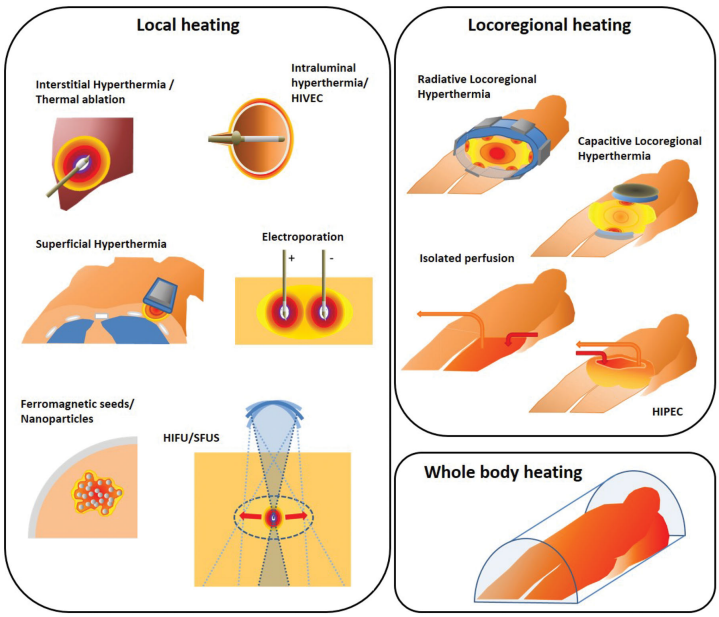

Figure 2.2: Graphic summary of the techniques available for the administration of the thermal dose in hyperthermia treatments, from [33].

The list of technologies available today to deliver hyperthermia is long [33], Fig. 2.2. However, only a few of them have been applied in the treatment of brain tumors. Among the techniques proposed in the past two decades to selectively induce a temperature increase [34], only interstitial hyperthermia, magnetic nanoparticle hyperthermia, and high-intensity focused ultrasound (HIFU) have been clinically applied to deep-seated brain tumors. Interstitial hyperthermia combined with brachytherapy applied to high-grade glioblastomas has been demonstrated to be a safe and attractive modality to improve the survival of these patients [35], [36]. Despite the promising results in terms of an improved treatment outcome, homogeneous tumor temperatures were difficult to achieve with the interstitial applicators used. More recently, the use of magnetic fluid hyperthermia to enhance heating precision was investigated [37]. Results demonstrated an increase in tumor temperatures and higher overall survival than conventional therapies [38], [39]. The disadvantage of this technology lies in the direct injection of iron oxide nanoparticles into the tumor. These nanoparticles can remain in the treated area for a lifetime, thus hindering the patient from undergoing future MRI scans, which is, despite the (minimally) invasive procedure, a clear limitation of this technique. HIFU provides localized energy delivery through small volumetric sonifications from an ultrasound phased array transmitter to destroy intracranial lesions by thermocoagulation [40]. Heating of large volumes, as is usually the case for childhood brain tumors, is nevertheless still demanding with the present technology. Furthermore, ultrasound based treatments suffer from high energy losses in the bone structures, and despite novel technical solutions, its implementation in the brain will very likely be limited to tumors located centrally and at a distance from the skull [41].

Microwave hyperthermia, which relies on the non-invasive deposition of focused EM energy into the tumor by a phased array of antennas [14], [25], has the potential to circumvent these limitations and achieve therapeutic temperatures in brain tumors without the need for surgical interventions [42]. However, several technological challenges must first be resolved to provide the centimeter-scale spatial control needed to compensate for vascular cooling in living tissues and to deal with the small anatomical features of the head. The typical setup for a non-invasive microwave hyperthermia treatment is shown in Fig. 2.3. The patient lies on a treatment bed or chair, and a so-called applicator is placed around the region to be treated. The applicator consists

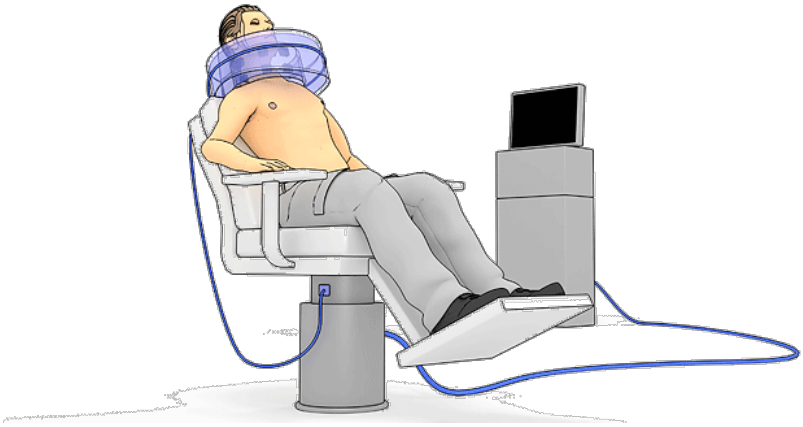

Figure 2.3: Microwave hyperthermia for cancer treatment, conceptual drawing.

of a phased array of antennas and a water bolus. The water bolus has two purposes: to realize an impedance match between the antenna and the patient and to cool the skin and dampen superficial hot spots. Each channel of the applicator array is independently steered in amplitude and phase to shape the interference pattern and power loss deposition inside the patient. In the case of a discrete multi-frequency UWB system, each frequency can be steered independently from the others, and the power loss is given by the superposition of the interference patterns at all frequencies. The RF amplifying system must deliver the phase-locked signals with adequate accuracy and precision. Deviations of amplitude and phase in modern hyperthermia systems do not exceed $\pm 5\%$ and $\pm 5°$ respectively from the nominal value [43], [44]. Because of the high power that each channel is supposed to deliver for adequate heating, the antennas must exhibit high directivity and low cross-coupling. Current clinical hyperthermia systems operate over a narrow frequency band, which makes their construction relatively simple. Examples are $70, 100$ MHz for the pelvic and abdominal region [45], [46] and 434 MHz for the head and neck [47]. Of course, if a UWB hyperthermia system is to be deployed, both the antennas and the RF cascade must be adapted to operate across the entire target frequency band. This represents an additional layer of difficulty with respect to the current technology.

Despite the impressive advances that microwave hyperthermia has witnessed in the past 30 years, present treatments (still) suffer from the inability to adequately heat tumors in several regions that could benefit from this type of therapy. This has resulted, among other things, in the study of Sneed *et al.* [36] being the sole experience with microwave heat delivery into the brain, albeit with promising results. We believe that the lack of accurate thermal dose delivery and reliable temperature monitoring in this region has made it extremely difficult to properly trace a dose-effect relationship. Fortunately, there is mounting evidence that the development of UWB applicators capable of operating at different frequencies can lead to improved target coverage and hot-spot suppression [48]–[50], which might once more motivate efforts in the development of brain applicators [51]–[53].

A UWB system can exploit the complementary interference patterns generated by different frequencies to increase the average net power delivered to the tumor while reducing the absorption in healthy tissues. This is expected to benefit treatments in the brain region, which is characterized by a combination of anatomical and physiological factors that require an extra degree of accuracy in the formation of the heating pattern. The cerebral tissue is more sensitive to deviations in temperature than other tissues [54], and the presence of cerebrospinal fluid, highly conductive at microwave frequencies [55], can cause strong and treatment-limiting hot spots to appear in the immediate vicinity of the brain. Yet, recent developments suggest that implementing microwave hyperthermia for brain cancer treatment is within reach [42]. However, tangible clinical evidence is necessary to gain the trust of oncologists and the medical community. A crucial precondition to successful clinical trials is the development of reliable hyperthermia systems and robust treatment planning methods. In the following chapters, we discuss how treatment planning optimization algorithms can be extended into the UWB domain and how these can be used in the design of UWB-optimized applicators for brain cancer treatment.

CHAPTER 3

Treatment Planning

Treatment planning is a fundamental stage of microwave hyperthermia treatments [56]. It consists of several steps aiming at determining the set of steering parameters that yield high temperatures in the tumor while sparing the surrounding healthy tissues from excessive heat, Fig. 3.1. In the case of deep hyperthermia administered by phased array applicators, the steering parameters are the amplitude and phase of each antenna. Varying these settings affects the wave propagation inside the patient and shapes the EM interference pattern and consequent power deposition. Historically, the tuning of the parameters in single-frequency applicators with up to a handful of independent channels has been performed manually with the help of EM probes [57]. The task is often carried out qualitatively, and with little information about the resulting power loss distribution inside the patient. Clinical experiences gathered over time, however, revealed that it is crucial to identify the location and severity of power deposition peaks, as these often lead to *hot spot*s in healthy tissues. When a hot spot is identified during treatment, the system output power has to be throttled to prevent discomfort, pain, or even burns in the patient, thereby effectively limiting the maximum achievable temperature in the target [58]. Today, clinical applicators can reach up to 12 independently

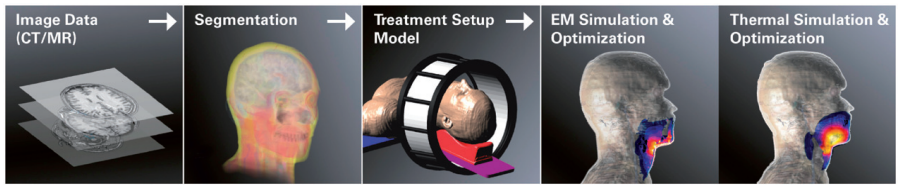

Figure 3.1: Stages of microwave hyperthermia treatment planning, from [60].

steered channels [47], and the problem of determining the optimal amplitude and phase settings for each antenna has become non-trivial. The situation is further complicated if a UWB system is to be deployed: the task of choosing the optimal combination of operating frequencies and their weight in the treatment plan is quite involved, and a global optimum is hard to determine [59].

Hot spots can arise in the healthy tissues as these lie in the path between the antennas and the target. As a consequence of their relatively high conductivity at microwave frequencies [55], tissues tend to absorb energy from the traveling wave and heat up. This is aggravated by the anatomical heterogeneity and the presence of (sharp) interfaces between tissues with different dielectric properties, which cause multiple reflections and localized intensity peaks. The imperfect interference pattern generated by the limited-aperture phased array also contributes to the uneven localization of the energy losses. The threshold temperature for hot-spot-related complaints is typically $\approx$ 45 °C [61]. However, in the brain, damage and thermal related toxicity can be detected already with temperatures above $\approx$ 42 °C [54]. It is therefore mandatory to manage occurring hot spots before and during treatment. Superficial hot spots within depths of one to two centimeters from the skin can be suppressed by applying a water bolus circulated with cool water. Hot spots that arise in deeper locations, however, are more difficult to address. The sole strategy to suppress or limit those hot spots is to reduce the power deposition at those locations while preserving the constructive interference (focus) in the target volume. The problem is challenging, but it can be tackled with the help of optimization algorithms.

A plethora of methods to determine the optimal amplitudes and phases for an applicator array have been reported in the literature and are still the subject of ongoing research [60], [62]. These methods can be classified into two

main categories: specific absorption rate (SAR) based and temperature (T) based. SAR-based techniques rely on the assumption that the SAR distribution is predictive of the temperature distribution in the patient [63]. However, since the thermal response of the body can be highly non-linear, SAR-based optimizers can yield sub-optimal, while still clinically relevant, steering solutions. On the other hand, T-based optimizers have evolved to include complex non-linear aspects such as discrete vasculature and systemic response under thermal stress [64]. Ideally, a full implementation of T-based treatment planning in the clinical routine is desirable since temperature is the objective dose [65]. In practice, however, the theoretical benefits of T-based optimizations are somewhat diminished due to the lack of accurate estimations of the thermal tissue properties [66]–[68]. These properties, and blood perfusion in particular, exhibit large variations across patients and differ even at an individual level between different sessions. As a result, both SAR-based and T-based approaches are being clinically applied as both require adjustments during treatment in response to hot spots [69], [70]. One clear advantage of SAR, however, is its reduced computational complexity and its direct relation to the steering parameters. In this work, we exploit these benefits and develop SAR-based methods that allow a quick comparison of a large number of treatment plans.

3.1 Patient modeling

In today's state-of-the-art treatment planning for microwave hyperthermia, virtual patient models are used to simulate the wave propagation in the body in conjunction with the specific applicator model in use [62]. The patient models are obtained from CT or MRI scans and subsequently segmented into a discrete number of tissues [71]. How detailed the segmentation should be, depends on the frequency utilized by the applicator as well as on the region to be treated. A study to determine the impact of the number of segmented tissues in the pelvic region on the SAR distribution revealed the importance of properly representing high water content tissues [72]. On the one hand, the set of segmented tissues must be limited to avoid over-fitting. On the other hand, all the spatial variations in electromagnetic properties that might affect the wave propagation have to be captured, as well as all critical healthy tissues where a strict temperature limit must be enforced.

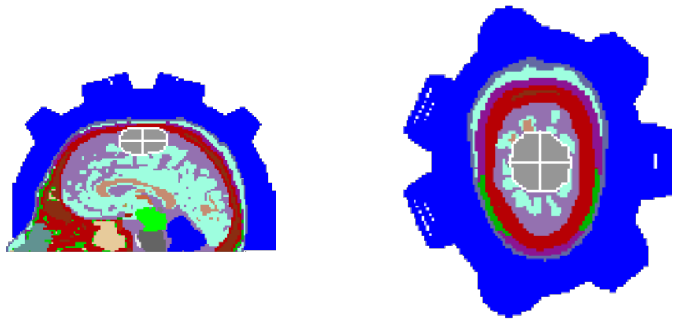

(a) Sagittal **(b)** Transverse

Figure 3.2: Example of a patient model, discretized at a resolution of 2 mm. The model encompasses the upper head and is terminated at the level of the nose to reduce its computational weight. The applicator and water bolus are also included (blue shape). The target, a 30 ml meningioma, is outlined in white.

The second aspect of patient modeling is the resolution. In the pelvic area, for instance, clinical treatment planning tools utilize resolutions of $2.5 \times 2.5 \times 2.5$ mm for both simulation and optimization purposes [70]. Conversely, in the neck region, the current practice is to perform a high-resolution simulation of the wave propagation followed by a lower resolution optimization step at $5 \times 5 \times 5$ mm [69], [73]. This is done to keep the computational burden of the optimization process at bay and enable online real-time adaptation of the steering parameters upon patient complaints. Whether this resolution is sufficient to capture the wave scattering in small anatomical features such as nerves and bones is however uncertain. In intracranial heating, the presence of the skull, whose thickness can be as little as 3 mm [74], is particularly relevant, as bone exhibits notably different dielectric properties than soft tissues. If the discretization is realized on a hexahedral grid, the maximum allowable voxel size has to be further restricted in order to properly sample the skull's curvature. Another critical issue is the presence of cerebrospinal fluid, due to its proneness to heating at microwave frequencies. The interconnected cavities where this fluid is free to move are also characterized by narrow passages and

thin strati. Consequently, all computations in this work have been realized on head models with resolution $2 \times 2 \times 2$ mm.

The subsequent phase in patient modeling is the assignment of the dielectric and thermal properties to the segmented tissues. As already mentioned, tissue properties exhibit large variations across the population and are difficult to obtain for a specific patient. Such variations depend on the person's age [75], fitness level, and other factors. The variation is typically larger for thermal properties than for electromagnetic ones [68]. In addition to the variance across the population, intra-patient variations can also be possible between subsequent treatment sessions. This is due to the body adapting to environmental and behavioral changes to better preserve its homeostasis. Factors that can affect the tissue response include the ambient temperature, the patient's hydration level [76], or whether the patient has carried out any recent physical activity. Finally, most thermal tissue properties, and blood perfusion in particular, are dependent on the local temperature itself [77], [78]. This temperature dependence can strongly affect the plan and ultimately the effectiveness of the treatment. Nevertheless, a useful and relevant estimation of the wave propagation and resulting thermal distribution inside the treated area can still be obtained with a good degree of approximation by relying on tissue property databases with modified perfusion values [66], [79]. The uncertainty in the resulting SAR and temperature distributions due to tissue property variations has been estimated to be around 20 % [80]. In the works reported here, all the healthy tissue properties have been obtained from the IT'IS database [55], a valuable collection of literature values from decades of measurements. To mimic the presence of a tumor in healthy patient models (Papers A and C), the artificial target volumes have been filled with a material exhibiting properties equal to the weighted average of the materials originally composing the volume. When the patient model included a tumor (Papers B and D), the average of the dielectric properties of all malignant tissues reported in [81] has been used instead, as recommended by [79]. Some thermal properties have been further adjusted to reflect the response of tissues to thermal stress: muscle perfusion is increased by a factor 4 due to the systemic response to heat [78], tumor perfusion is decreased by a factor 0.7 to account for its chaotic vasculature [82], and the thermal conductivity of the cerebrospinal fluid is increased by a factor 10 to emulate the convective transport of heat [42].

3.2 Simulation techniques

The next step in treatment planning optimization is to perform electromagnetic and thermal simulations [60], [62], by inserting the patient model in a virtual model of the applicator in use, which also includes the water bolus. The first simulation computes the E-field and power loss distributions generated by each antenna. A number of electromagnetic simulation methods have been described in the literature, either based on the differential or the integral form of Maxwell's equations. The electromagnetic field distribution can be calculated using either the finite-difference time-domain (FDTD) method or the finite-element (FEM) method. Both methods have seen wide application in biomedical engineering. Generally speaking, the FDTD method is more frequently used in hyperthermia treatment planning as it relies on hexahedral grids, which are easier to interface with patient voxel models. To avoid the reflection of the electromagnetic waves at the boundaries of the computational domain, a perfectly matched layer [83] is included. Once the E-field distributions are available, the resulting power loss distribution relative to each operating frequency is calculated by superposition after steering each channel in amplitude and phase according to the treatment plan (Section 3.4). The electromagnetic energy of the traveling wave is converted into heat as a consequence of the lossy nature of the tissue. The amount of energy absorbed in each point can be described by the SAR distribution, which measures the power loss per unit mass of tissue:

$$\mathrm{SAR}_f = \frac{1}{2}\frac{\sigma_f}{\rho}|E_f|^2 \tag{3.1}$$

where σ_f is the tissue conductivity at frequency f, ρ is the tissue density, and E_f the total electric field at this frequency. In a multi-frequency treatment plan, the overall power deposition can be obtained as the sum of the individual frequency components:

$$\mathrm{SAR} = \mathrm{SAR}_1 + \mathrm{SAR}_2 + \ldots + \mathrm{SAR}_f \tag{3.2}$$

The resulting temperature distribution inside the patient is estimated by means of a second, thermal simulation where the SAR term is included as a distributed heat source. The standard thermal modeling in hyperthermia treatment planning is based on Pennes' bioheat equation [84]:

$$\rho c \frac{\partial T}{\partial t} = k\nabla^2 T + \omega \rho_B c_B (T_B - T) + Q + \frac{\mathrm{SAR}}{\rho} \tag{3.3}$$

where ρ is the tissue's density, c the tissue's specific heat capacity, T the temperature, t is time, k is the tissue's thermal conductivity, ω is the tissue's blood perfusion coefficient, ρ_B is the blood's density, c_B is the blood's heat capacity, T_B is the blood's temperature, and Q is the heat generated by the tissue's metabolic activity. In the term representing the externally applied heat, the SAR is converted into volumetric power loss density (PLD). Pennes' equation describes the tissue's thermal behavior as a first-order dynamic system. By setting the time derivative on the left-hand side to zero, the steady state temperature distribution can be obtained, which shows the predicted location of hot spots and tumor temperatures. On this distribution, the temperature-based hyperthermia treatment quality indicators can be evaluated (Section 3.3), and the treatment's viability can be decided. In this work, the investigations reported in Papers A and C utilize CST Microwave Studio® as FDTD-based solver for both electromagnetic and thermal problems [85], while Papers B and D rely entirely on the FEM-based COMSOL® [86]. Both applications are established and validated commercial simulation software.

3.3 Treatment planning quality indicators

The goal of hyperthermia treatments is to achieve the prescribed thermal dose in the entire clinical target volume. For this to be possible, the thermal dose has to be defined with a quantitative measure. Since the therapeutic effect is reached by a combination of temperatures above 40 °C and prolonged exposure time, the dose metric has to capture these two notions simultaneously. To this end, the Cumulative Equivalent Minutes at 43 °C (CEM_{43}) metric has been proposed [87] and adopted in clinical trials [88]. The temperature exceeded by 90 % of the target volume is used as lumped temperature value for the evaluation of the metric, yielding $\mathrm{CEM}_{43}T_{90}$. The applicability of this metric in the context of the actual sub-optimal temperatures achieved in the clinics has been debated, but there appears to be consensus on the metric representing a good measure of the overall thermal dose [30], [89]. Another metric (TRISE) based on the median tumor temperature increase T_{50} and its duration has also been reported and correlated to clinical outcome [90].

Regardless of how one measures the cumulative dose, the minimum temperature recorded by a number of discrete invasive probes in the tumor during a session (presumably represented by T_{90} of a continuous distribution) has been directly related to treatment outcome in several clinical studies [65]. To a lesser extent, this relation has also been seen for the median temperature (T_{50}). In view of this, the treatment planning stage, where the steady-state temperature distribution is estimated and optimized, should aim at maximizing the temperatures in all parts of the tumor, with the only constraint of the maximum tolerable temperature in healthy tissues. Accordingly, we can assess the steady-state distribution using precisely the temperature indicators T_{90} and T_{50}. These, in turn, have been shown to correlate with the SAR-based indicators TC_{50} and HTQ when applied retrospectively to clinical data sets [91], [92]. These indicators are defined as follows:

- **HTQ**: hot spot to target quotient [93]:

$$\mathrm{HTQ} = \frac{\overline{\mathrm{SAR}}_{\mathrm{R1}}}{\overline{\mathrm{SAR}}_{\mathrm{T}}} \tag{3.4}$$

  i.e. the ratio between the average SAR in the sub-volume containing the highest 1-percentile SAR among the remaining tissues ($\overline{\mathrm{SAR}}_{\mathrm{R1}}$) and the average SAR in the target volume ($\overline{\mathrm{SAR}}_{\mathrm{T}}$). Values of HTQ around or below 1 are typically considered for clinical treatment.

- **TC_x**: iso-SAR target coverage [94]:

$$\mathrm{TC}_x = \frac{V_{\mathrm{T}}(x)}{V_{\mathrm{T}}} \quad , \quad V_{\mathrm{T}}(x) \;\mid\; SAR[V_{\mathrm{T}}(x)] \geq x \cdot SAR[V] \tag{3.5}$$

  i.e. the fraction of the target volume V_T where SAR values are above a given fraction x of the SAR peak value in the whole patient volume V. Both the TC_x value and the fraction x are usually expressed as percentage, and the TC_x index is evaluated in this work for $x = 25$ % or $x = 50$ % depending on the model at hand. Values of TC_{25} greater than 75 % are typically considered for clinical treatment.

This correlation enables the use of SAR as a surrogate for the temperature distribution during the treatment planning optimization process, thereby lowering the model complexity and saving computational resources. In particular, TC_{25} has been shown to directly correlate with clinical outcome [94].

However, point SAR, as given in Equation 3.1, has little value in terms of temperature prediction. In fact, Pennes' equation (3.3) acts as a spatial low-pass filter on the heat sources, while the SAR distribution is evaluated at the individual grid points and can therefore exhibit sharp changes at the tissue interfaces. Consequently, if the SAR distribution has to be used as a surrogate for the temperature, the point SAR has to be smoothed according to some averaging scheme. For instance, in SAR exposure standards for mobile phones and other body-contact RF devices, the evaluation of absorption peaks is carried out over a mass-averaged SAR distribution [95]. This approach is also adopted in hyperthermia treatment planning, and the averaging scheme involves the use of a convolution kernel whose size is increased until the mass of patient tissue inside it reaches a specified amount. The SAR values outside the patient or in internal lumina (trachea, esophagus, etc.) are excluded from the average, thus preventing surface hot spots from being potentially overlooked. The amount of averaging mass is however a matter of debate [96]–[99]. The consensus for low, non-medical exposures seems to lie on 10 g, which is also adopted in technical standards. For higher thermal doses, 1 g SAR mass averaging seems to be a better predictor of the temperature distribution [100]. During our internal evaluations, we noticed that the 1 g-based optimization in the brain region led to higher tumor temperatures than a 10 g-based one. Once again, this might be a result of the particular anatomy of the head, where the skull ($\approx$ 6 mm, [74]) is adjacent to a thin layer of skin ($\approx$ 5 mm, [101]) on one side and cerebrospinal fluid ($\approx$ 4 mm, [102]) on the other. All these tissues exhibit considerably different dielectric and thermal properties. In a rough estimation, assuming the kernel to be cubic and its contents homogeneous, the averaging cube for cortical bone ($\rho \approx 1900$ Kg/m^3, [55]) would be of side $\approx$ 1.7 cm in the 10 g case and $\approx$ 8.1 mm in the 1 g case . Conversely, in the case of skin or cerebrospinal fluid ($\rho \approx 1000$ Kg/m^3, [55]), the cube side becomes $\approx$ 2.1 cm (10 g) and $\approx$ 1.0 cm (1 g). Of course, where the cube is not entirely filled with a single tissue or part of it lies outside the patient, its size will vary in between these values or increase further. When compared with the anatomical layer thicknesses, these estimations suggest that 10 g averaging is

too coarse to capture the location and severity of hot spots in the superficial areas of the brain region, which absorb most of the incoming wave. Therefore, we opted for a 1 g SAR mass averaging scheme for all the treatment planning optimizations and distribution analyses reported in this work. One exception is the last study, Paper D, where we used a 5 g scheme due to the coarser patient model resolution. The averaging scheme is similar to the *CST Legacy* one as described in [103], albeit with a spherical kernel rather than cubic.

To further enhance the degree of correlation between the SAR and the temperature (increase) distributions, the cooling effect of the water bolus can also be modeled in SAR. Where the bolus is in contact with the patient, the skin surface is subjected to forced convective heat extraction, as long as $T_{\mathrm{WATER}} < 37\,^{\circ}\mathrm{C}$. The convection coefficient at this interface can be as high as $100\ \mathrm{W/m^2/K}$ [104]. At this rate, the water cooling effectively counterbalances the high SAR deposition in the first layers of tissue. This mechanism is known to affect the values of temperature in the body up to 1 cm of depth from the skin surface. One way to model this in SAR is to simply exclude the first centimeter of the patient surface in direct contact with the water bolus from the *remaining* mask (R) used in the evaluation of the SAR indicators. In Papers B and D, we do this by expanding the bolus mask in the 3D matrix model with a morphological operation using a spherical kernel of radius 1 *cm* and 2 *cm*, respectively, and subtracting it from R. This operation must not affect the areas of the patient that are in contact with air (including internal lumina), because typical values of natural convection at the air/skin interface lie in the order of $8\ \mathrm{W/m^2/K}$ [105] and do not justify neglecting the externally applied heating.

3.4 Treament planning optimization

Many approaches to determine the optimal amplitudes and phases for each antenna in the applicator have been proposed, as summarized in excellent reviews [60], [62]. These steering settings aim at maximizing the thermal dose. In particular, the multiple objectives of the hyperthermia treatment plan optimization problem, i.e., high target temperatures with extensive coverage and limited temperature increase in healthy tissues, are mathematically described by a lumped cost function. Different optimization algorithms, either direct or iterative, are then applied to solve for this cost function.

Cost functions for SAR-based optimization

In a study by Canters *et al.* [63], a number of cost functions for SAR-based treatment planning were summarized and analyzed in terms of their correlation with the temperatures achieved in the patient. As a result, the HTQ (Equation 3.4) was proposed and implemented in the clinical routine at the Erasmus University Medical Center, Rotterdam, The Netherlands [91]. Another, widely used, cost function is the target-to-remaining average SAR ratio defined in the early days by Böhm *et al.* [106] as follows:

$$\mathrm{SAF} = \frac{\overline{\mathrm{SAR}}_{\mathrm{T}}}{\overline{\mathrm{SAR}}_{\mathrm{R}}} \tag{3.6}$$

where SAF stands for SAR Amplification Factor, $\overline{\mathrm{SAR}}_{\mathrm{T}}$ is the average SAR in the target, and $\overline{\mathrm{SAR}}_{\mathrm{R}}$ is the average SAR in the remaining healthy tissues. The main benefit of SAF is that a ratio of quadratic polynomials in the unknowns (the steering parameters) can be solved directly using eigenvalue (EV) decomposition. When the resulting SAR (or temperature) distribution shows overheated healthy regions, a weighting factor can be introduced to iteratively reduce the power deposition at those locations [107], [108]. EV is a direct method that provides a fast and deterministic solution and has therefore been used extensively in clinical hyperthermia treatment planning. However, it is unclear whether solving for the maximum SAF ratio actually yields the highest and most homogeneous possible temperature distribution in the tumor. In fact, the analysis of Canters *et al.* [63] revealed that quadratic cost function predictions correlate poorly with the temperature rise in the target volume during clinical treatment. Yet, still to date, SAF and EV-based optimization methods are considered a means to evaluate the heating capabilities of an applicator design prior to its clinical use [109]–[111]. Furthermore, the role of the SAF ratio as a cost function for multi-frequency UWB treatment planning remains unclear.

We have therefore investigated the suitability of EV and SAF for single- and multi-frequency hyperthermia treatment planning in Paper A. Here, we show that the SAF ratio (3.6) cannot be maximized by more than one frequency at a time. In particular, even when the EV solver is complemented by an iterative optimization procedure that minimizes for another cost function, for instance, the HTQ as in [108], the final solution will always consist of only one operating frequency, regardless of how many frequencies are available for

concomitant treatment. Is this a problem for deep microwave hyperthermia? Is it a strong limitation to use only one frequency for treatment, as long as this frequency can be selected across a wideband range? Can the use of multiple operating frequencies improve target coverage and hot-spot suppression thanks to their complimentary interference patterns? To answer these questions, we went a step further and analyzed two realistic test cases, a tumor in the larynx and a tumor in the meninges. We compared the resulting temperature distributions when a single frequency is used to the case when two simultaneous frequencies are jointly optimized with respect to their overall SAR distribution. The latter optimization had to be carried out using some other cost function than (3.6) and a solver other than EV (in this case, the Particle Swarm global stochastic optimizer). Results for the larynx indicated that a single frequency treatment is sufficient to reach satisfying values of T_{50} and T_{90} in this region, and that adding a secondary frequency would not improve the thermal distribution further. However, when targeting a brain tumor, introducing a second frequency would increase SAR target coverage, TC_{50}, by 10 points, and temperature coverage, T_{90}, by 0.5 °C with respect to the best single-frequency solution (from 40.9 °C to 41.4 °C). In terms of $CEM_{43}T_{90}$, such an increase would correspond to a doubling of the thermal dose. This means that multi-frequency systems do have some potential to improve hyperthermia in regions typically difficult to treat, such as the brain, or the treatment of particular tumor shapes and locations.

Unfortunately, filling the gap between a UWB single-frequency RF system (where any single frequency across an octave bandwidth can be selected) and a UWB multi-frequency one (where any combination of frequencies across the octave can be selected for simultaneous radiation) is complicated and costly in terms of hardware design, especially if the strict requirements on amplitude and phase lock have to be met for each frequency [112]. A workaround could be to operate a UWB single-frequency system in finely time-interleaved sequences, switching from one operating frequency to another, and to exploit the temporal superposition of the power deposition patterns. This approach might work inasmuch as the switching period is so small that it does not induce relevant variations (< 0.1 °C) in the steady-state temperature distribution during the whole treatment. To avoid this, the switching period should be orders of magnitude smaller than the typical thermal washout rates measured in clinical sessions [113].

A relevant question to be asked at this point is: if SAF is not an appropriate cost function for treatment planning optimization, what cost function should be used to fulfill all the requirements of hyperthermia treatments and to fully exploit the potential of multi-frequency systems? At first glance, the HTQ (3.4) seems to be a promising candidate. The definition of HTQ includes a non-linear term through the evaluation of the highest 1-percentile SAR in the healthy tissues. Because of this, it is not subject to the single-frequency limitation that affects SAF. As mentioned before, HTQ is also used as a treatment quality indicator, and the correlation of its inverse, 1/HTQ, with the temperature increase in the target has been shown. However, HTQ is not the sole SAR-based treatment quality indicator. TC_{25} and TC_{50} (3.5) need also be evaluated to determine the viability of a plan prior to treatment. Yet, the relationship between these indicators is not straightforward. It is unclear, for instance, whether they assess contrasting objectives in treatment planning or if their optimal SAR distributions correspond. Furthermore, the limitations of both indicators when used as cost functions for treatment planning optimization should be clarified. The HTQ aims at suppressing the most relevant hot spot in the healthy tissues while raising the average power deposition in the target. Therefore, it does not account for inhomogeneities of the SAR distribution inside the target volume. As a direct implication, a low HTQ value, which would suggest a "good" plan, can be achieved with SAR distributions comprising narrow localized peaks in the tumor, while leaving most of the target volume uncovered and untreated. On the other hand, the TC_x indicator, if improperly used as a cost function, aims at extending the SAR coverage throughout the target volume with respect to a fixed fraction of the overall SAR peak inside the patient. This implicitly neglects the possibility to deliver more raw power to the target, i.e., when the SAR in the target can exceed this fixed fraction of the peak.

In view of these considerations, we investigated the relationship between HTQ and TC_{50} in [114]. In this study, we consider two realistic test cases of a larynx and a meningioma treatment and obtain the optimal plans with respect to HTQ and TC_{50}. The results confirm that the two indicators assess different and not necessarily correlated aspects of the plan. In particular, optimizing for the HTQ often yields too low values of TC_{50}, indicating poor coverage. An analog issue occurs when optimizing for TC_{50}: the resulting HTQ is systematically high. To circumvent this, we proposed a novel cost

function for deep microwave hyperthermia treatment planning whose aim is to combine the aspects assessed by HTQ and TC_x into one metric. The cost function, called the *hot-to-cold spot quotient* (HCQ), is defined as:

$$\mathrm{HCQ}_p = \frac{\overline{\mathrm{SAR}}_{Rq}}{\overline{\mathrm{SAR}}_{Tp}}. \tag{3.7}$$

where $\overline{\mathrm{SAR}}_V$ indicates the average SAR in volume V, while Rq (Tp) represent the q-percentile (p-percentile) sub-volume of healthy (tumor) tissue with highest (lowest) SAR. We fix the relationship between the two percentiles as:

$$q = p\frac{|T|}{|R|} \tag{3.8}$$

where $|V|$ is the size of the volume V. As in the HTQ, the purpose of the hot-spot term in the numerator is to suppress potentially treatment-limiting SAR peaks in the healthy tissues. The cold-spot term in the denominator, on the other hand, makes sure that all areas of the target volume are covered by sufficient SAR deposition for homogeneous heating. The relationship (3.8) guarantees that the HCQ is always normalized to the patient and target volume, rendering values of HCQ from different plans comparable.

In Paper B we thoroughly characterize this metric and validate it on a standardized patient repository prepared by the European Society for Hyperthermic Oncology (ESHO) [79]. The repository consists of six patients with targets in the pelvic region, the breast, and the head and neck. In general, HCQ-optimal solutions exhibit intermediate values of HTQ and TC_x, efficiently compromising between the two goals. Upon thermal simulation, HCQ-optimal plans produce higher minimum and median tumor temperatures than HTQ-optimal ones for the same maximum healthy tissue temperature. More importantly, the value of $1/\mathrm{HCQ}_p$ shows a higher degree of correlation with the corresponding temperature percentile $\mathrm{T}_{(1-p)}$, suggesting that the metric is a good predictor of the final treatment plan quality when evaluated on the mass-averaged and surface-treated SAR distribution. In a few patients, HCQ also promotes frequency diversity by letting some channels inject power at a second operating frequency to improve coverage. In one superficial breast case, however, the correlation between 1/HCQ and the temperature deteriorates severely, yielding a poor plan. This is due to the water bolus being close to the target volume and its convective cooling effect suddenly playing

an active role in determining the target temperature distribution. In this case, the treatment becomes more of a superficial one, and the water temperature itself should be included in a T-based optimization process [115]. It can be concluded that the single cost function formula (3.7) provides the means for an effective SAR-based UWB treatment plan optimization for deep-seated targets and enables meaningful comparisons between different solutions.

Algorithms for optimization

While non-linear cost functions yield more clinically relevant treatment planning solutions than quadratic ones, the price to pay is the impossibility of directly determining these solutions. Unlike the SAF ratio, non-linear cost functions require iterative optimization schemes. In modern clinical planning tools, the optimization is carried out by global stochastic optimizers, mainly Particle Swarm (PS) [116]. Another alternative is the use of genetic algorithms, as they allow for multi-objective optimization [117]. While these solvers can find the global optimum of any given problem with high probability, they suffer from slow execution times while demanding large computational resources. This drawback conveys relevant limitations for online treatment planning re-optimization, which is mandatory in clinical practice [70]. As discussed above, planning tools based on stochastic optimizers require coarse patient model resolutions to maintain real-time usability. However, for intracranial hyperthermia treatments, denser sampling grids and more detailed patient models are necessary. This calls for faster alternatives to stochastic optimizers. So far, only a few UWB solvers have been suggested, with a vast majority of them involving the use of quadratic-programming optimization [50], [53], [118]. As such, these solvers cannot be applied to non-linear cost functions, and neither are they able to return the HCQ-optimal distribution. Consequently, there is a need for fast iterative UWB solvers that can solve for non-linear cost functions.

One promising method is Time Reversal (TR). TR-focusing is a fast, intrinsically wide-band, and deterministic method that has been proposed and validated as an alternative treatment planning optimization technique for microwave hyperthermia [119], [120]. TR processing is a well-characterized inverse filter initially developed for focusing ultrasound pulses generated by transducer arrays inside a biological target [121], [122], and subsequently extended for use with electromagnetic antenna arrays [123]. It exploits the time

and space reciprocity of the wave equation to determine the optimal phase and amplitude settings of an array of radiators that will cause the highest constructive interference to occur at the desired location. In its basic implementation, with a single virtual source placed at the center of the tumor, TR yields solutions that exhibit good target coverage [49], [120], [124] albeit far from the global TC_x optimum. Further improvements for hot-spot management in TR have been proposed for high-intensity focused ultrasounds (HIFU), based on iterative methods [125]. In general, the major obstacle to the clinical introduction of TR-based treatment planning optimization is its limited ability to suppress hot spots.

To improve hot-spot suppression and target coverage in TR-based treatment planning, we propose a novel deterministic UWB TR-based iterative scheme (i-TR) in Paper C. The scheme aims at minimizing the HCQ (3.7) and is specifically tailored to this purpose. The procedure, Fig. 3.3, is initialized at the classic TR solution obtained by placing a virtual source at the center of the tumor mass. The resulting (time-reversed) SAR distribution is analyzed, and the most prominent cold spot is identified as the p-percentile sub-volume of the target containing the lowest SAR values. A virtual source is placed at

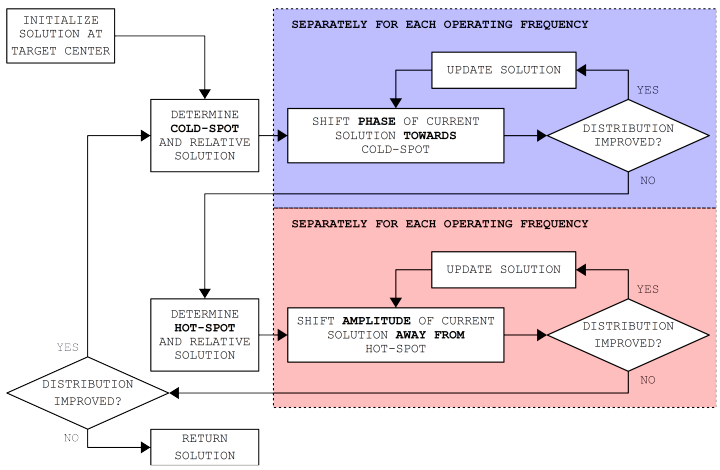

Figure 3.3: Simplified description of the proposed iterative time-reversal scheme. The blue section indicates a set of cold-spot (phase) iterations, while the red section refers to a set of hot-spot (amplitude) iterations.

the center of the cold spot, and a TR solution for focusing at that location is determined. Similarly, the most prominent hot spot is identified as the q-percentile sub-volume of healthy tissues containing the highest SAR values. A virtual source is placed at the center of the hot spot, and a TR solution for focusing at that location is determined. The algorithm then selects the first operating frequency in the set and begins improving the current solution by progressively shifting each channel's steering phase toward the phase of the cold-spot solution. At each step, the HCQ is evaluated over the focused SAR distribution, and the new solution is deemed improved if the HCQ exhibits a lower value than the previous. Subsequently, the solution is further improved by progressively shifting each channel's steering amplitude away from the amplitude of the hot-spot solution (i.e., towards the inverse of the hot-spot solution's amplitudes). If the HCQ does not improve, the next frequency in the set is selected, and a new attempt is made to improve the solution. Once the HCQ does no longer improve by either a cold- or a hot-spot step at any frequency, the SAR distribution is re-evaluated and a new pair of cold and hot spots are identified and their TR solutions computed. The whole procedure is then reiterated until the new set of cold-spot and hot-spot solutions does not bring any improvement in HCQ. The algorithm then halts, and the latest solution with lowest HCQ is returned as the optimized treatment plan.

In this study, we show that i-TR yields results comparable to those obtained via global stochastic optimization while being significantly faster. The algorithm is benchmarked numerically for two different applicator array topologies: a collar for tumors in the neck and a helmet for tumors in the brain. For the neck model, different target locations and sizes are considered to assess the algorithm's robustness to different scenarios. The algorithm is also applied to two realistic cases, a tumor in the larynx and one in the meninges. For each test case, treatment planning quality and performance indicators are computed and compared against those obtained with EV, PS, and classic (non-iterative) TR. Results suggest that the method is successful in finding viable multi-frequency solutions for a given problem, independently of the target's size, location, morphology, or composition. They further indicate that the method is robust to problems involving mixed polarization axes. The quality of the i-TR solution can depend on the selected set of operating frequencies. However, the high execution speed makes it possible to evaluate all frequency combinations and always determine one viable solution. The treatment plans

obtained via i-TR are further validated with thermal simulations. We verify that i-TR can achieve the same tumor temperatures (T_{50}) as the treatment plans based on global PS-based HTQ optimization. In the larynx case, i-TR outperforms the HTQ-based plan by 0.4 °C, potentially confirming HCQ's suitability as a cost function for optimization.

CHAPTER 4

Applicator Design

In microwave hyperthermia, the energy is delivered to the patient by a radiating antenna. The temperature elevation in deep-seated targets is often better achieved with a phased array, i.e., a set of coherently driven antennas placed around the patient. The antennas are suitably fed in amplitude and phase to create a constructive wave interference to selectively heat the target region. The steering parameters are optimized during treatment planning, as discussed in the previous chapter. Currently, all clinically utilized microwave applicators operate at a single frequency and consist of one or more concentric rings of antennas whose polarization is aligned with the symmetry axis [14]. In these applicators, the antennas are immersed in a common water bolus, Fig. 4.1, which fills the gap between the patient and the array. Beyond skin cooling and impedance matching, the water bolus also serves as a high permittivity medium to reduce the antenna size. Several parameters can be varied in this design to achieve the desired power loss distribution pattern, and they have been investigated in many studies [45], [126]–[128].

The design parameters typically include the operating frequency, the radius of the circular or elliptical arrangement, the number of rings, the number of antennas per ring, and the distance between the rings. The optimal combination

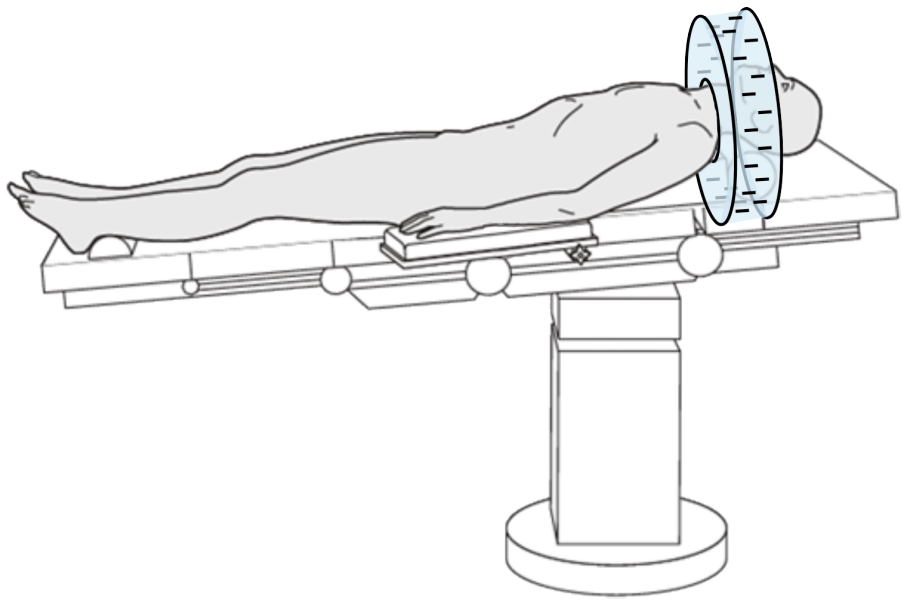

Figure 4.1: Clinical dual-ring applicator design, example in the neck region. The light blue shade represents water. The antennas are indicated with a pin following their main polarization direction.

of these parameters depends, in a more or less direct manner, on the operating frequency itself. The choice of operating frequency, in turn, determines the size of the resulting focal spot and the penetration depth [129]. For compliance, the operating frequency is usually selected among the limited set of frequencies allocated for medical use in the regulated spectrum. Therefore, the vast majority of systems operate at $434,915$ MHz or 2.45 GHz. Systems deployed for use in shielded rooms can operate outside the ISM bands and utilize lower frequencies for deeper penetration. In the pelvic and abdominal regions, for instance, the typical operating frequency is between 70 and 140 MHz. Accordingly, the consolidated recipe for the design of a single-frequency applicator involves the following steps: 1. determine the operating frequency based on the region to be treated, 2. choose a narrow-band directional antenna at the target frequency, 3. determine the best array arrangement based on the previous constraints (and other external constraints such as space, cost, etc.). The clinical systems used nowadays for treatments of tumors in the pelvic region, the abdomen, and the head and neck, have mostly been designed according to this approach [128].

In the UWB setting, this approach is no longer applicable. The design of UWB systems cannot be based on the target operating frequency precisely because this is no longer uniquely defined. Rather, an *operating band* must be chosen. This band can span more than an octave and is only constrained by external factors, such as the (commercial) availability of RF components and their cost. In fact, in terms of deep microwave heating, the operating band can be located anywhere between ≈ 1 MHz and ≈ 1 GHz. Beyond this limit, the penetration depth of the impinging wave becomes gradually irrelevant and its effect on the body temperature can only be seen within a few centimeters from the skin surface [25]. The actual penetration depth obtained by a conformal array of antennas is higher thanks to the array effect, but similar considerations apply. Ideally, lower frequencies should be included to support heating at depth, while higher frequencies can contribute to the spatial refinement of the thermal dose distribution. The microwave hyperthermia system for head, neck, and brain treatments, currently under development at Chalmers, features 16 channels designed to operate across the $300 \sim 800$ MHz frequency band. The diameter of the smallest achievable focal spot ($\lambda/2$) at 300 MHz is ≈ 5.3 cm in water, while at 800 MHz this diameter is ≈ 2.0 cm.

The ideal antenna for UWB treatments should exhibit the following characteristics across the whole bandwidth:

- high return loss (> 10 dB)
- directional (no back radiation)
- low cross coupling (< -10 dB) between nearby elements
- high operating power (≈ 150 W)
- small size ($< \frac{\lambda}{2}$)

Few designs are capable of fulfilling all these requirements over an octave or more. In our studies, we utilize self-grounded bow-tie (SGBT) antennas [130], Fig. 4.2a. These antennas are electrically small and exhibit natural directivity. Our group previously adapted the antennas for use in water [131].

In addition to the choice of bandwidth, the design of an applicator for the brain region entails yet another degree of freedom. Unlike other body parts, in fact, the head allows for a semi-spherical helmet array morphology, as visualized in Fig. 4.3a. The array can be entirely conformal to the head, fully exploiting the surface available on the scalp, Fig. 4.3b. In terms of heating capability, the inclusion of more antennas at different angles can lead

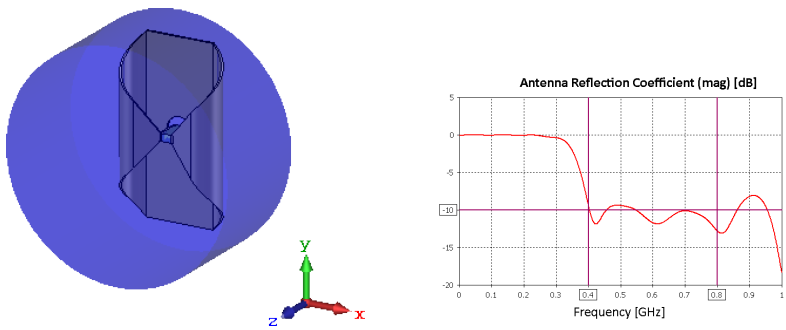

(a) Antenna Model **(b)** Reflection Coefficient

Figure 4.2: The $400 - 800$ MHz SGBT antenna for brain applicators. The blue shade indicates water. b) reports the reflection coefficient when the antenna is applied to a 1 cm thick water bolus surrounding the scalp.

to better tumor coverage [52]. Furthermore, these antennas can be polarized in different directions to compensate for the distortions and irregular wave scattering introduced by the strongly heterogeneous anatomy of this region. In other words, letting the antennas rotate around their directional axis might increase the average net power delivered to the target while reducing the magnitude of the SAR peaks in the surrounding healthy tissues. This gain, however small, might be crucial in the brain, where extraordinary control in the delivery of heat is essential to avoid damage to life-critical organs.

Having relaxed so many geometrical constraints, it is now clear that the commonly used strategies in applicator design, based on single parameter studies, become inadequate to tackle all the additional degrees of freedom. The logical next step in the design of a helmet applicator is to combine all these parameters into a global optimization process:

- the number of antennas
- the location of each antenna
- the rotation of each antenna

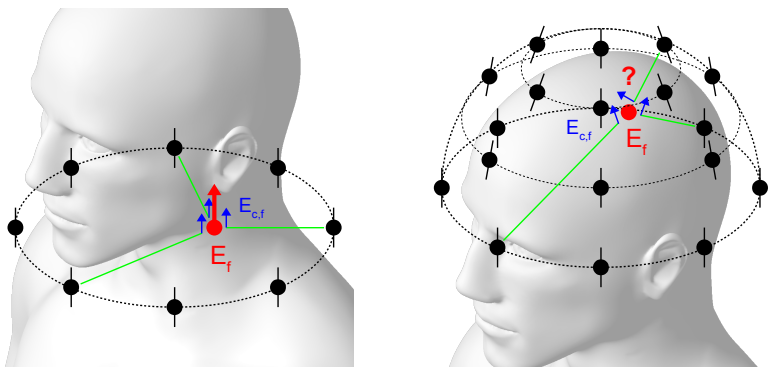

(a) Collar Applicator **(b)** Helmet Applicator

Figure 4.3: Collar versus helmet applicator topology. The antennas are indicated by black pins. The focal spot is indicated with a red dot, and the E-field of each channel at this location is indicated with a red arrow. In the helmet case, the resulting E-field polarization at the focal spot cannot be determined right away, as the antennas contribute each with a different angle to the power deposition at the focus.

The goal of the optimization is then to find the antenna arrangement that yields maximum target coverage and hot-spot suppression for a given patient. The optimization can be carried out with a global stochastic optimizer configured to minimize the HCQ, described in Section 3.4. In principle, the number of antennas should always be the highest possible to maximize the array effect, and is only limited by the available water bolus surface and the minimum distance between elements. At the same time, it is well known that for a given patient and target volume, only a subset of the array is typically active during treatment [110], [132]. This fact allows us to treat the number of antennas as fixed and let the optimizer determine their locations and rotations. The process can then be repeated for an increasing number of antennas until the HCQ no longer shows a relevant improvement. Thus, for a given number of antennas, the optimization variables are the coordinates of each antenna around the scalp together with its rotation angle. These variables are defined on continuous intervals and are therefore suitable for use with efficient global and local optimization algorithms. Such iterative algorithms demand an evaluation of the cost function for a new candidate solution at each step. Since each new solution corresponds to a previously unexplored array configuration, both the E-fields and the steering parameters have to be determined anew. The evaluation of the cost function consists of two stages:

1. Simulate the UWB wave propagation for each antenna in the current array configuration.

2. Determine an HCQ-optimal plan for the current configuration and return its HCQ value as cost.

Step 1 can be particularly time-consuming and resource-demanding. In a realistic case of a 16-channel UWB applicator, a full array plus patient simulation with curved antenna elements at the appropriate resolution can last days. At the same time, a global optimization procedure with 3 variables for each antenna can take up to thousands of iterations to complete. Consequently, for the optimization to be feasible, the evaluation of the cost function should run within minutes. Having developed a fast UWB treatment planning algorithm in Paper C to carry out Step 2 within a reasonable time, we need to accelerate the procedure in Step 1. To do so, we introduce a rapid E-field approximation method in the next section.

4.1 Field interpolation and array evaluation

In Paper D, the first part of the problem is tackled and a novel field interpolation technique is presented. This technique allows for a quick estimation of the E-field distribution generated by an antenna at any location across the applicator surface. The interpolation is based on a pre-calculated set of E-field distributions generated by a single antenna at fixed locations around the head, forming an interpolation grid, Fig. 4.4. The E-field generated by an individual antenna at a specific location is then obtained by a linear combination of the three nearest sampled locations. To address the distortion caused by coupling between nearby antennas, a recursive model to mimic the multiple reflections between pair of elements is proposed. The model utilizes the individual antenna fields to determine the overall field of one antenna in the array configuration. The fields of the passive antennas are added to the field of the active antenna according to a coupling constant that is proportional to the projection of the active antenna field onto the passive antenna's polarization axis, Fig. 4.5. This is repeated for each antenna in the array. Thereafter, it is possible to superpose the single antenna distributions with applied phase and amplitude steering to obtain a good estimate of the overall array pattern.

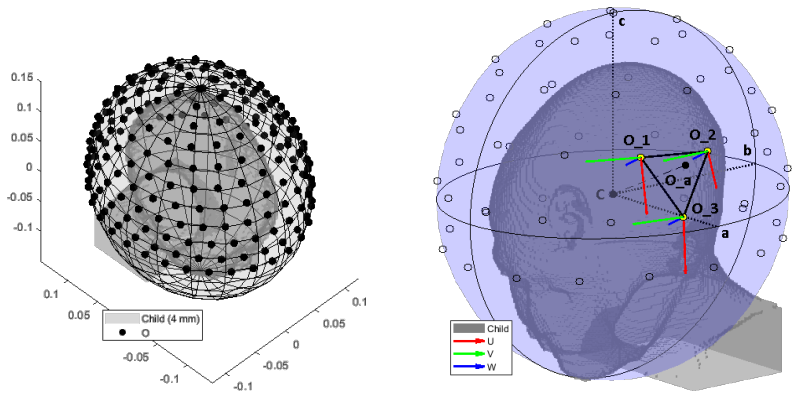

(a) Single Antenna Setup **(b)** Interpolation Grid

Figure 4.4: E-field interpolation method. (a): a single antenna is simulated at a number of fixed locations around the head. (b): the E-field due to an antenna at query location O_a is determined by linear weighted interpolation of the simulated E-fields at grid locations (O_1, O_2, O_3).

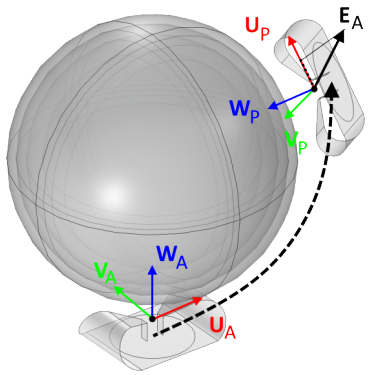

Figure 4.5: Coupling modeling method. An active antenna A and a passive antenna P are considered in a spherical brain applicator. A correlation factor between the coupled field E_{A+P} and the passive antenna field E_P is determined. This is found to be proportional to the projection onto U_P of the individual field E_A at the location of the passive antenna.

This field approximation method is validated and used in conjunction with the previously developed i-TR treatment plan optimization scheme to improve the design of an applicator for a specific paediatric brain cancer patient. The method is accurate enough to provide qualitative indications about the most suitable antenna arrangement for a given tumor shape and location. The optimized designs for a given number of array elements are compared to canonical solutions of one or two rings of equally spaced antennas. The results confirm that a helmet applicator with an optimized antenna arrangement can improve the temperature distribution with respect to a classical ring design. Future developments will include the relaxation of the antenna polarization angle and the approximation of any rotation around its W axis by means of two orthogonal simulations for each interpolation grid point.

4.2 Application to a pediatric patient model

The most common clinical use of hyperthermia in oncology is as an adjuvant modality to radiotherapy. In a combined workflow, the patient is irradiated following a typical fractionation schedule, and hyperthermia is added weekly or twice a week, after the radiotherapy session and possibly within four hours from it [133]. Thanks to efforts spent in modeling the impact of hyperthermia on the radio-biological dose [134], it has recently become possible to quantitatively estimate the gain in therapeutic outcome of the combined treatment with respect to radiotherapy alone. In Paper E, we develop a plan for a combined radiotherapy and hyperthermia treatment of a pediatric medulloblastoma patient (Fig. 4.6) using the biologically effective dose model.

In the study, an early prototype of an optimized helmet applicator, designed to operate across the $300 \sim 800$ MHz band, is used to deliver the hyperthermia treatment (Fig. 4.7). Since this investigation was conducted before the validation of HCQ, the HTQ has been used as a cost function for both the antenna arrangement and the treatment plan optimization. From the thermal simulation, Fig. 4.8, the achieved tumor temperatures are $T_{90} = 39.0$ °C and $T_{50} = 39.8$ °C. These relatively low temperatures are partly due to the strict limit of 42 °C that has to be imposed on healthy tissues in this region [135].

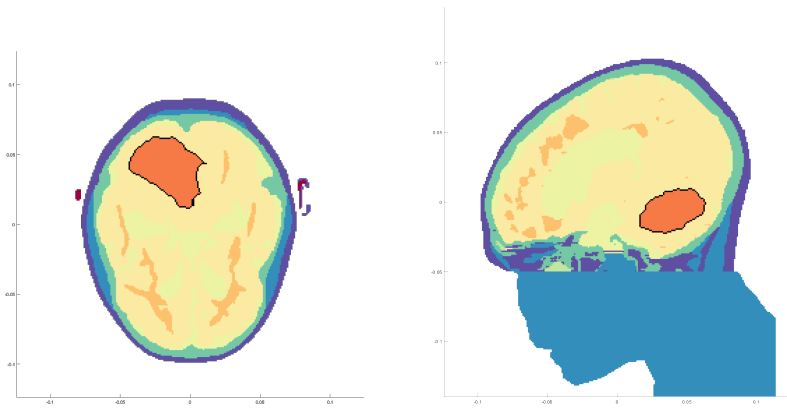

(a) Transverse **(b)** Sagittal

Figure 4.6: Model of a pediatric patient showing a medulloblastoma, outlined in black. Sections taken at tumor center.

The limiting hot spot emerges, as expected, in the pocket of cerebrospinal fluid adjacent to the brainstem.

Despite the sub-optimal range of tumor temperatures, the optimized helmet applicator manages to produce a selective temperature increase that is sufficient to halve the ionizing dose for the same clinical outcome. The importance of this result can be understood considering that, even with the latest and most precise stereotactic radiosurgery devices, part of the radiation will always leak into healthy brain tissue. This, in turn, is known to cause the emergence of long-term sequelae in survivors, such as cognitive impairment, growth disorders, and disability [136]. The shown potential of hyperthermia to reduce the overall radiation dose while maintaining its curative effect is thus extremely encouraging, especially in pediatric patients. The outcomes of this investigation indicate that microwave heat delivery into large intracranial tumors is feasible, and motivate further development of specific applicators for this site.

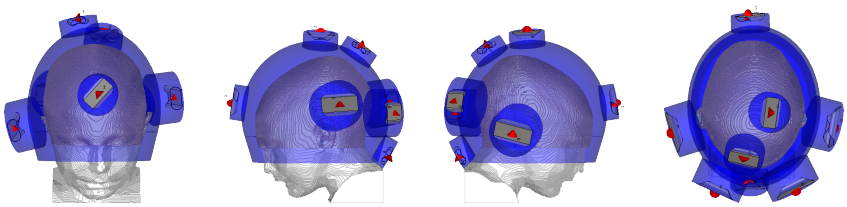

(a) Front **(b)** Left **(c)** Right **(d)** Top

Figure 4.7: Resulting helmet applicator antenna arrangement for the treatment of a large medulloblastoma in a pediatric patient. The array consists of 4 larger and 4 smaller antennas, operating at different and partially overlapping frequency bands.

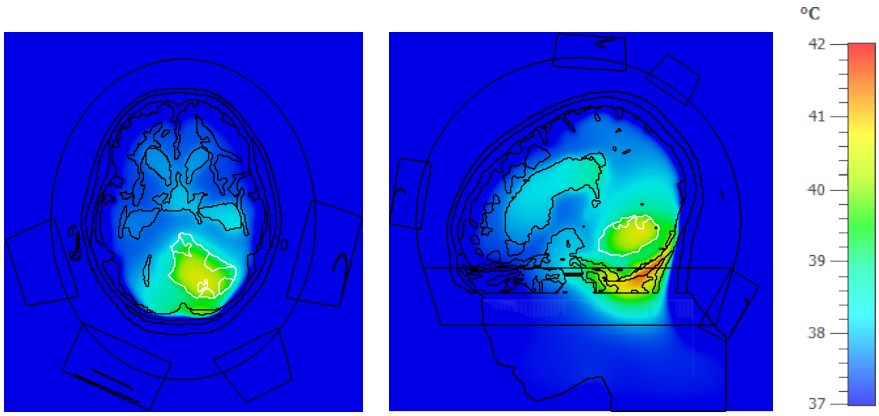

(a) Transverse **(b)** Sagittal

Figure 4.8: Temperature distribution obtained in the medulloblastoma patient using an early version of optimized helmet applicator. The maximum temperature in all healthy tissues is 42 °C. Note the main hot spot appearing in the pocket of cerebrospinal fluid ventral to the target volume (outlined in white).

CHAPTER 5

Remaining Challenges

This thesis deals with different aspects of the development of UWB hyperthermia applicators to treat intracranial tumors. Its purpose is to show that non-invasive UWB microwave hyperthermia is a viable treatment option in this location and that more research efforts should be spent in this direction. Patient-specific array design and treatment planning optimization can increase the tumor temperatures and the thermal dose to the levels required to achieve a therapeutic gain when combined with other treatment modalities. Nevertheless, from an engineering perspective, the task remains a challenging one and has to be tackled from many angles. The deployment of a robust, reliable, and safe microwave hyperthermia system is not limited to the design of a good applicator. Many practical issues must be considered and solved before such a system can be adopted for clinical use.

First of all, the applicator has to be backed by a reliable RF amplifying system. Each channel in the RF cascade must be able to be steered in amplitude and phase at any frequency of the operating band within the necessary precision. The hyperthermia system and the clinical setup have to match the accuracy required for the treatment plan to be meaningfully applied [112], [137]. The treatment plan optimization, in fact, assumes that the virtual

model corresponds exactly to the actual setup during each treatment session. Unfortunately, this is often not the case [138], [139], as the patient and the applicator can be slightly misplaced with respect to each other. Furthermore, the currently used water-boli are prone to unpredictable shape deformations due to their thin plastic casings and can also be subject to air leakages when the internal water pressure is insufficient. The presence of air bubbles and plastic layers between an antenna and the patient is detrimental to the treatment, as they cause unpredictable wave scattering and thus differences in the resulting power deposition pattern. A summary of possible mismatches is reported in Fig. 5.1.

Geometrical differences aside, the numerical model suffers also from the large spread in dielectric and thermal properties that characterize biological tissue [66], [80]. The use of an average value from the literature can produce shifts in the thermal pattern if the patient is an "outlier". The ideal way to address this would be to directly measure the tissue properties for each patient. Of course, this would entail an additional workload for the staff and the patient, so the methods used have to be accurate and automated enough to justify their adoption. Most techniques rely on the use of MRI scanners, which

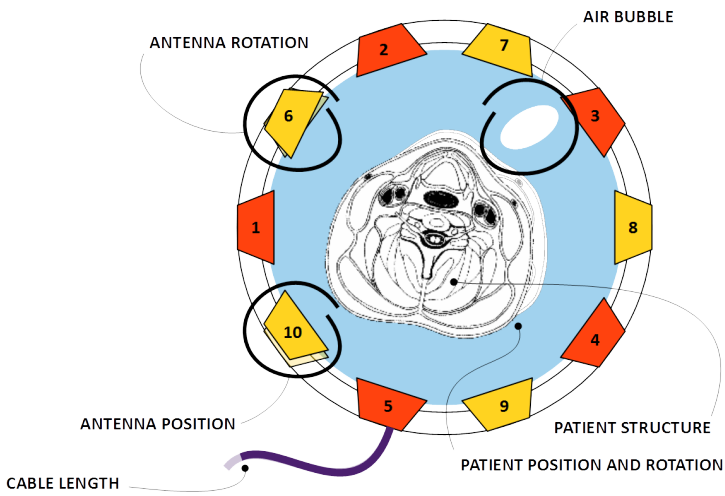

Figure 5.1: Potential mismatches between the assumptions made by the treatment planning optimizer and the actual treatment setup, example in the neck.

are unfortunately known to be expensive and cumbersome. MRI-derived measurements can provide information about the *in-vivo* dielectric properties and real-time thermometry during treatment [140], [141]. Thermal properties can theoretically be estimated via thermal washout model fitting [142]. Other non-MRI-based approaches include electric impedance tomography (providing a map of dielectric properties at lower RF frequencies) and ultrasound imaging (used for mass density measurements but also temperature tracking via differential imaging). All these techniques involve the use of some measuring device that is separated from the hyperthermia (and the radiotherapy) device.

To increase the accuracy of a hyperthermia treatment and reduce its burden on the clinical workflow, it would be very convenient if the same system used for treatment could also be used for imaging purposes. Microwave imaging is the perfect candidate to attain this [143]. In an embedded microwave system, the same array of antennas can be used to radiate focused power in the patient and to perform scattering measurements (S-parameters). The information contained in the S-matrix can then be processed to determine a map of permittivity and conductivity within the treated domain. We believe that correct quantitative imaging would be profitable under two fundamental aspects: as a patient- and frequency-specific dielectric property distribution for numerical simulations and treatment plan optimization, and as a means to detect the patient misplacement upon each session. Repeated differential measurements during treatment can in principle also be exploited to track changes in the distributions and perform real-time thermometry [144]–[146].

Our biomedical research group at Chalmers has a long-established experience in the field of theoretical and applied microwave image reconstruction [147]. In parallel with a novel helmet applicator design, we have initiated a study on the possibility of incorporating a Vector Network Analyzer (VNA) in the hyperthermia RF system, as illustrated in Fig. 5.2. Note that, in narrowband systems, the information acquired would be limited and very likely not sufficient for this purpose. In a UWB system, information about the group delay and pulse attenuation can be obtained across the same operating band used for treatment, providing a much larger base for tomography computations. From an engineer's point of view, the integration of a VNA has the potential to provide the feedback control necessary for more accurate power delivery and hopefully "close the loop" in microwave hyperthermia treatments.

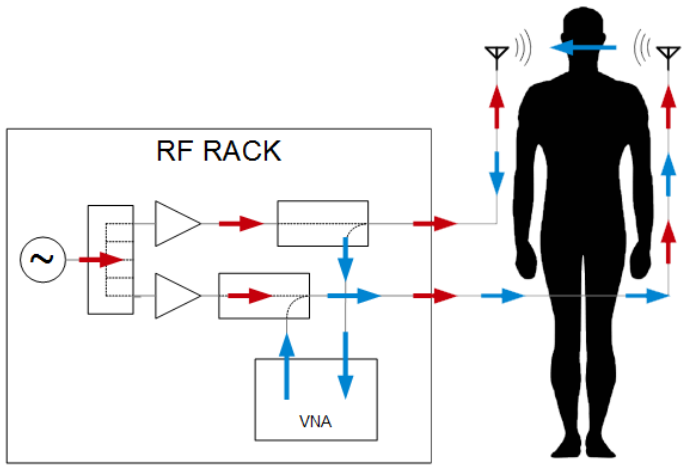

Figure 5.2: Integrating a VNA into a multi-channel UWB hyperthermia system has the potential to provide on-site measurement of the dielectric tissue properties and even real-time thermometry during treatment. Directional couplers or RF switches separate the high-power treatment signal (in red) from the low-power measurement signal (in blue).

CHAPTER 6

Summary of included papers

This chapter provides a summary of the included papers. Note that the papers are not presented in chronological order, but rather follow the sequential steps in the implementation of UWB treatment planning for deep microwave hyperthermia.

6.1 Paper A

Massimiliano Zanoli, Hana Dobšíček Trefná
Suitability of eigenvalue beamforming for discrete multi-frequency hyperthermia treatment planning
Medical Physics
16 September 2021

DOI: 10.1002/mp.15220

In this paper, we investigate whether using the eigenvalue (EV) decomposition to solve for the power deposition ratio Γ is a suitable method for single- and multi-frequency hyperthermia treatment planning optimization. We show that Γ cannot be maximized by more that one frequency at a time. In particular, even when the EV solver is complemented by an iterative optimization procedure that minimizes for another cost function, the final solution always consists of only one operating frequency, irrespective of how many frequencies are available for concomitant treatment. We further investigate whether the single-frequency limitation represents a problem for deep microwave hyperthermia, and whether the use of multiple operating frequencies can improve target coverage and hot-spot suppression. Two realistic test cases are considered: a tumor in the larynx and a tumor in the meninges. We compare the resulting temperature distributions for a single frequency to the case when two simultaneous frequencies are jointly optimized with respect to their overall SAR distribution. The latter optimization is carried out using non-linear cost functions (HTQ and TC_{50}) and a global stochastic optimizer, Particle Swarm (PS). Results for the larynx indicate that a single frequency treatment may be sufficient to reach satisfying values of T_{50} and T_{90} in this region, as adding a secondary frequency does not improve the thermal distribution further. However, in the brain case, introducing a second frequency increases the SAR target coverage, TC_{50}, by 10 points, and temperature coverage, T_{90}, by 0.5 °C with respect to the best single-frequency solution (from 40.9 °C to 41.4 °C). In terms of $CEM_{43}T_{90}$, such an increase corresponds to a doubling of the thermal dose. We can conclude that multi-frequency systems do have the potential to improve hyperthermia treatments in regions typically difficult to treat such as the brain, and that the average power deposition ratio is not a suitable cost function for multi-frequency optimization.

6.2 Paper B

Massimiliano Zanoli, Hana Dobšíček Trefná
The hot-to-cold spot quotient for SAR-based treatment planning in deep microwave hyperthermia
Submitted to the International Journal of Hyperthermia
01 June 2022

In this paper, we validate our recently proposed novel cost-function for SAR-based hyperthermia treatment planning optimization, the hot-to-cold spot quotient (HCQ). The HCQ is intended to combine the well known SAR metrics regarding hot-spot suppression and target coverage into one, thus enabling the concomitant optimization of both. To make the validation relevant, we use the ESHO patient repository for the *Grand Challenge on Computational Modeling*, consisting of six patients: two with targets in the pelvic region, two in the breast, and two in the head and neck. A global stochastic optimizer is used to obtain the optimal plans with respect to the novel HCQ and the consolidated HTQ cost functions in single- and multi-frequency settings. As the HCQ depends on a percentile p, we include a sensitivity analysis to this parameter. Upon thermal simulation, the HCQ-optimal plans outperform the HTQ ones in most patients, with up to 1 °C gain in T_{90}. Furthermore, the value of 1/HCQ exhibits a higher degree of correlation than 1/HTQ with the resulting tumor temperature. The sensitivity analysis on p suggests that this parameter reflects the behavior of the resulting temperature percentile in the target. Only in one superficial breast target does the performance of HCQ drop severely. We interpret this as due to the vicinity of the water bolus, whose cooling effect directly affects the temperature distribution in the target. In such case, the general correlation between SAR and temperature is hampered, and the use of a T-based optimizer, with the water temperature as optimization parameter, is recommended. It can be concluded that HCQ provides the means for an effective multi-frequency HTP optimization in deep microwave hyperthermia and enables meaningful comparisons between different solutions.

6.3 Paper C

Massimiliano Zanoli, Hana Dobšíček Trefná
Iterative time-reversal for multi-frequency hyperthermia
Physics in Medicine & Biology
16 December 2020

DOI: 10.1088/1361-6560/abd41a

In this paper, we propose a novel, deterministic UWB iterative scheme based on time-reversal (i-TR). The method, which aims at minimizing the hot-to-cold spot quotient (HCQ), improves hot-spot suppression and target coverage of classic time-reversal (TR) based microwave hyperthermia treatment planning. The procedure is initialized at the TR solution obtained by placing a virtual source at the center of the tumor mass. The resulting, time reversed, SAR distribution is analysed and the most prominent cold-spot and hot-spot are identified in the tumor and in the healthy tissues, respectively. Two TR solutions are then determined at the cold- and hot-spot centers. The algorithm improves the current solution by progressively shifting the steering phases towards the cold-spot solution and the steering amplitudes away from the cold-spot solution. In this study, we show that i-TR yields results comparable to those obtained via global stochastic optimization, while being significantly faster. The algorithm is benchmarked numerically for two different applicator array topologies: a collar for tumors in the neck and a helmet for intracranial tumors. For the neck model, different target locations and sizes are considered. The algorithm is also applied to two realistic cases: a tumor in the larynx and one in the meninges. For each case, HTP quality and performance indicators are measured and compared against those obtained with eigenvalue, particle swarm and classic TR. The results suggest that the method is successful in finding viable multi-frequency solutions for a given problem, independently of the target's size, location, morphology or composition. They further indicate that the method is robust to problems involving mixed polarization axes. The treatment plans obtained via i-TR are further validated with thermal simulations. It is shown that i-TR can achieve similar tumor temperatures (T_{50}) as the treatment plans based on global HTQ optimization. In the larynx case, i-TR outperforms the HTQ-based plan by 0.4 °C, advocating the suitability of the HCQ as cost function for optimization.

6.4 Paper D

Massimiliano Zanoli, Hana Dobšíček Trefná
Antenna arrangement in UWB helmet brain applicators for deep microwave hyperthermia
Submitted to Cancers
15 November 2022

In this paper, we propose a novel E-field interpolation technique that calculates the field due to an antenna at any location around the scalp from a limited number of initial simulations. We further devise a method for modeling the coupling between nearby antennas starting from the very same individual antenna fields. We evaluate the approximation error against full array simulations. We demonstrate the design technique in the optimization of a helmet applicator for the treatment of a large medulloblastoma in a paediatric patient. The field approximation provides a full array distribution in about 1/200 of the time typically necessary to simulate the same array on a commercial FEM software. The optimized applicator achieves 0.3 $^{\circ}C$ higher T90 than a conventional ring applicator with the same number of elements.

6.5 Paper E

Morteza Ghaderi Aram, **Massimiliano Zanoli**, Håkan Nordström, Iuliana Toma-Dasu, Klas Blomgren, Hana Dobšíček Trefná
Radiobiological Evaluation of Combined Gamma Knife Radiosurgery and Hyperthermia for Pediatric Neuro-Oncology
Cancers
30 June 2021

DOI: 10.3390/cancers13133277

This study aims to extend the interaction model of hyperthermia and radiotherapy for the computation of the combined dose by incorporating oxygenation effects. To illustrate the methodology, we present a clinically relevant application in pediatric oncology, which is novel in two ways. First, it deals with medulloblastoma, the most common malignant brain tumor in children, a type of brain tumors not previously reported in the literature of thermoradiotherapy studies. Second, it makes use of an optimized helmet applicator for the delivery of the microwave hyperthermia treatment and the Gamma Knife for the radiotherapy part. Quantitative metrics like the biologically effective dose (BED) and the tumor control probability (TCP) are used in a brain model to assess the efficacy of the combined plan.

References

[1] Global Burden of Disease Collaborative Network, "Global Burden of Disease Study 2017 (GBD 2017)," *Institute for Health Metrics and Evaluation (IHME)*, 2018.

[2] C. P. Wild, E. Weiderpass, and B. W. Stewart, *World cancer report: Cancer research for cancer prevention*, Feb. 2020.

[3] American Cancer Society, *Cancer Facts & Figures 2020*, Atlanta, US, 2020.

[4] N. H. S. (NHS), *Malignant brain tumour (brain cancer)*, Mar. 2018.

[5] I. F. Pollack, S. Agnihotri, and A. Broniscer, "Childhood brain tumors: Current management, biological insights, and future directions: Jnspg 75th anniversary invited review article," *Journal of Neurosurgery: Pediatrics*, vol. 23, no. 3, pp. 261–273, 2019.

[6] E. Livesey and C. Brook, "Gonadal dysfunction after treatment of intracranial tumours.," *Archives of disease in childhood*, vol. 63, no. 5, pp. 495–500, 1988.

[7] B. Lannering, I. Marky, A. Lundberg, and E. Olsson, "Long-term sequelae after pediatric brain tumors: Their effect on disability and quality of life," *Medical and pediatric oncology*, vol. 18, no. 4, pp. 304–310, 1990.

[8] E. Nicklin, G. Velikova, C. Hulme, *et al.*, "Long-term issues and supportive care needs of adolescent and young adult childhood brain tumour survivors and their caregivers: A systematic review," *Psycho-oncology*, vol. 28, no. 3, pp. 477–487, 2019.

[9] S. Roussakow, "The history of hyperthermia rise and decline," in *Conference Papers in Science*, Hindawi, vol. 2013, 2013.

[10] N. Cihoric, A. Tsikkinis, G. van Rhoon, *et al.*, "Hyperthermia-related clinical trials on cancer treatment within the clinicaltrials. gov registry," *International journal of hyperthermia*, vol. 31, no. 6, pp. 609–614, 2015.

[11] N. R. Datta, S. Rogers, S. G. Ordóñez, E. Puric, and S. Bodis, "Hyperthermia and radiotherapy in the management of head and neck cancers: A systematic review and meta-analysis," *International Journal of Hyperthermia*, vol. 32, no. 1, pp. 31–40, 2016.

[12] N. R. Datta, E. Puric, D. Klingbiel, S. Gomez, and S. Bodis, "Hyperthermia and radiation therapy in locoregional recurrent breast cancers: A systematic review and meta-analysis," *International Journal of Radiation Oncology* Biology* Physics*, vol. 94, no. 5, pp. 1073–1087, 2016.

[13] N. R. Datta, E. Stutz, S. Gomez, and S. Bodis, "Efficacy and safety evaluation of the various therapeutic options in locally advanced cervix cancer: A systematic review and network meta-analysis of randomized clinical trials," *International Journal of Radiation Oncology* Biology* Physics*, vol. 103, no. 2, pp. 411–437, 2019.

[14] M. Paulides, H. D. Trefná, S. Curto, and D. Rodrigues, "Recent technological advancements in radiofrequency-and microwave-mediated hyperthermia for enhancing drug delivery.," *Advanced Drug Delivery Reviews*, 2020.

[15] M. Franckena, L. J. Stalpers, P. C. Koper, *et al.*, "Long-term improvement in treatment outcome after radiotherapy and hyperthermia in locoregionally advanced cervix cancer: An update of the dutch deep hyperthermia trial," *International Journal of Radiation Oncology* Biology* Physics*, vol. 70, no. 4, pp. 1176–1182, 2008.

[16] R. D. Issels, L. H. Lindner, J. Verweij, *et al.*, "Effect of neoadjuvant chemotherapy plus regional hyperthermia on long-term outcomes among patients with localized high-risk soft tissue sarcoma: The eortc 62961-esho 95 randomized clinical trial," *JAMA oncology*, vol. 4, no. 4, pp. 483–492, 2018.

[17] A. Winter, J. Laing, R. Paglione, and F. Sterzer, "Microwave hyperthermia for brain tumors," *Neurosurgery*, vol. 17, no. 3, pp. 387–399, 1985.

[18] R. Tanaka, C. H. Kim, N. Yamada, and Y. Saito, "Radiofrequency hyperthermia for malignant brain tumors: Preliminary results of clinical trials," *Neurosurgery*, vol. 21, no. 4, pp. 1–3, 1987.

[19] P. K. Sneed, P. H. Gutin, P. R. Stauffer, *et al.*, "Thermoradiotherapy of recurrent malignant brain tumors," *International Journal of Radiation Oncology* Biology* Physics*, vol. 23, no. 4, pp. 853–861, 1992.

[20] P. Gas, "Essential facts on the history of hyperthermia and their connections with electromedicine," *arXiv preprint arXiv:1710.00652*, 2017.

[21] S. S. Evans, E. A. Repasky, and D. T. Fisher, "Fever and the thermal regulation of immunity: The immune system feels the heat," *Nature Reviews Immunology*, vol. 15, no. 6, pp. 335–349, 2015.

[22] N. van den Tempel, M. R. Horsman, and R. Kanaar, "Improving efficacy of hyperthermia in oncology by exploiting biological mechanisms," *International journal of hyperthermia*, vol. 32, no. 4, pp. 446–454, 2016.

[23] M. W. Dewhirst, C.-T. Lee, and K. A. Ashcraft, "The future of biology in driving the field of hyperthermia," *International Journal of Hyperthermia*, vol. 32, no. 1, pp. 4–13, 2016.

[24] K. F. Chu and D. E. Dupuy, "Thermal ablation of tumours: Biological mechanisms and advances in therapy," *Nature Reviews Cancer*, vol. 14, no. 3, pp. 199–208, 2014.

[25] P. R. Stauffer and M. M. Paulides, "Hyperthermia therapy for cancer," *Comprehensive biomedical physics*, vol. 10, no. 07, pp. 115–151, 2014.

[26] H. H. Kampinga, "Cell biological effects of hyperthermia alone or combined with radiation or drugs: A short introduction to newcomers in the field," *International journal of hyperthermia*, vol. 22, no. 3, pp. 191–196, 2006.

[27] R. Issels, E. Kampmann, R. Kanaar, and L. H. Lindner, "Hallmarks of hyperthermia in driving the future of clinical hyperthermia as targeted therapy: Translation into clinical application," *International Journal of Hyperthermia*, vol. 32, no. 1, pp. 89–95, 2016.

[28] A. Oei, H. Kok, S. Oei, *et al.*, "Molecular and biological rationale of hyperthermia as radio-and chemosensitizer," *Advanced drug delivery reviews*, 2020.

[29] M. R. Horsman and J. Overgaard, "Hyperthermia: A potent enhancer of radiotherapy," *Clinical oncology*, vol. 19, no. 6, pp. 418–426, 2007.

[30] M. W. Dewhirst, Z. Vujaskovic, E. Jones, and D. Thrall, "Re-setting the biologic rationale for thermal therapy," *International Journal of Hyperthermia*, vol. 21, no. 8, pp. 779–790, 2005.

[31] J. C. Peeken, P. Vaupel, and S. E. Combs, "Integrating hyperthermia into modern radiation oncology: What evidence is necessary?" *Frontiers in oncology*, vol. 7, p. 132, 2017.

[32] G. C. Van Rhoon and P. Wust, "Introduction: Non-invasive thermometry for thermotherapy," *International Journal of Hyperthermia*, vol. 21, no. 6, pp. 489–495, 2005.

[33] H. P. Kok, E. N. Cressman, W. Ceelen, *et al.*, "Heating technology for malignant tumors: A review," *International Journal of Hyperthermia*, vol. 37, no. 1, pp. 711–741, 2020.

[34] G. P. Skandalakis, D. R. Rivera, C. D. Rizea, *et al.*, "Hyperthermia treatment advances for brain tumors," *International Journal of Hyperthermia*, vol. 37, no. 2, pp. 3–19, 2020.

[35] M. Salcman and G. M. Samaras, "Interstitial microwave hyperthermia for brain tumors," *Journal of Neuro-oncology*, vol. 1, no. 3, pp. 225–236, 1983.

[36] P. K. Sneed, P. R. Stauffer, M. W. McDermott, *et al.*, "Survival benefit of hyperthermia in a prospective randomized trial of brachytherapy boost+hyperthermia for glioblastoma multiforme," *International Journal of Radiation Oncology* Biology* Physics*, vol. 40, no. 2, pp. 287–295, 1998.

[37] M. Wankhede, A. Bouras, M. Kaluzova, and C. G. Hadjipanayis, "Magnetic nanoparticles: An emerging technology for malignant brain tumor imaging and therapy," *Expert review of clinical pharmacology*, vol. 5, no. 2, pp. 173–186, 2012.

[38] R. Stupp, M. E. Hegi, W. P. Mason, *et al.*, "Effects of radiotherapy with concomitant and adjuvant temozolomide versus radiotherapy alone on survival in glioblastoma in a randomised phase iii study: 5-year analysis of the eortc-ncic trial," *The lancet oncology*, vol. 10, no. 5, pp. 459–466, 2009.

[39] K. Maier-Hauff, F. Ulrich, D. Nestler, *et al.*, "Efficacy and safety of intratumoral thermotherapy using magnetic iron-oxide nanoparticles combined with external beam radiotherapy on patients with recurrent glioblastoma multiforme," *Journal of neuro-oncology*, vol. 103, no. 2, pp. 317–324, 2011.

[40] Z. Ram, Z. R. Cohen, S. Harnof, *et al.*, "Magnetic resonance imaging-guided, high-intensity focused ultrasound forbrain tumortherapy," *Neurosurgery*, vol. 59, no. 5, pp. 949–956, 2006.

[41] F. Prada, M. Y. S. Kalani, K. Yagmurlu, *et al.*, "Applications of focused ultrasound in cerebrovascular diseases and brain tumors," *Neurotherapeutics*, vol. 16, no. 1, pp. 67–87, 2019.

[42] G. Schooneveldt, H. D. Trefná, M. Persson, *et al.*, "Hyperthermia treatment planning including convective flow in cerebrospinal fluid for brain tumour hyperthermia treatment using a novel dedicated paediatric brain applicator," *Cancers*, vol. 11, no. 8, p. 1183, 2019.

[43] M. Paulides, J. Bakker, E. Neufeld, *et al.*, "The HYPERcollar: A novel applicator for hyperthermia in the head and neck," *International Journal of Hyperthermia*, vol. 23, no. 7, pp. 567–576, 2007.

[44] P. Wust, H. Fähling, T. Helzel, *et al.*, "Design and test of a new multi-amplifier system with phase and amplitude control," *International journal of hyperthermia*, vol. 14, no. 5, pp. 459–477, 1998.

[45] J. Crezee, P. Van Haaren, H. Westendorp, *et al.*, "Improving locoregional hyperthermia delivery using the 3-d controlled amc-8 phased array hyperthermia system: A preclinical study," *International Journal of Hyperthermia*, vol. 25, no. 7, pp. 581–592, 2009.

[46] R. Zweije, H. P. Kok, A. Bakker, A. Bel, and J. Crezee, "Technical and clinical evaluation of the ALBA-4D 70mhz loco-regional hyperthermia system," in *2018 48th European Microwave Conference (EuMC)*, IEEE, 2018, pp. 328–331.

[47] M. Paulides, Z. Rijnen, P. Togni, *et al.*, "Clinical introduction of novel microwave hyperthermia technology: The hypercollar3d applicator for head and neck hyperthermia," in *2015 9th European Conference on Antennas and Propagation (EuCAP)*, IEEE, 2015, pp. 1–4.

[48] M. Converse, E. J. Bond, B. Veen, and C. Hagness, "A computational study of ultra-wideband versus narrowband microwave hyperthermia for breast cancer treatment," *IEEE transactions on microwave theory and techniques*, vol. 54, no. 5, pp. 2169–2180, 2006.

[49] H. D. Trefná, J. Vrba, and M. Persson, "Evaluation of a patch antenna applicator for time reversal hyperthemia," *International Journal of Hyperthermia*, vol. 26, no. 2, pp. 185–197, 2010.

[50] G. G. Bellizzi, L. Crocco, G. M. Battaglia, and T. Isernia, "Multi-frequency constrained SAR focusing for patient specific hyperthermia treatment," *IEEE Journal of Electromagnetics, RF and Microwaves in Medicine and Biology*, vol. 1, no. 2, pp. 74–80, 2017.

[51] L. Winter, C. Oezerdem, W. Hoffmann, *et al.*, "Thermal magnetic resonance: Physics considerations and electromagnetic field simulations up to 23.5 tesla (1ghz)," *Radiation Oncology*, vol. 10, no. 1, pp. 1–12, 2015.

[52] P. Takook, M. Persson, and H. D. Trefná, "Performance evaluation of hyperthermia applicators to heat deep-seated brain tumors," *IEEE Journal of Electromagnetics, RF and Microwaves in Medicine and Biology*, vol. 2, no. 1, pp. 18–24, 2018.

[53] A. Kuehne, E. Oberacker, H. Waiczies, and T. Niendorf, "Solving the time-and frequency-multiplexed problem of constrained radiofrequency induced hyperthermia," *Cancers*, vol. 12, no. 5, p. 1072, 2020.

[54] P. S. Yarmolenko, E. J. Moon, C. Landon, *et al.*, "Thresholds for thermal damage to normal tissues: An update," *International Journal of Hyperthermia*, vol. 27, no. 4, pp. 320–343, 2011.

[55] P. Hasgall, F. Di Gennaro, C. Baumgartner, *et al.*, *IT'IS Database for thermal and electromagnetic parameters of biological tissues*, version 4.0, May 2018.

[56] S. Gavazzi, A. L. van Lier, C. Zachiu, *et al.*, "Advanced patient-specific hyperthermia treatment planning," *International Journal of Hyperthermia*, vol. 37, no. 1, pp. 992–1007, 2020.

[57] P. F. Turner, "Regional hyperthermia with an annular phased array," *IEEE Transactions on Biomedical Engineering*, no. 1, pp. 106–114, 1984.

[58] H. Shoji, M. Motegi, K. Osawa, *et al.*, "Output-limiting symptoms induced by radiofrequency hyperthermia. are they predictable?" *International Journal of Hyperthermia*, vol. 32, no. 2, pp. 199–203, 2016.

[59] H. D. Trefná, B. Martinsson, T. Petersson, *et al.*, "Multifrequency approach in hyperthermia treatment planning: Impact of frequency on sar distribution in head and neck," in *2017 11th European Conference on Antennas and Propagation (EUCAP)*, IEEE, 2017, pp. 3710–3712.

[60] M. M. Paulides, P. R. Stauffer, E. Neufeld, *et al.*, "Simulation techniques in hyperthermia treatment planning," *International Journal of Hyperthermia*, vol. 29, no. 4, pp. 346–357, 2013.

[61] A. M. Stoll and L. C. Greene, "Relationship between pain and tissue damage due to thermal radiation," *Journal of applied physiology*, vol. 14, no. 3, pp. 373–382, 1959.

[62] H. Kok, P. Wust, P. R. Stauffer, F. Bardati, G. Van Rhoon, and J. Crezee, "Current state of the art of regional hyperthermia treatment planning: A review," *Radiation Oncology*, vol. 10, no. 1, p. 196, 2015.

[63] R. Canters, P. Wust, J. Bakker, and G. Van Rhoon, "A literature survey on indicators for characterisation and optimisation of sar distributions in deep hyperthermia, a plea for standardisation," *International Journal of Hyperthermia*, vol. 25, no. 7, pp. 593–608, 2009.

[64] H. P. Kok, J. Gellermann, C. A. van den Berg, P. R. Stauffer, J. W. Hand, and J. Crezee, "Thermal modelling using discrete vasculature for thermal therapy: A review," *International Journal of Hyperthermia*, vol. 29, no. 4, pp. 336–345, 2013.

[65] A. Bakker, J. van der Zee, G. van Tienhoven, H. P. Kok, C. R. Rasch, and H. Crezee, "Temperature and thermal dose during radiotherapy and hyperthermia for recurrent breast cancer are related to clinical outcome and thermal toxicity: A systematic review," *International Journal of Hyperthermia*, vol. 36, no. 1, pp. 1023–1038, 2019.

[66] M. De Greef, H. Kok, D. Correia, A. Bel, and J. Crezee, "Optimization in hyperthermia treatment planning: The impact of tissue perfusion uncertainty," *Medical physics*, vol. 37, no. 9, pp. 4540–4550, 2010.

[67] R. A. Canters, M. M. Paulides, M. F. Franckena, J. van der Zee, and G. C. van Rhoon, "Implementation of treatment planning in the routine clinical procedure of regional hyperthermia treatment of cervical cancer: An overview and the Rotterdam experience," *International journal of hyperthermia*, vol. 28, no. 6, pp. 570–581, 2012.

[68] R. Canters, M. Paulides, M. Franckena, J. Mens, and G. Van Rhoon, "Benefit of replacing the sigma-60 by the sigma-eye applicator," *Strahlentherapie und Onkologie*, vol. 189, no. 1, pp. 74–80, 2013.

[69] Z. Rijnen, J. F. Bakker, R. A. Canters, *et al.*, "Clinical integration of software tool vedo for adaptive and quantitative application of phased array hyperthermia in the head and neck," *International journal of Hyperthermia*, vol. 29, no. 3, pp. 181–193, 2013.

[70] H. P. Kok, L. Korshuize-van Straten, A. Bakker, *et al.*, "Online adaptive hyperthermia treatment planning during locoregional heating to suppress treatment-limiting hot spots," *International Journal of Radiation Oncology* Biology* Physics*, vol. 99, no. 4, pp. 1039–1047, 2017.

[71] R. F. Verhaart, V. Fortunati, G. M. Verduijn, *et al.*, "The relevance of mri for patient modeling in head and neck hyperthermia treatment planning: A comparison of ct and ct-mri based tissue segmentation on simulated temperature," *Medical physics*, vol. 41, no. 12, p. 123 302, 2014.

[72] I. VilasBoas-Ribeiro, G. C. van Rhoon, T. Drizdal, M. Franckena, and M. M. Paulides, "Impact of number of segmented tissues on sar prediction accuracy in deep pelvic hyperthermia treatment planning," *Cancers*, vol. 12, no. 9, p. 2646, 2020.

[73] G. G. Bellizzi, T. Drizdal, G. C. van Rhoon, L. Crocco, T. Isernia, and M. M. Paulides, "The potential of constrained sar focusing for hyperthermia treatment planning: Analysis for the head & neck region," *Physics in Medicine & Biology*, vol. 64, no. 1, p. 015 013, 2018.

[74] N. Lynnerup, "Cranial thickness in relation to age, sex and general body build in a danish forensic sample," *Forensic science international*, vol. 117, no. 1-2, pp. 45–51, 2001.

[75] A. Peyman, "Dielectric properties of tissues; variation with age and their relevance in exposure of children to electromagnetic fields; state of knowledge," *Progress in biophysics and molecular biology*, vol. 107, no. 3, pp. 434–438, 2011.

[76] D. A. Pollacco, L. Farina, P. S. Wismayer, L. Farrugia, and C. V. Sammut, "Characterization of the dielectric properties of biological tissues and their correlation to tissue hydration," *IEEE Transactions on Dielectrics and Electrical Insulation*, vol. 25, no. 6, pp. 2191–2197, 2018.

[77] C. W. Song, "Effect of local hyperthermia on blood flow and microenvironment: A review," *Cancer research*, vol. 44, no. 10 Supplement, 4721s–4730s, 1984.

[78] C. Rossmann and D. Haemmerich, "Review of temperature dependence of thermal properties, dielectric properties, and perfusion of biological tissues at hyperthermic and ablation temperatures," *Critical Reviews™ in Biomedical Engineering*, vol. 42, no. 6, 2014.

[79] M. M. Paulides, D. B. Rodrigues, G. G. Bellizzi, *et al.*, "Esho benchmarks for computational modeling and optimization in hyperthermia therapy," *International Journal of Hyperthermia*, vol. 38, no. 1, pp. 1425–1442, 2021.

[80] J. Van de Kamer, N. Van Wieringen, A. De Leeuw, and J. Lagendijk, "The significance of accurate dielectric tissue data for hyperthermia treatment planning," *International journal of hyperthermia*, vol. 17, no. 2, pp. 123–142, 2001.

[81] W. T. Joines, Y. Zhang, C. Li, and R. L. Jirtle, "The measured electrical properties of normal and malignant human tissues from 50 to 900 mhz," *Medical physics*, vol. 21, no. 4, pp. 547–550, 1994.

[82] J. Lang, B. Erdmann, and M. Seebass, "Impact of nonlinear heat transfer on temperature control in regional hyperthermia," *IEEE Transactions on Biomedical Engineering*, vol. 46, no. 9, pp. 1129–1138, 1999.

[83] J.-P. Berenger, "A perfectly matched layer for the absorption of electromagnetic waves," *Journal of computational physics*, vol. 114, no. 2, pp. 185–200, 1994.

[84] H. H. Pennes, "Analysis of tissue and arterial blood temperatures in the resting human forearm," *Journal of applied physiology*, vol. 1, no. 2, pp. 93–122, 1948.

[85] Dassault Systèmes SE, Vélizy-Villacoublay, France, *CST Studio Suite 2019*, 2019.

[86] COMSOL AB, Stockholm, Sweden, *COMSOL Multiphysics® v. 5.6*, 2020.

[87] W. C. Dewey, "Arrhenius relationships from the molecule and cell to the clinic," *International journal of hyperthermia*, vol. 10, no. 4, pp. 457–483, 1994.

[88] E. L. Jones, J. R. Oleson, L. R. Prosnitz, *et al.*, "Randomized trial of hyperthermia and radiation for superficial tumors," *Journal of Clinical Oncology*, vol. 23, no. 13, pp. 3079–3085, 2005.

[89] G. C. van Rhoon, "Is CEM43 still a relevant thermal dose parameter for hyperthermia treatment monitoring?" *International Journal of Hyperthermia*, vol. 32, no. 1, pp. 50–62, 2016.

[90] M. Franckena, D. Fatehi, M. de Bruijne, *et al.*, "Hyperthermia dose-effect relationship in 420 patients with cervical cancer treated with combined radiotherapy and hyperthermia," *European Journal of Cancer*, vol. 45, no. 11, pp. 1969–1978, 2009.

[91] M. M. Paulides, G. M. Verduijn, and N. Van Holthe, "Status quo and directions in deep head and neck hyperthermia," *Radiation Oncology*, vol. 11, no. 1, p. 21, 2016.

[92] G. G. Bellizzi, T. Drizdal, G. C. van Rhoon, L. Crocco, T. Isernia, and M. M. Paulides, "Predictive value of sar based quality indicators for head and neck hyperthermia treatment quality," *International Journal of Hyperthermia*, vol. 36, no. 1, pp. 455–464, 2019.

[93] R. Canters, M. Franckena, J. van der Zee, and G. Van Rhoon, "Optimizing deep hyperthermia treatments: Are locations of patient pain complaints correlated with modelled SAR peak locations?" *Physics in Medicine & Biology*, vol. 56, no. 2, p. 439, 2010.

[94] H. K. Lee, A. G. Antell, C. A. Perez, *et al.*, "Superficial hyperthermia and irradiation for recurrent breast carcinoma of the chest wall: Prognostic factors in 196 tumors.," *International journal of radiation oncology, biology, physics*, vol. 40, no. 2, pp. 365–375, 1998.

[95] I. E. C. (IEC), "Measurement procedure for the assessment of specific absorption rate of human exposure to radio frequency fields from hand-held and body-worn wireless communication devices - part 1528: Human models, instrumentation and procedures (frequency range of 4 mhz to 10 ghz)," 3, rue de Varembé, PO Box 131, CH-1211 Geneva 20, Switzerland, International Standard 62209-1528:2020, Oct. 2020.

[96] N. Stevens and L. Martens, "Study on the mass averaging of sar distributions," in *1999 IEEE MTT-S International Microwave Symposium Digest (Cat. No. 99CH36282)*, IEEE, vol. 2, 1999, pp. 595–598.

[97] A. Hirata, K. Shirai, and O. Fujiwara, "On averaging mass of sar correlating with temperature elevation due to a dipole antenna," *Progress In Electromagnetics Research*, vol. 84, pp. 221–237, 2008.

[98] A. Razmadze, L. Shoshiashvili, D. Kakulia, and R. Zaridze, "Influence on averaging masses on correlation between mass-averaged sar and temperature rise," *Journal of Applied Electromagnetism*, vol. 10, no. 2, pp. 8–21, 2008.

[99] A. Razmadze, L. Shoshiashvili, D. Kakulia, R. Zaridze, G. Bit-Babik, and A. Faraone, "Influence of specific absorption rate averaging schemes on correlation between mass-averaged specific absorption rate and temperature rise," *Electromagnetics*, vol. 29, no. 1, pp. 77–90, 2009.

[100] J. Bakker, M. Paulides, E. Neufeld, A. Christ, N. Kuster, and G. Van Rhoon, "Children and adults exposed to electromagnetic fields at the icnirp reference levels: Theoretical assessment of the induced peak temperature increase," *Physics in Medicine & Biology*, vol. 56, no. 15, p. 4967, 2011.

[101] K. Chopra, D. Calva, M. Sosin, *et al.*, "A comprehensive examination of topographic thickness of skin in the human face," *Aesthetic surgery journal*, vol. 35, no. 8, pp. 1007–1013, 2015.

[102] F. B. Haeussinger, S. Heinzel, T. Hahn, M. Schecklmann, A.-C. Ehlis, and A. J. Fallgatter, "Simulation of near-infrared light absorption considering individual head and prefrontal cortex anatomy: Implications for optical neuroimaging," *PloS one*, vol. 6, no. 10, e26377, 2011.

[103] N. Qi, M. Zhang, T. Wittig, and A. Prokop, "Application of CST time domain algorithm in the electromagnetic simulation standard of the SAR for mobile phone," in *2008 International Conference on Microwave and Millimeter Wave Technology*, IEEE, vol. 4, 2008, pp. 1717–1720.

[104] M. Van der Gaag, M. De Bruijne, T. Samaras, J. Van Der Zee, and G. Van Rhoon, "Development of a guideline for the water bolus temperature in superficial hyperthermia," *International journal of hyperthermia*, vol. 22, no. 8, pp. 637–656, 2006.

[105] R. F. Verhaart, G. M. Verduijn, V. Fortunati, *et al.*, "Accurate 3d temperature dosimetry during hyperthermia therapy by combining invasive measurements and patient-specific simulations," *International Journal of Hyperthermia*, vol. 31, no. 6, pp. 686–692, 2015.

[106] M. Böhm, J. Kremer, and A. Louis, "Efficient algorithm for computing optimal control of antennas in hyperthermia," *Surveys Math. Indust*, vol. 3, no. 4, pp. 233–251, 1993.

[107] T. Köhler, P. Maass, P. Wust, and M. Seebass, "A fast algorithm to find optimal controls of multiantenna applicators in regional hyperthermia," *Physics in Medicine & Biology*, vol. 46, no. 9, p. 2503, 2001.

[108] R. Mestrom, J. Van Engelen, M. Van Beurden, M. Paulides, W. Numan, and A. Tijhuis, "A refined eigenvalue-based optimization technique for hyperthermia treatment planning," in *The 8th European Conference on Antennas and Propagation (EuCAP 2014)*, IEEE, 2014, pp. 2010–2013.

[109] M. M. Paulides, S. H. Vossen, A. P. Zwamborn, and G. C. van Rhoon, "Theoretical investigation into the feasibility to deposit rf energy centrally in the head-and-neck region," *International Journal of Radiation Oncology* Biology* Physics*, vol. 63, no. 2, pp. 634–642, 2005.

[110] F. Bardati and P. Tognolatti, "Hyperthermia phased arrays pre-treatment evaluation," *International Journal of Hyperthermia*, vol. 32, no. 8, pp. 911–922, 2016.

[111] B. Guérin, J. F. Villena, A. G. Polimeridis, *et al.*, "Computation of ultimate SAR amplification factors for radiofrequency hyperthermia in non-uniform body models: Impact of frequency and tumour location," *International Journal of Hyperthermia*, vol. 34, no. 1, pp. 87–100, 2018.

[112] G. Bruggmoser, S. Bauchowitz, R. Canters, *et al.*, "Guideline for the clinical application, documentation and analysis of clinical studies for regional deep hyperthermia," *Strahlentherapie und Onkologie*, vol. 188, no. 2, pp. 198–211, 2012.

[113] T. V. Samulski, P. Fessenden, R. Valdagni, and D. S. Kapp, "Correlations of thermal washout rate, steady state temperatures, and tissue type in deep seated recurrent or metastatic tumors," *International Journal of Radiation Oncology* Biology* Physics*, vol. 13, no. 6, pp. 907–916, 1987.

[114] M. Zanoli and H. D. Trefná, "Combining target coverage and hot-spot suppression into one cost function: The hot-to-cold spot quotient," in *2021 15th European Conference on Antennas and Propagation (EuCAP)*, IEEE, 2021, pp. 1–4.

[115] H. Dobšíček Trefná, J. Crezee, M. Schmidt, *et al.*, "Quality assurance guidelines for superficial hyperthermia clinical trials," *Strahlentherapie und Onkologie*, vol. 193, no. 5, pp. 351–366, 2017.

[116] J. Kennedy and R. Eberhart, "Particle swarm optimization," in *Proceedings of ICNN'95-international conference on neural networks*, IEEE, vol. 4, 1995, pp. 1942–1948.

[117] G. Cappiello, T. Drizdal, B. Mc Ginley, *et al.*, "The potential of time-multiplexed steering in phased array microwave hyperthermia for head and neck cancer treatment," *Physics in Medicine & Biology*, vol. 63, no. 13, p. 135 023, 2018.

[118] E. Zastrow, S. C. Hagness, and B. D. Van Veen, "3d computational study of non-invasive patient-specific microwave hyperthermia treatment of breast cancer," *Physics in Medicine & Biology*, vol. 55, no. 13, p. 3611, 2010.

[119] B. Guo, L. Xu, and J. Li, "Time reversal based microwave hyperthermia treatment of breast cancer," *Microwave and Optical Technology Letters*, vol. 47, no. 4, pp. 335–338, 2005.

[120] H. D. Trefná, J. Vrba, and M. Persson, "Time-reversal focusing in microwave hyperthermia for deep-seated tumors," *Physics in Medicine & Biology*, vol. 55, no. 8, p. 2167, 2010.

[121] J.-L. Thomas and M. A. Fink, "Ultrasonic beam focusing through tissue inhomogeneities with a time reversal mirror: Application to transskull therapy," *IEEE Transactions on Ultrasonics, Ferroelectrics, and Frequency Control*, vol. 43, no. 6, pp. 1122–1129, 1996.

[122] M. Fink, G. Montaldo, and M. Tanter, "Time reversal acoustics," in *IEEE Ultrasonics Symposium, 2004*, IEEE, vol. 2, 2004, pp. 850–859.

[123] G. Lerosey, J. De Rosny, A. Tourin, A. Derode, G. Montaldo, and M. Fink, "Time reversal of electromagnetic waves," *Physical review letters*, vol. 92, no. 19, p. 193 904, 2004.

[124] P. Takook, H. D. Trefná, A. Fhager, and M. Persson, "Evaluation of the 3D time reversal method for hyperthermia treatment planning in head and neck tumors," in *2015 9th European Conference on Antennas and Propagation (EuCAP)*, IEEE, 2015, pp. 1–5.

[125] N. Leduc, K. Okita, K. Sugiyama, S. Takagi, and Y. Matsumoto, "Focus control in HIFU therapy assisted by time-reversal simulation with an iterative procedure for hot spot elimination," *Journal of Biomechanical Science and Engineering*, vol. 7, no. 1, pp. 43–56, 2012.

[126] M. Seebass, R. Beck, J. Gellermann, J. Nadobny, and P. Wust, "Electromagnetic phased arrays for regional hyperthermia: Optimal frequency and antenna arrangement," *International Journal of Hyperthermia*, vol. 17, no. 4, pp. 321–336, 2001.

[127] M. M. Paulides, J. F. Bakker, A. P. Zwamborn, and G. C. Van Rhoon, "A head and neck hyperthermia applicator: Theoretical antenna array design," *International journal of hyperthermia*, vol. 23, no. 1, pp. 59–67, 2007.

[128] P. Togni, Z. Rijnen, W. Numan, *et al.*, "Electromagnetic redesign of the hypercollar applicator: Toward improved deep local head-and-neck hyperthermia," *Physics in Medicine & Biology*, vol. 58, no. 17, p. 5997, 2013.

[129] J. Vrba, M. Lapeš, and L. Oppl, "Technical aspects of microwave thermotherapy," *Bioelectrochemistry and bioenergetics*, vol. 48, no. 2, pp. 305–309, 1999.

[130] J. Yang and A. Kishk, "A novel low-profile compact directional ultra-wideband antenna: The self-grounded bow-tie antenna," *IEEE Transactions on Antennas and Propagation*, vol. 60, no. 3, pp. 1214–1220, 2011.

[131] P. Takook, M. Persson, J. Gellermann, and H. D. Trefná, "Compact self-grounded bow-tie antenna design for an uwb phased-array hyperthermia applicator," *International Journal of Hyperthermia*, vol. 33, no. 4, pp. 387–400, 2017.

[132] G. G. Bellizzi, M. M. Paulides, T. Drizdal, G. C. van Rhoon, L. Crocco, and T. Isernia, "Selecting the optimal subset of antennas in hyperthermia treatment planning," *IEEE Journal of Electromagnetics, RF and Microwaves in Medicine and Biology*, vol. 3, no. 4, pp. 240–246, 2019.

[133] J. Overgaard, "The current and potential role of hyperthermia in radiotherapy," *International Journal of Radiation Oncology* Biology* Physics*, vol. 16, no. 3, pp. 535–549, 1989.

[134] C. Van Leeuwen, A. Oei, R. Ten Cate, *et al.*, "Measurement and analysis of the impact of time-interval, temperature and radiation dose on tumour cell survival and its application in thermoradiotherapy plan evaluation," *International Journal of Hyperthermia*, vol. 34, no. 1, pp. 30–38, 2018.

[135] J. Haveman, P. Sminia, J. Wondergem, J. van der Zee, and M. Hulshof, "Effects of hyperthermia on the central nervous system: What was learnt from animal studies?" *International journal of hyperthermia*, vol. 21, no. 5, pp. 473–487, 2005.

[136] M. T. Makale, C. R. McDonald, J. Hattangadi-Gluth, and S. Kesari, "Brain irradiation and long-term cognitive disability: Current concepts," *Nature reviews. Neurology*, vol. 13, no. 1, p. 52, 2017.

[137] J. Lagendijk, G. Van Rhoon, S. Hornsleth, *et al.*, "Esho quality assurance guidelines for regional hyperthermia," *International journal of hyperthermia*, vol. 14, no. 2, pp. 125–133, 1998.

[138] R. Canters, M. Franckena, M. Paulides, and G. Van Rhoon, "Patient positioning in deep hyperthermia: Influences of inaccuracies, signal correction possibilities and optimization potential," *Physics in Medicine & Biology*, vol. 54, no. 12, p. 3923, 2009.

[139] B. Aklan, P. Gierse, J. Hartmann, O. J. Ott, R. Fietkau, and C. Bert, "Influence of patient mispositioning on sar distribution and simulated temperature in regional deep hyperthermia," *Physics in Medicine & Biology*, vol. 62, no. 12, p. 4929, 2017.

[140] H. Kok and J. Crezee, "Progress and future directions in hyperthermia treatment planning," in *2017 First IEEE MTT-S International Microwave Bio Conference (IMBIOC)*, IEEE, 2017, pp. 1–4.

[141] E. Oberacker, A. Kuehne, J. Nadobny, *et al.*, "Radiofrequency applicator concepts for simultaneous mr imaging and hyperthermia treatment of glioblastoma multiforme," *Current Directions in Biomedical Engineering*, vol. 3, no. 2, pp. 473–477, 2017.

[142] L. C. Sebeke, P. Rademann, A. C. Maul, *et al.*, "Visualization of thermal washout due to spatiotemporally heterogenous perfusion in the application of a model-based control algorithm for mr-hifu mediated hyperthermia," *International Journal of Hyperthermia*, vol. 38, no. 1, pp. 1174–1187, 2021.

[143] R. C. Conceição, J. J. Mohr, M. O'Halloran, *et al.*, *An introduction to microwave imaging for breast cancer detection*. Springer, 2016.

[144] P. M. Meaney, T. Zhou, M. W. Fanning, S. D. Geimer, and K. D. Paulsen, "Microwave thermal imaging of scanned focused ultrasound heating: Phantom results," *International Journal of Hyperthermia*, vol. 24, no. 7, pp. 523–536, 2008.

[145] M. Haynes, J. Stang, and M. Moghaddam, "Real-time microwave imaging of differential temperature for thermal therapy monitoring," *IEEE Transactions on Biomedical Engineering*, vol. 61, no. 6, pp. 1787–1797, 2014.

[146] M. G. Aram, L. Beilina, and H. D. Trefná, "Microwave thermometry with potential application in non-invasive monitoring of hyperthermia," *Journal of Inverse and Ill-posed Problems*, vol. 1, no. ahead-of-print, 2020.

[147] P. Hashemzadeh, A. Fhager, and M. Persson, "Experimental investigation of an optimization approach to microwave tomography," *Electromagnetic biology and medicine*, vol. 25, no. 1, pp. 1–12, 2006.

Part II

Papers

PAPER A

Suitability of eigenvalue beamforming for discrete multi-frequency hyperthermia treatment planning

Massimiliano Zanoli, Hana Dobšíček Trefná

Medical Physics
16 September 2021

DOI: 10.1002/mp.15220

The layout has been revised.

Abstract

Purpose: Thermal dose delivery during microwave hyperthermia (HT) cancer treatment is expected to benefit from the introduction of ultrawide-band (UWB) phased array applicators. A full exploitation of the combination of different frequencies to improve the deposition pattern is however a non-trivial problem. It is unclear whether the cost functions used for HTP optimisation in the single-frequency setting can be meaningfully extended to the UWB case.
Method: We discuss the ability of the eigenvalue (EV) and a novel implementation of iterative-eigenvalue (i-EV) beamforming methods to fully exploit the available frequency spectrum when a discrete set of simultaneous operating frequencies is available for treatment. We prove that the quadratic power deposition ratio solved by the methods can be maximized by only one frequency in the set, therefore rendering EV inadequate for UWB treatment planning. We further investigate whether this represents a limitation in two realistic test cases, comparing the thermal distributions resulting from EV and i-EV to those obtained by optimizing for other non-linear cost functions that allow for multi-frequency.
Results: The classical EV-based single-frequency HTP yields systematically lower target SAR deposition and temperature values than non-linear HTP. In a larynx target, the proposed single-frequency i-EV scheme is able to compensate for this and reach temperatures comparable to those given by global non-linear optimisation. In a meninges target, the multi-frequency setting outperforms the single-frequency one, achieving better target coverage and 0.5 °C higher T_{90} in the tumor than single-frequency based HTP.
Conclusions: Classical EV should be avoided for HT treatment planning purposes. The proposed single-frequency i-EV scheme can be a viable option depending on the patient and tumor to be treated, as long as the proper operating frequency can be selected. Multi-frequency HT can bring a considerable benefit in regions typically difficult to treat such as the brain.

1 Introduction

In deep microwave hyperthermia (MW-HT) for cancer treatment, RF energy is deposited into a tumor by a phased array of antennas surrounding the patient [1], [2]. The aim is to heat the tumor up to temperatures of $40-44°$, which have been proven to enhance the therapeutic effects of radio- and chemo-therapy [3], [4]. The challenge in deep MW-HT is to reach an adequate thermal dose coverage of the target volume while sparing the surrounding healthy tissues from excessive temperatures. To this end, each array channel is independently steered in amplitude and phase at the chosen operating frequency to shape the interference pattern inside the patient and generate a focus in the target volume.

The list of regional deep MW-HT applicators currently used in the clinics includes systems working at $70 \sim 100$ MHz for the pelvic and abdominal region [5], [6] and 434 MHz for the head and neck [7]. All these system are designed to operate at a single frequency. The choice of this frequency is a trade-off between expected penetration depth and focal size [8]–[10]. The balance between these requirements might however change depending on the particular patient and target to be treated. If the target volume is small compared to the wavelength, a larger region is heated, which increases the risk for treatment-limiting hot-spots to arise in the adjacent healthy tissues. On the other hand, larger tumors might not be sufficiently covered by heat deposition when the focal spot is small, leaving out untreated areas. Thus, a one-fits-all operating frequency approach, while allowing for simpler RF system design, might lead to the impossibility of achieving high thermal doses in some patients, who might end up being excluded from the treatment [11], [12].

For the above reasons, a ultrawide-band (UWB) system providing the possibility to select among different operating frequencies for the treatment is desirable. The benefit is expected to be even higher if the treatment can happen at two or more concomitant and independently-steerable frequencies, as the superposition of their interference patterns might improve target coverage and hot-spot suppression [13], [14]. Provided that such a system is available, the hyperthermia treatment planning (HTP) stage, where the array's steering

settings are determined, has to be adapted for the UWB setting. A limited number of UWB HTP methods have been suggested in the literature: time reversal focusing [15], [16], stochastic global optimization [10], [17], quadratic programming [14], [18], and a form of eigenvalue beam-forming using FIR filters (UWB pulses) [19]. The latter, FIR-based approach, would however require the manufacturing of a RF amplifying system with an independently programmable FIR line for each channel. This solution is difficult and costly to realize, especially with the level of accuracy required for MW-HT treatments [20]. A good compromise between robustness and complexity is given by a multi-frequency system, where two or more discrete operating frequencies are selected across the available UWB range for simultaneous or finely time-interleaved treatment [21]. Time-reversal (TR) beam-forming is a promising approach in this respect, however current forms [22] lack the ability to properly control hot-spot formation. Recent and ongoing work is aiming at improving TR-based UWB HTP by means of iterative hot-spot suppression and cold-spot coverage [23]. Stochastic optimization, usually implemented via particle swarm (PS), is computationally demanding already in the single-frequency setting. Current applications of PS-based HTP require in fact a considerable coarsening of the patient model resolution to keep the execution times within reasonable limits for clinical use [24], and research is ongoing to improve on this aspect [25]. While PS can be easily extended to the multi-frequency problem, it is unlikely a viable option in practice due to the higher number of iterations and the longer time required for convergence.

An attractive alternative for HTP optimization is the clinically established eigenvalue (EV) beam-forming algorithm [26]. In EV-based HTP, the problem is defined as follows: find the set of steering parameters that maximizes the ratio of the average specific absorption rate (SAR) in the target to the average SAR in the healthy tissues. The problem can be solved directly because the ratio is quadratic in the unknown terms, i.e. the steering parameters. This makes EV-based HTP fast and deterministic, a clear benefit under many aspects. However, quadratic cost functions have been shown to poorly correlate with the temperature rise in the target, because they do not address the presence and severity of localized SAR peaks outside the target which can result in treatment limiting hot-spots[27]. Consequently, more suitable cost-functions have been proposed to better fulfil the quality requirements of hyperthermia treatments. However, these cost-functions are in general non-linear and can-

not be solved for directly via EV. Nevertheless, several workarounds have been suggested in the literature to improve the EV solution with respect to such non-linear cost functions by means of iterative procedures[28], [29]. These procedures return good approximations of the optimal SAR deposition pattern in the single-frequency setting. Still, it is unclear whether the EV method can be meaningfully extended to the case of a discrete set of operating frequencies. Multi-frequency constrained quadratic-programming HTP methods have been suggested[14], [18], yet these, while promising, do not aim at solving for the more clinically relevant non-linear cost-functions needed in hyperthermia. In this paper, we derive the EV problem for the multi-frequency case and show that the steering solution maximizing the SAR ratio cannot include more than one active frequency at a time. Subsequently, we propose a novel EV-based iterative scheme for HTP optimisation that minimizes a clinically relevant non-linear cost-function, the HTQ. This method is also subjected to the same single-frequency limitation of classical EV. Therefore, we investigate whether the single-frequency constraint can be a limiting factor in hyperthermia treatments by comparing the temperature distributions resulting from single- and multi-frequency HTP optimizations in two realistic targets, one in the neck region and one in the brain.

2 Theory

In the following analysis, a lower-case a denotes a real scalar value, an upper-case A denotes a real vector value, a tilde $\tilde{a}, \tilde{A}$ denotes a complex value, a bold symbol $\boldsymbol{a}, \boldsymbol{A}$ denotes an array or matrix. $\tilde{\boldsymbol{A}}^*$ is the element-wise complex conjugate of $\tilde{\boldsymbol{A}}$, while $\tilde{\boldsymbol{A}}^t$ is the transpose of $\tilde{\boldsymbol{A}}$. Field distributions and material properties are assumed to be space-dependent. The E-field is also further assumed to be linearly polarized everywhere, with unitary direction vector denoted by $\hat{E}$. However, the analysis can be easily extended to multi-polarized fields by superposition.

Once the complex vector E-field distributions $\tilde{E}_{c,f}$ due to each channel/antenna c have been obtained inside the patient for each frequency f by means of simulations, the total field at frequency f is obtained by superposition:

$$\tilde{E}_f = \sum_c^{n_c} \tilde{p}_{c,f} \tilde{E}_{c,f} = \tilde{p}_{1,f} \tilde{E}_{1,f} + \tilde{p}_{2,f} \tilde{E}_{2,f} + \cdots + \tilde{p}_{n_c,f} \tilde{E}_{n_c,f} \tag{A.1}$$

where $\tilde{p}_{c,f}$ is the steering parameter for channel c at frequency f, and n_c is the number of channels. The time-averaged power loss density $\bar{\mathcal{P}}_f$ of this sinusoidal field is given by:

$$\bar{\mathcal{P}}_f = \frac{1}{2}\sigma_f ||\tilde{E}_f||^2 = \frac{1}{2}\sigma_f \langle \tilde{E}_f^*, \tilde{E}_f^t \rangle = \frac{1}{2}\sigma_f \langle \tilde{\boldsymbol{p}}_f^{t*} \tilde{\boldsymbol{E}}_f^*, \tilde{\boldsymbol{E}}_f^t \tilde{\boldsymbol{p}}_f \rangle \tag{A.2}$$

where σ_f is the frequency-dependent material conductivity and $\langle \cdot, \cdot \rangle$ denotes the scalar product. The quadratic vector-matrix multiplication form in the rightmost term of (A.2) has been obtained by expanding each $\tilde{E}_f$ with the sum in (A.1) and by defining the following vectors:

$$\begin{aligned} \tilde{\boldsymbol{p}}_f &= [\ \tilde{p}_{1,f}\ \tilde{p}_{2,f}\ \ \ldots\ \tilde{p}_{n_c,f}\ ]^t \\ \tilde{\boldsymbol{E}}_f &= [\ \tilde{E}_{1,f}\ \tilde{E}_{2,f}\ \ \ldots\ \tilde{E}_{n_c,f}\ ]^t \end{aligned} \tag{A.3}$$

The total SAR deposition within a volume V due to frequency f is obtained by dividing the time-averaged power $\bar{\mathcal{P}}_f$ by the material density ρ and integrating:

$$\mathrm{SAR}_f^V = \int_V \frac{\bar{\mathcal{P}}_f}{\rho}\, dv = \frac{1}{2}\tilde{\boldsymbol{p}}_f^{t*} \left(\int_V \frac{\sigma_f}{\rho} \langle \tilde{\boldsymbol{E}}_f^*, \tilde{\boldsymbol{E}}_f^t \rangle\, dv \right) \tilde{\boldsymbol{p}}_f \tag{A.4}$$

The inner term within parentheses can be identified as the *SAR correlation matrix* for the volume V:

$$\tilde{\boldsymbol{q}}_f^V = \int_V \frac{\sigma_f}{\rho} \langle \tilde{\boldsymbol{E}}_f^*, \tilde{\boldsymbol{E}}_f^t \rangle\, dv \quad \in \quad \mathbb{C}^{\,n_c \times n_c} \tag{A.5}$$

The single-frequency SAR focusing problem consists in determining the set of optimal steering parameters $\hat{\tilde{\boldsymbol{p}}}_f$ that maximizes the ratio of the SAR in the target volume T to the SAR in the remaining tissues R:

$$\hat{\tilde{\boldsymbol{p}}}_f = \mathrm{argmax}_{\tilde{\boldsymbol{p}}_f} \left\{ \Gamma_f = \frac{\mathrm{SAR}_f^T}{\mathrm{SAR}_f^R} = \frac{\tilde{\boldsymbol{p}}_f^{t*} \tilde{\boldsymbol{q}}_f^T \tilde{\boldsymbol{p}}_f}{\tilde{\boldsymbol{p}}_f^{t*} \tilde{\boldsymbol{q}}_f^R \tilde{\boldsymbol{p}}_f} \right\} \tag{A.6}$$

The ratio Γ has assumed different names in the literature, depending on

which material properties are included as weighing factors in (A.5). Examples are the average power absorption (aPA, [9]) and the SAR amplification factor (SAF, [30]).

The problem (A.6) is a generalized eigenvalue form where the solution $\hat{\tilde{\boldsymbol{p}}}_f$ is given by the eigenvector $\boldsymbol{u}$ relative to the largest eigenvalue λ of:

$$\boldsymbol{a}\boldsymbol{u} = \lambda \boldsymbol{b}\boldsymbol{u} \tag{A.7}$$

with $\boldsymbol{a} \equiv \tilde{\boldsymbol{q}}_f^T$ and $\boldsymbol{b} \equiv \tilde{\boldsymbol{q}}_f^R$. In order to extend the analysis to a finite set of n_f discrete frequencies, we start again from the complex E-field distribution at each frequency as given by (A.1). However, since the resulting field is no longer purely sinusoidal, we need to derive the time-averaged power $\bar{\mathcal{P}}$ from the real and instantaneous E, which can be described by the superposition of the linearly polarized fields at each frequency:

$$E = \sum_f^{n_f} E_f = \sum_f^{n_f} \hat{E}_f ||\tilde{E}_f|| cos(2\pi f t + \angle\langle \hat{E}_f, \tilde{E}_f \rangle) \tag{A.8}$$

Let us consider only two separate frequencies f_i and f_j. Their resulting instantaneous power deposition in the tissue is given by:

$$\mathcal{P} = \langle J, E \rangle = \langle \sigma_i E_i + \sigma_j E_j, E_i + E_j \rangle \tag{A.9}$$

where J is the electric current density. The time-averaged power loss density is obtained by integrating $\mathcal{P}$ over a period T which is common to both frequencies. Such common period might not exist if the ratio f_i/f_j is irrational. In practical cases, however, the operating frequencies can be assumed to be integer numbers (e.g. 500 MHz) and the common period can be found as the inverse of the greatest common divisor among the set: $T = 1/\mathrm{GCD}(f_1, f_2, \ldots, f_{n_f})$. In particular, if the frequencies are chosen to be integer multiples of, e.g., 10 MHz, then the common period will be at most 1/10 MHz = 100 ns. Since this is orders of magnitude smaller than the typical thermal response time of biological tissues, it is safe to assume that the resulting power distribution can always be time-averaged for HTP evaluation purposes. Consequently, the time-averaged power deposition can be obtained as:

$$\bar{\mathcal{P}} = \frac{1}{T}\int_{-T/2}^{+T/2} \mathcal{P}\ dt = \frac{1}{T}\int_{-T/2}^{+T/2} \langle \sigma_i E_i + \sigma_j E_j, E_i + E_j \rangle\ dt \tag{A.10}$$

The scalar product in (A.10) can be expanded using (A.8). The cross-frequency terms $cos(2\pi f_i) \cdot cos(2\pi f_j)$ resulting from this multiplication have zero mean over the common period T. The only terms thus left are $cos^2(2\pi f_i)$ and $cos^2(2\pi f_j)$, yielding:

$$\bar{\mathcal{P}} = \frac{1}{2}\sigma_i ||\tilde{E}_i||^2 + \frac{1}{2}\sigma_j ||\tilde{E}_j||^2 \tag{A.11}$$

which is the sum of the independent contributions from each frequency, in the same form as (A.2). This result is valid for an arbitrary number n_f of separate discrete operating frequencies, and generalizes as follows:

$$\bar{\mathcal{P}} = \sum_f^{n_f} \frac{1}{2}\sigma_f ||\tilde{E}_f||^2 = \sum_f^{n_f} \frac{1}{2}\sigma_f \langle \tilde{\boldsymbol{p}}_f^{t*} \tilde{\boldsymbol{E}}_f^*, \tilde{\boldsymbol{E}}_f^t \tilde{\boldsymbol{p}}_f \rangle \tag{A.12}$$

To preserve the compact quadratic vector-matrix multiplication form, the steering parameter vectors and the power correlation matrices can be concatenated into:

$$\tilde{\boldsymbol{p}} = \begin{bmatrix} \tilde{\boldsymbol{p}}_1^t & \tilde{\boldsymbol{p}}_2^t & \cdots & \tilde{\boldsymbol{p}}_{n_f}^t \end{bmatrix}^t \tag{A.14}$$

$$\tilde{\boldsymbol{q}}^V = \begin{bmatrix} \tilde{\boldsymbol{q}}_1^V & 0 & \cdots & 0 \\ 0 & \tilde{\boldsymbol{q}}_2^V & \cdots & 0 \\ \vdots & \vdots & \ddots & \vdots \\ 0 & 0 & \cdots & \tilde{\boldsymbol{q}}_{n_f}^V \end{bmatrix} \quad \in \quad \mathbb{C}^{(n_c n_f)\times(n_c n_f)} \tag{A.15}$$

where $\tilde{\boldsymbol{q}}^V$ is block-diagonal. The overall SAR deposition within a volume V resulting from the sum in (A.12) can then be expressed as:

$$\mathrm{SAR}^V = \tilde{\boldsymbol{p}}^{t*} \tilde{\boldsymbol{q}}^V \tilde{\boldsymbol{p}} \tag{A.16}$$

and the SAR focusing problem (A.6) is generalized to many frequencies as:

$$\hat{\tilde{\boldsymbol{p}}} = \text{argmax}_{\tilde{\boldsymbol{p}}} \left\{ \Gamma = \frac{\text{SAR}^T}{\text{SAR}^R} = \frac{\tilde{\boldsymbol{p}}^{t*} \tilde{\boldsymbol{q}}^T \tilde{\boldsymbol{p}}}{\tilde{\boldsymbol{p}}^{t*} \tilde{\boldsymbol{q}}^R \tilde{\boldsymbol{p}}} \right\} \tag{A.17}$$

An important consequence of $\tilde{\boldsymbol{q}}^V$ being block-diagonal is that the eigenvectors and eigenvalues of (A.17) are all and only those of the individual single-frequency problems (A.6). This means that only an eigenvector of the following form can maximize Γ:

$$\hat{\tilde{\boldsymbol{p}}} = [\ \mathbf{0}\ \ldots\ \hat{\tilde{\boldsymbol{p}}}_f^t\ \ldots\ \mathbf{0}\ ]^t \tag{A.18}$$

where only one operating frequency f is active, and that there is no combination of two or more frequencies that can further improve this ratio. In other words, the optimal target-to-remaining average SAR ratio can be achieved only with one frequency, even if a discrete set of separate available operating frequencies is available.

This result might at first seem in contradiction with Zastrow et al. [19] and other wide-band impulse focusing techniques, where the weights of a FIR filter are jointly optimized to maximize the SAR ratio. However, these studies adopt a continuous wide-band approach, leading to different conclusions than those drawn in the present case. In particular, FIR filters are described by continuous and smooth frequency spectra, such that $\tilde{p}(f_0) \approx \tilde{p}(f_0 + df)$. This implies strong correlation between nearby frequencies, so that the time-averaged power $\bar{\mathcal{P}}$ is no longer given by (A.12).

Since SAR^V represents an average of all the SAR values in volume V, no considerations are made over the actual distribution of SAR within the volume. In other words, using the plain integral in (A.5) might result in unacceptably high SAR peaks in the healthy tissues (hot-spots) or insufficient coverage of certain tumor areas. To improve on this aspect, a weighing distribution $w(v)$ can be introduced[28], [29]. The SAR matrix calculation (A.5) becomes:

$$\tilde{\boldsymbol{q}}_f^V = \int_V w \frac{\sigma_f}{\rho} \langle \tilde{\boldsymbol{E}}_f^*, \tilde{\boldsymbol{E}}_f^t \rangle \, dv \tag{A.19}$$

In general, the weight distribution cannot be determined directly, but the EV procedure can be iterated by updating w according to the resulting SAR distribution. Starting with an initial weight distribution $w(v) = 1,\ \forall\ v$, we

propose the following update scheme:

$$w'(v) = \begin{cases} w(v) + 1 & v \in R1 \\ w(v) & v \notin R1 \end{cases} \tag{A.20}$$

where $R1$ is the sub-volume of the remaining healthy tissues containing the highest 1-percentile of SAR. An iteration can be considered successful if it improved the SAR deposition within the target and reduced the peak hot-spot in healthy tissues, represented by $R1$. To this end, the *hot-spot to target quotient*[31] (HTQ) can be used:

$$\mathrm{HTQ} = \frac{\overline{\mathrm{SAR}}_{R1}}{\overline{\mathrm{SAR}}_{T}} \tag{A.21}$$

where $\overline{\mathrm{SAR}}_T$ is the average SAR in the target, and $\overline{\mathrm{SAR}}_{R1}$ the average SAR in the most prominent hot-spot. This HTP quality indicator can be used as a non-linear cost function for the iterative process, which consists in applying (A.20) until the HTQ no longer improves.

3 Materials & Methods

To benchmark the proposed iterative scheme, highlight the limits of single-frequency HTP, and investigate the overall suitability of the SAR-ratio as cost function for HTP, we consider two examples of realistic targets treated with single- and multi-frequency MW-HT. The first target is anatomically identified in the larynx, while the second is a meningioma (Fig. 1 and 2). The applicator arrays consist of 10 wideband self-grounded bow-tie antennas [32] each, working across the $400 - 800$ MHz frequency band. The applicators include a surface and an antenna water bolus that fulfil three purposes: cool the patient's skin, realize a dielectric matching between antenna and patient, and reduce cross-coupling between nearby antennas. The set of operating frequencies available for treatment is obtained by stepping 100 MHz within the antenna operational frequency band for the single-frequency case and considering all possible 2-frequency combinations for the multi-frequency case, yielding a total of 15 operating frequency settings.

The upper body part used in electromagnetic and thermal simulations is a subset of the *Duke* human voxel model from the IT'IS Foundation [33], and all healthy tissue properties are obtained from the IT'IS Database [34]. The E-

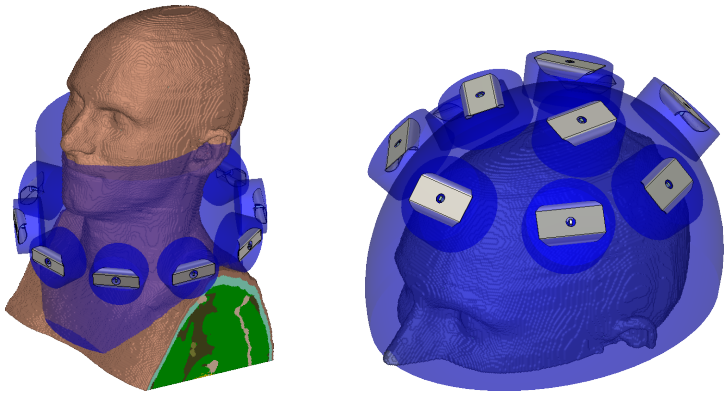

(a) **(b)**

Figure 1: Applicator models: a) neck applicator for the larynx target, b) brain applicator for the meningioma target.

field and temperature distributions, generated by a circular array for the neck and a semi-spherical array for the brain, are obtained via the commercial solver CST Microwave Studio® [35]. For HTP optimization and quality assessment purposes, the SAR distributions are smoothed by a 1g-mass averaging scheme. Surface voxels are treated by expanding the convolution kernel until the mass of patient tissues within reaches 1g.

The tumor targets (Fig. 2) are manually delineated inside the model and filled with a material exhibiting dielectric and thermal properties equal to the weighed average of the materials originally composing the volume. Some thermal properties are further adjusted to reflect the response of tissues to thermal stress: muscle perfusion is increased by a factor 4 due to the systemic response to heat [36], tumor perfusion is decreased by a factor 0.7 to account for its chaotic vasculature [37], and the thermal conductivity of the cerebrospinal fluid is increased by a factor 10 to emulate the convective transport of heat [38]. The resulting tumor properties are reported in Table 1.

We compare the SAR distributions obtained via different HTP methods using two clinically established quality indicators: the HTQ, as defined above in (A.21), and the 50% iso-SAR target coverage, TC_{50}, defined as follows[39], [40]:

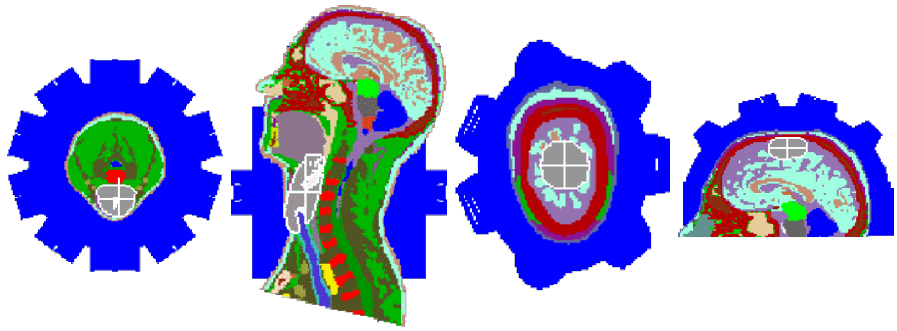

(a) (b) (c) (d)

Figure 2: Patient models: a) transverse and b) sagittal sections of the neck setup, c) transverse and d) sagittal sections of the brain setup. The targets are outlined in white. The target center is indicated by a white cross.

Table 1: Properties of the tumor materials used to fill the target volumes.

Tumor	ϵ [$\sim$]	σ [$\frac{S}{m}$]	ρ [$\frac{kg}{m^3}$]	k [$\frac{W}{Km}$]	c [$\frac{kJ}{Kkg}$]	ω_b [$\frac{kW}{Km^3}$]	Q_m [$\frac{kW}{m^3}$]
Larynx	47.8	0.674	1088	0.423	3.285	22.033	5.456
Meninges	57.3	1.372	1063	0.535	3.754	17.048	5.478

$$\mathrm{TC}_{50} = \frac{|T'|}{|T|} \quad , \quad T' \;\mid\; \mathrm{SAR}[T'] \geq \frac{1}{2}\mathrm{SAR}[R \cup T] \tag{A.22}$$

that is, the fraction of target volume whose SAR values are above 50% of the highest SAR peak in the patient. We further assess the thermal distributions obtained when either Γ, HTQ or TC_{50} are used as cost functions for the SAR-based HTP. In thermal simulations, the power deposition is scaled until the temperature peak in healthy tissues reaches 43°C [41], [42]. The quality of each distribution is then evaluated in terms of target median temperature, T_{50}, and temperature reached by 90 % of the target volume, T_{90}. The four HTP methods are labelled as follows:

`EV[Γ]`	solving for the Γ ratio via EV
`i-EV[HTQ]`	minimizing the HTQ via iterative EV

`PS[HTQ]`	minimizing the HTQ via PS
`PS[TC_50]`	maximizing the TC_{50} via PS

where PS stands for particle swarm, a clinically used global stochastic optimizer, which is capable of solving single- and multi-frequency problems for non-linear cost-functions [17]. All HTP algorithms are implemented in MATLAB® [43].

4 Results

Fig. 3 reports the optimal values of the SAR absorption ratio Γ for each individual frequency for both targets. These values are obtained by directly solving (A.6) using eigenvalue decomposition. The power ratio exhibits a clear frequency-dependent behavior, with one frequency yielding the highest Γ value. The values yielded by other frequencies decrease nearly monotonically with the distance from this optimal frequency. The best frequency for the larynx target is 800 MHz, while for the meningioma it is 400 MHz.

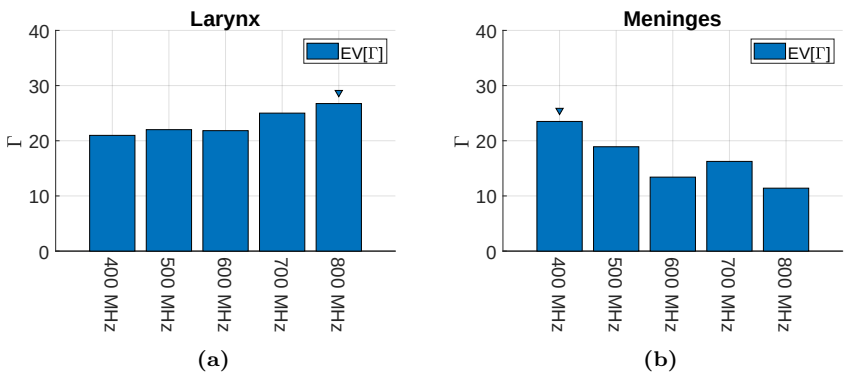

Figure 3: The maximum SAR absorption ratio, Γ, at each single operating frequency for the two selected targets, obtained via direct solution. The triangle indicates the best Γ value and operating frequency for a given model.

The assessment of the SAR distributions resulting from each HTP method in terms of HTQ is reported in Fig. 4. The benefit introduced by shifting

from a single- to a multi-frequency setting is indicated by the gray bars in the plots. It can be seen that, in terms of HTQ, virtually no improvement is achieved by a multi-frequency setting, regardless of the target. Naturally, the methods that aim at minimizing the HTQ, such as `i-EV[HTQ]` and `PS[HTQ]` yield the lowest, i.e. best, values for this indicator. Noticeably, the iterative EV implementing the proposed weight update scheme (A.20) is capable of minimizing the HTQ to levels comparable to the global optimum provided by PS in all single-frequency cases. At 600 MHz, in the larynx case, the HTQ provided by i-EV is even better than PS's, indicating that PS might not have converged to the global optimum. The SAR distributions resulting from direct EV, which solves for the maximum Γ, exhibit consistently high HTQ, regardless of the frequency. Similarly high HTQ values are obtained even by the PS optimization when TC_{50} is used as goal function.

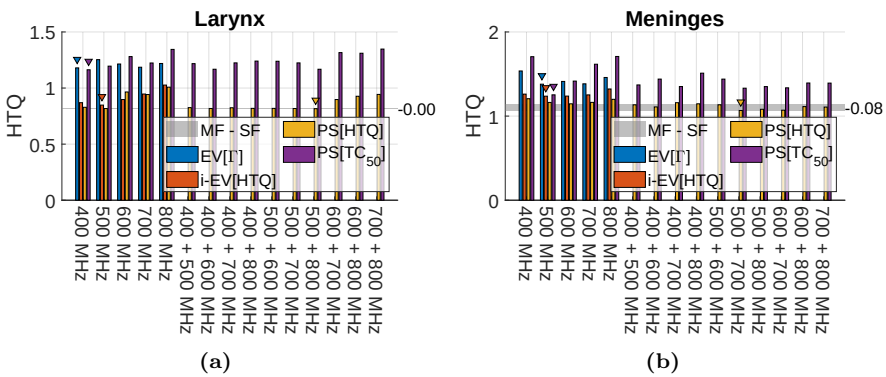

Figure 4: HTQ values for the two selected targets and for all frequency combinations, obtained via the methods specified in the legend. The triangles indicate the best result and frequency combination for the corresponding method. The gray `MF - SF` bar and the value next to it report the difference between the best single-frequency result and the best multi-frequency result.

Fig. 5 reports the values of TC_{50} as quality indicator for the two targets. The difference in TC_{50} between the best single- and multi-frequency solutions reveals that the benefit of introducing a second operating frequency is limited in the larynx case, but relevant in the brain case. The `PS[TC_50]` solution at $600 + 700$ MHz gains more than 10 % in TC_{50} for the meningioma

target with respect to the best single-frequency solution. The HTQ-optimal solutions, `i-EV[HTQ]` and `PS[HTQ]`, yield poor target coverage in almost all cases. In particular, TC_{50} in the meninges is extremely low for these solutions. At 500 MHz, `PS[HTQ]` gains about 16 % in target coverage with respect to `i-EV[HTQ]`, despite the negligible difference of 0.07 in HTQ between the two solutions seen in Fig. 4b. In the larynx, only one single-frequency case and two multi-frequency cases yield coverage above 50% when solved for HTQ. The `EV[Γ]` solutions yield poor target coverage in all cases. The `PS[TC_50]` optimisation strategy yields the best values for this indicator, as expected.

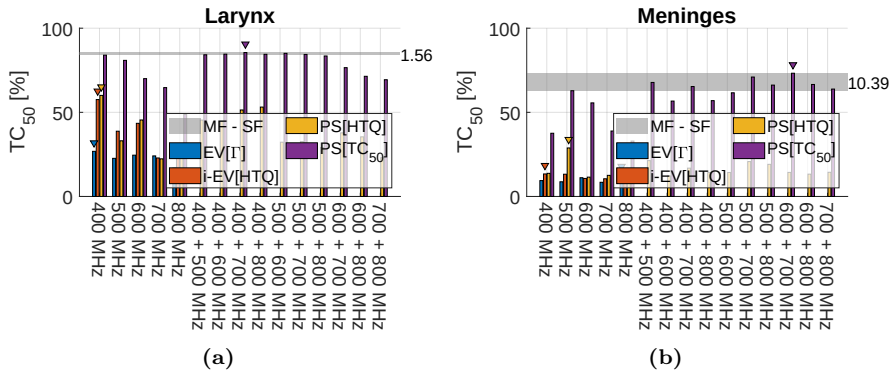

Figure 5: TC_{50} for the two selected targets and for all frequency combinations, obtained via the methods specified in the legend. The triangles indicate the best result and frequency combination for the corresponding method. The gray `MF - SF` bar and the value next to it report the difference between the best single-frequency result and the best multi-frequency result.

To gain a better understanding of the differences between the HTP methods considered in this work, the SAR distributions achieved by each method at its optimal combination of frequencies in terms of final cost function value are visualized in Figures 6 and 7. In the larynx case, the `EV[Γ]` solution at 800 MHz reflects the poor target coverage, especially in deeper parts of the target, and the inefficient hot-spot suppression suggested by the values of the HTP quality indicators. The main heating spot is outside the target and located in the adjacent skin layer, between the target and the bolus. The `i-EV[HTQ]` and `PS[HTQ]` solutions exhibit very similar SAR patterns, with

relatively homogeneous energy deposition thorough the target and maxima located near the target center. This correspondence can be explained by the major contribution of the frequency component at 500 MHz. The role of the second frequency component at 800 MHz in the `PS[HTQ]` solution is rather limited, nevertheless it increases the SAR deposition in the deeper parts of the tumor by radiation from the antennas lying on the posterior side of the neck. The `PS[TC_50]` optimisation strategy yields a remarkably different solution from all the previous methods. In this solution, almost all antennas are active and their power contribution is in the same order of magnitude. This results in a very high and homogeneous energy deposition in the tumor, which is however accompanied by considerable heating of the surrounding healthy tissues. In fact, both superficial and deep healthy tissue heating spots are present in this solution.

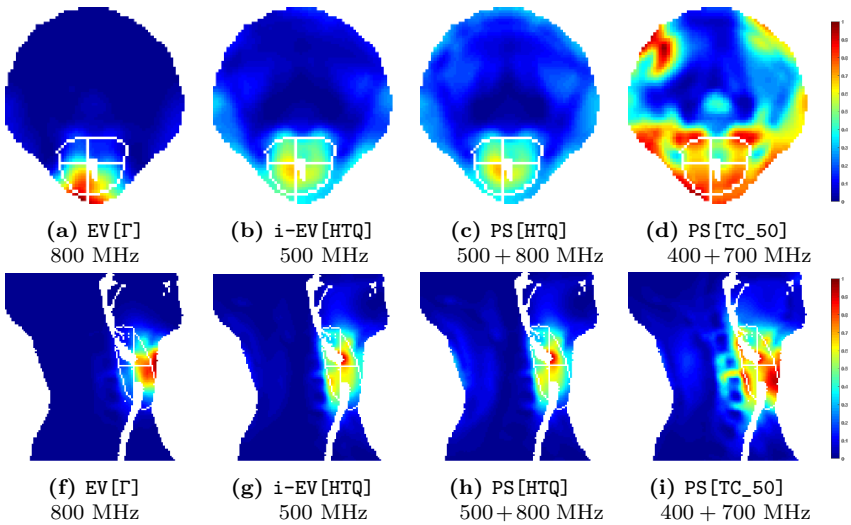

(a) `EV[Γ]` 800 MHz **(b)** `i-EV[HTQ]` 500 MHz **(c)** `PS[HTQ]` 500 + 800 MHz **(d)** `PS[TC_50]` 400 + 700 MHz

(f) `EV[Γ]` 800 MHz **(g)** `i-EV[HTQ]` 500 MHz **(h)** `PS[HTQ]` 500 + 800 MHz **(i)** `PS[TC_50]` 400 + 700 MHz

Figure 6: SAR distributions in the larynx case for each optimisation strategy at its optimal frequency or combination of frequencies. a) to d) transverse sections, f) to i) sagittal sections. The target is outlined in white. The sections are taken at the target center, which is indicated by a white cross. The SAR values are normalized to the highest peak inside the patient. The SAR is not calculated for those voxels belonging to background or to the patient's lumina, since they do not represent biological tissue.

In the meningioma case, Fig. 7, the main SAR peak of the `EV[Γ]` solution is located inside the target. Nevertheless, this peak is rather narrow and only affects the superficial part of the tumor, leaving the deeper parts unheated. The `i-EV[HTQ]` slightly improves on this aspect by extending the SAR deposition into the deeper parts of the brain. The `PS[HTQ]` method further enhances the coverage of deeper tumor areas with the help of a second frequency component at 700 MHz. The `PS[TC_50]` solution once more distinguishes itself from the other methods by actively using all antennas and frequency components to considerably extend the SAR deposition throughout the whole target volume. This is done at the expenses of a substantial heating of the healthy tissues, however the heating spots are now located more superficially and closer to the water bolus than in the larynx case.

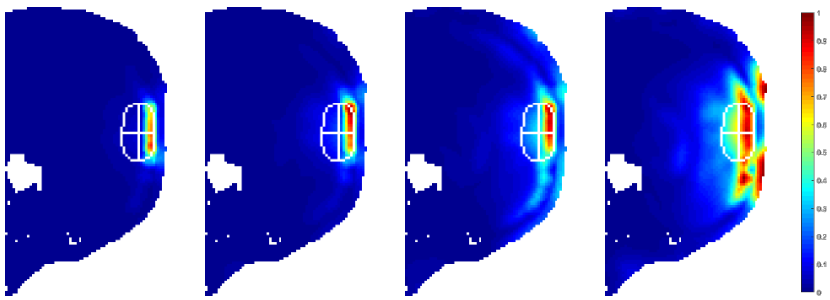

(a) `EV[Γ]` 400 MHz **(b)** `i-EV[HTQ]` 500 MHz **(c)** `PS[HTQ]` 500 + 700 MHz **(d)** `PS[TC_50]` 600 + 700 MHz

Figure 7: SAR distributions in the meninges case for each optimisation strategy at its optimal frequency or combination of frequencies. Sagittal sections. The target is outlined in white. The sections are taken at the target center, which is indicated by a white cross. The SAR values are normalized to the highest peak inside the patient. The SAR is not calculated for those voxels belonging to background or to the patient's lumina, since they do not represent biological tissue. The sections are rotated by 90° for optimal layout.

Figures 8 and 9 report the temperature profiles corresponding to the SAR distributions above. Again, each profile corresponds to the frequency combination that yielded the best cost function value for the given optimisation algorithm. The analysis of the temperature distributions obtained inside the

targets is summarized into cumulative histograms in Fig. 10, while the median temperature T_{50} and 90-percentile temperature T_{90} achieved in the target volumes are reported in Table 2.

Table 2: Median and 90-percentile temperature values in the targets, for each HTP method at its optimal frequency combination.

	Larynx			
	`EV[Γ]`	`i-EV[HTQ]`	`PS[HTQ]`	`PS[TC_50]`
MHz	800	500	500 + 800	400 + 700
T_{50}	39.5	40.9	41.0	40.2
T_{90}	38.1	38.6	38.6	38.6

	Meninges			
	`EV[Γ]`	`i-EV[HTQ]`	`PS[HTQ]`	`PS[TC_50]`
MHz	400	500	500 + 700	600 + 700
T_{50}	39.2	41.0	42.2	42.9
T_{90}	38.2	39.4	40.6	41.4

For the larynx case, the `EV[Γ]` solution results in high temperatures in the frontal area of the target, while the deeper parts of the target, behind the trachea, do not achieve therapeutic temperatures, as expected from the low SAR values at this location. The resulting median and 90-percentile target temperatures are therefore relatively low, below 40 °C and 39 °C, respectively. The `i-EV[HTQ]` and `PS[HTQ]` methods yield similar distributions, with most of the target volume reaching 40 °C in both cases. The performances of the single-frequency `i-EV[HTQ]` and `PS[HTQ]` are almost coincident, as predicted by their similar HTQ and TC_{50} values and SAR distributions. In the TC_{50}-optimal solution the main temperature peak is found outside the target, near the spinal cord. This results in a median temperature 0.8 °C lower than the HTQ-optimal solutions. However, the temperature homogeneity inside the target is still high, achieving the same value of T_{90} as for `i-EV[HTQ]` and `PS[HTQ]`.

In the meninges, the `EV[Γ]` solution results in neither a localized high temperature peak nor good coverage. The cooling effect of the water bolus coun-

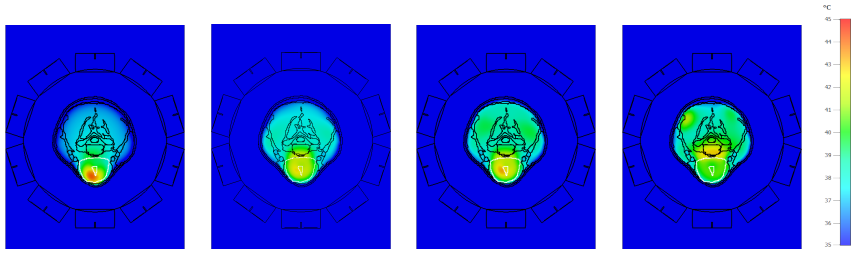

(a) `EV[Γ]` 800 MHz **(b)** `i-EV[HTQ]` 500 MHz **(c)** `PS[HTQ]` 500 + 800 MHz **(d)** `PS[TC_50]` 400 + 700 MHz

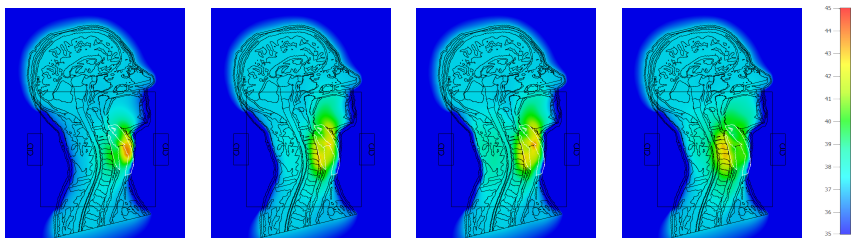

(f) `EV[Γ]` 800 MHz **(g)** `i-EV[HTQ]` 500 MHz **(h)** `PS[HTQ]` 500 + 800 MHz **(i)** `PS[TC_50]` 400 + 700 MHz

Figure 8: Temperature distributions achieved in the larynx case by the SAR-based treatment plans at their optimal frequency or combination of frequencies. a) to d) transverse sections, f) to i) sagittal sections. The target is outlined in white. The maximum temperature in the healthy tissues is 43 °C in all cases.

teracts the high SAR deposition close to the skull, damping the temperature peak. The cumulative histogram indicates that most of the tumor is subjected to temperatures below 40 °C. The single-frequency `i-EV[HTQ]` solution partially improves on this aspect by shifting the power deposition towards the deeper part of the target. The most relevant enhancement of the median and 90-percentile temperatures is however achieved by the multi-frequency solutions `PS[HTQ]` and `PS[TC_50]`. The `PS[HTQ]` solution utilizing two frequencies gains 1.2 °C both in T_{50} and T_{90} with respect to the single-frequency `i-EV[HTQ]`. The multi-frequency TC_{50}-optimal solution further increases both temperature indicators, gaining 0.7 °C in T_{50} and 0.8 °C in T_{90} with respect to `PS[HTQ]`.

To further investigate the benefits of including a second operating fre-

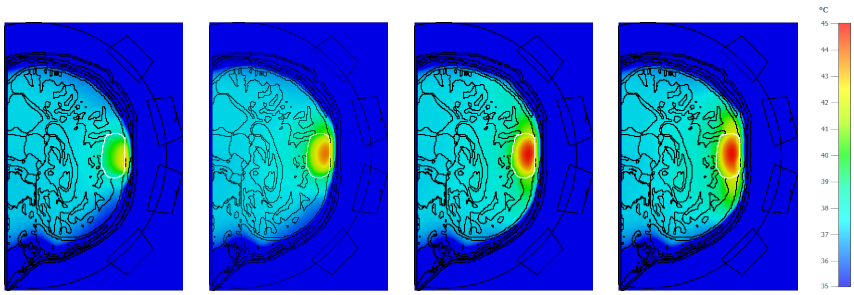

(a) `EV[Γ]` 400 MHz **(b)** `i-EV[HTQ]` 500 MHz **(c)** `PS[HTQ]` 500 + 700 MHz **(d)** `PS[TC_50]` 600 + 700 MHz

Figure 9: Temperature distributions achieved in the meninges case by the SAR-based treatment plans at their optimal frequency or combination of frequencies. Sagittal sections. The target is outlined in white. The maximum temperature in the healthy tissues is 43 °C in all cases. The sections are rotated by 90° for optimal layout.

quency in the meningioma example, we report the cumulative histograms of the temperatures inside the target for the TC_{50}-optimal solutions in the single-frequency and multi-frequency cases in Fig. 11. In the multi-frequency setting, the cumulative curve is steeper and above the single-frequency one, indicating that high temperatures are achieved inside the entire target volume. The multi-frequency setting exhibits 0.5 °C higher T_{90} and 0.3 °C higher T_{50} than the best single-frequency setting.

5 Discussion

The outcome and toxicity of hyperthermia treatments have been shown to correlate with the temperatures achieved in the treated region. Various thermal dose metrics have been proposed under this perspective, and their relationship with the therapeutic effect has been validated in retrospective clinical studies. In particular, the 25% iso-SAR contour (TC_{25}) has been suggested as a predictive SAR-based factor for clinical outcome [39]. Temperature-based metrics include the temperature indicators T_{50}, T_{90} and T_{MAX} when these temperature levels can be held for a specified amount of time [44]. To incorporate the notions of temperature and treatment duration into one metric, the cu-

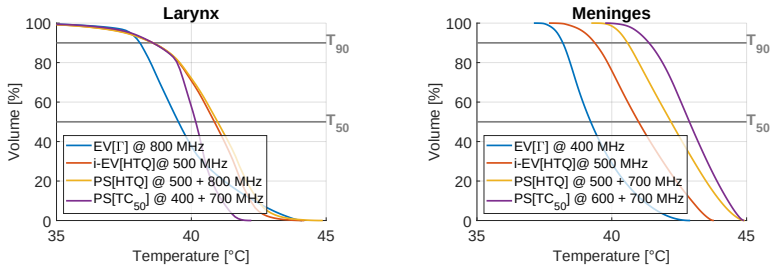

(a) **(b)**

Figure 10: Cumulative histograms of the temperatures reached inside the two selected targets. The gray lines indicate the reference for the 50th and 90th volume percentiles.

mulative equivalent minutes at 43 °C (CEM_{43}) metric has been proposed and its dose-effect relationship has been reported [11]. CEM_{43} is a local measure, and the dose can vary substantially across the target volume depending on the temperature distribution. To address this, T_{90} is used as lumped temperature value, and the resulting metric is termed $CEM_{43}T_{90}$. A strong relationship between the achieved tumor temperature and the cytotoxic effect, as modelled by the $CEM_{43}T_{90}$ metric, suggests that a decrease of 1 °C from the reference temperature of 43 °C inside the tumor corresponds to a four fold drop in the resulting thermal dose. Striving to achieve high tumor temperatures and controlled heat delivery is therefore of paramount importance. The modern HT technology, typically combined with external beam radiotherapy and/or chemotherapy, should aim at achieving homogeneous temperature distributions inside the tumor. Furthermore, to avoid thermal related toxicity in healthy tissues, the peak temperature in regions outside the target should be kept below a critical level, usually 43 °C [21]. This thermal threshold is particularly critical for sensitive tissues such as the brain, the cerebrospinal fluid and the nerves of the spinal cord.

The present work discusses the capability of several SAR-based HTP methods to fulfil the above mentioned contrasting requirements for successful hyperthermia treatments. In order to reach high temperatures inside the tumor while at the same time limiting the peak temperature in healthy tissues, the SAR deposition pattern has to be shaped to focus the heating inside the target and not elsewhere. A classic way to achieve EM focusing in a sub-region of a

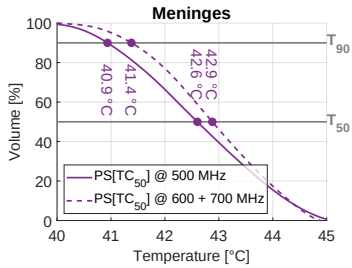

(a)

Figure 11: Cumulative histograms of the temperatures reached inside the meningioma target using the TC_{50}-best single-frequency (solid line) and multi-frequency (dashed line) solutions. The gray lines indicate the reference for the 50th and 90th volume percentiles. The dots further report the actual values of T_{50} and T_{90} for these solutions.

domain is by maximizing the quadratic ratio (A.6) between the average power deposition in the target and the average power deposition in the remaining healthy tissues. As mentioned before, this problem can be efficiently solved for using eigenvalue decomposition. In fact, EV beam-forming for HTP was introduced almost three decades ago [26] and is still repeatedly used in the clinical setting albeit with modifications and improvements [28], [29]. Still to date, the power ratio (A.6) and EV-based HTP are considered a means to evaluate the heating capabilities of an applicator design prior its clinical use [30], [45].

The clinical implementation of HTP in the past decade, however, revealed that the average power deposition inside a region is not a good predictor of the thermal distribution achieved inside the treated region, and that local hot spots in healthy tissues are relevant limiting factors [31], [46]. The temperature profiles relative to the Γ-optimal solutions reported in this work confirm this limitation, as the `EV[Γ]` median target temperature falls below the `PS[HTQ]` one by 1 °C in the larynx and below the `PS[TC_50]` one by 3 °C in the meninges. More modern HTP cost functions, such as the HTQ, overcome this limitation of the average operator. Unfortunately, their intrinsic non-linearity hinders a direct solution and requires an iterative procedure such as the one reported in this work and others [29]. At the same time, the use of fast direct-iterative solvers instead of slower global stochastic optimiz-

ers such as particle swarm is still desirable, due to the high speed required for online HTP adjustments in the clinical setting [47].

The SAR-based analysis carried out in this work indicates that the proposed iterative EV scheme (A.20) is capable of reaching HTQ values that are comparable to those yielded by a global stochastic optimizer for different operating frequencies and array topologies. This is however valid only when the treatment options are limited to a single operating frequency. In particular, the larynx case suggests that a single-frequency treatment might be sufficient for this patient, as long as the most suitable frequency can be selected across a UWB range. Note in fact that both HTQ and TC_{50} exhibit frequency-dependent behaviors regardless of the optimisation algorithm used.

The results further indicate that the suitability of the chosen HTP cost function is also region- and tumor-dependent. The HTQ-optimal temperature distribution proves better than the TC_{50}-optimal one in terms of median and peak temperatures in the larynx example considered here. In the meningioma case, however, the situation is reversed and the TC_{50}-based HTP proves the best choice. This might be due to a number of factors. First of all, the presence of the skull in close contact with the cerebrospinal fluid generates sharp and narrow SAR peaks that might be better captured by the local peak term used in the TC_{50} definition. In contrast, HTQ considers the hot-spot as larger sub-volume of healthy tissues (1 %), which might be too coarse to accurately identify the location of the limiting peak. Note that defining the hot-spot as 1 % of the patient model also renders the HTQ values model-dependent, thus preventing meaningful comparisons between the larynx and meningioma cases discussed here.

The thermal distributions achieved in the mengioma case indicate that MW-HT treatments can benefit significantly from the multi-frequency approach in this region. In the best case, using TC_{50} as cost function, the multi-frequency approach yields $T_{50} = 42.9$ °C and $T_{90} = 41.4$ °C, implying that the high temperatures are uniformly distributed across the target volume. These are higher than the HTQ-based HTP by 0.7 °C and 0.8 °C, respectively. The use of a second frequency is particularly beneficial in increasing the tumor coverage, demonstrated by a 0.5 °C gain in T_{90} with respect to the best single-frequency solution. The advantages of the multi-frequency setting are also highlighted when considering the HTQ as cost-function for HTP. The single-frequency `i-EV[HTQ]` results in 1.2 °C lower T_{50} than the multi-frequency

`PS[HTQ]`. It is worth to observe that a relatively small difference of 0.2 in HTQ between these two solutions results in considerable hot-spot suppression and subsequent temperature increase in the target. This might once more be a consequence of the definition of hot-spot in the HTQ. As a final note, we realize that, while the results reported here highlight the varying suitability of single- and multi-frequency HTP and of the cost-function adopted for HTP optimisation, a larger patient data set is needed to better characterize these behaviors.

6 Conclusion

This study discusses the suitability of classic EV beam-forming for HTP, proposes a novel iterative scheme that improves the single-frequency EV-based HTP, and investigates the potential advantages of multi-frequency versus single-frequency HTP. As previously found in other studies, the examples reported here indicate that EV in its basic form should be avoided as HTP method, since it yields target temperatures far below the desired therapeutic values. However, EV can be still be used in its iterative form to minimize non-linear cost-functions for single-frequency HTP problems, when one frequency is sufficient to achieve target coverage and hot-spot suppression. The operational frequency should nevertheless be carefully selected from a wide frequency band depending on the tumor size and location. In regions such as the brain, the use of two or more concomitant frequencies can improve significantly the thermal distributions, increasing median temperature and temperature homogeneity within the target while not exceeding the set temperature limit in healthy tissues. Overall, these results suggest that a comparison between applicators should not be grounded on average power ratios, but rather on non-linear indicators such as HTQ and TC_{50}, and further motivate the design and development of UWB applicators for MW-HT.

Conflict of Interest

The authors report no conflict of interest.

Acknowledgement

This work was financially supported by the VINN EXcellence Center of ChaseOn (Chalmers Antenna Systems) and The Swedish Childhood Cancer Fund.

References

[1] P. R. Stauffer and M. M. Paulides, "Hyperthermia therapy for cancer," *Comprehensive biomedical physics*, vol. 10, no. 07, pp. 115–151, 2014.

[2] M. Paulides, H. D. Trefná, S. Curto, and D. Rodrigues, "Recent technological advancements in radiofrequency-and microwave-mediated hyperthermia for enhancing drug delivery.," *Advanced Drug Delivery Reviews*, 2020.

[3] N. R. Datta, S. Rogers, S. G. Ordóñez, E. Puric, and S. Bodis, "Hyperthermia and radiotherapy in the management of head and neck cancers: A systematic review and meta-analysis," *International Journal of Hyperthermia*, vol. 32, no. 1, pp. 31–40, 2016.

[4] P. B. Elming, B. S. Sørensen, A. L. Oei, *et al.*, "Hyperthermia: The optimal treatment to overcome radiation resistant hypoxia," *Cancers*, vol. 11, no. 1, p. 60, 2019.

[5] J. Crezee, P. Van Haaren, H. Westendorp, *et al.*, "Improving locoregional hyperthermia delivery using the 3-d controlled amc-8 phased array hyperthermia system: A preclinical study," *International Journal of Hyperthermia*, vol. 25, no. 7, pp. 581–592, 2009.

[6] R. Zweije, H. P. Kok, A. Bakker, A. Bel, and J. Crezee, "Technical and clinical evaluation of the ALBA-4D 70mhz loco-regional hyperthermia system," in *2018 48th European Microwave Conference (EuMC)*, IEEE, 2018, pp. 328–331.

[7] M. Paulides, Z. Rijnen, P. Togni, *et al.*, "Clinical introduction of novel microwave hyperthermia technology: The hypercollar3d applicator for head and neck hyperthermia," in *2015 9th European Conference on Antennas and Propagation (EuCAP)*, IEEE, 2015, pp. 1–4.

[8] M. Seebass, R. Beck, J. Gellermann, J. Nadobny, and P. Wust, "Electromagnetic phased arrays for regional hyperthermia: Optimal frequency and antenna arrangement," *International Journal of Hyperthermia*, vol. 17, no. 4, pp. 321–336, 2001.

[9] M. M. Paulides, S. H. Vossen, A. P. Zwamborn, and G. C. van Rhoon, "Theoretical investigation into the feasibility to deposit rf energy centrally in the head-and-neck region," *International Journal of Radiation Oncology* Biology* Physics*, vol. 63, no. 2, pp. 634–642, 2005.

[10] H. Kok, M. De Greef, P. Borsboom, A. Bel, and J. Crezee, "Improved power steering with double and triple ring waveguide systems: The impact of the operating frequency," *International Journal of Hyperthermia*, vol. 27, no. 3, pp. 224–239, 2011.

[11] E. L. Jones, J. R. Oleson, L. R. Prosnitz, *et al.*, "Randomized trial of hyperthermia and radiation for superficial tumors," *Journal of Clinical Oncology*, vol. 23, no. 13, pp. 3079–3085, 2005.

[12] M. Franckena, D. Fatehi, M. de Bruijne, *et al.*, "Hyperthermia dose-effect relationship in 420 patients with cervical cancer treated with combined radiotherapy and hyperthermia," *European Journal of Cancer*, vol. 45, no. 11, pp. 1969–1978, 2009.

[13] M. Converse, E. J. Bond, B. Veen, and C. Hagness, "A computational study of ultra-wideband versus narrowband microwave hyperthermia for breast cancer treatment," *IEEE transactions on microwave theory and techniques*, vol. 54, no. 5, pp. 2169–2180, 2006.

[14] A. Kuehne, E. Oberacker, H. Waiczies, and T. Niendorf, "Solving the time-and frequency-multiplexed problem of constrained radiofrequency induced hyperthermia," *Cancers*, vol. 12, no. 5, p. 1072, 2020.

[15] B. Guo, L. Xu, and J. Li, "Time reversal based microwave hyperthermia treatment of breast cancer," *Microwave and Optical Technology Letters*, vol. 47, no. 4, pp. 335–338, 2005.

[16] H. D. Trefná, J. Vrba, and M. Persson, "Time-reversal focusing in microwave hyperthermia for deep-seated tumors," *Physics in Medicine & Biology*, vol. 55, no. 8, p. 2167, 2010.

[17] M. M. Paulides, P. R. Stauffer, E. Neufeld, *et al.*, "Simulation techniques in hyperthermia treatment planning," *International Journal of Hyperthermia*, vol. 29, no. 4, pp. 346–357, 2013.

[18] G. G. Bellizzi, L. Crocco, G. M. Battaglia, and T. Isernia, "Multifrequency constrained SAR focusing for patient specific hyperthermia treatment," *IEEE Journal of Electromagnetics, RF and Microwaves in Medicine and Biology*, vol. 1, no. 2, pp. 74–80, 2017.

[19] E. Zastrow, S. C. Hagness, and B. D. Van Veen, "3d computational study of non-invasive patient-specific microwave hyperthermia treatment of breast cancer," *Physics in Medicine & Biology*, vol. 55, no. 13, p. 3611, 2010.

[20] G. Bruggmoser, S. Bauchowitz, R. Canters, *et al.*, "Quality assurance for clinical studies in regional deep hyperthermia," *Strahlentherapie und Onkologie*, vol. 187, no. 10, p. 605, 2011.

[21] H. D. Trefná, B. Martinsson, T. Petersson, *et al.*, "Multifrequency approach in hyperthermia treatment planning: Impact of frequency on sar distribution in head and neck," in *2017 11th European Conference on Antennas and Propagation (EUCAP)*, IEEE, 2017, pp. 3710–3712.

[22] P. Takook, H. Dobsicek Trefna, X. Zeng, A. Fhager, and M. Persson, "A computational study using time reversal focusing for hyperthermia treatment planning," *Progress In Electromagnetics Research*, vol. 73, pp. 117–130, 2017.

[23] M. Zanoli and H. D. Trefná, "Iterative time-reversal for multi-frequency hyperthermia," *Physics in Medicine & Biology*, vol. 66, no. 4, p. 045 027, 2021.

[24] Z. Rijnen, J. F. Bakker, R. A. Canters, *et al.*, "Clinical integration of software tool vedo for adaptive and quantitative application of phased array hyperthermia in the head and neck," *International journal of Hyperthermia*, vol. 29, no. 3, pp. 181–193, 2013.

[25] G. Cappiello, B. Mc Ginley, M. A. Elahi, *et al.*, "Differential evolution optimization of the sar distribution for head and neck hyperthermia," *IEEE Transactions on Biomedical Engineering*, vol. 64, no. 8, pp. 1875–1885, 2016.

[26] M. Böhm, J. Kremer, and A. Louis, "Efficient algorithm for computing optimal control of antennas in hyperthermia," *Surveys Math. Indust*, vol. 3, no. 4, pp. 233–251, 1993.

[27] R. Canters, P. Wust, J. Bakker, and G. Van Rhoon, "A literature survey on indicators for characterisation and optimisation of sar distributions in deep hyperthermia, a plea for standardisation," *International Journal of Hyperthermia*, vol. 25, no. 7, pp. 593–608, 2009.

[28] T. Köhler, P. Maass, P. Wust, and M. Seebass, "A fast algorithm to find optimal controls of multiantenna applicators in regional hyperthermia," *Physics in Medicine & Biology*, vol. 46, no. 9, p. 2503, 2001.

[29] R. Mestrom, J. Van Engelen, M. Van Beurden, M. Paulides, W. Numan, and A. Tijhuis, "A refined eigenvalue-based optimization technique for hyperthermia treatment planning," in *The 8th European Conference on Antennas and Propagation (EuCAP 2014)*, IEEE, 2014, pp. 2010–2013.

[30] B. Guérin, J. F. Villena, A. G. Polimeridis, *et al.*, "Computation of ultimate SAR amplification factors for radiofrequency hyperthermia in non-uniform body models: Impact of frequency and tumour location," *International Journal of Hyperthermia*, vol. 34, no. 1, pp. 87–100, 2018.

[31] R. Canters, M. Franckena, J. van der Zee, and G. Van Rhoon, "Optimizing deep hyperthermia treatments: Are locations of patient pain complaints correlated with modelled SAR peak locations?" *Physics in Medicine & Biology*, vol. 56, no. 2, p. 439, 2010.

[32] P. Takook, M. Persson, J. Gellermann, and H. D. Trefná, "Compact self-grounded bow-tie antenna design for an uwb phased-array hyperthermia applicator," *International Journal of Hyperthermia*, vol. 33, no. 4, pp. 387–400, 2017.

[33] M.-C. Gosselin, E. Neufeld, H. Moser, *et al.*, "Development of a new generation of high-resolution anatomical models for medical device evaluation: The Virtual Population 3.0," *Physics in Medicine & Biology*, vol. 59, no. 18, p. 5287, 2014.

[34] P. Hasgall, F. Di Gennaro, C. Baumgartner, *et al.*, *IT'IS Database for thermal and electromagnetic parameters of biological tissues*, version 4.0, May 2018.

[35] Dassault Systèmes SE, Vélizy-Villacoublay, France, *CST Studio Suite 2019*, 2019.

[36] C. Rossmann and D. Haemmerich, "Review of temperature dependence of thermal properties, dielectric properties, and perfusion of biological tissues at hyperthermic and ablation temperatures," *Critical Reviews™ in Biomedical Engineering*, vol. 42, no. 6, 2014.

[37] J. Lang, B. Erdmann, and M. Seebass, "Impact of nonlinear heat transfer on temperature control in regional hyperthermia," *IEEE Transactions on Biomedical Engineering*, vol. 46, no. 9, pp. 1129–1138, 1999.

[38] G. Schooneveldt, H. D. Trefná, M. Persson, *et al.*, "Hyperthermia treatment planning including convective flow in cerebrospinal fluid for brain tumour hyperthermia treatment using a novel dedicated paediatric brain applicator," *Cancers*, vol. 11, no. 8, p. 1183, 2019.

[39] H. K. Lee, A. G. Antell, C. A. Perez, *et al.*, "Superficial hyperthermia and irradiation for recurrent breast carcinoma of the chest wall: Prognostic factors in 196 tumors.," *International journal of radiation oncology, biology, physics*, vol. 40, no. 2, pp. 365–375, 1998.

[40] P. Togni, Z. Rijnen, W. Numan, *et al.*, "Electromagnetic redesign of the hypercollar applicator: Toward improved deep local head-and-neck hyperthermia," *Physics in Medicine & Biology*, vol. 58, no. 17, p. 5997, 2013.

[41] S. A. Sapareto and W. C. Dewey, "Thermal dose determination in cancer therapy," *International Journal of Radiation Oncology • Biology • Physics*, vol. 10, no. 6, pp. 787–800, 1984.

[42] P. S. Yarmolenko, E. J. Moon, C. Landon, *et al.*, "Thresholds for thermal damage to normal tissues: An update," *International Journal of Hyperthermia*, vol. 27, no. 4, pp. 320–343, 2011.

[43] The MathWorks Inc., Natick, Massachusetts, "MATLAB R2019," 2019.

[44] M. Sherar, F.-F. Liu, M. Pintilie, *et al.*, "Relationship between thermal dose and outcome in thermoradiotherapy treatments for superficial recurrences of breast cancer: Data from a phase iii trial," *International Journal of Radiation Oncology* Biology* Physics*, vol. 39, no. 2, pp. 371–380, 1997.

[45] F. Bardati and P. Tognolatti, "Hyperthermia phased arrays pre-treatment evaluation," *International Journal of Hyperthermia*, vol. 32, no. 8, pp. 911–922, 2016.

[46] H. P. Kok, S. Ciampa, R. de Kroon-Oldenhof, *et al.*, "Toward online adaptive hyperthermia treatment planning: Correlation between measured and simulated specific absorption rate changes caused by phase steering in patients," *International Journal of Radiation Oncology* Biology* Physics*, vol. 90, no. 2, pp. 438–445, 2014.

[47] H. P. Kok, L. Korshuize-van Straten, A. Bakker, *et al.*, "Online adaptive hyperthermia treatment planning during locoregional heating to suppress treatment-limiting hot spots," *International Journal of Radiation Oncology* Biology* Physics*, vol. 99, no. 4, pp. 1039–1047, 2017.

PAPER B

The hot-to-cold spot quotient for SAR-based treatment planning in deep microwave hyperthermia

Massimiliano Zanoli, Hana Dobšíček Trefná

Submitted to the International Journal of Hyperthermia
01 June 2022

The layout has been revised.

Abstract

Background: A necessary precondition for a successful microwave hyperthermia (HT) treatment delivered by phased arrays is the ability of the HT applicator to selectively raise the temperature of the entire tumor volume. SAR-based treatment plan (HTP) optimization methods exploit the correlation between specific absorption rate (SAR) and temperature increase in order to determine the set of steering parameters for optimal focusing, while allowing for lower model complexity. Several cost functions have been suggested in the past for this optimization problem. However, their correlation with high and homogeneous tumor temperatures remains sub-optimal in many cases. Previously, we proposed the hot-to-cold spot quotient (HCQ) as a novel cost function for SAR-based HTP optimization and showed its potential to address these issues.
Materials and methods: In this work, we validate the HCQ on the ESHO patient repository within the context of single and multiple operating frequency settings. We verify its correlation with clinical SAR and temperature indices, and compare it to HTPs obtained using the current standard for SAR-based HTP (HTQ).
Results and discussion: The results show that low HCQ values produce better SAR (TC_{50}, TC_{75}) and temperature metrics (T_{50}, T_{90}) than HTQ in most patient models and frequency settings. For the deep seated tumors, the correlation between the clinical indicators and 1/HCQ is more favourable than the correlation exhibited by 1/HTQ.
Conclusion: The validation on a standardized patient repository suggests that HCQ is a valid alternative to HTQ for SAR-based HTP optimization in deep microwave hyperthermia. For superficial tumors, we recommend temperature-based optimization strategies.

1 Introduction

In deep microwave hyperthermia cancer treatment, the tumor temperature is elevated to $40 \sim 44\ ^{\circ}C$ for about an hour by a conformal array of antennas called applicator [1], [2]. This adjuvant therapy has been shown to enhance the tumor response and survival rate of cancer patients in many clinical trials [3]–[5]. The antennas radiate coherently at one or more frequencies with different amplitude and phase to generate a focalized power deposition pattern. The aim of the treatment is to reach a therapeutic temperature range in the target volume while not exceeding thermal toxicity thresholds for (nearby) healthy tissues [6], [7].

To this end, a preliminary hyperthermia treatment planning (HTP) step is prescribed by current guidelines [8]. In this stage, the set of optimal steering parameters for each antenna is determined by means of numerical simulations involving a segmented model of the patient and a model of the applicator in use [9]. Iterative optimization algorithms explore the space of possible solutions and determine the one that minimizes a certain cost function. As the aim of the treatment is to reach and maintain a therapeutic temperature in the target volume for a specified duration, the goal of the optimization should ideally be the temperature itself. To date, a few in-house built and commercial HTP optimization software packages offer the possibility to carry out thermal simulations and optimizations [10]. Thermal HTP can be particularly effective when large blood vessels are present in the vicinity of the tumor [11], [12], as these extract a large amount of heat. Thermal simulations can also account for heat redistribution due to convection [13]. Despite these benefits, thermal modelling can be difficult or too demanding to implement in the clinic, as it entails additional segmentation and computational burdens. As a surrogate to the temperature distribution, the specific absorption rate (SAR) distribution can be used, thanks to its correlation to the temperature increase [14].

SAR-based HTP optimization is a well known problem and has been tackled in numerous ways [15]. When the cost function has a particular form, SAR-focusing can even be reduced to a quadratic problem with an exact solution [16]–[19]. Unfortunately, cost functions in quadratic form often fail to capture the complexity of the hyperthermia requirements and lead to sub-optimal solutions in terms of resulting temperature distribution [20]. In particular, the temperature increase in the patient during treatment is known to be limited by the occurrence of hot-spots [21]. A hot-spot is defined as a localized

temperature increase outside the target volume, and can result in pain and discomfort for the patient, but also induce thermal toxicity in healthy tissue. When a hot-spot is reported by the patient or detected by thermal probes, the power of the applicator device has to be lowered or redistributed to different channels [22], [23]. In general, the temperature achievable in the tumor will be constrained by the maximum power than can be radiated into the patient without causing hot-spots.

The location and severity of hot-spots is not straightforward to predict, because they arise from the inhomogeneity of the patient anatomy together with the finite aperture of the applicator array. As such, they need to be addressed by the cost function during the HTP optimization stage. In SAR, hot-spots are detectable as local power deposition peaks [14]. The current standard in SAR-based optimization relies on the target to hot-spot quotient (THQ) as optimization goal [24]. The THQ identifies the hot-spot(s) as the highest first percentile of the SAR distribution outside the target. The percentile sub-volume needs to be recomputed at each iteration, rendering the metric non-linear. Note however that we consider the inverse of this metric, the hot-spot to target quotient (HTQ = 1/THQ), for consistency with the concept of cost. By minimizing the HTQ, the average SAR deposition in the tumor increases while the most prominent hot-spot in the healthy tissues is suppressed.

Despite their prominent role in HTP, hot-spots represent only part of the challenge in hyperthermia heating. The second fundamental element of a successful treatment is the homogeneity of the thermal dose administered to the tumor, which can be expressed in terms of the minimum temperature achieved in the target [25]. Ideally, all regions of the delineated target volume should reach 43 $^{\circ}C$ for the treatment to be effective. This condition, however, is not directly addressed by the definition of HTQ, because its denominator is a mere average of the SAR values across the whole target, which implicitly neglects the inhomogeneities in SAR deposition. As a result, some areas of the tumor, so called cold-spots, may remain untreated as they fail to reach the prescribed thermal dose. A low correlation between 1/HTQ and the temperature achieved by at least 90 % of the target volume (T_{90}) supports this concern [26]. Due to the paramount importance of the T_{90} metric, which has been shown to directly correlate with clinical outcome [27], it is crucial that SAR-based optimizations yield HTPs that strive for the highest possible T_{90}.

To this end, we have recently proposed a novel cost function for SAR-based HTP optimization, the hot-to-cold spot quotient (HCQ) [28]. Together with hot-spots in healthy tissues, this cost function also identifies cold-spots in the target volume as the average SAR in the lowest percentile. The definition of the healthy tissue and tumor percentiles in HCQ makes the values obtained from different HTPs and patients quantitatively comparable. Our preliminary data indicated that HCQ is capable of yielding higher T_{90} than conventional SAR-based optimizations.

The aim of this study is to validate the HCQ as goal function for the optimization of single and multi-frequency HTP on a set of six patient models that cover some of the most common hyperthermia treatment sites. The models have been made publicly available by the Erasmus Medical Center (EMC, Rotterdam, The Netherlands) via the *Grand Challenge on Computational Modeling* organised by the European Society of Hyperthermic Oncology (ESHO) as a first step in the establishment of HTP standards [29], [30]. We benchmark the SAR and temperature distributions of the HCQ-optimal plans against the plans obtained by optimizing for the current standard, the HTQ. We further investigate the sensitivity of the HCQ metric to the percentile value for hot- and cold-spot identification. Finally, we compare the correlation of 1/HCQ and 1/HTQ with clinical SAR (TC_{50}, TC_{75}) and temperature (T_{50}, T_{90}) indicators.

2 Method

In the following subsections we describe in detail the validation protocol from patient and applicator modeling to the quantitative assessment of the thermal distributions.

2.1 Patient models

Six representative patient models have recently been prepared as a means for standardization in HTP development, validation and comparison [30]. The models include two head and neck patients, one with a nasopharyngeal tumor (Alex) and one post-operative oropharyngeal case (Murphy) with metal dental implants. Two breast models represent patients with a superficial tumor (Venus) and a deep seated tumor (Luna). The last two models are for pelvic

targets and include a rectal (Will) and a cervical (Clarice) case. All models are shown in Fig. 1 and 2.

The models are provided as already segmented volume matrices. The head and neck models are segmented into 16 biological tissues (*tumor*, *muscle*, *fat*, *sclera*, *vitreous humor*, *optical nerve*, *spinal cord*, *cartilage*, *eye lens*, *cerebrum*, *cerebellum*, *cartilage*, *brain stem*, *thyroid*, *bone*, *lung*) plus internal air and metal implants where applicable. The breast models are segmented into 6 tissues (*tumor*, *bone*, *breast gland*, *skin*, *muscle*, *fat*) and exhibit no internal air lumina. The pelvis models are segmented into 4 tissues (*tumor*, *muscle*, *fat*, *bone*) plus internal air.

The three body sites are sampled with different resolutions: the head and neck models have a resolution of 2.5 mm, the pelvis models 5.0 mm, and the breast models 1.0 mm. To reduce the computational burden, we down-sample the breast models to 2.0 mm using a winner-takes-all strategy [31], in line with the recommendations of the reference paper for the benchmark dataset [30].

2.2 Tissue properties

Material properties are retrieved from the IT'IS database [32] for each healthy tissue in the dataset, as prescribed by the benchmark paper [30]. The properties include density (ρ, $[kg/m^3]$), dispersive relative permittivity (ϵ, [1]) and dispersive conductivity (σ, $[S/m]$), specific heat capacity (c_p, $[J/kg/K]$), thermal conductivity (κ, $[W/m/K]$), heat transfer rate (q_t, $[ml/min/kg]$), and heat generation rate (Q_g, $[W/kg]$). All thermal properties are taken under normothermic conditions.

Dispersive dielectric tumor properties are obtained as an average of all malignant tissue properties reported in [33], as recommended by [30]. Other tumor properties are taken directly from the reference paper [30]: $\rho = 1090\ [kg/m^3]$, $c_p = 3421\ [J/kg/K]$, and $\kappa = 0.49\ [W/m/K]$. The paper does not provide details regarding the origin of these values. The given heat transfer rate under thermal stress for the tumor is $q_t = 94.4\ [ml/min/kg]$.

2.3 Applicator design

Customized array applicators are designed for each patient. Two topologies are employed: cylindrical for neck and pelvis models, semi-spherical for breast models. The applicators utilize ultra wide-band (UWB) self-grounded bow-

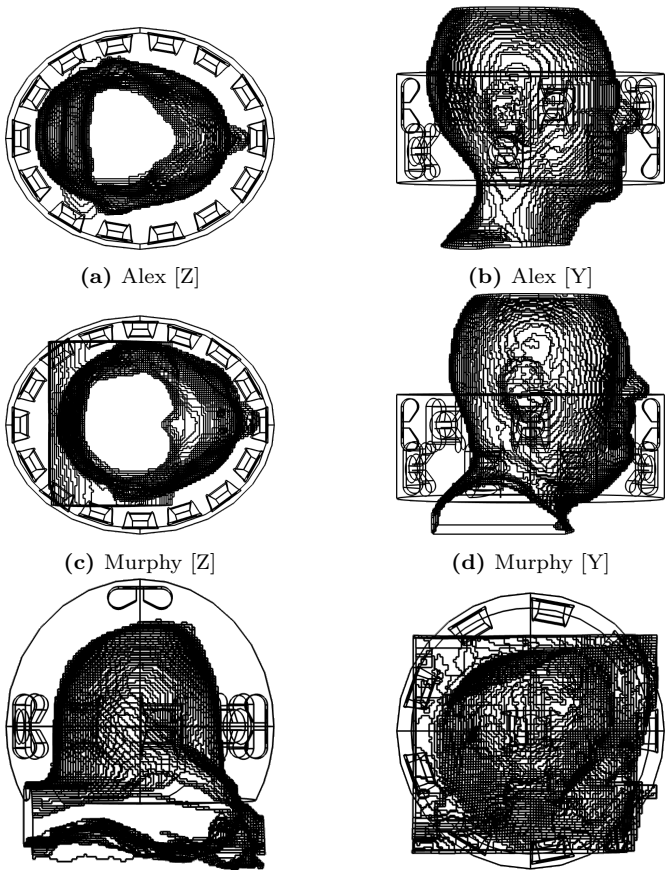

(a) Alex [Z] **(b)** Alex [Y]

(c) Murphy [Z] **(d)** Murphy [Y]

(e) Venus [Z] **(f)** Venus [Y]

Figure 1: Schematic of the patient models and the applicator (water bolus + antennas).

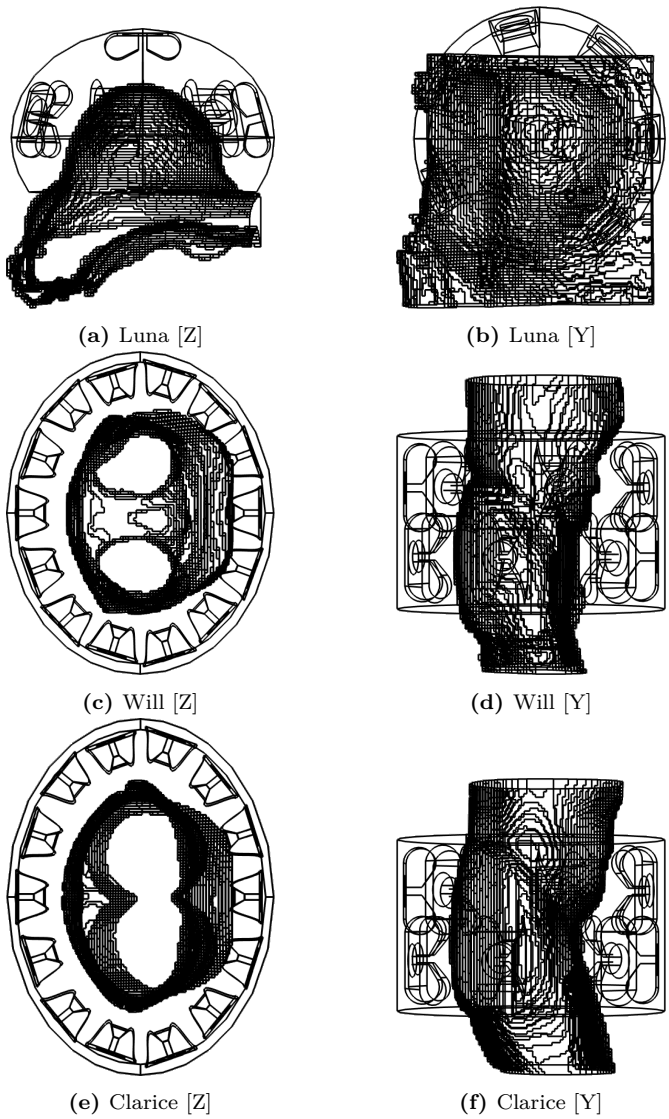

(a) Luna [Z] **(b)** Luna [Y]

(c) Will [Z] **(d)** Will [Y]

(e) Clarice [Z] **(f)** Clarice [Y]

Figure 2: Schematic of the patient models and the applicator (water bolus + antennas).

tie antennas [34], and the operating frequency band is selected for each target region according to the expected focal size and penetration depth [35]–[37]. In particular, the band is $400 \approx 800\ MHz$ for the neck models, $500 \approx 1000\ MHz$ for the breast models, and $150 \approx 300\ MHz$ for the pelvis models. The antennas are immersed in a water bolus which encloses the target body region, to achieve dielectric matching and implement skin cooling. The thickness of the water bolus, defining also the distance of the antenna ground plane to the body, is 5 *cm* for the neck models, 4 *cm* for the breast models, and 12 *cm* for the pelvis models.

Since the scope of the present study is limited to the evaluation and comparative assessment of the HCQ in HTP optimization, we summarize only in brief the design procedure of the applicators:

1. Optimize the antenna proportions to provide a good response and radiation pattern across the intended operating octave.

2. Obtain the bolus dimensions by fitting an ellipsoidal cylinder or sphere over the shape of the target body region, maintaining as much a possible the specified bolus thickness.

3. Construct the antenna array by inserting as many antennas as possible while respecting the minimum distance between antennas to limit cross coupling.

Reiterating the design procedure for each patient model results in six applicators, as illustrated in Fig. 1 and 2. Each applicator has a different number of antennas (Alex = 14, Murphy = 16, Luna = 8, Venus = 10, Clarice = 14, Will = 14). While the personalization of the applicator array might be impracticable in the clinical setting, it provides us with a heterogeneous set of test cases for a more robust assessment of the HTP optimization in different setups.

2.4 Electromagnetic simulations

Electromagnetic simulations are performed in COMSOL Multiphysics®, a FEM-based commercial software [38]. Mesh resolutions vary from $\lambda/20$ in proximity of the metal antenna parts, to $\lambda/5$ in regions far from the peak field gradients, where λ is the wavelength at the operating frequency. The patient

models are uploaded in the COMSOL project after converting the volumetric tissue masks to CAD shapes. The three dimensional distributions of the material properties inside the patient are captured by custom space-varying functions. Air is modelled as vacuum, while distilled water is modelled as a dispersive first-order Debye model. The surface of metal implants is treated as perfect electric conductor. At the domain boundaries, absorbing conditions (PML) are defined.

At this simulation stage, the E-field distributions inside the patient are calculated for each antenna at each operating frequency. We solve for three frequency points for each patient, which are minimum, maximum and center frequency within the applicator's operating band. Thus, the frequency sweep is $[400, 600, 800]\ MHz$ for the neck models, $[500, 750, 1000]\ MHz$ for the breast models, and $[150, 225, 300]\ MHz$ for the pelvis models.

2.5 Treatment planning

The SAR-based HTP optimization is carried out for each model to produce single and multi-frequency treatment plans. The plans are obtained at the minimum, the center and the maximum frequency, and at binary combinations of these, for a total of six operating frequency settings. The optimization setup is identical for all patients, and for the comparative analysis we alter only the cost function.

The hot-to-cold spot quotient (HCQ) is the goal we propose for SAR-based HTP-optimization, and is defined as follows [28]:

$$\mathrm{HCQ}_p = \frac{\overline{\mathrm{SAR}}_{Rq}}{\overline{\mathrm{SAR}}_{Tp}}. \tag{B.1}$$

where $\overline{\mathrm{SAR}}_{Tp}$ is the average SAR in the lowest p-percentile of target (tumor) tissue, while $\overline{\mathrm{SAR}}_{Rq}$ is the average SAR in the highest q-percentile of remaining (healthy) tissue. To render the HCQ metric comparable between different patients and targets, the percentiles are related as follows:

$$q = p\frac{|T|}{|R|} \tag{B.2}$$

where $||$ denotes the volume of the argument (T target, R remaining). As one of the aims of the current study is to determine the optimal target per-

centile p, we let p vary from 1 % (the SAR value at the single point of minimum inside the target) to 99 % (the average of all SAR values inside the target) and obtain HTPs and corresponding thermal distributions for a range of values in between these extremes.

The standard cost function for SAR-based HTP-optimization is the hot-spot to target quotient (HTQ), defined as follows [14]:

$$\mathrm{HTQ} = \frac{\overline{\mathrm{SAR}}_{R1}}{\overline{\mathrm{SAR}}_{T}} \tag{B.3}$$

where $\overline{\mathrm{SAR}}_{R1}$ is the average SAR in the highest 1-percentile of remaining (healthy) tissue, while $\overline{\mathrm{SAR}}_{T}$ is the average SAR in the target (tumor) tissue.

The optimization process determines the set of steering parameters, i.e. amplitude and phase for each array channel and at each operating frequency, that minimizes the value of the cost function when evaluated over a patient model. After exporting the E-fields computed by the FEM solver, the steering parameters are applied and a conversion to SAR is carried out in MATLAB® [39] according to the following:

$$\mathrm{SAR}(x,y,z) = \sum_{f} \frac{1}{2} \frac{\sigma(x,y,z,f)}{\rho(x,y,z)} ||E(x,y,z,f)||^2 \tag{B.4}$$

where E is the focused E-field distribution, resulting from the sum of the steered channel contributions. The SAR distribution is further convoluted to an averaging spherical kernel of varying size. At each point, the size of the kernel is expanded until it covers 1 g of patient tissue, excluding anything that is not patient. Thus, at the patient surface, water from the bolus and air from the background are excluded from the averaging process.

In the evaluation of the SAR distribution, we exclude the first centimeter of patient surface that is in direct contact with the water bolus. This allows us to model the cooling effect of the water bolus, which effectively extracts heat from the skin and counteracts the high SAR deposition in the first layers of tissue [40]. This step is realized by expanding the bolus mask in the 3D matrix model with a morphological operation using a spherical kernel of radius 1 *cm*. Consequently, the skin surface that is in contact with air is not subjected to this exclusion.

The optimization problem is solved using the *particle swarm* global minimization algorithm [41]. The solution is further refined using a local gradient

descent (`lsqnonlin`). All algorithms are readily available in MATLAB. To speed up the computations, the SAR calculations are performed in single precision on a high-speed GPU.

2.6 Thermal simulations

Thermal simulations are also carried out in COMSOL Multiphysics®, but with domain restricted to the biological tissues only. The mesh resolution is set to vary from $r/3$ at material interfaces to $r \cdot 3$ in the material bulks, where r is the patient model resolution.

The heat transfer rate q_t $[ml/min/kg]$ is converted to blood perfusion rate ω_b $[1/s]$ using the known value of tissue density. A similar transformation is done to obtain the basal metabolic rate Q_m $[W/m^3]$ from the available heat generation rate Q_g $[W/kg]$. For the metal implants in Murphy, we utilize the mechanical and thermal properties of the titanium alloy Ti-6 Al-4 V, solid and oxidized at 816 $°C$, as this is one of the most common solutions for dental implants [42].

At the interface between patient and air or water, heat flux boundary conditions modeling the convective extraction of heat are implemented. The chosen convection coefficient for skin/air is 8 $[W/m^2/K]$ [43], while the coefficient for skin/water is 100 $[W/m^2/K]$ [40]. In all test cases, both the air and the water temperatures are set to 20 $°C$.

The external heat source, or power loss distribution (PLD), is prepared by applying the steering parameters according to the HTP:

$$\mathrm{PLD}(x,y,z) = \sum_f \frac{1}{2}\sigma(x,y,z,f)||E(x,y,z,f)||^2 \tag{B.5}$$

The relationship between SAR and PLD is straightforward. However, the PLD matrix is not manipulated with mass averaging or surface exclusion. The PLD distribution is iteratively scaled until the maximum temperature in the remaining (healthy) tissue reaches 43 $°C$.

2.7 Evaluation metrics

We quantitatively assess the SAR and temperature distributions for each HTP. According to clinical practice, tumor coverage is evaluated by the indexed temperatures T_{50} and T_{90} metrics [8], which represent the lowest temperature

achieved in the highest 50 % and 90 % of the target volume, respectively. These metrics have been shown to directly correlate with clinical outcome [44].

In SAR-based assessment, we evaluate the iso-contour target coverage (TC_n) for $n = 50$ % and $n = 75$ %, defined as:

$$\mathrm{TC}_n = \frac{|T'|}{|T|} \quad [\%] \quad , \quad T' \;\mid\; \mathrm{SAR}(T') \geq n \cdot \mathrm{SAR}(R \cup T) \tag{B.6}$$

that is, the fraction of target volume T'/T subjected to SAR values greater than a fraction n of the maximum SAR peak in the whole patient. The TC_{25} metric has been shown to be a prognostic factor for local control in HT [45], while the TC_{50} metric has been shown to correlate with the clinical temperature indicators T_{50} and T_{90} in the head and neck [26]. In the present study, due to the extensive SAR processing consisting of both averaging and exclusion of surface layers, the SAR distributions do not exhibit sharp peaks nor strong gradients. Consequently, the TC_{25} metric saturates at 100 % for most plans. Therefore, we report values of target coverage only for the 50 % and 75 % of the peak SAR.

2.8 Correlation analysis

In total, 36 treatment plans (6 patients, 6 frequency combinations) are obtained for each cost function definition. On these evaluation points, we carry out a correlation analysis between the inverse of the cost value (1/HTQ, 1/HCQ) and each HTP quality indicator (TC_{50}, TC_{75}, T_{50}, T_{90}). The metric is the standard Pearson's correlation coefficient r.

3 Results

The values of the SAR indicator TC are reported for all patients and treatment plans in Fig. 3. As this metric varies widely and saturates for different patients regardless of the cost function used for optimization, we report the value at the fraction that is most relevant for the tumor site. The single-frequency plans exhibit a clear frequency dependent trend. Within the studied bands, the lowest frequency yields best coverage, even in smaller tumors (Venus). The addition of a second frequency is beneficial in Venus, Luna, and Clarice,

especially when HCQ is used as cost function. Overall, the HCQ optimal solutions yield systematically higher coverage than the HTQ optimal ones, except in Alex. However, the selection of the percentile p has a strong impact on the overall performance of HCQ. Low percentile values yield higher coverage with the maximum coverage often achieved at the lowest value of $p = 1$ %.

The values of the T_{50} and T_{90} indicators for the resulting temperature distributions are presented in Fig. 4 and 5. The temperature variations highlight the heterogeneity of the patient dataset. In a similar way as in the SAR analysis, the HCQ-based HTPs perform equally or better than the HTQ ones. As an example, the SAR and temperature distributions for Alex in a multi-frequency HTP are shown in Fig. 6. The HCQ extends the SAR deposition to cover the entire target, which leads to higher tumour temperatures. The SAR distributions of the individual frequencies support the homogeneous heating with complementary patterns (not shown). One notable exception in the set is the superficial breast tumor in Venus. The SAR and thermal distributions of both HTQ and HCQ plans for this patient are illustrated in Fig. 7. The SAR distribution after HCQ optimization is more homogeneous than in the HTQ case. However, the heating pattern is affected by the proximity of the water bolus. HTQ is favored by this mechanism and achieves almost 1.5 $^{\circ}C$ higher T than the HCQ solution. In all remaining cases, HCQ yields temperature indices up to half a degree higher than the HTQ solution, and is particularly beneficial in Alex and Will with almost 1 $^{\circ}C$ higher T_{90}.

The correlation coefficients between the inverse of the cost functions and the clinical indicators are summarized in Table 1. Values of cross-correlation between clinical indicators are also included. We report the values obtained for deep seated targets, i.e. excluding the superficial case of Venus, and for the entire dataset (within parenthesis). In the first case, the HCQ evaluated at a low percentile ($p \leq 30$ %) exhibits a high correlation with both the target coverage indicators TC_{50}, TC_{75} and the temperature indicators T_{50}, T_{90}. HTQ, on the other hand, is adequately correlated with TC_{50}, but the correlation deteriorates for other indicators, confirming that tumor coverage is not captured by this metric. The overall correlation is preserved for HTQ when the superficial case (Venus) is included, but the correlation of HCQ with the temperature indicators drops on average by 5 points with T_{50} and by 8 points with T_{90}. Simultaneously, the optimal percentile shifts towards higher volume fractions, $p \approx 50$ %. It is worth noting that the cross-correlation between

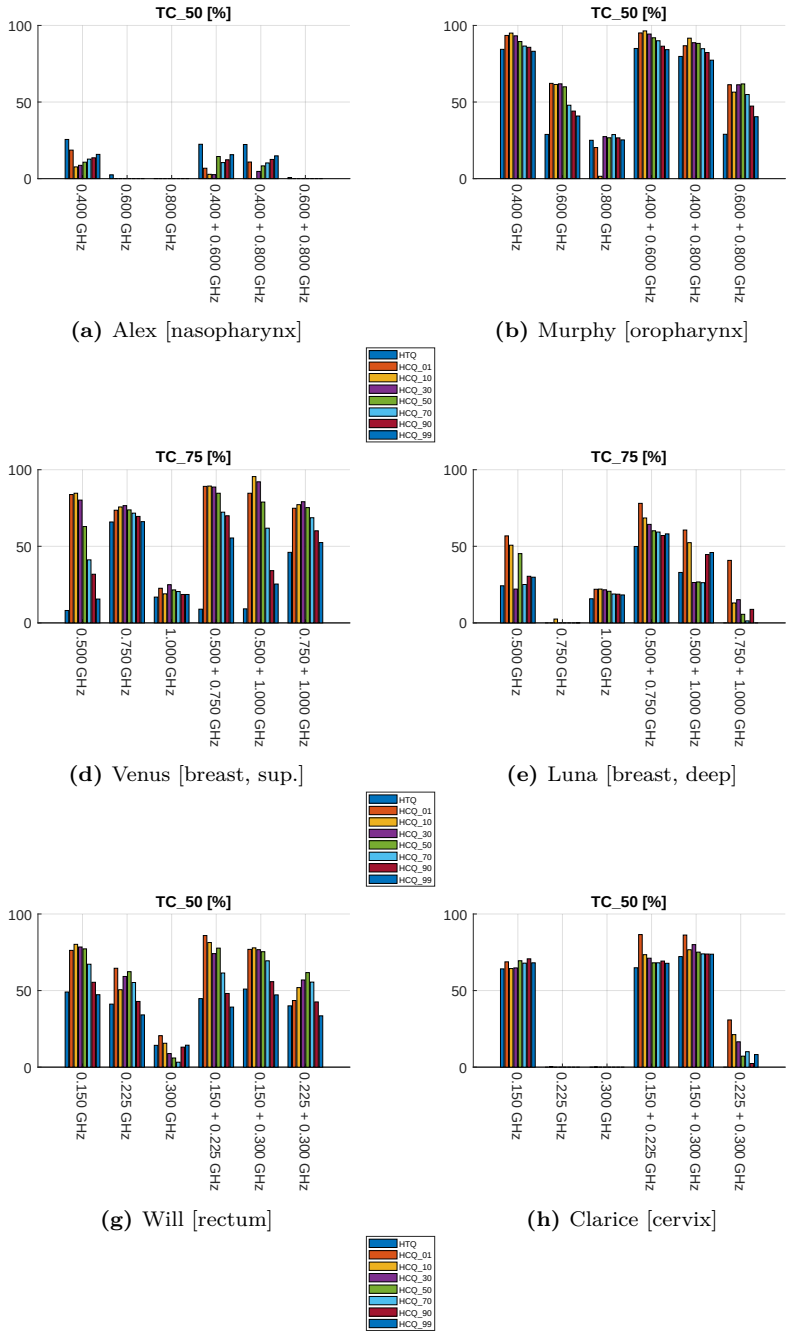

(a) Alex [nasopharynx] **(b)** Murphy [oropharynx]

(d) Venus [breast, sup.] **(e)** Luna [breast, deep]

(g) Will [rectum] **(h)** Clarice [cervix]

Figure 3: Treatment plan values of TC for each patient, frequency combination, and optimization cost function.

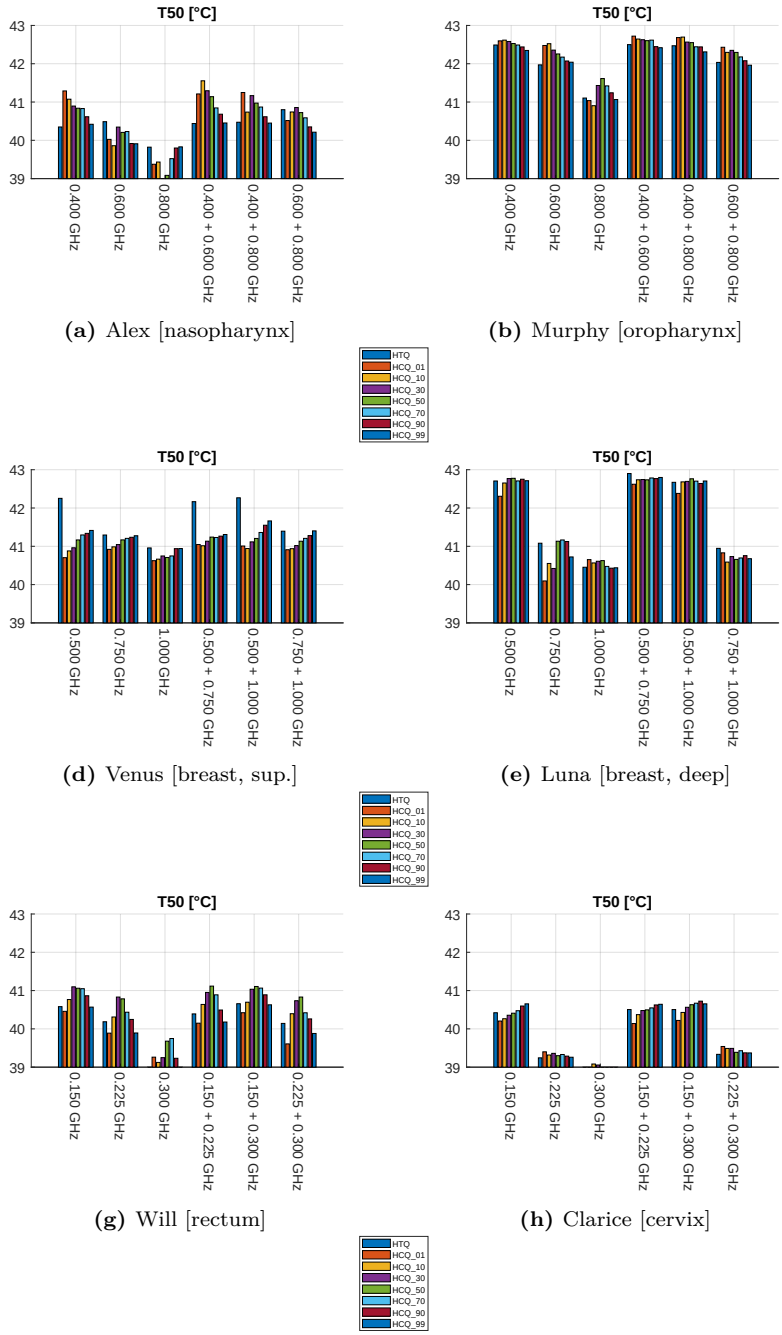

(a) Alex [nasopharynx] **(b)** Murphy [oropharynx]

(d) Venus [breast, sup.] **(e)** Luna [breast, deep]

(g) Will [rectum] **(h)** Clarice [cervix]

Figure 4: Treatment plan values of T_{50} for each patient, frequency combination, and optimization cost function.

R17

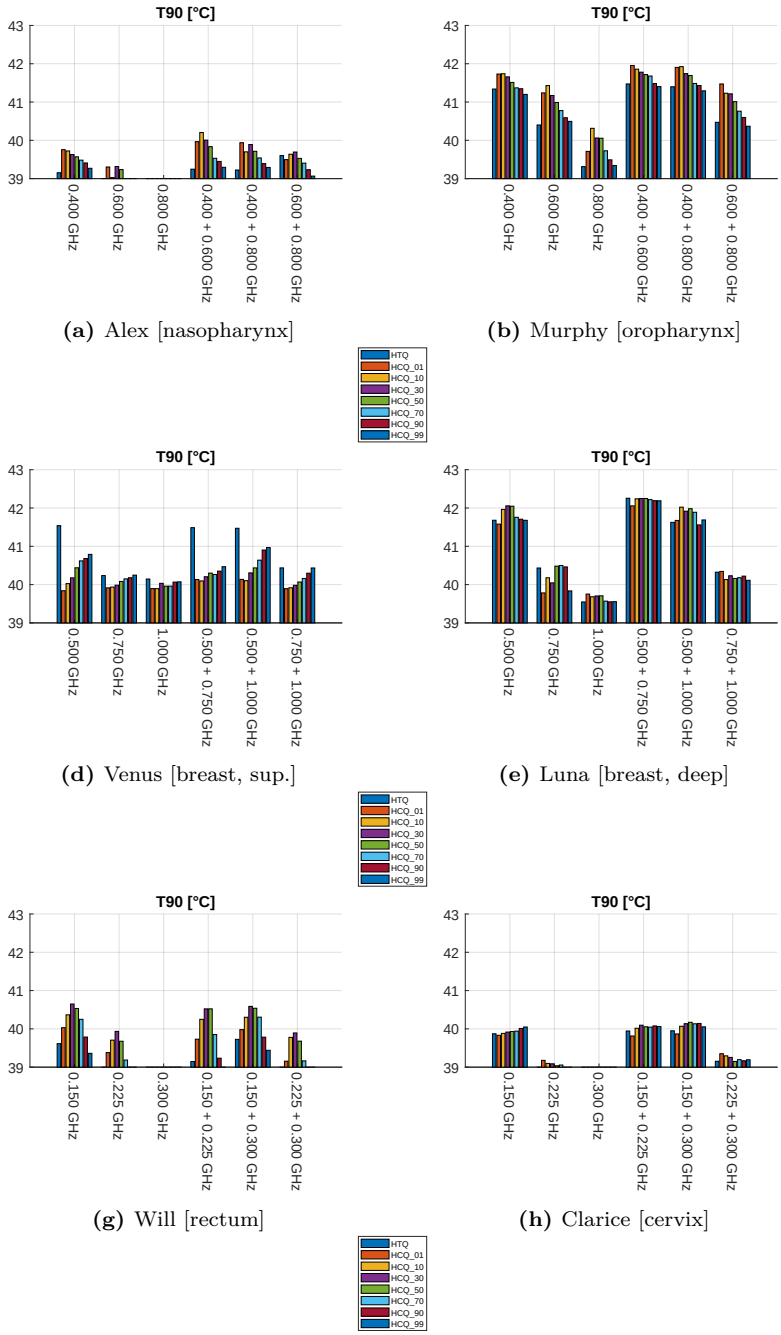

(a) Alex [nasopharynx] **(b)** Murphy [oropharynx]

(d) Venus [breast, sup.] **(e)** Luna [breast, deep]

(g) Will [rectum] **(h)** Clarice [cervix]

Figure 5: Treatment plan values of T_{90} for each patient, frequency combination, and optimization cost function.

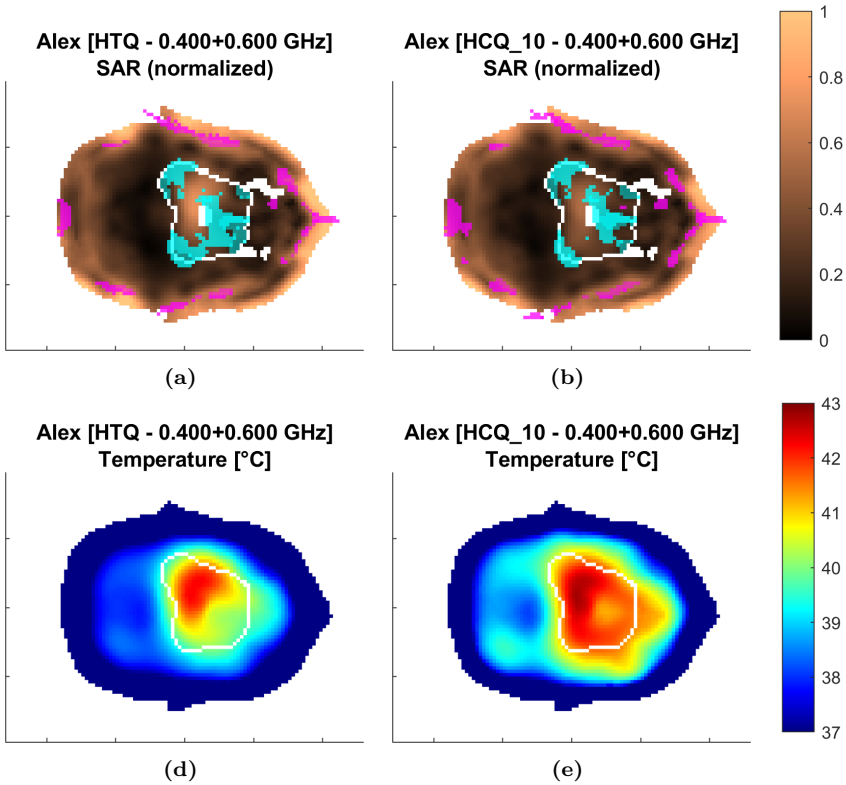

Figure 6: Treatment plans at $400 + 600\ MHz$ for Alex. The SAR is normalized to the highest value in the patient. Transverse sections at target center. The target is delineated in white. The magenta/cyan voxels represent locations of highest/lowest SAR (hot-spot/cold-spot), excluding the first centimeter of tissue from the skin surface.

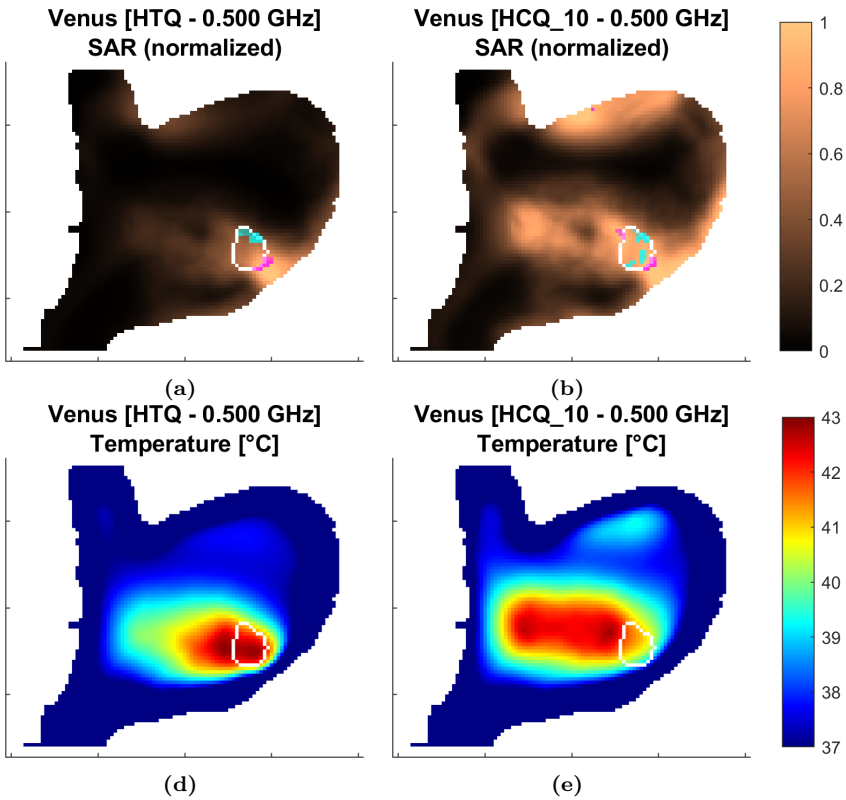

Figure 7: Treatment plans at 500 MHz for Venus. The SAR is normalized to the highest value in the patient. Sagittal sections at target center. The target is delineated in white. The magenta/cyan voxels represent locations of highest/lowest SAR (hot-spot/cold-spot), excluding the first centimeter of tissue from the skin surface.

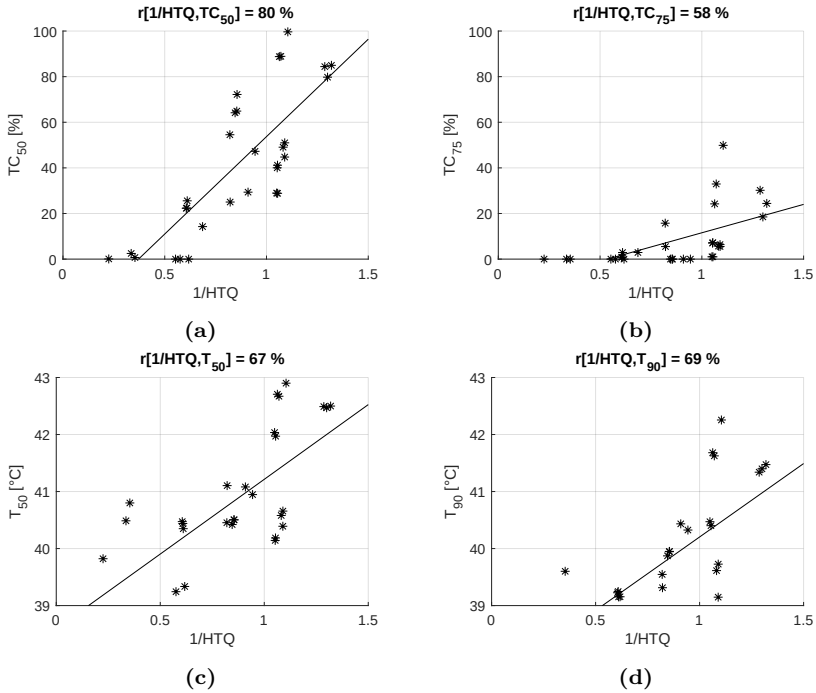

Figure 8: Dispersion plots and linear regression models for the relationship between HTQ and the clinical indicators.

SAR and temperature indicators also decreases substantially, loosing up to 31 points between TC_{75} and T_{90}. To better visualize the relationships between cost functions and clinical indicators, Fig. 8 and 9 display the dispersion plots and the fitted linear regression models for HTQ and HCQ_{30}.

To address the question of the sensitivity of HCQ to the target percentile parameter, we report in Fig. 10 the average values of the clinical indicators as a function of p. While the SAR indicators peak at $p = 1$ %, the temperature indicators are maximized at larger percentiles. The optimal percentile for T_{50} is $p = 50$ %, while T_{90} is highest at $p = 10$ %, although high values are obtained up to $p \leq 50$ %. Overall, HCQ achieves higher SAR and temperature values than HTQ for most percentile settings.

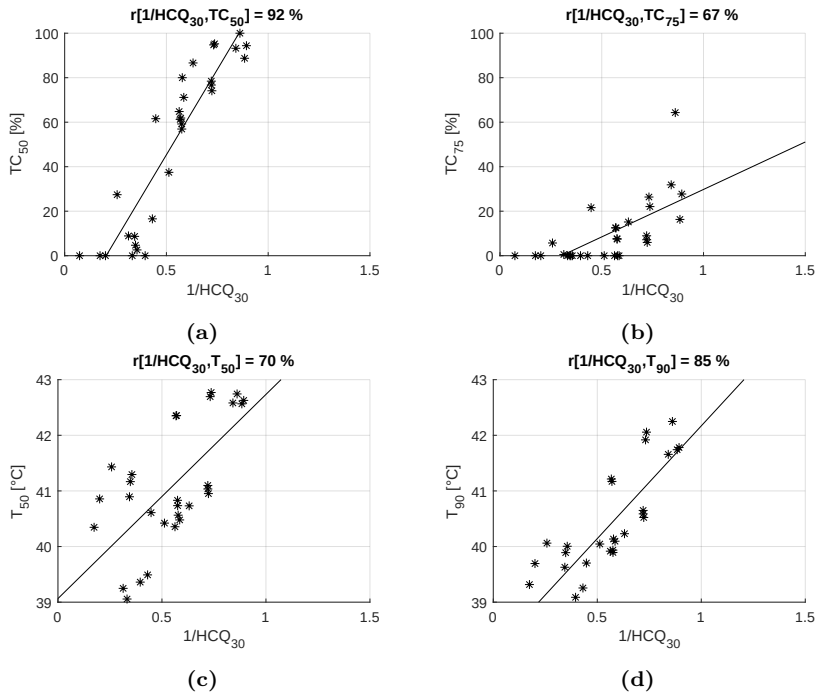

Figure 9: Dispersion plots and linear regression models for the relationship between HCQ_{30} and the clinical indicators. Model fit on all treatment plan values excluding samples relative to Venus.

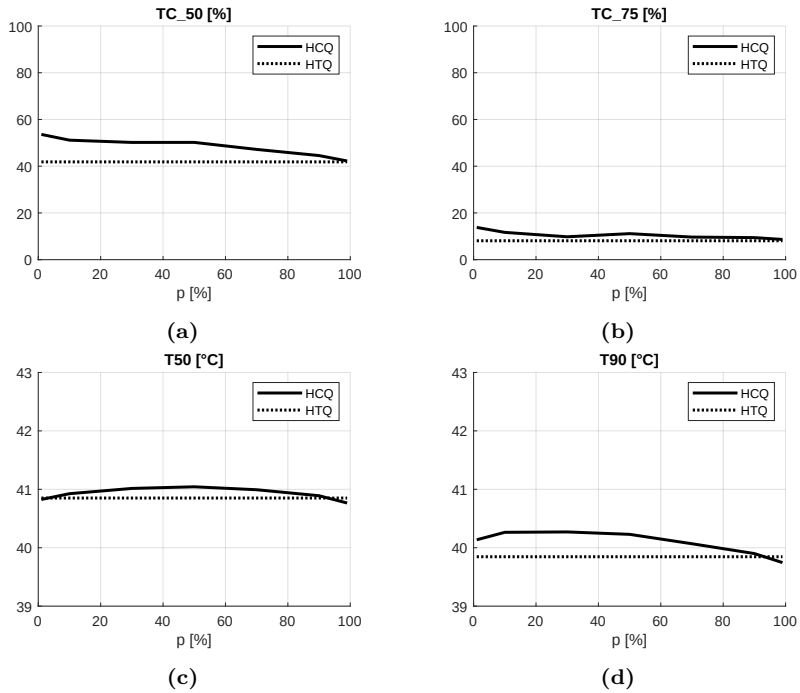

Figure 10: Average value of each clinical indicator as a function of the HCQ target percentile parameter p (solid line). The average values relative to HTQ are also reported for comparison (dotted line). The average is taken across all treatment plans excluding samples relative to Venus.

Table 1: Correlation coefficients between the inverse of the cost functions (HTQ, HCQ) and the clinical indicators (T, TC). The main value is obtained excluding the results from Venus, while the value between parenthesis is obtained including the results from Venus. The best correlation coefficient for each indicator is highlighted in yellow. The last four rows report the cross-correlation between clinical indicators.

r [%]	TC_50	TC_75	T50	T90
1/HTQ	80 (82)	58 (55)	67 (70)	69 (73)
$1/HCQ_{01}$	90 (91)	69 (80)	59 (49)	79 (61)
$1/HCQ_{10}$	93 (94)	71 (76)	68 (58)	83 (65)
$1/HCQ_{30}$	92 (93)	67 (68)	70 (62)	85 (72)
$1/HCQ_{50}$	92 (93)	69 (68)	72 (67)	84 (76)
$1/HCQ_{70}$	88 (89)	65 (64)	70 (67)	76 (73)
$1/HCQ_{90}$	77 (78)	52 (54)	65 (66)	61 (62)
$1/HCQ_{99}$	67 (68)	45 (47)	55 (57)	47 (50)
TC_50	−100−	70 (72)	70 (64)	81 (73)
TC_75	70 (72)	−100−	69 (43)	75 (44)
T50	70 (64)	69 (43)	−100−	93 (94)
T90	81 (73)	75 (44)	93 (94)	−100−

4 Discussion

According to clinical evidence, treatment planning in hyperthermia therapy should always strive to achieve high temperatures everywhere in the target volume, as this is crucial for a successful outcome [46]–[48]. This requirement is represented by the clinical indicators T_{50} and T_{90}. SAR-based optimization is a means to obtain the desired temperature distribution in the treated region, as shown for instance in [14], [23], [49], and temperature changes have been shown to accurately follow SAR-based steering during treatment [50].

Still, SAR is not temperature, and the relationship between local SAR and local temperature is not immediate. Therefore, it is of paramount importance that the goal in SAR-based treatment planning translates to optimal values of temperature indicators. Numerous efforts have been spent in this regard, as summarized by [15]. To date, the golden standard in clinical SAR-based optimization is the THQ, the inverse of HTQ as proposed by the same author and shown to correlate with T_{50} in pelvic tumors [14]. The relationship between 1/HTQ and the temperature indicators T_{50} and T_{90} has been further

examined in head and neck carcinomas [26] and shown to be sub-optimal for many cases ($\leq$ 60 %). A possible explanation is the fact that HTQ considers the average SAR in the whole target volume, implicitly neglecting areas of low deposition (cold-spots). Another limitation of HTQ is the definition of the hot-spot as a percentile of healthy tissue, which makes the resulting value sensitive to volumetric changes in patient segmentation. A possible workaround is to keep the hot-spot sub-volume constant, for instance 50 ml as proposed in [30]. In our opinion, this is only a partial solution to the problem because it does not consider the actual target volume size, which renders the results incomparable between different targets. Furthermore, it might not necessarily generalize to octave UWB systems where the size of the focal spot, and potentially even the size of the hot-spots, can vary double-fold.

To improve on this aspect, we have proposed the HCQ as a means to obtain high and homogeneous SAR deposition in the target, while limiting the most prominent hot-spot [28]. We observed that HCQ has the potential to extend SAR deposition in cold regions of the target. The current work, which benchmarks the performances of HCQ against the current standard on a comprehensive set of patients, confirms this claim. In the deep seated targets, HCQ yields systematically higher values than HTQ in all clinical indicators. Moreover, in at least three cases (Alex, Murphy, Luna), the multi-frequency HCQ-optimal treatment plans increase the temperature indicators T_{50} and T_{90} by up to half a degree with respect to the best single-frequency or HTQ solutions. Despite the discrepancies between *absolute* temperature predictions by thermal simulations and clinically measured values [51], the gain is nevertheless relevant in view of the proven accuracy in predicted *relative* temperature changes [52]. These results confirm previous indications that, in a multi-frequency setting, the HCQ-optimal solution can achieve broader target coverage by exploiting complementary SAR deposition patterns [53].

We carried out the analysis on the ESHO patient repository, which is meant to be the first step towards the creation of a standard for the quantitative comparison of different HTP optimization strategies [30]. In the benchmark paper, three patient models are devoted to SAR-based optimization, and another three are reserved to temperature-based optimization. To increase the statistical significance of our results, we carried out HTP optimizations for all six patients. Our thermal simulations result in slightly different tumor temperatures than those reported in [30], even when applying HTQ as cost

function. For comparison, we report our results in terms of T_{90} with the corresponding values from the benchmark paper in Table 2. There might be several reasons behind these deviations. The major difference lies in the applicator design. In our study, all patients are treated with tailored applicators based on more efficient antennas than the monopoles used in the benchmark. The arrays are assembled by maximizing the number of antennas with given constraints on the minimum distance between them, while the distance between each antenna and the patient is kept as close as possible to the optimum. This results in a higher number of antennas per applicator than in [30], except in the breast models. Thermal modeling can also be a factor. We applied a water bolus convection coefficient of 100 $[W/m^2/K]$, an average value in the range reported by [40] and previously adopted by [54]. The benchmark paper [30] recommends a maximum value of 40 $[W/m^2/K]$, with space for adjustments. However, it is not entirely clear whether this applies to the air/skin or the water/skin interface. Finally, we strictly followed the material properties reported in [32], while the benchmark paper applies adjustments for thermal stress (muscle, fat, breast) and custom baseline values for breast gland. In this study, however, we are interested in the correlation between HCQ and the HTP indicators, and therefore we opted for a worst case scenario without perfusion enhancements.

Table 2: Values of T_{90} for our HTQ-optimal treatment plans compared to those reported in [30]. We report between parenthesis the operating frequency at which the treatment plan has been obtained.

T_{90} $[°C(MHz)]$	Alex	Murphy	Luna	Venus	Clarice	W
Present work	39.2 (400)	41.3 (400)	41.7 (500)	41.5 (500)	39.9 (150)	39.6
Paulides *et. al.*	40.0 (434)	39.1 (434)	41.1 (434)	39.4 (434)	39.4 (120)	41.3

This study indicates that HCQ is an effective metric for SAR-based treatment planning, providing high correlation with the temperature indicators for targets located deeply in the body, where the cooling effect of the water bolus is negligible. If the tumor is closer to the surface, the overall correlation between SAR and temperature degrades. This can be seen in the lower part of Table 1, where the cross-correlations between SAR and temperature indicators are reported. When the superficial case (Venus) is excluded, the correlation between TC and T is high (average $r \approx 74$ %). On the other hand, when the whole dataset is considered, the correlation drops severely (average

$r \approx 56$ %). This degradation affects the HCQ-based plan for Venus, where it underperforms compared to HTQ. Although one case is not statistically significant for a general conclusion, it is possible to identify a rationale behind this specific result by visual inspection of the SAR and temperature distributions (Fig 7). In SAR, the main hot-spot of the HTQ-optimal solution lies in the layer of healthy tissue between the tumor and the water bolus. Normally, this deposition peak would limit the maximum power to the tumor, which in turn would result in poor coverage of its deeper parts. However, due to the cooling effect of the water bolus, the hot-spot is efficiently suppressed, leading to preferential power absorption and thus high temperatures in the tumor. The HCQ-optimal solution, conversely, extends the SAR deposition deeper in the target. As a consequence, the main deposition peak arises on the proximal side of the tumor. This hot-spot, however, is not counterbalanced by cooling, and becomes the limiting factor in the power scaling. For these reasons, we believe that superficial targets are better tackled by temperature-based optimization strategies, that inherently account for the heat extraction of the bolus. In such a context, the temperature of the water bolus can also be left as an optimization parameter [55].

Although the choice of an appropriate cost function is crucial to achieve an adequate SAR-based treatment plan, other parameters play an important role as well. In fact, the SAR optimization relies on the assumption that the SAR and temperature distributions are spatially correlated. For this to be true, the raw SAR distribution must be treated with a smoothing filter. This problem has been thoroughly addressed in the literature [56]–[58], resulting in number of proposed averaging schemes. In our investigations, we have identified the 1 g tissue mass scheme as most suitable for our purposes. Concurrently, the correlation of SAR and temperature can be further enhanced by the exclusion of the first centimeter of tissue that is in contact with the water bolus [40]. Under these conditions, the HCQ is capable of achieving high correlation with the temperature indicators. The strength of this relationship can also be inferred from Fig. 10, where the peak T_{50} is obtained for the 50-percentile HCQ, while the peak T_{90} is achieved for the $100 - 90 = 10$-percentile HCQ.

5 Conclusion

This work validates the HCQ as goal for SAR-based treatment planning on the ESHO benchmark patient repository. The HCQ-based optimization exhibits high correlation with clinical SAR and temperature indicators. This correlation is a result of the metric definition, along with careful pre-processing of the SAR distribution. The results indicate that HCQ-optimal treatment plans can achieve higher and more homogeneous temperatures in the target than plans based on current SAR standards. The use of HCQ as cost function promotes the exploitation of additional operating frequencies to increase target coverage. The validation performed on a set of six patient models that cover some of the most common hyperthermia treatment sites demonstrates that HCQ-based optimization is a powerful and robust alternative to the current standards, provided the target is located far from the range of effect of the water bolus. For superficial targets, we suggest the implementation of temperature-based treatment planning optimization strategies.

References

[1] H. P. Kok, E. N. Cressman, W. Ceelen, *et al.*, "Heating technology for malignant tumors: A review," *International Journal of Hyperthermia*, vol. 37, no. 1, pp. 711–741, 2020.

[2] M. Paulides, H. D. Trefná, S. Curto, and D. Rodrigues, "Recent technological advancements in radiofrequency-and microwave-mediated hyperthermia for enhancing drug delivery.," *Advanced Drug Delivery Reviews*, 2020.

[3] P. B. Elming, B. S. Sørensen, A. L. Oei, *et al.*, "Hyperthermia: The optimal treatment to overcome radiation resistant hypoxia," *Cancers*, vol. 11, no. 1, p. 60, 2019.

[4] R. D. Issels, L. H. Lindner, J. Verweij, *et al.*, "Effect of neoadjuvant chemotherapy plus regional hyperthermia on long-term outcomes among patients with localized high-risk soft tissue sarcoma: The eortc 62961-esho 95 randomized clinical trial," *JAMA oncology*, vol. 4, no. 4, pp. 483–492, 2018.

[5] N. Datta, S. G. Ordóñez, U. Gaipl, *et al.*, "Local hyperthermia combined with radiotherapy and-/or chemotherapy: Recent advances and promises for the future," *Cancer treatment reviews*, vol. 41, no. 9, pp. 742–753, 2015.

[6] P. S. Yarmolenko, E. J. Moon, C. Landon, *et al.*, "Thresholds for thermal damage to normal tissues: An update," *International Journal of Hyperthermia*, vol. 27, no. 4, pp. 320–343, 2011.

[7] S. A. Sapareto and W. C. Dewey, "Thermal dose determination in cancer therapy," *International Journal of Radiation Oncology • Biology • Physics*, vol. 10, no. 6, pp. 787–800, 1984.

[8] G. Bruggmoser, S. Bauchowitz, R. Canters, *et al.*, "Quality assurance for clinical studies in regional deep hyperthermia," *Strahlentherapie und Onkologie*, vol. 187, no. 10, p. 605, 2011.

[9] H. Kok, P. Wust, P. R. Stauffer, F. Bardati, G. Van Rhoon, and J. Crezee, "Current state of the art of regional hyperthermia treatment planning: A review," *Radiation Oncology*, vol. 10, no. 1, p. 196, 2015.

[10] H. Kok and J. Crezee, "Progress and future directions in hyperthermia treatment planning," in *2017 First IEEE MTT-S International Microwave Bio Conference (IMBIOC)*, IEEE, 2017, pp. 1–4.

[11] S. Gavazzi, A. L. van Lier, C. Zachiu, *et al.*, "Advanced patient-specific hyperthermia treatment planning," *International Journal of Hyperthermia*, vol. 37, no. 1, pp. 992–1007, 2020.

[12] H. Kok, A. Kotte, and J. Crezee, "Planning, optimisation and evaluation of hyperthermia treatments," *International journal of hyperthermia*, vol. 33, no. 6, pp. 593–607, 2017.

[13] G. Schooneveldt, H. D. Trefná, M. Persson, *et al.*, "Hyperthermia treatment planning including convective flow in cerebrospinal fluid for brain tumour hyperthermia treatment using a novel dedicated paediatric brain applicator," *Cancers*, vol. 11, no. 8, p. 1183, 2019.

[14] R. Canters, M. Franckena, J. van der Zee, and G. Van Rhoon, "Optimizing deep hyperthermia treatments: Are locations of patient pain complaints correlated with modelled SAR peak locations?" *Physics in Medicine & Biology*, vol. 56, no. 2, p. 439, 2010.

[15] R. Canters, P. Wust, J. Bakker, and G. Van Rhoon, "A literature survey on indicators for characterisation and optimisation of sar distributions in deep hyperthermia, a plea for standardisation," *International Journal of Hyperthermia*, vol. 25, no. 7, pp. 593–608, 2009.

[16] A. Kuehne, E. Oberacker, H. Waiczies, and T. Niendorf, "Solving the time-and frequency-multiplexed problem of constrained radiofrequency induced hyperthermia," *Cancers*, vol. 12, no. 5, p. 1072, 2020.

[17] G. G. Bellizzi, T. Drizdal, G. C. van Rhoon, L. Crocco, T. Isernia, and M. M. Paulides, "The potential of constrained sar focusing for hyperthermia treatment planning: Analysis for the head & neck region," *Physics in Medicine & Biology*, vol. 64, no. 1, p. 015 013, 2018.

[18] R. Mestrom, J. Van Engelen, M. Van Beurden, M. Paulides, W. Numan, and A. Tijhuis, "A refined eigenvalue-based optimization technique for hyperthermia treatment planning," in *The 8th European Conference on Antennas and Propagation (EuCAP 2014)*, IEEE, 2014, pp. 2010–2013.

[19] T. Köhler, P. Maass, P. Wust, and M. Seebass, "A fast algorithm to find optimal controls of multiantenna applicators in regional hyperthermia," *Physics in Medicine & Biology*, vol. 46, no. 9, p. 2503, 2001.

[20] M. Zanoli and H. D. Trefná, "Suitability of eigenvalue beam-forming for discrete multi-frequency hyperthermia treatment planning," *Medical Physics*, vol. 48, no. 11, pp. 7410–7426, 2021.

[21] H. Shoji, M. Motegi, K. Osawa, *et al.*, "Output-limiting symptoms induced by radiofrequency hyperthermia. are they predictable?" *International Journal of Hyperthermia*, vol. 32, no. 2, pp. 199–203, 2016.

[22] H. P. Kok, L. Korshuize-van Straten, A. Bakker, *et al.*, "Online adaptive hyperthermia treatment planning during locoregional heating to suppress treatment-limiting hot spots," *International Journal of Radiation Oncology* Biology* Physics*, vol. 99, no. 4, pp. 1039–1047, 2017.

[23] Z. Rijnen, J. F. Bakker, R. A. Canters, *et al.*, "Clinical integration of software tool vedo for adaptive and quantitative application of phased array hyperthermia in the head and neck," *International journal of Hyperthermia*, vol. 29, no. 3, pp. 181–193, 2013.

[24] R. Canters, M. Franckena, M. Paulides, and G. Van Rhoon, "Patient positioning in deep hyperthermia: Influences of inaccuracies, signal correction possibilities and optimization potential," *Physics in Medicine & Biology*, vol. 54, no. 12, p. 3923, 2009.

[25] M. Sherar, F.-F. Liu, M. Pintilie, *et al.*, "Relationship between thermal dose and outcome in thermoradiotherapy treatments for superficial recurrences of breast cancer: Data from a phase iii trial," *International Journal of Radiation Oncology* Biology* Physics*, vol. 39, no. 2, pp. 371–380, 1997.

[26] G. G. Bellizzi, T. Drizdal, G. C. van Rhoon, L. Crocco, T. Isernia, and M. M. Paulides, "Predictive value of sar based quality indicators for head and neck hyperthermia treatment quality," *International Journal of Hyperthermia*, vol. 36, no. 1, pp. 455–464, 2019.

[27] S. Triantopoulou, E. Efstathopoulos, K. Platoni, N. Uzunoglou, N. Kelekis, and V. Kouloulias, "Radiotherapy in conjunction with superficial and intracavitary hyperthermia for the treatment of solid tumors: Survival and thermal parameters," *Clinical and Translational Oncology*, vol. 15, no. 2, pp. 95–105, 2013.

[28] M. Zanoli and H. D. Trefná, "Combining target coverage and hot-spot suppression into one cost function: The hot-to-cold spot quotient," in *2021 15th European Conference on Antennas and Propagation (EuCAP)*, IEEE, 2021, pp. 1–4.

[29] G. G. Bellizzi, K. Sumser, I. VilasBoas-Ribeiro, *et al.*, "Standardization of patient modeling in hyperthermia simulation studies: Introducing the erasmus virtual patient repository," *International Journal of Hyperthermia*, vol. 37, no. 1, pp. 608–616, 2020.

[30] M. M. Paulides, D. B. Rodrigues, G. G. Bellizzi, *et al.*, "Esho benchmarks for computational modeling and optimization in hyperthermia therapy," *International Journal of Hyperthermia*, vol. 38, no. 1, pp. 1425–1442, 2021.

[31] B. J. James and D. M. Sullivan, "Creation of three-dimensional patient models for hyperthermia treatment planning," *IEEE transactions on biomedical engineering*, vol. 39, no. 3, pp. 238–242, 1992.

[32] P. Hasgall, F. Di Gennaro, C. Baumgartner, *et al.*, *IT'IS Database for thermal and electromagnetic parameters of biological tissues*, version 4.0, May 2018.

[33] W. T. Joines, Y. Zhang, C. Li, and R. L. Jirtle, "The measured electrical properties of normal and malignant human tissues from 50 to 900 mhz," *Medical physics*, vol. 21, no. 4, pp. 547–550, 1994.

[34] P. Takook, M. Persson, J. Gellermann, and H. D. Trefná, "Compact self-grounded bow-tie antenna design for an uwb phased-array hyperthermia applicator," *International Journal of Hyperthermia*, vol. 33, no. 4, pp. 387–400, 2017.

[35] M. Seebass, R. Beck, J. Gellermann, J. Nadobny, and P. Wust, "Electromagnetic phased arrays for regional hyperthermia: Optimal frequency and antenna arrangement," *International Journal of Hyperthermia*, vol. 17, no. 4, pp. 321–336, 2001.

[36] M. M. Paulides, S. H. Vossen, A. P. Zwamborn, and G. C. van Rhoon, "Theoretical investigation into the feasibility to deposit rf energy centrally in the head-and-neck region," *International Journal of Radiation Oncology* Biology* Physics*, vol. 63, no. 2, pp. 634–642, 2005.

[37] H. Kok, M. De Greef, P. Borsboom, A. Bel, and J. Crezee, "Improved power steering with double and triple ring waveguide systems: The impact of the operating frequency," *International Journal of Hyperthermia*, vol. 27, no. 3, pp. 224–239, 2011.

[38] COMSOL AB, Stockholm, Sweden, *COMSOL Multiphysics® v. 5.6*, 2020.

[39] The MathWorks Inc., Natick, Massachusetts, "MATLAB R2019," 2019.

[40] M. Van der Gaag, M. De Bruijne, T. Samaras, J. Van Der Zee, and G. Van Rhoon, "Development of a guideline for the water bolus temperature in superficial hyperthermia," *International journal of hyperthermia*, vol. 22, no. 8, pp. 637–656, 2006.

[41] M. Clerc, *Particle swarm optimization*. John Wiley & Sons, 2010, vol. 93.

[42] X. Liu, S. Chen, J. K. Tsoi, and J. P. Matinlinna, "Binary titanium alloys as dental implant materials - a review," *Regenerative biomaterials*, vol. 4, no. 5, pp. 315–323, 2017.

[43] R. F. Verhaart, G. M. Verduijn, V. Fortunati, *et al.*, "Accurate 3d temperature dosimetry during hyperthermia therapy by combining invasive measurements and patient-specific simulations," *International Journal of Hyperthermia*, vol. 31, no. 6, pp. 686–692, 2015.

[44] A. Bakker, J. van der Zee, G. van Tienhoven, H. P. Kok, C. R. Rasch, and H. Crezee, "Temperature and thermal dose during radiotherapy and hyperthermia for recurrent breast cancer are related to clinical outcome and thermal toxicity: A systematic review," *International Journal of Hyperthermia*, vol. 36, no. 1, pp. 1023–1038, 2019.

[45] H. K. Lee, A. G. Antell, C. A. Perez, *et al.*, "Superficial hyperthermia and irradiation for recurrent breast carcinoma of the chest wall: Prognostic factors in 196 tumors.," *International journal of radiation oncology, biology, physics*, vol. 40, no. 2, pp. 365–375, 1998.

[46] T. Refaat, S. Sachdev, V. Sathiaseelan, *et al.*, "Hyperthermia and radiation therapy for locally advanced or recurrent breast cancer," *The Breast*, vol. 24, no. 4, pp. 418–425, 2015.

[47] M. Franckena, D. Fatehi, M. de Bruijne, *et al.*, "Hyperthermia dose-effect relationship in 420 patients with cervical cancer treated with combined radiotherapy and hyperthermia," *European Journal of Cancer*, vol. 45, no. 11, pp. 1969–1978, 2009.

[48] E. L. Jones, J. R. Oleson, L. R. Prosnitz, *et al.*, "Randomized trial of hyperthermia and radiation for superficial tumors," *Journal of Clinical Oncology*, vol. 23, no. 13, pp. 3079–3085, 2005.

[49] G. Verduijn, E. de Wee, Z. Rijnen, *et al.*, "Deep hyperthermia with the HYPERcollar system combined with irradiation for advanced head and neck carcinoma–a feasibility study," *International Journal of Hyperthermia*, vol. 34, no. 7, pp. 994–1001, 2018.

[50] H. P. Kok, S. Ciampa, R. de Kroon-Oldenhof, *et al.*, "Toward online adaptive hyperthermia treatment planning: Correlation between measured and simulated specific absorption rate changes caused by phase steering in patients," *International Journal of Radiation Oncology* Biology* Physics*, vol. 90, no. 2, pp. 438–445, 2014.

[51] B. Aklan, B. Zilles, P. Paprottka, *et al.*, "Regional deep hyperthermia: Quantitative evaluation of predicted and direct measured temperature distributions in patients with high-risk extremity soft-tissue sarcoma," *International Journal of Hyperthermia*, 2019.

[52] H. Kok, G. Schooneveldt, A. Bakker, *et al.*, "Predictive value of simulated sar and temperature for changes in measured temperature after phase-amplitude steering during locoregional hyperthermia treatments," *International Journal of Hyperthermia*, vol. 35, no. 1, pp. 330–339, 2018.

[53] M. Zanoli and H. D. Trefná, "Iterative time-reversal for multi-frequency hyperthermia," *Physics in Medicine & Biology*, vol. 66, no. 4, p. 045 027, 2021.

[54] J. Kumaradas and M. Sherar, "Edge-element based finite element analysis of microwave hyperthermia treatments for superficial tumours on the chest wall," *International journal of hyperthermia*, vol. 19, no. 4, pp. 414–430, 2003.

[55] H. Dobšíček Trefná, J. Crezee, M. Schmidt, *et al.*, "Quality assurance guidelines for superficial hyperthermia clinical trials," *Strahlentherapie und Onkologie*, vol. 193, no. 5, pp. 351–366, 2017.

[56] A. Razmadze, L. Shoshiashvili, D. Kakulia, R. Zaridze, G. Bit-Babik, and A. Faraone, "Influence of specific absorption rate averaging schemes on correlation between mass-averaged specific absorption rate and temperature rise," *Electromagnetics*, vol. 29, no. 1, pp. 77–90, 2009.

[57] A. Hirata and O. Fujiwara, "The correlation between mass-averaged sar and temperature elevation in the human head model exposed to rf near-fields from 1 to 6 ghz," *Physics in Medicine & Biology*, vol. 54, no. 23, p. 7227, 2009.

[58] J. Bakker, M. Paulides, E. Neufeld, A. Christ, N. Kuster, and G. Van Rhoon, "Children and adults exposed to electromagnetic fields at the icnirp reference levels: Theoretical assessment of the induced peak temperature increase," *Physics in Medicine & Biology*, vol. 56, no. 15, p. 4967, 2011.

PAPER C

Iterative time-reversal for multi-frequency hyperthermia

Massimiliano Zanoli, Hana Dobšíček Trefná

Physics in Medicine & Biology
16 December 2020

DOI: 10.1088/1361-6560/abd41a

The layout has been revised.

Abstract

Time-reversal (TR) is a known wideband array beam-forming technique that has been suggested as a treatment planning alternative in deep microwave hyperthermia for cancer treatment. While the aim in classic TR is to focus the energy at a specific point within the target, no assumptions are made on secondary lobes that might arise in the healthy tissues. These secondary lobes, together with tissue heterogeneity, may result in hot-spots, which are known to limit the efficiency of the thermal dose delivery to the tumor. This paper proposes a novel wideband TR focusing method that iteratively shifts the focus away from hot-spots and towards cold-spots from an initial TR solution, a procedure that improves tumor coverage and reduces hot-spots. We verify this method on two different applicator topologies and several target volume configurations. The algorithm is deterministic and runs within seconds, enabling its use for real-time applications. At the same time, it yields results comparable to those obtained with global stochastic optimizers such as Particle Swarm.

1 Introduction

In deep microwave hyperthermia (MW-HT) for cancer treatment, a conformal array of antennas, called applicator, is used to non-invasively and selectively increase the temperature of a deep-seated tumor up to $40-44$ °C for approximately one hour [1], [2]. Randomized clinical trials have demonstrated the efficacy of this technique in enhancing the therapeutic effects of chemo- and radio-therapy [3]–[5]. The challenge in MW-HT is to reach deep-seated targets with adequate power deposition while keeping the nearby healthy tissues below a safety temperature threshold. These healthy tissues lie in the path between the antenna and the target, and they tend to absorb energy from the traveling wave, as a consequence of their relatively high conductivity at RF frequencies. The power loss in these tissues can cause hot-spots (HSs), which effectively limit the maximum temperature achievable in the target. This can prevent the treatment from reaching high therapeutic thermal doses [6], [7].

Superficial HSs within depths of one to two centimeters from the skin can be suppressed by applying a water bolus circulated with cool water. Other HSs might arise deeper in the body due to the anatomical heterogeneity and interfaces between tissues with different dielectric properties, together with the imperfect interference pattern generated by the phased array. In such cases, the pattern has to be improved by means of amplitude and phase steering of the applicator array, with parameters obtained by a hyperthermic treatment planning (HTP) step [8].

Several methods for determining the optimal amplitudes and phases for an applicator array yielding satisfying target coverage and limited HS temperatures have been developed in the past and are still subject of ongoing research [9], [10]. These methods can be classified into two main categories: specific absorption rate (SAR) based and temperature (T) based. SAR based techniques rely on the assumption that the SAR distribution is predictive of the temperature distribution in the patient [11]. However, since the thermal response of the body can be highly non-linear, SAR-based optimizers can yield sub-optimal, while still clinically relevant, HTP parameters. T-based optimizers, on the other hand, have evolved to include complex non-linear aspects such as discrete vasculature and systemic response under thermal stress [12]. Ideally, a full implementation of T-based HTP in the clinical routine is desirable, since temperature is the objective dose. In current practice, however, the theoretical benefits of T-based HTP are somewhat diminished due to the lack of accurate estimations of the thermal tissue properties [13]–[15]. Such thermal properties, and blood perfusion in particular, exhibit large variations across patients and even at individual level in different treatment sessions. Therefore, both SAR-based and T-based approaches are being clinically applied as both require adjustments during treatment in response to hot spots [6], [16]. Considering the current equivalence of these two approaches, in the present work we consider only SAR based HTP techniques.

Among them, the Eigenvalue (EV) and, more recently, the Particle Swarm (PS) algorithms have become the most established in the literature [9], [10]. The EV method maximizes the ratio between the average SAR in the target and in the remaining tissues [17], [18]. When the resulting temperature distribution is showing overheated healthy regions, a weighing factor can be introduced to iteratively reduce the power deposition at those locations [19]. EV is a direct method that provides a fast and deterministic solution, but its main

limitation lies in the form of the cost function, which has to be a quadratic ratio between polynomials. Quadratic cost function predictions have been shown to correlate poorly with the SAR or temperature rise in the tumour target volume during clinical treatment [11]. For this reason, more clinically relevant and temperature-predicting indicators such as the hotspot-to-target quotient (HTQ) have been proposed [20]. Since the evaluation of the HTQ involves at least one non-linear step with respect to the complex array steering parameters, EV cannot be directly used to determine the HTQ-optimal solution. A second limitation of EV occurs with multi-frequency optimization: the generalized eigenvalue form can not be defined for multiple simultaneous operating frequencies in a conjoint manner [21], [22].

There is mounting evidence that the development of UWB applicators capable of operating at different frequencies will lead to improved target coverage and hot-spot suppression [23]–[26]. An UWB system can exploit the complementary interference patterns generated by different frequencies to increase the net average power delivered to the tumor while reducing the absorption in healthy tissues. The benefit of UWB is even more pronounced for the treatment of tumors in challenging locations, such as the brain [27], [28]. The brain region is in fact characterized by a combination of anatomical and physiological factors that require an extra degree of accuracy in the formation of the heating pattern. The cerebral tissue is more sensitive to deviations in temperature than other tissues [29], and the presence of cerebrospinal fluid causes strong HSs to appear in the immediate vicinity of the brain [30]. The single-frequency constraint of EV might therefore represent an insurmountable limitation for multi-frequency HTP.

Particle Swarm (PS) is another type of HTP optimizer used in clinical practice [10]. If the PS optimization is configured to minimize the HTQ, the resulting steering settings can exhibit significant differences from those given by EV. In particular, the resulting raw power deposition ratio might be worse than the one obtained via EV, but the SAR distribution is often better in terms of more relevant clinical parameters: target coverage and heating homogeneity. Furthermore, the PS method can easily be extended for use with multiple operating frequencies. The drawback with PS, being a stochastic algorithm, is its long execution time needed to consistently converge to the same global optimum between different executions. A typical run with 100 iterations, as usually required for reasonable accuracy, can take half an

hour or more to complete, depending on the model resolution.

Time reversal (TR) focusing is a fast, intrinsically wide-band and deterministic method that has been proposed and validated as an alternative microwave HTP technique [31], [32]. TR processing is a well characterized inverse filter initially developed for focusing ultrasound pulses generated by transducer arrays inside a biological target [33], [34], and subsequently extended for use with electromagnetic antenna arrays [35]. It exploits the time and space reciprocity of the wave equation to determine the optimal phase and amplitude settings of an array of radiators that will cause the highest constructive interference to occur at the desired location. In its basic implementation, with a single virtual source placed at the center of the tumor, TR already exhibits improved target coverage and HTQ than EV [24], [32], [36], though not comparable to PS optimization. Further improvements for HS-management in TR have been proposed for high-intensity focused ultrasounds (HIFU), based on iterative methods [37]. In general, the major hindrance for the clinical introduction of TR-based HTP is its limited ability to suppress HSs. In this work, we present a novel deterministic HS suppression algorithm for TR-based HTP that yields results comparable to those obtained via global PS optimization, while being significantly faster. The rest of the paper is organized as follows: we first introduce the iterative procedure in detail, to later benchmark its performances numerically for two different applicator array topologies: a collar for tumors in the neck and a helmet for tumors in the brain. For the neck model, we further consider different target locations and sizes, to assess the algorithm's robustness to different scenarios. For each test case, HTP quality and performance indicators are computed and compared against those obtained with EV, PS and classic TR.

2 Theory

2.1 Classic TR Focusing

TR focusing is achieved by placing a so-called *virtual source* at the desired focal spot and by recording the impulse response at the antenna locations (Fig. 1a). The recorded signals are then back-propagated simultaneously by all the antennas, generating an interference pattern that exhibits full phase coherence at the original source location (Fig. 1b). Together with the desired

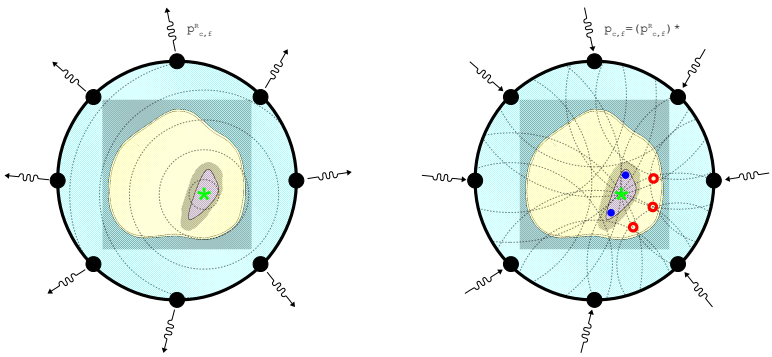

(a) Recording phase. **(b)** Steering phase.

Figure 1: Conceptual scheme for Time-Reversal treatment planning, example in the neck region. In the recording phase (a) a virtual source (green asterisk) is placed at the desired focal spot inside the tumor. The source is then excited and the phasors $p^R_{c,f}$ are determined. In the steering phase (b) the conjugate phasors are used as steering parameters to obtain a focal spot where the virtual source was located. Due to imperfect interference, hot-spots (red circles) arise in the healthy tissues and cold-spot (blue dots) can be identified in the target volume.

peak, however, secondary lobes appear due to both the limited aperture of the array and the anatomy of the patient. In the frequency domain, the TR operator corresponds to a complex conjugation (*):

$$p_c(f) = \left[p_c^R(f)\right]^* \tag{C.1}$$

where p_c^R is the complex phasor recorded by the array channel c at frequency f during source excitation, while p_c is the complex steering parameter for the same channel to focus at the source location. Under this perspective, a discrete set of simultaneous operating frequencies can be selected for treatment, rather than wideband pulses. In practice, an applicator can be operated to switch between single frequencies in finely interleaved time slots, if the duration of each slot is small compared to the biological response [22]. This simplifies the complexity of the hardware needed for feeding the HT applicator [38]. The rest of the analysis will therefore be carried out assuming that n_f simultaneous operating frequencies can be independently controlled in phase and amplitude for each of the n_c channels of the array applicator.

TR focusing requires in principle only one EM simulation per virtual source, which makes it attractive in terms of computational resources. Unfortunately, this single simulation is not sufficient to assess the quality of the resulting treatment planning. The HTP quality indicators must in fact be evaluated over the focused SAR distribution (Fig. 1b). Moreover, since the immediate TR solution for HTP might not be optimal or clinically viable, further adjustments might be needed, which would require additional simulations. In view of this, it is more convenient to run a separate simulation for each antenna/channel c in the array, as is the case for EV or PS. The TR solution at any point can then be determined from this set of E-field distributions via a generalized and source-free TR method described later in Sec. 2.2. Denoting with ^{t} the transpose operation (without conjugate), the complex E-field distributions and steering parameters relative to all channels at a certain frequency can be joined into column vectors for compactness:

$$\boldsymbol{p}_f = [\ p_{1,f}\ p_{2,f}\ \ldots\ p_{n_c,f}\ ]^t \qquad \boldsymbol{E}_f = [\ E_{1,f}\ E_{2,f}\ \ldots\ E_{n_c,f}\ ]^t \tag{C.2}$$

2.2 Challenges for TR Focusing in MW-HT

A number of challenges arise when implementing TR as HTP. First of all, the choice of the source location, or focal spot. Intuitively, the source should be placed at the center of the tumor, but this is often hard to define, especially for irregular shapes. The center of mass of the tumor can be picked as an initial guess, but this choice often leads to inhomogeneous or insufficient heating of deep or peripheral tumor areas. Cold-spots in the target volume should be avoided, as they reduce the treatment's efficacy. Better coverage can be achieved, for example, by translating the focal spot progressively towards the internal, deeper part of the target volume [39]. Second, hot-spots arising in healthy tissues must be suppressed, to allow a higher deposition in the target. In order to shift the focus away from these locations, the natural approach under the TR perspective would be to place secondary sources, record their impulse response, and subtract these secondary solutions from the primary one. Taken together, these considerations suggest that an initial TR solution with source at the tumor center can be iteratively improved by shifting the set of complex steering parameters away from hot-spots and towards cold-spots.

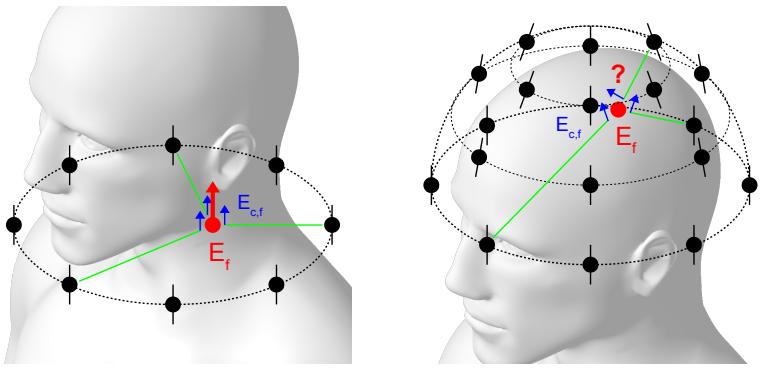

(a) Collar applicator, neck. **(b)** Helmet applicator, brain.

Figure 2: The virtual source polarization problem. In the collar case (a) the main polarization of the fields interfering at the focal spot (red dot) is evident. In the helmet case (b) each antenna contributes to the power loss at the focal spot along a different polarization axis.

A second aspect of TR focusing is the choice of the polarization axis for the virtual source. The polarization problem in vector field focusing has been ad-

dressed in several ways in the literature, also recently [40], [41]. In the case of a cylindrical applicator, the antennas can be aligned to the symmetry axis (Fig. 2a): the virtual source should then also be aligned with this principal axis. In more complex array topologies such as a semi-spherical helmet, the E-field generated by each antenna can vary significantly in polarization, depending on the location of the focal spot (Fig. 2b). The resulting interference is no longer characterized by a single main polarization, and the concept of virtual source becomes inadequate. This concept should then be dropped in favor of the more generalized concept of complex power contribution at the focal spot. We know that the SAR at a location ζ resulting from the superposition of all channel fields at a particular frequency f is given by:

$$SAR_f(\zeta) = \frac{1}{2}\frac{\sigma_f(\zeta)}{\rho(\zeta)} \boldsymbol{p}_f^{*t} \langle \boldsymbol{E}_f^*(\zeta), \boldsymbol{E}_f^t(\zeta) \rangle \boldsymbol{p}_f \tag{C.3}$$

where $\langle \cdot, \cdot \rangle$ denotes the scalar product, while σ_f and ρ are the local material conductivity (frequency-dependent) and density, respectively. The outer product, called *SAR matrix* and denoted $\boldsymbol{Q}_f$, contains information about the complex SAR contributions from each channel irrespective of their polarization directions:

$$\boldsymbol{Q}_f = \frac{1}{2}\frac{\sigma_f}{\rho} \langle \boldsymbol{E}_f^*, \boldsymbol{E}_f^t \rangle \tag{C.4}$$
$$\langle \boldsymbol{E}_f^*, \boldsymbol{E}_f^t \rangle = (\boldsymbol{e}_f^X)^* (\boldsymbol{e}_f^X)^t + (\boldsymbol{e}_f^Y)^* (\boldsymbol{e}_f^Y)^t + (\boldsymbol{e}_f^Z)^* (\boldsymbol{e}_f^Z)^t$$

where a Cartesian coordinate system has been assumed. By construction, $\boldsymbol{Q}_f$ is Hermitian and positive semi-definite. This property allows us to perform an inverse operation and decompose $\boldsymbol{Q}_f$ into an outer product, such that:

$$\boldsymbol{Q}_f = \hat{\boldsymbol{p}}_f^* \hat{\boldsymbol{p}}_f^t \tag{C.5}$$

where $\hat{\boldsymbol{p}}_f$ is a column vector containing the complex contribution of every channel at ζ. The solution $\hat{\boldsymbol{p}}_f$ of the decomposition can be obtained as the only non-singular eigenvector of $\boldsymbol{Q}_f$. The sought set of steering parameters for focusing at ζ in a generalized TR perspective is the complex conjugate of this solution:

$$p_{c,f} = \hat{p}^{*}_{c,f} \tag{C.6}$$

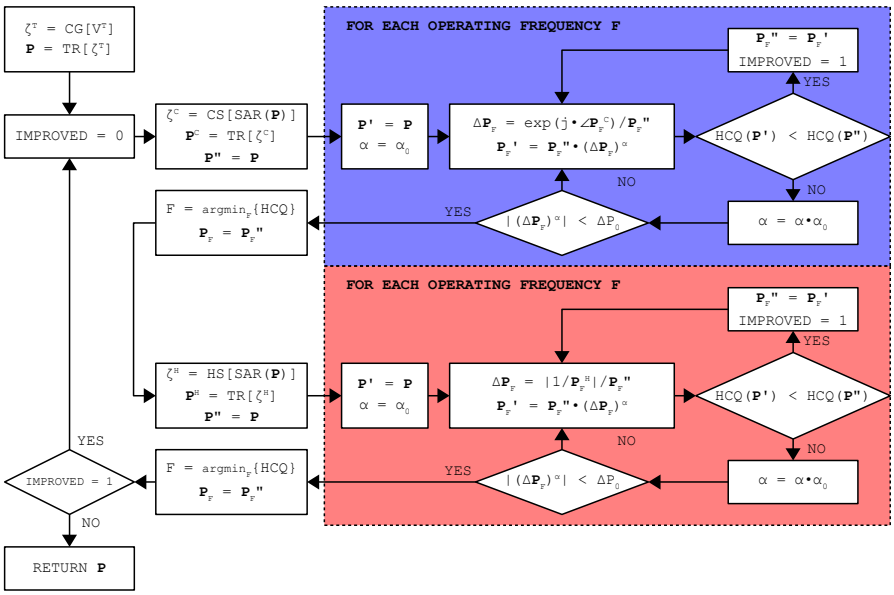

Figure 3: Schematic of the proposed i-TR focusing algorithm. `CG[V^T]` stands for the center of gravity of the target volume. `TR[ζ]` indicates the TR solution obtained by placing the virtual source at ζ, normalized to the amplitude of the strongest channel. The `C` subscript refers to a cold-spot solution, and the blue section represents a cold-spot iteration. The `H` subscript refers to a hot-spot solution, and the red section represents a hot-spot iteration. The `CS` sub-routine determines the location of a cold-spot as the center of mass of the target sub-volume containing the lowest 1-percentile of SAR values. `HS` does the equivalent for the highest 1-percentile in the remaining. Within each iterative section, only the subset of steering parameters relative to the current frequency is changed, while the values relative to the other frequencies are left at the current solution `P`. The HCQ is evaluated over the total SAR.

2.3 Iterative Time-Reversal

The proposed iterative TR (i-TR) focusing technique takes into account all the points discussed above to improve an initial TR solution for HTP. The schematic of the procedure is shown in Fig. 3. The initial solution $\boldsymbol{p}$ is found at the center of mass of the tumor using Eq. C.6. The resulting SAR distribution is analysed and the most prominent cold-spot is identified as the center of mass of the contiguous sub-volume containing the lowest 1-percentile of SAR within the target volume. The TR solution at the cold-spot is calculated and the iterations begin for one frequency at a time, shifting the *phase* of the current parameter set *towards* that of the cold-spot solution $\boldsymbol{p}^C$.

The iterative section aims at minimizing a novel cost function specifically tailored for i-TR, which we will call the *hot-to-cold spot quotient* (HCQ), defined as:

$$\mathrm{HCQ} = \frac{\overline{\mathrm{SAR}}_{\mathrm{R1}}}{\overline{\mathrm{SAR}}_{\mathrm{T1}}} \tag{C.7}$$

where $\overline{\mathrm{SAR}}_{\mathrm{R1}}$ is the average SAR in the sub-volume of remaining healthy tissues containing the highest 1-percentile of SAR values, while $\overline{\mathrm{SAR}}_{\mathrm{T1}}$ is the equivalent for the lowest 1-percentile in the target volume. The individual frequency iteration is carried out stepping by a geometrical factor α, with $0 < \alpha < 1$:

$$\boldsymbol{p}'_f = \boldsymbol{p}''_f \cdot \Delta\boldsymbol{p}_f^{\alpha} \tag{C.8}$$

$$\Delta\boldsymbol{p}_f = \begin{cases} (e^{j\angle \boldsymbol{p}_f^C})/\boldsymbol{p}''_f & \text{, for cold-spot iteration} \\ (|1/\boldsymbol{p}_f^H|)/\boldsymbol{p}''_f & \text{, for hot-spot iteration} \end{cases} \tag{C.9}$$

where j is the imaginary unit, and all operations are intended to be element-wise. The buffer variable $\boldsymbol{p}''_f$, initially set as $\boldsymbol{p}_f$, is replaced by the search direction $\boldsymbol{p}'_f$ only if the stepping was successful, i.e. if the resulting $\mathrm{HCQ}(\boldsymbol{p}')$ is better than the current $\mathrm{HCQ}(\boldsymbol{p}'')$. Note that, while only the subset of steering parameters relative to one frequency is iterated at a time, the assessment of hot-spots, cold-spots and HCQ at each iteration is always carried out over the total SAR distribution:

$$\mathrm{SAR} = \mathrm{SAR}_1 + \mathrm{SAR}_2 + \cdots + \mathrm{SAR}_{n_f} \tag{C.10}$$

If the stepping was not successfull, the step factor α is geometrically reduced and another attempt is made. If the norm of the step $|\Delta \boldsymbol{p}^{\alpha}|$ falls below a threshold value Δp_0 without any improvement on the HCQ, the next frequency is considered and iterated. Once all frequencies have been iterated, only the subset of parameters $\boldsymbol{p}_f$ relative to the frequency that yielded the best improvement in HCQ is updated with $\boldsymbol{p}''_f$.

A similar procedure is then carried out for the hot-spot. The updated SAR distribution is analysed and the most prominent hot-spot is identified as the highest 1-percentile of SAR within the healthy tissues. However this time the *amplitude* of the parameters is shifted *away from* the hot-spot solution $\boldsymbol{p}^H$. If at least one spot iteration was successful in improving the HCQ, a new cold-spot is considered and iterated, and so on. Otherwise, the algorithm terminates.

The parameter Δp_0 is directly related to the desired precision on the steering parameters. We select a precision of 1% ($\Delta p_0 = 0.01$) since RF systems usually do not provide steering accuracy higher than $\pm 5\%$ [42], [43]. The parameter α_0, on the other hand, decides the length of the first iterative step and its subsequent geometrical progression. As shown later in Sec. 4.3, the value of α_0 affects mainly the algorithm's convergence speed and number of iterations, and has almost no effect on the overall accuracy. Its optimal value $\alpha_0 = 0.1$ is determined by means of a sensitivity analysis, and this value is kept throughout all executions reported here.

3 Method

We compare the proposed i-TR technique with eigenvalue (EV), particle swarm (PS), and classic time reversal (TR). The evaluation is carried out in two steps: we first assess the quality of the HTPs via SAR-based indicators, then validate them in terms of resulting thermal distributions. The test cases include 3 inhomogeneous artificial targets of increasing size in the neck region and 2 tumor-filled realistic targets, one in the neck and one in the brain. The thermal validation is carried out only for the realistic targets. The HTP methods are benchmarked in terms of the following quality indicators:

- **HTQ**: hot-spot to target quotient, as defined in [20]:

$$\mathrm{HTQ} = \frac{\overline{\mathrm{SAR}}_{\mathrm{R1}}}{\overline{\mathrm{SAR}}_{\mathrm{T}}} \tag{C.11}$$

  i.e. the ratio between the average SAR in the sub-volume containing the highest 1-percentile SAR among the remaining tissues ($\overline{\mathrm{SAR}}_{\mathrm{R1}}$) and the average SAR in the target volume ($\overline{\mathrm{SAR}}_{\mathrm{T}}$). Values of HTQ around or below 1 are typically considered for clinical treatment.

- **TC**$_x$: iso-SAR target coverage, as defined in [44]:

$$\mathrm{TC}_x = \frac{V_{\mathrm{T}}(x)}{V_{\mathrm{T}}} \quad , \quad V_{\mathrm{T}}(x) \;\mid\; SAR[V_{\mathrm{T}}(x)] \geq x \cdot SAR[V] \tag{C.12}$$

  i.e. the fraction of the target volume V_T where SAR values are above a given fraction x of the SAR peak value in the whole patient volume V. Both the TC_x value and the fraction x are usually expressed as percentage, and the TC_x index is evaluated in this work for $x = 25$ % or $x = 50$ % depending on the model at hand. Values of TC_{25} greater than 75 % are typically considered for clinical treatment.

Both the HTQ and TC indicators are evaluated over the 1g-averaged SAR distribution as detailed in Sec. 3.3. The TR, i-TR, EV and PS focusing algorithms are all implemented in MATLAB® [45]. Field processing steps are parallelised and executed in single precision on a high performance GPU (nVidia Quadro RTX 6000) where possible. We further evaluate the speed and computational cost of each method using the following metrics:

- **Running time,** t_r: time needed for the HTP optimization algorithm to complete, excluding SAR matrix preparations.
- **Number of evaluations,** n_e: how many times the cost function is evaluated by the algorithm (zero for EV and classic TR).

For the thermal validation, whose setup is detailed in Sec. 3.4, the following HTP quality indicators are used to evaluate the resulting temperature distributions:

- **Cumulative histograms**: of the temperature distribution within the target.

- $\mathbf{T}_{50}$: median temperature in the target volume, as defined in [46].

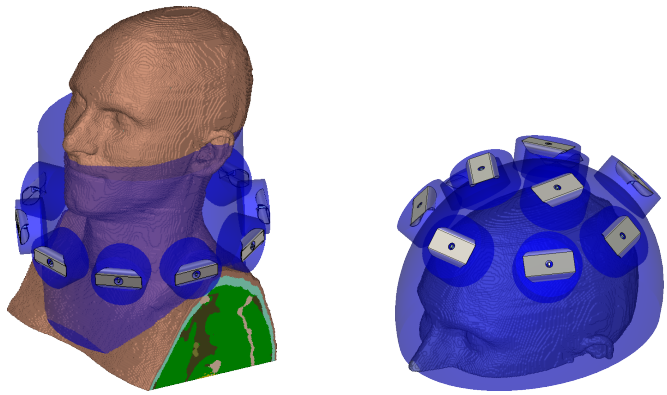

(a) Collar applicator, neck.

(b) Helmet applicator, brain.

Figure 4: The simulation setups for the collar (a) and the helmet (b) applicators, consisting of patient voxel model, water bolus, and 10 SGBT antennas each.

3.1 Applicator array topologies

The HTP algorithms are tested on two array topologies: cylindrical and semi-spherical. The cylindrical applicator (Fig. 4a) is meant for treatment of tumors in the neck region. It consists of 10 radiators arranged on one ring of 20 cm diameter. The radiators are self-grounded bow-tie antennas (SGBT), which work across the range $400-800$ MHz and have been adapted specifically for ultra-wideband MW-HT [47]. A cylindrical water bolus, with average thickness 4 cm, is included between the antennas and the patient to improve matching. The SGBT antennas are further immersed each into a protruding cylindrical extension of the water bolus, to enhance their directivity and reduce cross-coupling between array elements.

The semi-spherical applicator (Fig. 4b) represents a simplified version of a helmet applicator for brain tumors. It consists of 10 SGBT antennas radially arranged from the top of the scalp and following the skull's curvature. The applicator covers only a small part of the head and, as such, can only be

meaningfully used for targeting volumes close to the the skull. This applicator is not optimized for an effective treatment of deep-seated brain tumors, but it is intended for the investigation of the i-TR method's robustness to mixed polarization axes. The average water bolus thickness for this applicator is 1.5 cm.

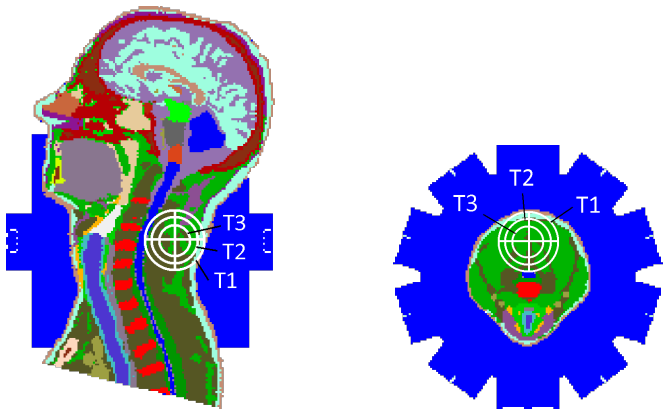

(a) Dorsal, $T_{1,2,3}$, sagittal.

(b) Dorsal, $T_{1,2,3}$, transverse.

Figure 5: Artificial heterogeneous target volumes. The targets are spherical and concentric. They are delineated in white. The volume center is indicated with a cross. Sections are taken at the volume center.

3.2 Human model and target volumes

The *Duke* human voxel model from the IT'IS Foundation [48] is used as virtual patient for both regional treatment plannings. The original resolution of $1\times1\times1$ mm is down-sampled to $2\times2\times2$ mm to spare computational resources. The constant (density) and dispersive (permittivity, conductivity) tissue properties are obtained from the IT'IS Foundation database [49]. A $230\times260\times390$ mm subset of the model is selected to represent the neck region, Fig. 4a. The resulting voxel matrix includes 47 segmented tissues. For the brain applicator, a smaller subset is selected, $230\times260\times138$ mm, Fig. 4b. The resulting voxel matrix includes 31 tissues.

For the preliminary SAR investigation, three spherical target volumes are

Table 1: List of target volumes. The most relevant tissues within the target are reported in percent of volume. For the *artificial* targets: M is muscle, F is fat, O is other. For the *realistic* targets: X is mucous membrane, M is muscle, L is larynx, T is tendon ligament, C is cerebrospinal fluid, G is grey matter, W is white matter, S is skull, O is other.

Label	Region	Volume	Location	Topology	Composition
T_1	Neck	113 ml	Dorsal	Spherical	73% M, 18% F, 09% O
T_2	Neck	48 ml	Dorsal	Spherical	77% M, 21% F, 02% O
T_3	Neck	14 ml	Dorsal	Spherical	78% M, 22% F, 00% O
T_4	Neck	85 ml	Larynx	Concave	25% X, 20% M, 18% L, 13% T
T_5	Brain	30 ml	Meninges	Convex	46% C, 28% G, 22% W, 04% O

defined in MATLAB® after the E-field simulations. As the original dielectric properties within the target volumes are kept, these targets are heterogeneous. In addition to these, two realistic test cases are considered: one in the larynx for the neck applicator and one in the meninges for the brain applicator. These targets are defined before the E-field simulations, and their volumes are filled with a homogeneous material whose properties are determined by taking the weighed average of the materials originally inside. This results in a conservative approach where the tumor does not exhibit increased conductivity. The volume and composition of the 5 targets are described in Table 1 and shown in Fig. 5 and 6. Resulting tumor properties for the realistic cases are reported in Table 2.

In all cases, the target volume is a contiguous shape, as multi-target treatment planning is beyond the scope of the present work. The artificial targets are included to evaluate the i-TR scheme's ability to achieve target coverage and hot-spot suppression for different tumor sizes. The larynx case is included to assess the HTP's ability to target concave shapes with both superficial and deep areas. Note that the trachea lumen creates a cavity in the target volume. The meningioma is included to investigate the case where multiple polarization directions are interfering in the target volume.

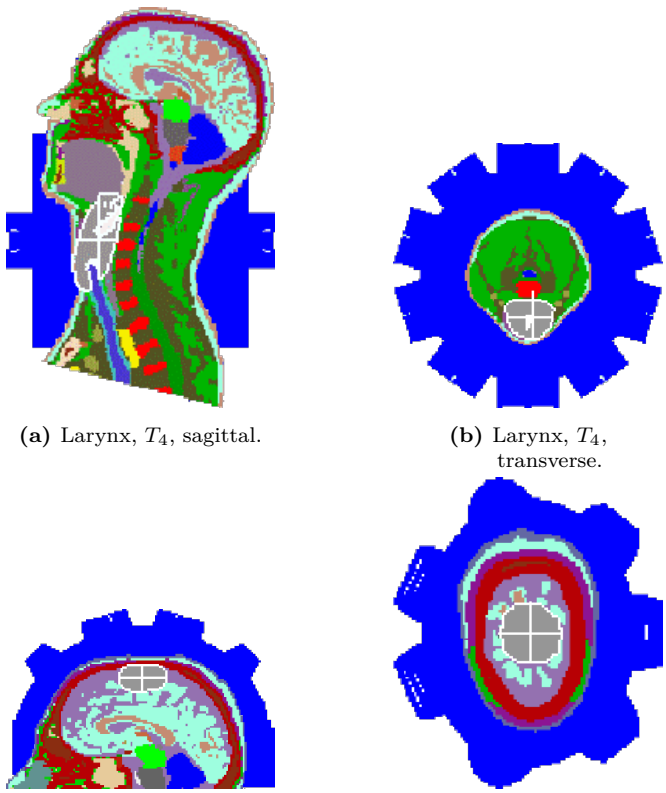

(a) Larynx, T_4, sagittal.

(b) Larynx, T_4, transverse.

(c) Meninges, T_5, sagittal.

(d) Meninges, T_5, transverse.

Figure 6: Realistic homogeneous target volumes. The targets are delineated in white. The volume center is indicated with a cross. Sections are taken at the volume center.

3.3 E-field simulations and SAR computation

The E-field distributions of each antenna within the applicator are obtained numerically using the commercial software CST Microwave Studio® [50]. The software implements an FDTD scheme on a hexahedral mesh with possibility for locally denser sampling grids. The complex geometrical curves of the SGBT antennas are sampled at $0.5/\sqrt{3}$ mm to correctly represent at any angle the 0.5 mm thick copper plate with which they are realized. The mesh resolution within the patient varies between this value and a maximum of 2 mm. Together with the water bolus, this results in $\approx 125/220$ million cells for the collar/helmet setups, respectively. The almost doubled amount of mesh cells for the helmet setup is due to the antenna arrangement occupying more effectively all 3 dimensions in space. Absorbing boundary conditions (PML) are defined for all sides of the computational domain.

Upon import for post-processing in MATLAB®, the E-field distributions are re-sampled to a constant grid resolution of 2 mm. Out of these distributions, the local SAR matrices $Q_f(x, y, z)$ are constructed according to Eq. C.4. This results in 1.1 million matrices for the neck model and 0.3 million for the brain one (considering the patient only). Each element $q_{i,j}(x, y, z)$ is further spatially averaged according to a 1g SAR mass-averaging scheme. The averaging scheme is similar to the *CST Legacy* one as described in [51]: we treat surface voxels by expanding a spherical kernel until the mass of patient tissues within reaches 1g.

3.4 Thermal simulations

To validate the HTP plans, steady-state thermal simulations are performed with CST Microwave Studio®. We consider only the realistic scenarios and only the frequency combination that yields the lowest HTQ after i-TR optimization. This combination would be the one selected for treatment after quickly surveying all possible combinations with i-TR. The thermal properties of the healthy tissues are also taken from the IT'IS database. However, to mimic the hyperthermic stress condition of the body, the muscle's blood flow perfusion is increased by a factor 4 [15], [52]. Moreover, the thermal conductivity of the cerebrospinal fluid is increased by a factor 10 to emulate the convective transport of heat [30]. The tumor thermal properties are calculated as a weighed average of the tissues originally composing its volume, in the

Table 2: Properties of the homogeneous materials filling the target volumes in the realistic cases, obtained as the weighed average of the original materials within the volume. Some properties are adjusted for hyperthermic conditions.

Tumor	ϵ [$\sim$]	σ [$\frac{S}{m}$]	ρ [$\frac{kg}{m^3}$]	k [$\frac{W}{Km}$]	c [$\frac{kJ}{Kkg}$]	ω_b [$\frac{kW}{Km^3}$]	Q_m [$\frac{kW}{m^3}$]
Larynx	47.8	0.674	1088	0.423	3.285	22.033	5.456
Meninges	57.3	1.372	1063	0.535	3.754	17.048	5.478

same way as for the electromagnetic properties. The tumor blood perfusion rate is further diminished by a factor 0.7 to account for the chaotic vascular structure that characterizes neoplasms [52], [53]. The tumor properties are summarized in Table 2.

3.5 Choice of operating frequencies

The set of possible operating frequencies is constructed by stepping 100 MHz within the antenna working range $400 - 800$ MHz, yielding the following set:

$$F = [400, 500, 600, 700, 800]^t \text{ MHz} \tag{C.13}$$

Out of this set, all the single and double frequency combinations are evaluated, resulting in 15 operating frequency settings. This is to highlight potential frequency-dependent phenomena within the patient and to evaluate the i-TR scheme's robustness to different combinations of operating frequencies, while at the same time keeping the amount of test cases at a minimum.

3.6 Implementation of eigenvalue and particle-swarm

The EV implementation is similar to the one used in [54]. It determines via a direct solution the set of steering parameters that maximizes the SAR amplification factor (SAF), defined as the following quadratic ratio:

$$\text{SAF} = \frac{\overline{\text{SAR}}_\text{T}}{\overline{\text{SAR}}_\text{R}} \tag{C.14}$$

where $\overline{\text{SAR}}_\text{T}$ is the average SAR in the target, and $\overline{\text{SAR}}_\text{R}$ is the average SAR in the rest. An important consequence of how Eq. C.14 is constructed

is that only one frequency at a time from any working set can maximize such ratio [21]. The amplitude of the other frequencies must be set to zero, and the only active frequency is the one whose interference pattern best fits the target shape and location. This approach differs substantially from the continuous FIR solution described in [23], which, to the best of the authors' knowledge, is the only published study on wide-band EV beam-forming. Their approach is not applicable here since the spectrum is discrete. Naturally, maximizing the SAF is not the same as minimizing non-linear indicators such as HTQ, which usually correlate better with the resulting thermal dose.

The PS implementation used for this study is the one readily available in MATLAB® (`particleswarm`). The cost function is the HTQ as described at the beginning of this section. In order for PS to properly converge regardless of the problem's complexity [55], some of its settings are made proportional to the number of variables, $n_v = 2 \cdot n_c \cdot n_f$, i.e. phase and amplitude for each channel at each frequency. In particular, the number of particles is set to $10 \cdot n_v$, and the optimization is halted when n_v consecutive iterations have produced a relative change in the objective function smaller than 0.1. Other settings have been kept to their default values. When the `particleswarm` algorithm has completed, the optimization is handed over to a local optimizer (`fmincon`) and the solution is further refined until the relative parameter change falls below 0.01, thus reaching the desired precision of 1 %.

4 Results

Fig. 7 shows a typical i-TR processing and its results for a representative artificial target case. Starting from the classic TR solution, the HCQ is progressively minimized until no further improvement is achieved by either cold- or hot-spot iterations. During this process, the HTQ and TC_{25} vary according to the current solution. In general, HTQ floats around the initial value, while TC_{25} is strongly enhanced within a few iterations. The HCQ value is improved significantly throughout the entire process. This reflects in a more homogeneous SAR distribution within the target and in a reduction of the most relevant hot-spot, which, in this case, is located in the skin layer adjacent to the target. The initial steering parameter amplitudes, Fig. 7b, exhibit the typical TR pattern where each antenna radiates power proportionally to its vicinity to the target. The final amplitude settings clearly demonstrate

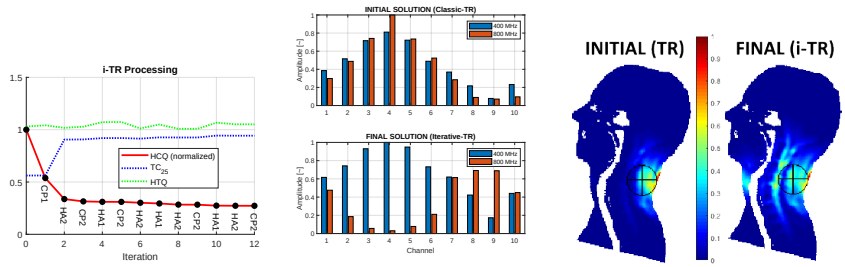

(a) **(b)** **(c)**

Figure 7: Example of i-TR processing of a double-frequency problem, 400 + 800 MHz. T_1 artificial heterogeneous target. (a) values of HCQ (normalized to the initial value), HTQ and TC_{25} at each iteration. Black dot labels report which spot has caused the improvement: `CPn` cold-spot/phase at frequency `n`, `HAn` hot-spot/amplitude. (b) initial and final steering amplitudes for all channels. (c) corresponding SAR distributions (normalized to the highest value). Sagittal section at target center.

how i-TR can exploit different frequencies to cover both superficial and deeper parts of the target volume, as confirmed also by the SAR distribution in Fig. 7c.

4.1 SAR evaluation

SAR-based HTP quality indicators for the artifical test cases are reported in Fig. 8. The lowest HTQ for any given problem and frequency combination is achieved by PS, being configured to minimize this indicator. However, this does not always translate into better coverage. The i-TR returns sensibly higher TC_{25} values in the large and medium cases, at the expense of an increase in HTQ with respect to the initial TR solution. While some solutions become impractical due to this increase, there is always at least one optimal frequency combination where i-TR achieves HTQ ≈ 1 and $TC_{25} \approx 100\%$. In the small target case, i-TR also lowers the HTQ provided by classic TR while achieving remarkably higher TC_{50} values. For this target, which is less heterogeneous than T_1 and T_2 (see Table 1), the solutions provided by PS and i-TR are comparable in quality. EV exhibits consistently high HTQ and poor coverage in all cases.

SAR-based HTP indicators for the realistic targets are reported in Fig. 9.

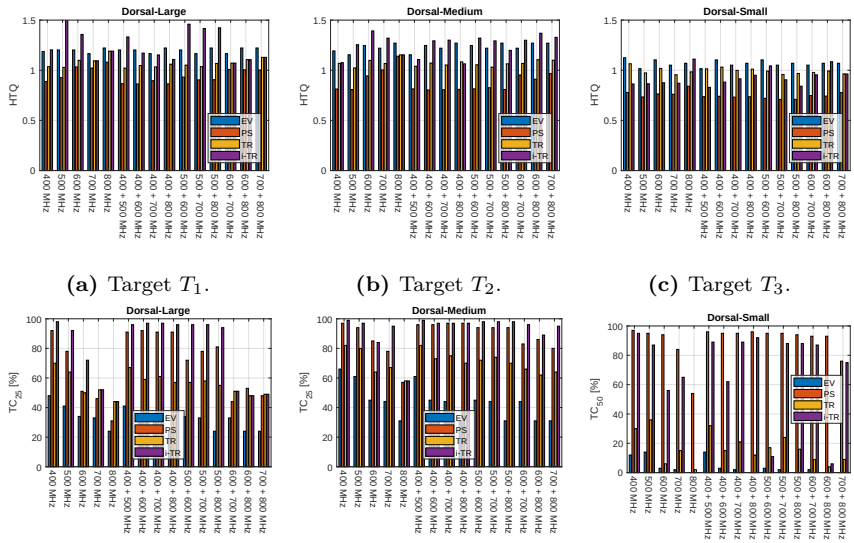

(a) Target T_1. **(b)** Target T_2. **(c)** Target T_3.

(d) Target T_1. **(e)** Target T_2. **(f)** Target T_3.

Figure 8: SAR-based HTP quality indicators in the artificial test cases, for all operating frequency combinations. (a) to (c) report the HTQ while (d) to (f) report target coverage. TC_{50} is shown in (f) due to TC_{25} being 100 % in T_3.

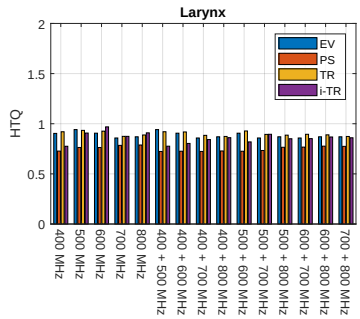

(a) Target T_4.

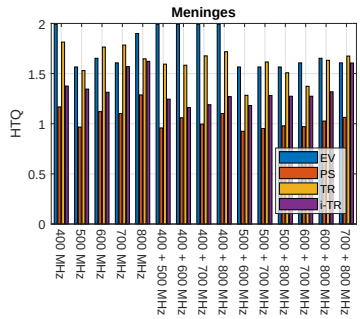

(b) Target T_5.

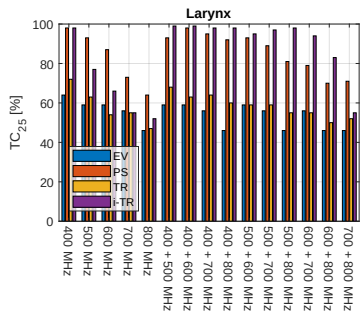

(c) Target T_4.

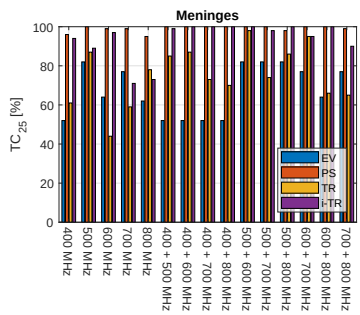

(d) Target T_5.

Figure 9: SAR-based HTP quality indicators in the realistic test cases, for all operating frequency combinations. (a) and (b) report the HTQ while (c) and (d) report target coverage.

Once more, PS returns the lowest HTQ for each case. All algorithms yield comparable HTQ values below 1 in the larynx, while only PS manages to reach values below 1 in the meninges. EV and classic TR perform similarly in the larynx case, achieving acceptable HTQ, but suboptimal coverage. EV fails to provide viable solutions for the meninges, with HTQ always above 1.5, and TC_{25} above threshold only at 500 MHz and 700 MHz. In contrast, i-TR yields HTQ values much closer to the global PS optimum for this case. More importantly, it does so with simultaneous extensive target coverage. In the larynx model, TC_{25} is often higher for i-TR than for PS when more than one frequency is considered. The SAR results for these two realistic cases are further summarized into two combined HCQ - TC_{25} plots in Fig. 10. In both plots, the dual-frequency solutions provided by i-TR are seen to be located near the TC_{25} optimum (100%) and close to PS's global HTQ optimum.

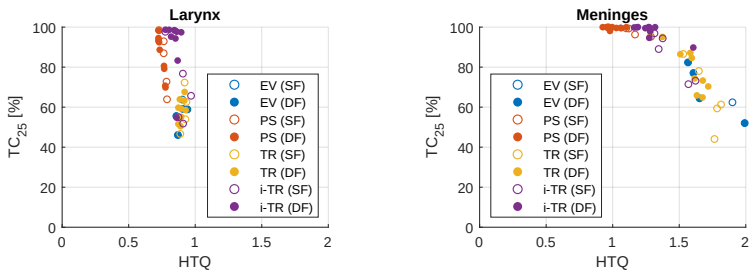

(a) Target T_4. **(b)** Target T_5.

Figure 10: Combined HTQ - TC_{25} plots for the HTP solutions in the realistic test cases. Empty circles denote single-frequency (SF) solutions. Filled circles denote dual-frequency (DF) solutions.

4.2 Performance analysis

Speed performance metrics for the artificial test cases are reported in Fig. 11. Since EV and TR are direct solution methods, they take less than a second to complete. About 6 000 cost function evaluations are needed for PS to return a single-frequency solution, and up to 30 000 in the case of two frequencies. This translates into long execution times, with a typical run taking about 10 minutes for one frequency and 50 minutes for two frequencies. Conversely, i-TR manages to return a single-frequency solution within at most 50 evalua-

tions, and a double-frequency solution in 100 evaluations. This reflects into at most 10 seconds running time in the single-frequency case, and on average 50 seconds for a double-frequency problem. Performance metrics for the realistic cases are not reported since they indicate similar trends.

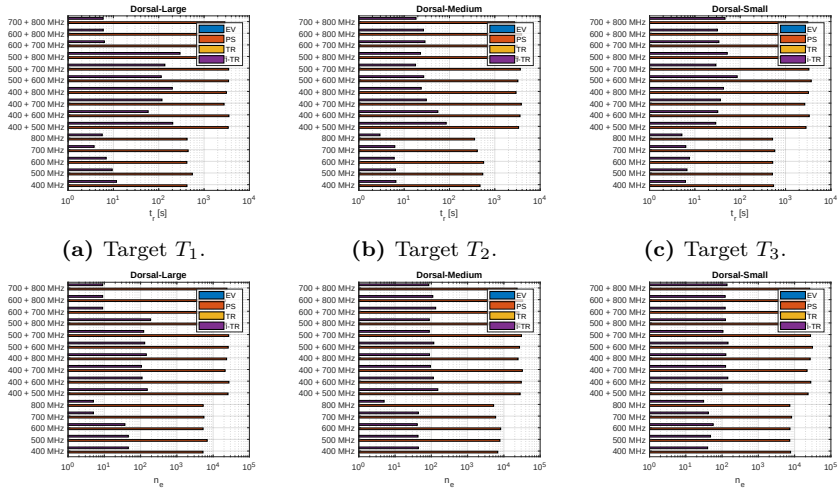

(a) Target T_1. **(b)** Target T_2. **(c)** Target T_3.

(d) Target T_1. **(e)** Target T_2. **(f)** Target T_3.

Figure 11: Algorithm speed performance metrics in the artificial test cases, for all operating frequency combinations, on a X-logarithmic scale. (a) to (c) report the running time while (d) to (f) report the number of cost function evaluations. $t_e \approx 0.5$ s and $n_e = 0$ for both EV and classic TR since they are direct solution methods.

4.3 Sensitivity analysis

The results of the sensitivity analysis with respect to the initial step factor α_0 are reported in Fig. 12. Both HTP quality indicators exhibit negligible variations across the sweep, meaning that the solution provided by i-TR is stable in this respect. A closer look suggests that the optimum is located at the lowest end of the α_0 range. This can be intuitively explained by the fact that smaller stepping allows the algorithm to get closer to the HCQ optimum. High α_0 values exponentially increase the convergence time and computational burden of the algorithm, indicating that the initial classic TR

solution is already close to the optimum and only small steps are needed to improve its HCQ value. On the other hand, both t_r and n_e tend to increase again towards $\alpha_0 = 0$, as a consequence of the step being too small to quickly reach the optimum HCQ. In conclusion, $\alpha_0 = 0.1$ seems to be an appropriate value for this parameter.

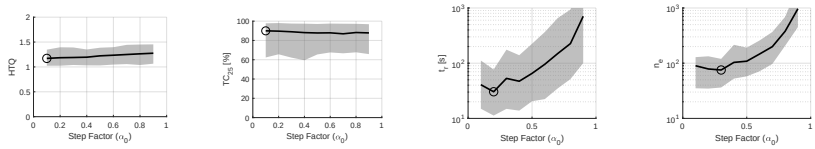

(a) **(b)** **(c)** **(d)**

Figure 12: Analysis of the i-TR algorithm's sensitivity to the stepping parameter α_0. The plots report mean (black line) and standard deviation (gray shade) of all the artificial test cases for all frequency combinations ($n = 45$). The black circle indicates the optimal value across a parametric sweep. (a) and (b) report the SAR-based HTP quality indicators while (c) and (d) report the performance metrics (Y-log plot).

4.4 Thermal validation

Fig. 13 and 14 show the thermal distributions for the realistic cases. It can be seen that both direct solvers, EV and TR, fail to reach therapeutic temperatures in the deeper parts of the tumors. In the larynx case, the trachea acts as a heat barrier between opposing sides of the target volume, whose morphology is toroidal. PS and i-TR manage to overcome this barrier by extending the SAR coverage to the inner side, at the expense of higher average temperatures in the healthy tissues. This higher power deposition, however, does not result in additional hot-spots. i-TR performs better in this sense than PS by gaining half a degree in median temperature, see Table 3. For the meningioma, both EV and TR end up maximizing the peak SAR in the target which results in a focal spot close to the skull. This spot is however mitigated by the cooling effect of the bolus, so that neither high peak temperatures nor sufficient coverage are achieved within the target. Both PS and i-TR shift this main SAR peak deeper in the brain, reaching high median temperatures. i-TR closely follows PS by only half a degree lower T_{50}. These results are further illustrated in the cumulative histograms, Fig. 15.

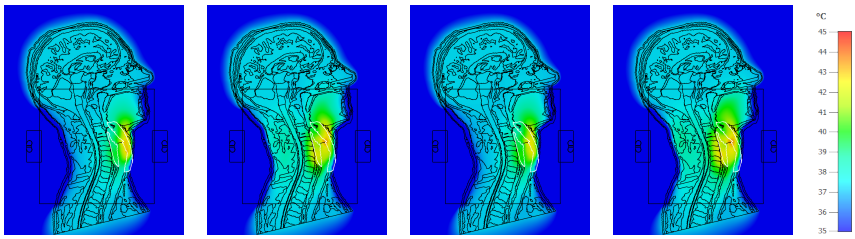

(a) EV. **(b)** PS. **(c)** TR. **(d)** i-TR.

Figure 13: Temperature distributions in the larynx realistic case for all HTP algorithms at $400 + 500$ MHz. Maximum temperature in healthy tissues is 43°C in all cases. The target volume is outlined in white. Sagittal section at tumor center.

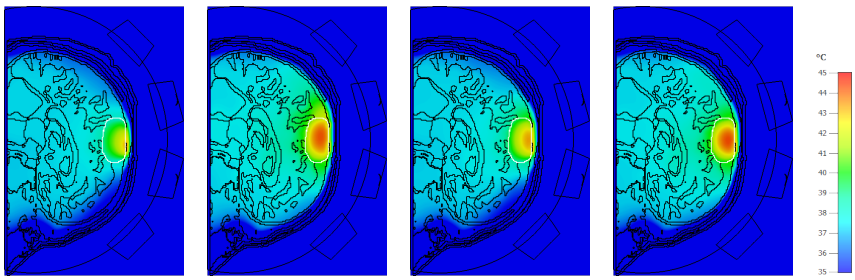

(a) EV. **(b)** PS. **(c)** TR. **(d)** i-TR.

Figure 14: Temperature distributions in the meninges realistic case for all HTP algorithms at $400+600$ MHz. Maximum temperature in healthy tissues is 43°C in all cases. The target volume is outlined in white. Sagittal section at tumor center.

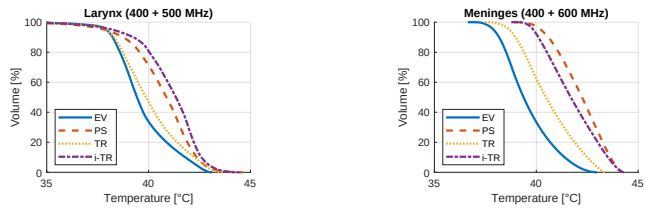

(a) **(b)**

Figure 15: Cumulative histograms of the temperature distribution within the targets.

Table 3: Median temperatures (T_{50}) reached inside the target volume in each of the thermal test cases for all HTP algorithms. Values in °C.

Tumor	EV	PS	TR	i-TR
Larynx	39.43	40.87	39.87	41.34
Meninges	39.37	42.24	40.47	41.69

5 Discussion

Hyperthermia requires an optimal SAR distribution in the patient in terms of raw target power deposition, target coverage, and hot-spot suppression in healthy tissues. Target SAR coverage has in fact been shown to be predictive for the therapeutic outcome of the treatment [56], [57]. To improve on these aspects, the HTQ and the TCx indicators have been proposed and shown to be effective when applied retrospectively to clinical data sets [58], [59]. However, HTQ and TC_x are two different cost functions whose optimal distributions do not coincide. In particular, a single-frequency HTP might yield acceptable HTQ, but poor target coverage. This effect is apparent in Figures 8 and 9: even when the HTQ closely fluctuates around 1, the TC_x exhibits a strong frequency-dependent trend, quickly falling below the acceptance threshold. To satisfy both HTQ < 1 and $TC_x > 75$ %, one must carefully select the optimal operating frequency, which depends on the applicator in use, the patient's anatomy, and the target shape. For the larynx case used in this study, the optimal frequency lies around 400 MHz, while for the meninges 500 MHz appears to be a better choice. This motivates the need for wide-band applicators and for treatment planning tools capable of seeking the best treatment frequency within the available band. Figures 8 and 9 further show that in a multi-frequency setting, the requirements on the HTQ and TC_x can be more easily fulfilled when two frequencies are selected simultaneously. In other words, the multi-frequency approach helps reaching the multiple objectives needed for a successful hyperthermia dose delivery.

The proposed i-TR technique aims at quickly determining such an overall optimal SAR distribution by exploiting the different frequency components to minimize a custom cost function, the HCQ. This cost function is designed to reach the multiple objectives above while enabling a TR-based iterative approach. The SAR-based results, Sec. 4.1, suggest that the method is successful

in finding viable solutions for a given problem, independently of the target's size, location, morphology or composition. They further indicate that the method is robust to problems involving mixed polarization axes. The quality of the i-TR solution can depend on the selected set of operating frequencies, however the high execution speed makes it possible to evaluate all frequency combinations and always determine one viable solution. Note that this solution might not be the global optimum in terms of HCQ. We further point out that, although there is no guarantee of improvement of an initial TR solution by i-TR, the process is stable as it can never return a solution worse than the initial one in terms of HCQ.

The thermal validation, Sec. 4.4, fundamentally confirms the i-TR's ability to provide viable HTP solutions and further emphasizes the difference in HTQ and TC_x as treatment planning goals. In the larynx case, for instance, all HTP algorithms exhibit similar HTQ values below 1 at the selected frequency combination. However, only for i-TR and PS this translates into high thermal doses, thanks to their higher SAR coverage. EV and classic TR fail to fully exploit the applicator's heating capabilities, falling short of 2 °C on average in T_{50} for the two cases. The small improvement in HTQ brought about by PS, negligible at a first glance, results in a significantly higher median tumor temperature. It is however i-TR to perform best in the larynx, with half a degree higher T_{50} than PS. This is likely due to the compromise that HCQ seeks between low HTQ and high coverage. In the meninges, the situation is similar for EV and TR, while i-TR provides again a solution very close to PS, with only half a degree lower T_{50}. While it is not possible to draw general conclusions about the relationship between HTQ, TC_x, HCQ and the resulting temperature distribution due to the limited amount of test cases, the thermal validation indicates that the HTP solutions provided by i-TR can be considered as clinically relevant.

Regarding EV, many improvements have been suggested over the years in an effort to exploit this extremely fast solution method. Works such as those of [19] and [60] apply weighing functions to the SAR distribution in order to reduce the SAR peak in healthy tissues (hot-spots) and improve the SAR homogeneity within the target. The weight distribution itself, however, needs to be determined by means of an iterative procedure. Moreover, these modifications only apply to the single-frequency scenario. In a multi-frequency setting, the fundamental single-frequency limitation of the EV cost function

($\overline{\mathrm{SAR}}_\mathrm{T}/\overline{\mathrm{SAR}}_\mathrm{R}$) needs to be resolved to fully exploit the treatment capabilities of wide-band applicators [21]. Recently, an emerging time- and frequency-multiplexed beam-forming method has been proposed by [26]. The method is based on quadratic programming (QP) and is therefore extremely fast in determining the optimal set of frequencies, steering parameters and temporal sequences that best approximate a specified SAR pattern. However, the method does not determine the optimal SAR pattern in itself. While this is a very powerful approach, we believe that a relevant comparison between applicators should be grounded on clinically relevant HTP quality indicators, such as HTQ and TC_x. These have been shown to correlate with high tumor temperatures [59], which are the ultimate goal in hypethermia. However, since these indicators involve a non-linear step, they cannot be solved for with fast QP-based algorithms.

The proposed i-TR technique runs in nearly real-time even in the case of high-resolution model matrices such as those considered in this study. The 2 mm resolution is necessary to model the thin anatomical features of the vertebrae and the skull, which strongly affect the wave propagation. Current clinical HTP tools for online complaint-adaptive steering use coarse resolutions of 5 mm for 70 MHz and 434 MHz applicators to be able to quickly recompute the steering parameters [6], [16]. For UWB applicators utilizing frequencies up to 800 MHz, this resolution is no longer sufficient, especially when considering tumors in the brain.

We point out that the proposed i-TR technique differs substantially from the iterative time-reversal method developed by Montaldo and colleagues for ultrasound applications [61]. In HIFU, the aim is to restore the sharp TR focal spot after distortions caused by lossy and heterogeneous media. In MW-HT, the problem faced is the opposite: to de-focus the sharp SAR peak caused by TR in order to achieve better coverage across the whole target volume. As a final consideration, we note that the i-TR implementation described in this paper is not unique. For example, the *cold-spot* $\rightarrow$ *hot-spot* order in the iterative scheme, Fig. 3, could be swapped. Similarly, the identification of hot- and cold-spots could be performed right before each spot iteration, as done here, or only once before both iterations. During internal tests, we could not identify any major effects of these choices on the HTP outcome.

6 Conclusion

The proposed i-TR beam-forming technique is shown to deliver HTP solutions equivalent to those provided by global optimizers such as particle swarm, while being orders of magnitude faster. Results indicate that the method is robust to different array and target configurations. The custom HCQ cost function solved for by the iterative method leads to solutions that exhibit a good compromise between raw power deposition in the tumor, hot-spot suppression in healthy tissues, and target coverage even in deeper regions. Overall, the described i-TR technique provides the means for fast comparisons of a large number of potential array configurations and frequency combinations to optimally treat a given patient. In a clinical setting, i-TR might be further extended for use as a real-time steering parameter re-optimization procedure upon localized complaint from the patient.

Acknowledgement

This work was financially supported by the VINN EXcellence Center of ChaseOn (Chalmers Antenna Systems) and The Swedish Childhood Cancer Fund.

References

[1] P. B. Elming, B. S. Sørensen, A. L. Oei, *et al.*, "Hyperthermia: The optimal treatment to overcome radiation resistant hypoxia," *Cancers*, vol. 11, no. 1, p. 60, 2019.

[2] M. Paulides, H. D. Trefná, S. Curto, and D. Rodrigues, "Recent technological advancements in radiofrequency-and microwave-mediated hyperthermia for enhancing drug delivery.," *Advanced Drug Delivery Reviews*, 2020.

[3] N. Datta, S. G. Ordóñez, U. Gaipl, *et al.*, "Local hyperthermia combined with radiotherapy and-/or chemotherapy: Recent advances and promises for the future," *Cancer treatment reviews*, vol. 41, no. 9, pp. 742–753, 2015.

[4] N. Cihoric, A. Tsikkinis, G. van Rhoon, *et al.*, "Hyperthermia-related clinical trials on cancer treatment within the clinicaltrials. gov registry," *International journal of hyperthermia*, vol. 31, no. 6, pp. 609–614, 2015.

[5] N. R. Datta, S. Rogers, S. G. Ordóñez, E. Puric, and S. Bodis, "Hyperthermia and radiotherapy in the management of head and neck cancers: A systematic review and meta-analysis," *International Journal of Hyperthermia*, vol. 32, no. 1, pp. 31–40, 2016.

[6] H. P. Kok, L. Korshuize-van Straten, A. Bakker, *et al.*, "Online adaptive hyperthermia treatment planning during locoregional heating to suppress treatment-limiting hot spots," *International Journal of Radiation Oncology* Biology* Physics*, vol. 99, no. 4, pp. 1039–1047, 2017.

[7] M. Paulides, J. Bakker, M. Linthorst, *et al.*, "The clinical feasibility of deep hyperthermia treatment in the head and neck: New challenges for positioning and temperature measurement," *Physics in Medicine & Biology*, vol. 55, no. 9, p. 2465, 2010.

[8] S. Gavazzi, A. L. van Lier, C. Zachiu, *et al.*, "Advanced patient-specific hyperthermia treatment planning," *International Journal of Hyperthermia*, vol. 37, no. 1, pp. 992–1007, 2020.

[9] H. Kok, P. Wust, P. R. Stauffer, F. Bardati, G. Van Rhoon, and J. Crezee, "Current state of the art of regional hyperthermia treatment planning: A review," *Radiation Oncology*, vol. 10, no. 1, p. 196, 2015.

[10] M. M. Paulides, P. R. Stauffer, E. Neufeld, *et al.*, "Simulation techniques in hyperthermia treatment planning," *International Journal of Hyperthermia*, vol. 29, no. 4, pp. 346–357, 2013.

[11] R. Canters, P. Wust, J. Bakker, and G. Van Rhoon, "A literature survey on indicators for characterisation and optimisation of sar distributions in deep hyperthermia, a plea for standardisation," *International Journal of Hyperthermia*, vol. 25, no. 7, pp. 593–608, 2009.

[12] H. P. Kok, J. Gellermann, C. A. van den Berg, P. R. Stauffer, J. W. Hand, and J. Crezee, "Thermal modelling using discrete vasculature for thermal therapy: A review," *International Journal of Hyperthermia*, vol. 29, no. 4, pp. 336–345, 2013.

[13] R. A. Canters, M. M. Paulides, M. F. Franckena, J. van der Zee, and G. C. van Rhoon, "Implementation of treatment planning in the routine clinical procedure of regional hyperthermia treatment of cervical cancer: An overview and the Rotterdam experience," *International journal of hyperthermia*, vol. 28, no. 6, pp. 570–581, 2012.

[14] R. Canters, M. Paulides, M. Franckena, J. Mens, and G. Van Rhoon, "Benefit of replacing the sigma-60 by the sigma-eye applicator," *Strahlentherapie und Onkologie*, vol. 189, no. 1, pp. 74–80, 2013.

[15] M. De Greef, H. Kok, D. Correia, A. Bel, and J. Crezee, "Optimization in hyperthermia treatment planning: The impact of tissue perfusion uncertainty," *Medical physics*, vol. 37, no. 9, pp. 4540–4550, 2010.

[16] Z. Rijnen, J. F. Bakker, R. A. Canters, *et al.*, "Clinical integration of software tool vedo for adaptive and quantitative application of phased array hyperthermia in the head and neck," *International journal of Hyperthermia*, vol. 29, no. 3, pp. 181–193, 2013.

[17] M. Böhm, J. Kremer, and A. Louis, "Efficient algorithm for computing optimal control of antennas in hyperthermia," *Surveys Math. Indust*, vol. 3, no. 4, pp. 233–251, 1993.

[18] F. Bardati, A. Borrani, A. Gerardino, and G. A. Lovisolo, "SAR optimization in a phased array radiofrequency hyperthermia system," *IEEE Transactions on biomedical engineering*, vol. 42, no. 12, pp. 1201–1207, 1995.

[19] T. Köhler, P. Maass, P. Wust, and M. Seebass, "A fast algorithm to find optimal controls of multiantenna applicators in regional hyperthermia," *Physics in Medicine & Biology*, vol. 46, no. 9, p. 2503, 2001.

[20] R. Canters, M. Franckena, J. van der Zee, and G. Van Rhoon, "Optimizing deep hyperthermia treatments: Are locations of patient pain complaints correlated with modelled SAR peak locations?" *Physics in Medicine & Biology*, vol. 56, no. 2, p. 439, 2010.

[21] M. Zanoli and H. D. Trefná, "Suitability of eigenvalue beam-forming for discrete multi-frequency hyperthermia treatment planning," *Medical Physics*, vol. 48, no. 11, pp. 7410–7426, 2021.

[22] H. D. Trefná, B. Martinsson, T. Petersson, *et al.*, "Multifrequency approach in hyperthermia treatment planning: Impact of frequency on sar distribution in head and neck," in *2017 11th European Conference on Antennas and Propagation (EUCAP)*, IEEE, 2017, pp. 3710–3712.

[23] M. Converse, E. J. Bond, B. Veen, and C. Hagness, "A computational study of ultra-wideband versus narrowband microwave hyperthermia for breast cancer treatment," *IEEE transactions on microwave theory and techniques*, vol. 54, no. 5, pp. 2169–2180, 2006.

[24] H. D. Trefná, J. Vrba, and M. Persson, "Evaluation of a patch antenna applicator for time reversal hyperthemia," *International Journal of Hyperthermia*, vol. 26, no. 2, pp. 185–197, 2010.

[25] G. G. Bellizzi, L. Crocco, G. M. Battaglia, and T. Isernia, "Multifrequency constrained SAR focusing for patient specific hyperthermia treatment," *IEEE Journal of Electromagnetics, RF and Microwaves in Medicine and Biology*, vol. 1, no. 2, pp. 74–80, 2017.

[26] A. Kuehne, E. Oberacker, H. Waiczies, and T. Niendorf, "Solving the time-and frequency-multiplexed problem of constrained radiofrequency induced hyperthermia," *Cancers*, vol. 12, no. 5, p. 1072, 2020.

[27] P. Takook, M. Persson, and H. D. Trefná, "Performance evaluation of hyperthermia applicators to heat deep-seated brain tumors," *IEEE Journal of Electromagnetics, RF and Microwaves in Medicine and Biology*, vol. 2, no. 1, pp. 18–24, 2018.

[28] L. Winter, C. Oezerdem, W. Hoffmann, *et al.*, "Thermal magnetic resonance: Physics considerations and electromagnetic field simulations up to 23.5 tesla (1ghz)," *Radiation Oncology*, vol. 10, no. 1, pp. 1–12, 2015.

[29] P. S. Yarmolenko, E. J. Moon, C. Landon, *et al.*, "Thresholds for thermal damage to normal tissues: An update," *International Journal of Hyperthermia*, vol. 27, no. 4, pp. 320–343, 2011.

[30] G. Schooneveldt, H. D. Trefná, M. Persson, *et al.*, "Hyperthermia treatment planning including convective flow in cerebrospinal fluid for brain tumour hyperthermia treatment using a novel dedicated paediatric brain applicator," *Cancers*, vol. 11, no. 8, p. 1183, 2019.

[31] B. Guo, L. Xu, and J. Li, "Time reversal based microwave hyperthermia treatment of breast cancer," *Microwave and Optical Technology Letters*, vol. 47, no. 4, pp. 335–338, 2005.

[32] H. D. Trefná, J. Vrba, and M. Persson, "Time-reversal focusing in microwave hyperthermia for deep-seated tumors," *Physics in Medicine & Biology*, vol. 55, no. 8, p. 2167, 2010.

[33] M. Fink, G. Montaldo, and M. Tanter, "Time reversal acoustics," in *IEEE Ultrasonics Symposium, 2004*, IEEE, vol. 2, 2004, pp. 850–859.

[34] J.-L. Thomas and M. A. Fink, "Ultrasonic beam focusing through tissue inhomogeneities with a time reversal mirror: Application to transskull therapy," *IEEE Transactions on Ultrasonics, Ferroelectrics, and Frequency Control*, vol. 43, no. 6, pp. 1122–1129, 1996.

[35] G. Lerosey, J. De Rosny, A. Tourin, A. Derode, G. Montaldo, and M. Fink, "Time reversal of electromagnetic waves," *Physical review letters*, vol. 92, no. 19, p. 193 904, 2004.

[36] P. Takook, H. D. Trefná, A. Fhager, and M. Persson, "Evaluation of the 3D time reversal method for hyperthermia treatment planning in head and neck tumors," in *2015 9th European Conference on Antennas and Propagation (EuCAP)*, IEEE, 2015, pp. 1–5.

[37] N. Leduc, K. Okita, K. Sugiyama, S. Takagi, and Y. Matsumoto, "Focus control in HIFU therapy assisted by time-reversal simulation with an iterative procedure for hot spot elimination," *Journal of Biomechanical Science and Engineering*, vol. 7, no. 1, pp. 43–56, 2012.

[38] H. D. Trefná, P. Togni, R. Shiee, J. Vrba, and M. Persson, "Design of a wideband multi-channel system for time reversal hyperthermia," *International Journal of Hyperthermia*, vol. 28, no. 2, pp. 175–183, 2012.

[39] P. Takook, H. Dobsicek Trefna, X. Zeng, A. Fhager, and M. Persson, "A computational study using time reversal focusing for hyperthermia treatment planning," *Progress In Electromagnetics Research*, vol. 73, pp. 117–130, 2017.

[40] D. A. Iero, L. Crocco, T. Isernia, and E. Korkmaz, "Optimal focused electromagnetic hyperthermia treatment of breast cancer," in *2016 10th European Conference on Antennas and Propagation (EuCAP)*, IEEE, 2016, pp. 1–2.

[41] G. Battaglia, A. Morabito, R. Palmeri, and T. Isernia, "Constrained focusing of vector fields intensity in near zone and/or complex scenarios as a low-dimensional global optimization," *Journal of Electromagnetic Waves and Applications*, vol. 34, no. 15, pp. 1977–1989, 2020.

[42] M. Paulides, J. Bakker, E. Neufeld, *et al.*, "The HYPERcollar: A novel applicator for hyperthermia in the head and neck," *International Journal of Hyperthermia*, vol. 23, no. 7, pp. 567–576, 2007.

[43] P. Wust, H. Fähling, T. Helzel, *et al.*, "Design and test of a new multi-amplifier system with phase and amplitude control," *International journal of hyperthermia*, vol. 14, no. 5, pp. 459–477, 1998.

[44] P. Togni, Z. Rijnen, W. Numan, *et al.*, "Electromagnetic redesign of the hypercollar applicator: Toward improved deep local head-and-neck hyperthermia," *Physics in Medicine & Biology*, vol. 58, no. 17, p. 5997, 2013.

[45] The MathWorks Inc., Natick, Massachusetts, "MATLAB R2019," 2019.

[46] D. Fatehi, J. Van Der Zee, A. Notenboom, and G. C. van Rhoon, "Comparison of intratumor and intraluminal temperatures during locoregional deep hyperthermia of pelvic tumors," *Strahlentherapie und Onkologie*, vol. 183, no. 9, pp. 479–486, 2007.

[47] P. Takook, M. Persson, J. Gellermann, and H. D. Trefná, "Compact self-grounded bow-tie antenna design for an uwb phased-array hyperthermia applicator," *International Journal of Hyperthermia*, vol. 33, no. 4, pp. 387–400, 2017.

[48] M.-C. Gosselin, E. Neufeld, H. Moser, *et al.*, "Development of a new generation of high-resolution anatomical models for medical device evaluation: The Virtual Population 3.0," *Physics in Medicine & Biology*, vol. 59, no. 18, p. 5287, 2014.

[49] P. Hasgall, F. Di Gennaro, C. Baumgartner, *et al.*, *IT'IS Database for thermal and electromagnetic parameters of biological tissues*, version 4.0, May 2018.

[50] Dassault Systèmes SE, Vélizy-Villacoublay, France, *CST Studio Suite 2019*, 2019.

[51] N. Qi, M. Zhang, T. Wittig, and A. Prokop, "Application of CST time domain algorithm in the electromagnetic simulation standard of the SAR for mobile phone," in *2008 International Conference on Microwave and Millimeter Wave Technology*, IEEE, vol. 4, 2008, pp. 1717–1720.

[52] J. Lang, B. Erdmann, and M. Seebass, "Impact of nonlinear heat transfer on temperature control in regional hyperthermia," *IEEE Transactions on Biomedical Engineering*, vol. 46, no. 9, pp. 1129–1138, 1999.

[53] C. W. Song, "Effect of local hyperthermia on blood flow and microenvironment: A review," *Cancer research*, vol. 44, no. 10 Supplement, 4721s–4730s, 1984.

[54] B. Guérin, J. F. Villena, A. G. Polimeridis, *et al.*, "Computation of ultimate SAR amplification factors for radiofrequency hyperthermia in non-uniform body models: Impact of frequency and tumour location," *International Journal of Hyperthermia*, vol. 34, no. 1, pp. 87–100, 2018.

[55] A. P. Piotrowski, J. J. Napiorkowski, and A. E. Piotrowska, "Population size in particle swarm optimization," *Swarm and Evolutionary Computation*, vol. 58, p. 100 718, 2020.

[56] H. K. Lee, A. G. Antell, C. A. Perez, *et al.*, "Superficial hyperthermia and irradiation for recurrent breast carcinoma of the chest wall: Prognostic factors in 196 tumors.," *International journal of radiation oncology, biology, physics*, vol. 40, no. 2, pp. 365–375, 1998.

[57] R. J. Myerson, C. A. Perez, B. Emami, *et al.*, "Tumor control in long-term survivors following superficial hyperthermia," *International Journal of Radiation Oncology* Biology* Physics*, vol. 18, no. 5, pp. 1123–1129, 1990.

[58] M. M. Paulides, G. M. Verduijn, and N. Van Holthe, "Status quo and directions in deep head and neck hyperthermia," *Radiation Oncology*, vol. 11, no. 1, p. 21, 2016.

[59] G. G. Bellizzi, T. Drizdal, G. C. van Rhoon, L. Crocco, T. Isernia, and M. M. Paulides, "Predictive value of sar based quality indicators for head and neck hyperthermia treatment quality," *International Journal of Hyperthermia*, vol. 36, no. 1, pp. 455–464, 2019.

[60] R. Mestrom, J. Van Engelen, M. Van Beurden, M. Paulides, W. Numan, and A. Tijhuis, "A refined eigenvalue-based optimization technique for hyperthermia treatment planning," in *The 8th European Conference on Antennas and Propagation (EuCAP 2014)*, IEEE, 2014, pp. 2010–2013.

[61] G. Montaldo, M. Tanter, and M. Fink, "Real time inverse filter focusing through iterative time reversal," *The Journal of the Acoustical Society of America*, vol. 115, no. 2, pp. 768–775, 2004.

PAPER D

Antenna arrangement in UWB helmet brain applicators for deep microwave hyperthermia

Massimiliano Zanoli, Hana Dobšíček Trefná

Submitted to Cancers
15 November 2022

The layout has been revised.

Abstract

Deep microwave hyperthermia (MW-HT) applicators are typically designed as narrow-band conformal antenna arrays with equally spaced elements, arranged in one or more rings. This solution, while adequate for most body regions, might be sub-optimal for brain treatments. The introduction of ultra wide-band semi-spherical applicators, with elements arranged around the head and not necessarily aligned, has the potential to enhance the selective thermal dose delivery in this challenging anatomical region. However, the additional degrees of freedom in this design make the problem non-trivial. We address this by treating the antenna arrangement as a global SAR-based optimization process aiming at maximizing target coverage and hot-spot suppression in a given patient. To enable the quick evaluation of a certain arrangement, we propose a novel E-field interpolation technique that calculates the field due to an antenna at any location around the scalp from a limited number of initial simulations. We evaluate the approximation error against full array simulations. We demonstrate the design technique in the optimization of a helmet applicator for the treatment of a large medulloblastoma in a paediatric patient. The optimized applicator achieves 0.3 $°C$ higher T90 than a conventional ring applicator with the same number of elements.

1 Introduction

Local hyperthermia for cancer treatment consists in the selective increase of the tumor temperature to $40 \sim 44°C$ for about an hour [1]. In combination with radio- or chemo-therapy, the technique has been shown to enhance the therapeutic outcome for several tumor types in clinical trials [1]–[3]. Conformal phased arrays are used in microwave (MW) hyperthermia (HT) to non-invasively deliver the prescribed thermal dose to a tumor seated deep in the body [4]. In this process, it is of paramount importance to subject the target volume to a high and uniform temperature increase while keeping the

surrounding healthy tissues within physiologically tolerated temperatures [5].

External MW-HT has been successfully applied to targets in the pelvis and the head and neck with remarkable results. To date, however, no clinical applications in the treatment of brain tumors have been reported, despite early encouraging results obtained with interstitial techniques [6]. The implementation of MW-HT for the treatment of solid brain tumors could be particularly beneficial in paediatric patients, where the incidence of such malignancies is the highest [7]. Current treatment modalities based on radiotherapy are known to cause long term disorders in survivors [8]. There is thus a strong motivation for the development of brain applicators and the introduction of hyperthermia as a means to lower the ionizing dose while maintaining the same clinical output.

Local heating of tissues in the head is a challenging task due to the presence of critical organs and their extra sensitivity to hyperthermic temperatures [9]. Ideally, the therapeutic range of $40 \sim 44°C$ should be reached everywhere in the tumor, while healthy tissues should not exceed $42°C$. Particular care should be devoted to avoiding MW radiation in the eyes [10]. Unfortunately, radio-frequency (RF) waves in the MW range are known to be easily absorbed by biological tissues [11], resulting in poor penetration depth. This is especially true for the cerebrospinal fluid (CSF) due to its high conductivity at these frequencies [12]. The enclosure of the skull (cortical bone) adds to the complication as its dielectric contrast causes irregular wave scattering and multiple reflections. For these reasons, additional efforts must be spent in ensuring that the applicator can reliably target the tumor while minimizing losses in healthy tissue. The latter may result in the formation of hot-spots, which are known to be the limiting factor for the maximum achieved tumor temperature during a treatment session [13].

In a typical MW-HT applicator design, the array is a conformal ring of equally spaced antennas immersed in a water bolus, which fills the gap between the antennas and the patient's skin. The bolus realizes a dielectric match for an increased power transfer to the body and simultaneously cools off the first layer of tissue where the electromagnetic losses are the strongest [14]. Several groups in the past decades have investigated the relationship between the array design parameters and the resulting ability of the applicator to selectively heat tumors in the pelvis and the neck. These include: operating frequency, array topology (usually ring), distance between antennas, number of antennas, their

distance from the body [15]–[19]. For brain tumors, external MW-HT has not yet been clinically tested, and the few available non-invasive heating solutions rely on magnetic nano-particles or focused ultra-sound [20]. More recently, however, researches have begun investigating the feasibility of MW-HT in this anatomical region [21], [22]. Preliminary results suggest that high-quality heating can be better achieved when the array configuration is customized to the specific tumor location, shape and size [23].

In this work, we attempt to go beyond the classical single-frequency ring array configuration and exploit the spherical morphology of the head to develop a ultra-wideband helmet applicator ($250 \sim 500\ MHz$). In doing so, we relax the constraints of fixed distance between the antennas and of their mutual alignment. We treat the antenna arrangement around the surface of the scalp as a global optimization problem where each element's location is left as a degree of freedom. At each iteration of the optimization algorithm, we determine the E-field due to each antenna in the array as the interpolation of a grid of simulated individual antennas at fixed locations. As cost-function for the assessment of a particular array configuration we utilize a novel metric, the hot-to-cold spot quotient (HCQ), which is based on the specific absorption rate (SAR) distribution and has been shown to correlate well with the resulting temperature increase in deeply seated targets [24], [25]. We demonstrate the procedure in the design of several helmet applicators of increasing number of elements for the treatment of a paediatric patient with a large medulloblastoma. We assess the quality of the interpolated field by analyzing the approximation error when compared to an actual simulation. Finally, we quantitatively compare the optimized, semi-spherical arrays to classical elliptical designs of the same order, by developing full thermal treatment plans for each solution.

2 Method

2.1 Patient model

The patient is a 13 years old male with a 126 ml medullo-blastoma in the dorsal area of the brain, shown in Fig. 1. The tumor is relatively large and extends from the medulla to the skull. The challenge in this patient is due to the hyperthermia target volume (HTV) presenting both superficial and deep

regions. The model is obtained via MRI scans with 1 mm resolution. The raw data is subsequently segmented by a trained oncologist into 10 distinct tissues: skin, muscle, bone (cortical), pharynx, cerebrospinal fluid, brain (grey matter), brain (white matter), eye (vitreous humor), cartilage, and tumor. The rostral part of the model, below the brain stem, is filled with muscle to emulate the presence of the rest of the body for accurate wave propagation, while reducing the segmentation complexity.

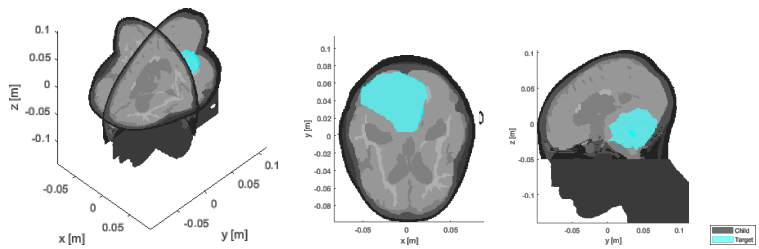

(a) 3D View **(b)** XY View **(c)** YZ View

Figure 1: Sections of the segmented patient model (gray) with superimposed target volume (cyan).

2.2 Antenna and bolus design

The array elements utilized in our applicator design are self-grounded bow-tie (SGBT) antennas [26], Fig. 2. The geometrical parameters of the antennas are optimized to obtain a stable impedance, radiation pattern, and insertion loss above 10 dB across the whole $250 \sim 500$ MHz band when positioned at a distance of ≈ 5 cm from the head (measured at the antenna ground plate). The water bolus shape is obtained by fitting a spheroid over a cloud of points randomly located around the scalp and offset by ≈ 5 cm, as shown in Fig. 3. The resulting spheroid has a different radius in each direction: 12.5 cm along the x axis, 14.2 cm along y, and 14.4 cm along z. The spheroid is trimmed just above the nostrils to provide an opening for breathing. Each antenna is placed with its background plate lying as far as possible from the patient while preventing the metal from protruding out of the water.

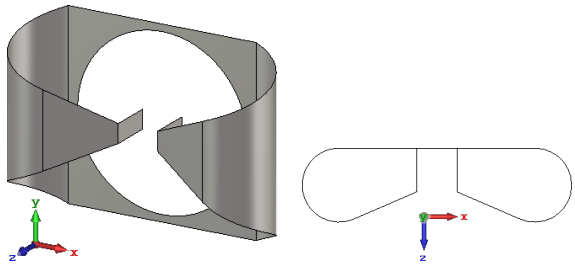

(a) 3D View **(b)** XZ View

Figure 2: Self-grounded bow-tie antenna optimized for the $250 \sim 500\ MHz$ band. The antenna's polarization axis u is aligned with the x axis (red), while its main directivity axis w is aligned with the z axis (blue). The center of the antenna's local coordinate system corresponds to the center of its ground plate, which is also the center of the circular feed opening. The overall dimensions are 8.7 cm along x, 6.2 cm along y, and 2.4 cm along z.

2.3 Numerical simulations

Electromagnetic (EM) simulations are performed in COMSOL Multiphysics® 5.6 [27]. To reduce the computational burden for the simulation of the interpolation grid (Section 2.5), the patient model is down-sampled to 4 mm using a winner-takes-all strategy [28]. This corresponds to approximately $\lambda/18$ in the tissue with highest permittivity (CSF), where λ is the wavelength at the highest considered frequency (500 MHz). A regular hexahedral mesh is assembled in the patient respecting this step, while the water bolus and the surrounding air background are discretized with a tetrahedral mesh whose resolution varies from $\lambda/30$ at the antenna feed and metal corners to $\lambda/5$ in the bulk. The antennas are modelled as sheets of perfect electric conductor (PEC) and excited via a TEM port. Absorbing conditions (PML) are defined at the domain boundaries. Dispersive healthy tissue properties are retrieved from the IT'IS database [12]. Dispersive tumor properties are obtained as an average of all malignant tissue properties reported in [29], as recommended by [30].

Thermal (TH) simulations are performed in the same software. The steady-state temperature distribution is determined for each final applicator design. The patient model is added and meshed in the same fashion as for the EM

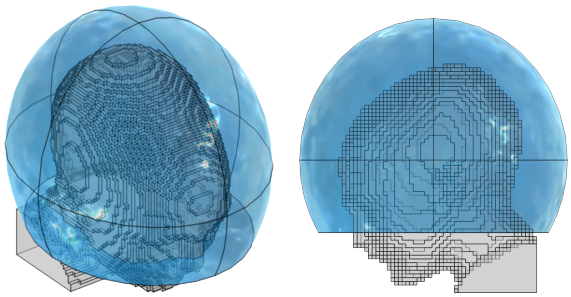

(a) 3D View **(b)** YZ View

Figure 3: Patient model (gray) with water bolus shape (blue). The spheroid is clipped right above the shoulders.

simulation. We add heat flux boundary conditions to model the convective extraction of heat at the interface between patient and air or water. The chosen convection coefficient between skin and air is 8 $W/m^2/K$ [31], while the coefficient between skin and water is 100 $W/m^2/K$ [14]. The air temperature is set to 20 $°C$. Due to the proximity of the tumor to the surface, the water bolus directly affects the temperatures in the target volume [14]. Therefore, the water temperature is set to a higher 30 $°C$. Thermal properties are once more obtained from the IT'IS database for each healthy tissue, while the following properties are used for the tumor [30]: density $\rho = 1090\ kg/m^3$, specific heat capacity $c_p = 3421\ J/kg/K$, and thermal conductivity $\kappa = 0.49\ W/m/K$.

In the TH simulation, the EM losses are added as a distributed term in the bio-heat equation [32]. This term is obtained from the array's E-field distribution at each frequency (E_f) as shaped by the treatment planning optimization stage (Section 2.4) and obtained by a full array simulation (no interpolation involved):

$$\mathrm{PLD} = \kappa \sum_f \frac{1}{2} \sigma_f |E_f|^2 \tag{D.1}$$

where PLD stands for power loss density $[W/m^3]$ and κ is a scaling factor. Note that, unlike the SAR distribution in Section 2.4, the PLD distribution is not smoothed out nor masked. The value of κ is determined by a local gradient descent optimization whose goal is to obtain a maximum temperature in the healthy tissue equal to 42 $°C$, to respect the toxicity limits in the

central nervous system [9]. The resulting temperature distribution in the target volume is assessed by means of the T_{50} and T_{90} indices [33], i.e. the minimum temperature achieved within the highest 50 % and 90 % of the temperature distribution in the target, respectively.

2.4 Treatment planning

For each applicator configuration, either during the optimization stage or for final validation, a full multi-frequency SAR-based treatment plan optimization is carried out. The plans are prepared considering the $[250, 375, 500]\ MHz$ set of frequencies for simultaneous operation. The optimization variables are the phase and amplitude of each array channel and for each frequency, for a total of $2 \cdot n_f \cdot n_c$ degrees of freedom, where n_f is the number of frequencies and n_c is the number of channels (antennas). The cost-function and goal to be minimized is the hot-to-cold spot quotient (HCQ), defined as follows [24], [25]:

$$\mathrm{HCQ}_p = \frac{\overline{\mathrm{SAR}}_{Rq}}{\overline{\mathrm{SAR}}_{Tp}}. \tag{D.2}$$

where $\overline{\mathrm{SAR}}_{Tp}$ is the average SAR in the lowest p-percentile of target (tumor) tissue, while $\overline{\mathrm{SAR}}_{Rq}$ is the average SAR in the highest q-percentile of remaining (healthy) tissue. The relationship between percentiles is fixed:

$$q = p\frac{||T||}{||R||} \tag{D.3}$$

where $||\diamond||$ denotes the volume of the argument. A target percentile p of 50 % is selected to promote coverage even in the deepest parts of the tumor and increase the resulting temperature indices.

The procedure is implemented in MATLAB® R2021a [34] using our previously devised scheme for the fast minimization of HCQ in multi-frequency problems [35], which is based on an iterative form of time-reversal. When a full array simulation is performed on COMSOL, the E-field distributions due to each antenna are directly exported from the software and re-sampled to a uniform matrix with 4 mm spatial resolution and single precision. During the array optimization, on the other hand, the individual E-fields are determined by linear interpolation as described in Sections 2.5 and 2.5. The SAR distri-

bution, in $[W/kg]$, upon which Eq. (D.2) has to be evaluated is determined by superposition of the frequency contributions:

$$\mathrm{SAR} = \sum_f \frac{1}{2}\frac{\sigma_f}{\rho}|\sum_c \chi_{f,c} E_{f,c}|^2 \tag{D.4}$$

where σ is the local material conductivity and ρ its density, while $\chi_{f,c}$ and $E_{f,c}$ are the complex steering parameter and E-field distribution of channel c at frequency f, respectively.

The SAR is then further processed to increase its correlation with temperature. First, the distribution is smoothed out by a 5 g mass averaging scheme within the patient, where surface voxels are treated by expanding the convolution kernel until the mass of tissue within reaches 5 g [36]. Secondly, the voxels belonging to the first 20 mm of healthy tissue at the surface in contact with the water bolus are completely excluded from the patient mask for the evaluation of the cost-function. This step is included to model the cooling effect of the water bolus in SAR, as the EM losses are effectively counteracted by the convective heat extraction [14]. Additionally, the exclusion of such a thick layer of patient surface is motivated by the knowledge that the most prominent hot-spot is expected to arise in the deep-seated pocket of CSF caudal to the target volume [37], while the peripheral *strati* of CSF are kept within safe temperatures by the joint action of the water bolus and the naturally high perfusion rate of gray matter [12]. Altogether, these measures ensure a high degree of correlation between the SAR and the resulting temperature distribution. All parallel SAR calculations are performed in single precision on a GPU (nVidia® RTX™ A6000).

2.5 Field interpolation

To determine the E-field distribution due to a single antenna at any location across the surface of the helmet, we introduce a linear interpolation scheme that relies on a limited number of pre-simulated locations around the head (grid). The procedure consists of several steps and makes use of a local 2D spherical coordinate system (θ, ϕ) mapping the surface of the water bolus, illustrated in Fig. 4.

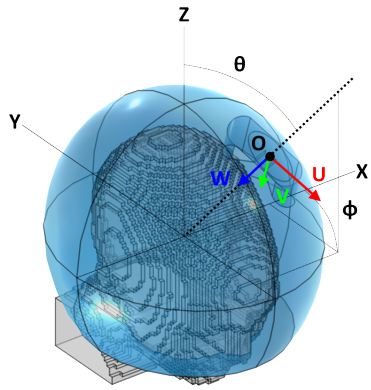

Figure 4: Reference schematic for the arrangement of a single antenna. Note that the angle ϕ, while following the classic right-hand convention, is shown here on the negative Y quadrant for readability.

Interpolation grid

Given the fitted bolus spheroid obtained in Section 2.2, a number of points n_p are randomly placed around its available surface. The spherical coordinates of each point (θ, ϕ) are then fed to a local least-squares minimization algorithm (`lsqnonlin`) that aims at minimizing the sum of the squared distances between each pair of points (emulating the repulsion of charged particles). The procedure is repeated for increasing n_p until the maximum distance between any pair of nearby points falls below a certain target sampling distance. In the patient model at hand, we prepare a grid of $n_p = 221$ points resulting in a maximum distance of 2.9 cm, which is slightly below a half of the minimum wavelength in water (6.8 cm @ 500 MHz) to provide adequate sampling resolution. The full grid is shown in Fig. 5.

For each grid point, a local antenna coordinate system is generated. The origin $O = (x, y, z)$ is initially placed at the surface point corresponding to the spherical coordinates (θ, ϕ) of this grid point. Indicating with U the antenna's orientation (polarization axis), with W its main directivity axis (pointing direction), and with V a third axis that completes a right-handed (U, V, W) triple, the local coordinate system is obtained by making W inwards perpendicular to the spheroid's surface at the point location and finding U as the vector tangent to the bolus surface and lying on the ZW plane, where Z

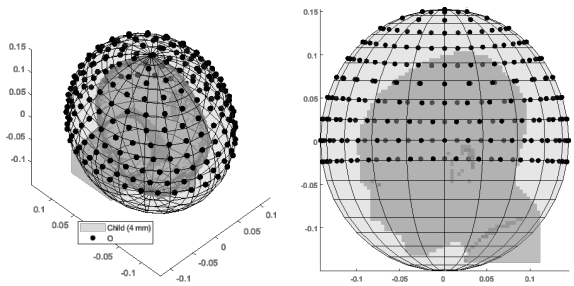

(a) 3D View **(b)** YZ View

Figure 5: Interpolation grid made of 221 points (black) uniformly distributed around the child patient model (gray) and lying on the surface of a fitted spheroid. The average distance between pairs of nearby points is 2.6 *cm*.

is the patient's rostro-caudal axis. Finally, the origin O is translated towards the positive W direction by the amount necessary to prevent the antenna's back plate from projecting out of the water spheroid. In COMSOL, $n_p \cdot n_f$ full EM simulations are performed, each with a single antenna model rigidly transformed to match the coordinate system previously prepared. The E-field distributions relative to the individual frequencies are then exported to MATLAB and uniformly re-sampled.

Linear interpolation

Once the grid distributions are available, the E-field due to a single antenna a at arbitrary coordinates $(\theta_a, \phi_a) \equiv (x_a, y_a, z_a) = O_a$ can be obtained by a linear interpolation of the distributions relative to the 3 closest grid points O_1, O_2, O_3 (triangular patch), as illustrated in Fig. 6:

1. A local coordinate system $(U, V, W)_a$ is built for the antenna, in a similar way as for the grid points in Section 2.5.

2. The complex vector E-field distribution E_1 of the first grid point at frequency f is divided everywhere by the local impedance η_f of the material, yielding a surrogate $\hat{H}_1$ of the H-field of an antenna at that location. This important step is included to render the field distribution less dependent on the patient's anatomy, thanks to the biological tissues being predominantly non-magnetic.

3. This complex vector H-field distribution is transformed to $\hat{H}_1$ according to a translation $\mathcal{T}'$, a rotation $\mathcal{R}$, and a second translation $\mathcal{T}''$, such that:

$$\begin{aligned} \mathcal{T}'[O_1] &= (0,0,0) \\ \mathcal{R}[(U,V,W)_1] &= (U,V,W)_a \\ \mathcal{T}''[(0,0,0)] &= O_a \end{aligned} \tag{D.5}$$

4. The transformed H-field distribution $\hat{H}_1$ is multiplied by the material impedance η_f to restore the transformed E-field intensity $\hat{E}_1$.

5. Steps 2 to 4 are repeated for each of the 3 closest grid points.

6. The E-field distribution relative to the individual antenna is obtained as a weighed average of the transformed distributions. The weights $\omega_1, \omega_2, \omega_3$ are determined as the ratio between the area of the subtended triangle to the area of the interpolation patch:

$$\begin{aligned} E_a &= \omega_1 \hat{E}_1 + \omega_2 \hat{E}_2 + \omega_3 \hat{E}_3 \\ \omega_1 &= ||(O_a, O_2, O_3)||/||(O_1, O_2, O_3)|| \\ \omega_2 &= ||(O_1, O_a, O_3)||/||(O_1, O_2, O_3)|| \\ \omega_3 &= ||(O_1, O_2, O_a)||/||(O_1, O_2, O_3)|| \end{aligned} \tag{D.6}$$

   where $||\diamond||$ denotes the area of the argument.

Coupling modeling

The above procedure provides a rough approximation of the E-field of a single antenna in a particular position across the water bolus surface. In any array configuration with two or more antennas, however, coupling phenomena affect the E-field distribution of the single element. We tackle this by utilizing the very individual fields of each antenna to model the coupling distortion of each array element.

To this end, we prepare a separate simulation where a spherical brain phantom is enclosed in a spherical water bolus of the same thickness of our applicator design ($\approx 5\ cm$), Fig. 7a. The phantom includes the same tissues found in the upper hemisphere of the head: brain, cerebrospinal fluid, cortical bone, skin. These are modelled as concentric shells whose thickness is determined

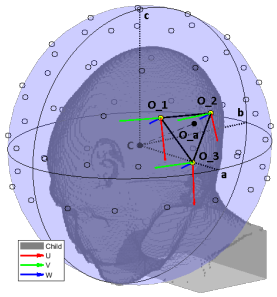

Figure 6: Reference schematic for the field interpolation procedure, using a less dense grid to facilitate the reader. The spheroid is shown in its entirety to highlight the different radii. However, in the actual simulation model, the bolus is clipped at the level of the shoulders. We show the spheroid center C and its radii a, b, c. The interpolation grid is shown with black circles. The selected interpolation patch (O_1, O_2, O_3) for an antenna at location O_a is highlighted with thick black edges and yellow vertices. The local coordinate systems of the selected grid points are also shown. An equivalent system is built for the query antenna location O_a (not shown).

by averaging a number of radial samples taken from the patient model, Fig. 1. The result is 6.3 mm for the skin, 6.8 mm for the bone, and 10.7 mm for the cerebrospinal fluid. The outer radius of the phantom is 96.9 mm, determined in a similar way (average head radius). The inner core is filled with brain material.

Using this model, we determine the coupling factor between two antennas located anywhere inside the bolus. We add a fixed active antenna (A) and generate a number of random locations for a passive antenna (P), including random rotations of its polarization axis, Fig. 7b. For each arrangement of this pair, we simulate the individual E-field distributions E_A and E_P generated when the other antenna is absent, and we extract the value of E_A at the phase center of the passive antenna, $E_A(O'_P)$. For our SGBT antennas, the phase center $O' = O + W \cdot 1.4\ cm$ lies in between the flaps, at the end of the feed line, Fig. 7c. We project this value onto the polarization axis of the passive antenna, U_P, to obtain the complex scalar:

$$e_{AP} = \langle U_P, E_A(O'_P) \rangle \tag{D.7}$$

where $\langle \diamond, \diamond \rangle$ denotes the scalar product. Subsequently, we simulate the E-

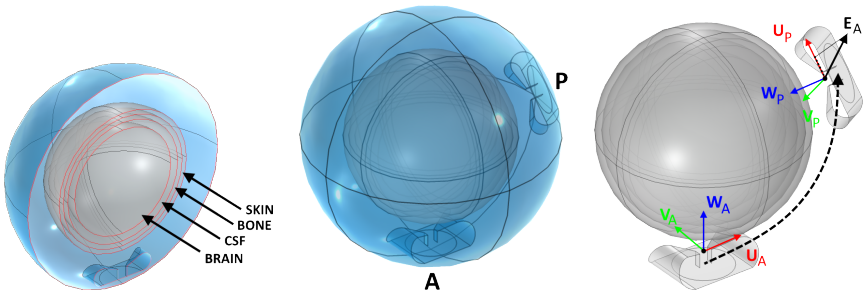

(a) Phantom **(b)** Model **(c)** Geometry

Figure 7: Procedure to determine the coupling between antenna pairs. A spherical brain phantom (a) is inserted into a spherical bolus (b). An active (A) and a passive (P) antenna are added inside the bolus. First, the individual fields E_A and E_P of each antenna are determined without the presence of the other antenna (not shown). Subsequently, the active antenna is excited with the presence of the passive antenna and the overall coupled field E_{A+P} is determined. A correlation factor between the coupled field E_{A+P} and the passive antenna field E_P is determined. This is found to be proportional to the projection on U_P of the individual field E_A at the location of the passive antenna (c).

field distribution E_{A+P} due to the active antenna A when the passive antenna P is present. Since both antennas are perfect conductors, the overall field is an infinite sum of reflections between the active and passive elements:

$$E_{A+P} = E_A + k_{AP} \cdot (E_P + k_{PA} \cdot (E_A + \ldots)) \tag{D.8}$$

where $k_{AP} = k_{PA}$ is the coupling factor between A and P. Because of losses in the domain, wave propagation and antenna misalignment, the coefficients are expected to be very small. Therefore, one can approximate the overall field as the sum of the impinging field and the first reflection only:

$$E_{A+P} \approx E_A + k_{AP} \cdot E_P \tag{D.9}$$

From this relationship, the coupling factor k_{AP} can be determined as the spatial average of the ratio between the remainder $E_{A+P} - E_A$ and the coupled field E_P. A more robust fit, however, can be obtained by means of decorrelation:

$$k_{AP} \approx \frac{\int_M (E_{A+P} - E_A) \cdot \bar{E}_P \quad dM}{\int_M |E_P|^2 \quad dM} \tag{D.10}$$

where M is the domain of the model, i.e. the bolus sphere including the phantom. Once e_{AP} and k_{AP} have been determined for different arrangements of A and P, one can study the correlation between the two. For the present study, we generated 30 random pairs and obtained the complex scatter plots shown in Fig. 8. The plots confirm the straightforward linear relationship between e_{AP} and k_{AP}. A complex coefficient c can be fitted on this set of points such that:

$$k_{AP} = c \cdot e_{AP} \tag{D.11}$$

for any arbitrary arrangement of A and P along the boundary of the water bolus.

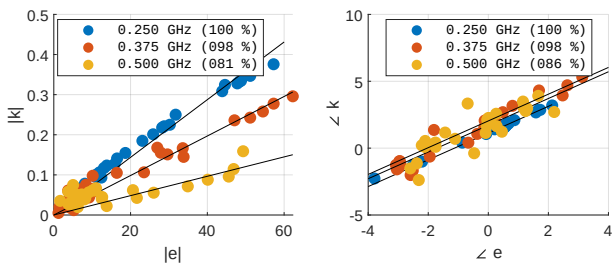

Figure 8: Correlation between the projection e_{AP} of the active antenna's field E_A on the passive antenna's polarization axis U_P at O'_P, and the coupling coefficient k_{AP} obtained by decorrelation of the remainder field $E_{A+P} - E_A$ with respect to E_P. The results are reported for each frequency in the operating set. The solid black lines show the fitted complex coupling coefficient c, while the legends report the correlation coefficients for each fit.

This important result enables the calculation of the overall field of an antenna in any array configuration given the individual fields E of the single antennas approximated in Sec. 2.5. For an array of n elements, the approximated true field distributions $\hat{E}$ relative to each antenna can be found as:

$$\begin{bmatrix} \hat{E}_1 \\ \hat{E}_2 \\ \vdots \\ \hat{E}_n \end{bmatrix} = \begin{bmatrix} 1 & ce_{12} & \cdots & ce_{1n} \\ ce_{21} & 1 & \cdots & ce_{2n} \\ \vdots & \vdots & \ddots & \vdots \\ ce_{n1} & ce_{n2} & \cdots & 1 \end{bmatrix}^{(K-1)} \cdot \begin{bmatrix} E_1 \\ E_2 \\ \vdots \\ E_n \end{bmatrix} \tag{D.12}$$

where K is the number of reflections that should be accounted for. As shown later in Sec. 3, a sufficient number of reflections is $K = 3$, and throughout the rest of the article we present results obtained utilizing this value.

2.6 Approximation analysis

We quantitatively assess the approximation error of a single antenna field by comparing the interpolated distribution to an equivalent full simulation in COMSOL. The comparison is carried out for a series of 5 locations within the largest interpolation patch and of increasing distance from a simulated grid point, as shown in Fig. 9. We assess four different aspects of the average relative error between the simulated (SIM) and interpolated (INT) complex vector E-fields: the distribution (DIS), the amplitude (ABS), the phase (ANG), and the direction (DIR). These are calculated as:

$$\begin{aligned} \epsilon_{\mathrm{DIS}} &= \int_M \frac{|E^{\mathrm{SIM}} - E^{\mathrm{INT}}|}{|E^{\mathrm{SIM}}|} dM \ / \ ||M|| \\ \epsilon_{\mathrm{ABS}} &= \int_M \frac{||\langle U, E^{\mathrm{SIM}}\rangle| - |\langle U, E^{\mathrm{INT}}\rangle||}{|\langle U, E^{\mathrm{SIM}}\rangle|} dM \ / \ ||M|| \\ \epsilon_{\mathrm{ANG}} &= \int_M \frac{|\mathtt{wrap}(\angle\langle U, E^{\mathrm{SIM}}\rangle - \angle\langle U, E^{\mathrm{INT}}\rangle)|}{\pi} dM \ / \ ||M|| \\ \epsilon_{\mathrm{DIR}} &= \int_M \frac{\mathtt{acos}(\langle |E^{\mathrm{SIM}}|, |E^{\mathrm{INT}}|\rangle / ||E^{\mathrm{SIM}}|| / ||E^{\mathrm{INT}}||)}{\pi/2} dM \ / \ ||M|| \end{aligned} \tag{D.13}$$

where M denotes the patient model volume excluding the first 20 mm of tissue in contact with the water bolus, and U is the (unitary) polarization vector of the antenna. The SIM and INT distributions are preliminarily mass-averaged according to the scheme described in Section 2.4. The values are evaluated for each individual frequency in the operating set.

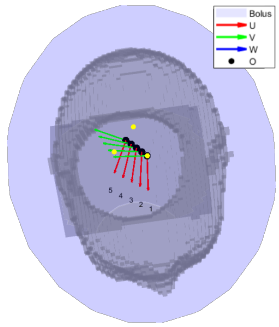

Figure 9: Location sweep for the sensitivity analysis of the field interpolation error. The black circles represent the interpolation grid points. The yellow dots are the grid points selected for interpolation, and are the corners of the triangular patch of largest area. The gray shade is the patient in bird's eye view. The local coordinate systems of each antenna location to be approximated are shown as superimposed triplets.

2.7 Array optimization

The optimization task must determine the location of each antenna in an array of a given size (number of elements or channels, n_c). The solver must also make sure that the solution represents a physically feasible arrangement. In particular, the antennas must be placed within the bolus boundaries and they must not overlap with each other. The first requirement is met by providing lower and upper boundaries to the θ_a and ϕ_a coordinates of each antenna. In the present case, ϕ_a is unbounded since the spheroid covers a full 360° on the XY plane. The second requirement can be implemented as a set of non-linear constraints. If r is the radius of the smallest circle enclosing the antenna on its local UV plane, then the following has to be true for any pair (i, j) of antennas:

$$
\begin{aligned}
|L| - l_i - l_j > 0 \\
L &= O_i - O_j \\
l_i &= \sqrt{(r\frac{\langle U_i, L\rangle}{|L|})^2 + (r\frac{\langle V_i, L\rangle}{|L|})^2} \\
l_j &= \sqrt{(r\frac{\langle U_j, L\rangle}{|L|})^2 + (r\frac{\langle V_j, L\rangle}{|L|})^2}
\end{aligned}
\tag{D.14}
$$

where L is the vector from antenna j to antenna i. This constraint is sufficient as long as the curvature of the bolus spheroid is large compared to the size of the antenna along its W axis. Further constraints relevant for the HT treatment are the locations of the eyes. The optimizer should not place any antenna in front of these organs as they can be easily damaged by MW radiation. We determine the center O and radius r of each eye in the model as projected on the water bolus surface, and append these terms to the set of constraints that is assembled according to Eq. (D.14).

If the pair (θ_a, ϕ_a) describes one antenna a, then the design procedure must solve a minimization problem consisting of $2 \cdot n_c$ degrees of freedom. These degrees of freedom, however, are not truly independent from each other. For instance, in the case of 3 antennas, the solution vector:

$$[(\theta_1, \phi_1)(\theta_2, \phi_2)(\theta_3, \phi_3)] \tag{D.15}$$

represents an array arrangement that is identical to:

$$[(\theta_2, \phi_2)(\theta_1, \phi_1)(\theta_3, \phi_3)] \tag{D.16}$$

and similar permutations. In other words, there exists a semantic overlap between the optimization variables. Because of this, classical global optimization algorithms (particle swarm, genetic evolution, simulated annealing, etc.) cannot be employed for an efficient solution of this problem. Therefore, we adopt a simpler random search (RS) strategy [38] followed by local refinement (LR). The RS stage generates a random set of uniformly distributed solutions within the optimization boundaries. This step also has to make sure that the generated points fulfill the non-intersection criterion discussed above. The number of initial solutions has to be enough to reasonably cover all qualitatively different array arrangements across the bolus surface. Intuitively, it can

be expected that the translation of one element of the array in any direction by an amount smaller than $\lambda/2$ does not result in a qualitatively different illumination of the body. This is also the rationale behind the choice of number of grid points in Section 2.5. At the same time, increasing the number of array elements (n_c) produces more redundancy among a set of solutions, because different antennas can end up covering the same spot. Consequently, we estimate the number of initial random solutions to be generated as:

$$n_r = \lfloor n_p/n_c \rceil; \tag{D.17}$$

where n_p is the number of triangular patches available from the interpolation grid (which is inversely related to the minimum wavelength in water), and $\lfloor \diamond \rceil$ denotes rounding to the nearest integer.

Once all n_r arrangements have been evaluated, the optimization enters the LR stage, which is implemented using `fmincon` from MATLAB's library. This function easily allows for the inclusion of the non-linear constraints, Eq. (D.14). To reduce the computational time, we sort the randomly generated solutions in ascending order according to their cost. We then apply the LR to the first solution, obtaining the minimum achievable HCQ for this qualitative arrangement. We proceed with the next solution until the refined HCQ becomes worse, thereby assuming that the remaining qualitative arrangements are not likely to yield more favourable SAR patterns. The overall array design procedure is summarized in Fig. 10.

Here we note that the rationale behind developing the analytical expressions reported in Section 2.5 and geometrical expressions for the bolus shape and the antenna coordinate system with respect to the spherical surface coordinates (θ, ϕ), is to make the landscape of the cost-function (HCQ) as smooth as possible with respect to the array optimization variables (θ and ϕ themselves). This is crucial for the LR step, which requires the gradients of the cost function to be numerically evaluated with respect to each optimization variable.

2.8 Design validation

We prepare 8 optimized array designs of increasing order: $n_c \in [01, 02, 03, 04, 06, 08, 10, 12]$. For each arrangement, we perform a full array simulation in COMSOL. We compare the predicted and the actual SAR distributions according to the following metrics:

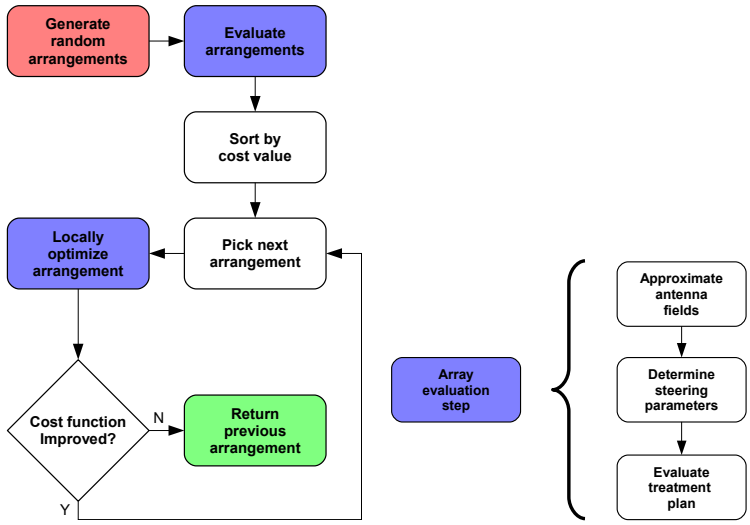

(a) Overall procedure **(b)** Inner loop

Figure 10: Applicator optimization procedure to determine the best antenna arrangement for a given patient. The procedure begins at the red step and ends at the green step. The steps highlighted in blue involve the sub-steps shown in (b) to determine the cost function value of a certain array arrangement.

$$\begin{aligned} \epsilon_{\text{DIS}} &= \int_M \frac{|\text{SAR}^{\text{SIM}} - \text{SAR}^{\text{INT}}|}{|\text{SAR}^{\text{SIM}}|} dM \;/\; ||M|| \\ \eta_{\text{H-S}} &= ||H^{\text{SIM}} \cap H^{\text{INT}}||/||H^{\text{SIM}}|| \\ \eta_{\text{C-S}} &= ||C^{\text{SIM}} \cap C^{\text{INT}}||/||C^{\text{SIM}}|| \end{aligned} \tag{D.18}$$

where H denotes the hot-spot sub-volume mask (highest q-percentile of remaining healthy tissue) and C denotes the cold-spot sub-volume mask (lowest p-percentile of target volume). While ϵ_{DIS} denotes an error metric (the lower the better), $\eta_{\text{H-S}}$ and $\eta_{\text{C-S}}$ are coverage metrics (the higher the better).

To quantify the overall improvement in heating capability of the optimized arrays, we carry out thermal simulations to evaluate the clinically relevant hyperthermia indexes T_{50} and T_{90} for each treatment plan. We also prepare a set of "canonical" applicator designs consisting of one or two rings of equally

spaced antennas for $n_c \in [06, 08, 10, 12]$ and report their achieved temperature indexes. These applicators are shown in Fig. 11. Since the canonical designs might violate the constraints relative to the avoidance of the eyes, during the evaluation of the treatment plans we turn off the channels relative to the antennas that overlap with the projected eye locations. This results in channel 02 being turned off in the canonical applicator design of order $n_c = 10$, while in the applicator of order $n_c = 12$ this applies to channels 02 and 03.

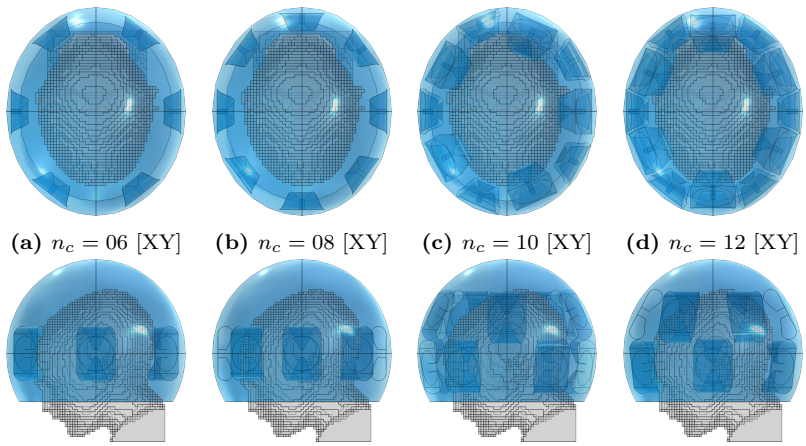

(a) $n_c = 06$ [XY] **(b)** $n_c = 08$ [XY] **(c)** $n_c = 10$ [XY] **(d)** $n_c = 12$ [XY]

(e) $n_c = 06$ [YZ] **(f)** $n_c = 08$ [YZ] **(g)** $n_c = 10$ [YZ] **(h)** $n_c = 12$ [YZ]

Figure 11: Canonical applicator designs for increasing number of elements.

3 Results

3.1 Grid simulation

The 221 simulations of the interpolation grid took about 200 h on a 32 cores Intel Xeon 2.90 GHz system with 192 Gb of RAM. For comparison, a full 8 channel array simulation takes around 1 h on the same computer system, while the interpolated approximation of the same array takes about 15 s, yielding a speedup of roughly 240 times. As the optimizer evaluates around 2000 potential array configurations to determine the best arrangement for 8 antennas, the use of the approximation method renders the global optimization feasible.

The numbers are even more compelling for higher array sizes.

An example of interpolated versus simulated SAR distribution is shown in Fig. 12 for the optimized array design of size $n_c = 08$ (applicator shown in Fig. 14j and 14n). The two distributions agree well qualitatively. The relative error becomes unacceptable ($\gg 50$ %) only in regions far from the antennas, such as the mouth (Fig. 12f), where the SAR intensity is almost negligible. The cold-spot is predicted with high accuracy ($\eta_{\text{C-S}} = 81$ %), while the hot-spot identification suffers the most from the approximation error ($\eta_{\text{H-S}} = 46$ %).

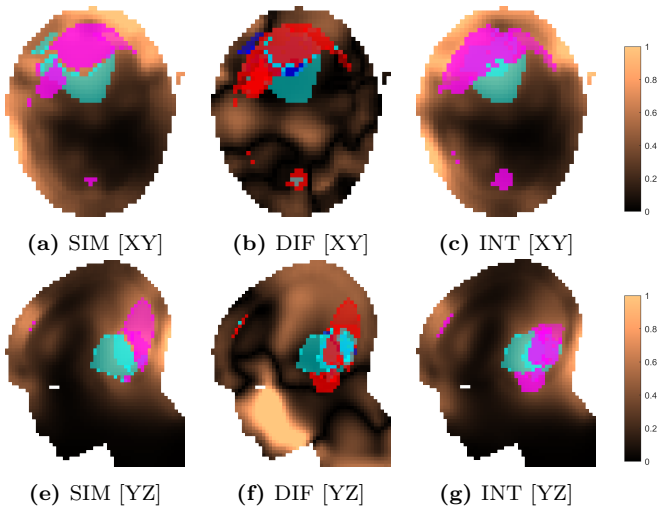

(a) SIM [XY] **(b)** DIF [XY] **(c)** INT [XY]

(e) SIM [YZ] **(f)** DIF [YZ] **(g)** INT [YZ]

Figure 12: Comparison of the normalized SAR distributions obtained via approximation (INT) and full simulation (SIM) for the optimized applicator design of order $n_c = 08$. Sections taken at target center. The volumes in magenta represent the highest q-percentile in the remaining healthy tissue (hot-spot), while the volumes in cyan represent the lowest p-percentile in the target (cold-spot). The difference (DIF) distribution is relative to the simulated one, i.e $\text{SAR}^{\text{DIF}} = |\text{SAR}^{\text{SIM}} - \text{SAR}^{\text{INT}}|/|\text{SAR}^{\text{SIM}}|$. In (b) and (f), the volumes in magenta represent $H^{\text{SIM}} \cap H^{\text{INT}}$ (hot-spot coverage), while the volumes in cyan represent $C^{\text{SIM}} \cap C^{\text{INT}}$ (cold-spot coverage). The volumes in red represent $H^{\text{SIM}} \oplus H^{\text{INT}}$ (hot-spot exclusion), while the volumes in blue represent $C^{\text{SIM}} \oplus C^{\text{INT}}$ (cold-spot exclusion).

Figure 13 reports the results of the analysis of the approximation for a single

antenna at locations of increasing distance from a simulated grid point. Because the selected patch is the largest triangle across the grid, this represents a worst-case scenario. The overall average distribution error ϵ_{DIS} reaches a peak of almost 30 % when the query location is near the center of the patch. This error is mainly due to a difference in amplitude, as can be seen from Fig. 13b. The phase is approximated with the highest accuracy.

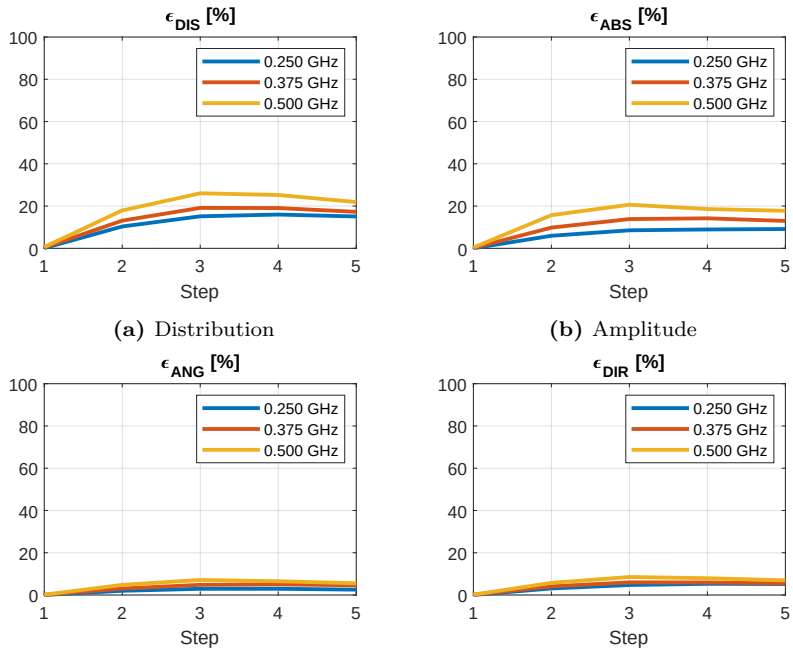

(a) Distribution **(b)** Amplitude

(c) Phase **(d)** Direction

Figure 13: Average relative error between the interpolated and simulated E-field distributions of a single antenna at increasing distance from a grid point. A phase error ϵ_{ANG} of 100 % means that the fields are in opposition. A direction error ϵ_{DIR} of 100 % means that the fields are orthogonal.

The optimized applicator designs for each array size are shown in Fig. 14. These should be compared with the location and shape of the target volume, recall Fig. 1. The designs of order up to 4 consistently place an antenna in the closest proximity to the distal part of the tumor. Beginning from order 4, an antenna is also placed on the opposite, frontal side of the head. The

design for $n_c = 6$ closely resembles a canonical one with two interleaved rings of 3 antennas.

The treatment plans prepared using the optimized designs yield the values of HCQ and temperature indexes shown in Fig. 15. The figure also reports the corresponding values for the canonical designs. The HCQ predicted by the interpolated distribution follows quite closely the actual HCQ evaluated on the simulated distribution, except for the 10 antennas canonical case, which however performs poorly in terms of target temperature increase. The relative changes in interpolated 1/HCQ values correlate well with the variations in temperature indexes for both canonical and optimized designs. The only exception is the 12 antennas optimized case, likely due to the main hot-spot becoming superficial, as discussed in the following section. The improvement in T_{50} from the best canonical solution ($n_c = 8$) to the best optimized solution ($n_c = 10$) is $\approx 0.2\ ^\circ C$. The improvement in T_{90} from the best canonical solution ($n_c = 8$) to the best optimized solution ($n_c = 10$) is $\approx 0.3\ ^\circ C$.

The SAR and temperature distributions relative to the plans obtained with each optimized design are reported in Fig. 16 and 17. The progressive inclusion of more antennas reduces the rostro-caudal elongation of the hot-spot volumes in SAR and simultaneously shifts them closer to and more uniformly surrounding the target volume, which is the desired behavior. The hot-spot masks in SAR follow well the actual resulting location of the temperature peak, except for the 12 antennas case. Here, the hot-spot becomes superficial and the SAR prediction degrades. In the majority of dense array applicator designs, however, the limiting hot-spot arises in the pocket of cerebrospinal fluid caudal to the target volume.

Table 1 reports the average relative approximation errors and spot mask coverage of each SAR distribution, for both optimized and canonical designs. It is interesting to notice that the distribution error and the mask coverage do not necessarily agree. In particular, ϵ_{DIS} is relatively high for the smaller array sizes 02 and 03, but the spot identification has a high degree of accuracy ($\eta_{\text{H-S}}, \eta_{\text{C-S}} > 79\ \%$). On the contrary, ϵ_{DIS} diminishes for denser arrays but the hot-spot identification $\eta_{\text{H-S}}$ becomes worse.

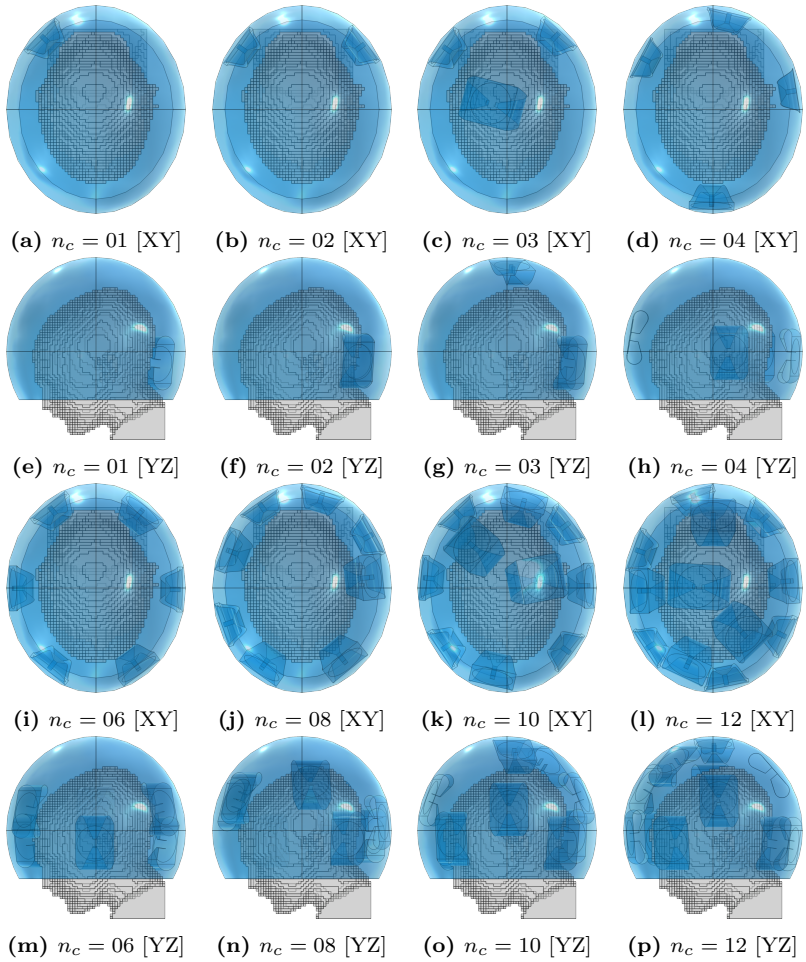

(a) $n_c = 01$ [XY] **(b)** $n_c = 02$ [XY] **(c)** $n_c = 03$ [XY] **(d)** $n_c = 04$ [XY]

(e) $n_c = 01$ [YZ] **(f)** $n_c = 02$ [YZ] **(g)** $n_c = 03$ [YZ] **(h)** $n_c = 04$ [YZ]

(i) $n_c = 06$ [XY] **(j)** $n_c = 08$ [XY] **(k)** $n_c = 10$ [XY] **(l)** $n_c = 12$ [XY]

(m) $n_c = 06$ [YZ] **(n)** $n_c = 08$ [YZ] **(o)** $n_c = 10$ [YZ] **(p)** $n_c = 12$ [YZ]

Figure 14: Optimized applicator designs for increasing number of elements.

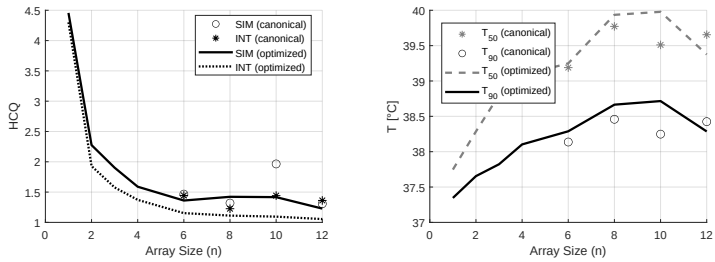

(a) SAR Cost **(b)** Temperature Indexes

Figure 15: Values of HCQ, T_{50} and T_{90} relative to the treatment plans prepared using canonical and optimized applicator designs of increasing order (line plots). The values for the canonical applicator designs are also reported as scatter plots. In SAR, the value of HCQ predicted by the field approximation is compared against the value from the actual simulated field.

4 Discussion

The purpose of the approximation method developed in the present work is to make practical the qualitative evaluation of a large number of array configurations prior to the HT treatment of a brain cancer patient. The established clinically relevant parameters for the assessment of a treatment plan are the median temperature T_{50} and 90-percentile temperature T_{90} indexes, which have been extensively studied in relation to the clinical outcome [5], [39], [40]. Due to the added computational complexity of thermal simulations, however, the direct assessment of the temperature distribution for thousands of array configurations becomes impractical. The proposed SAR-based field approximation method circumvents this limitation and enables the qualitative evaluation of a given antenna arrangement within seconds. Together with our previously devised SAR-based iterative time-reversal multi-frequency treatment plan optimization [35], these tools can be used in combination with optimization algorithms to refine an applicator design for a specific patient.

We argue that the proposed approximation method is accurate enough for the relative comparison between different design solutions. While this is true for most of the reported cases, we also acknowledge that the approximation of two specific solutions (canonical $n_c = 10$ and optimized $n_c = 12$) failed

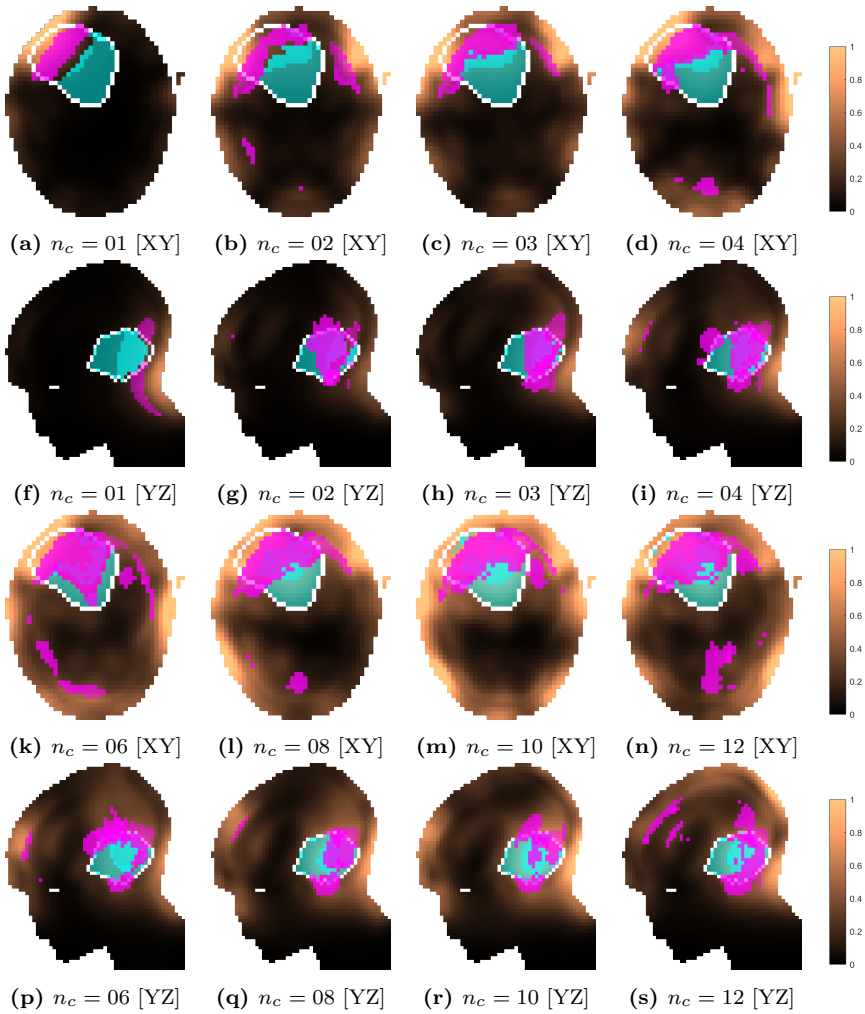

(a) $n_c = 01$ [XY] **(b)** $n_c = 02$ [XY] **(c)** $n_c = 03$ [XY] **(d)** $n_c = 04$ [XY]

(f) $n_c = 01$ [YZ] **(g)** $n_c = 02$ [YZ] **(h)** $n_c = 03$ [YZ] **(i)** $n_c = 04$ [YZ]

(k) $n_c = 06$ [XY] **(l)** $n_c = 08$ [XY] **(m)** $n_c = 10$ [XY] **(n)** $n_c = 12$ [XY]

(p) $n_c = 06$ [YZ] **(q)** $n_c = 08$ [YZ] **(r)** $n_c = 10$ [YZ] **(s)** $n_c = 12$ [YZ]

Figure 16: Normalized SAR distributions relative to each optimized applicator design. Sections taken at target center. The white line delineates the target volume. The volumes in magenta represent the highest q-percentile in the remaining healthy tissue (hot-spot), while the volumes in cyan represent the lowest p-percentile in the target (cold-spot).

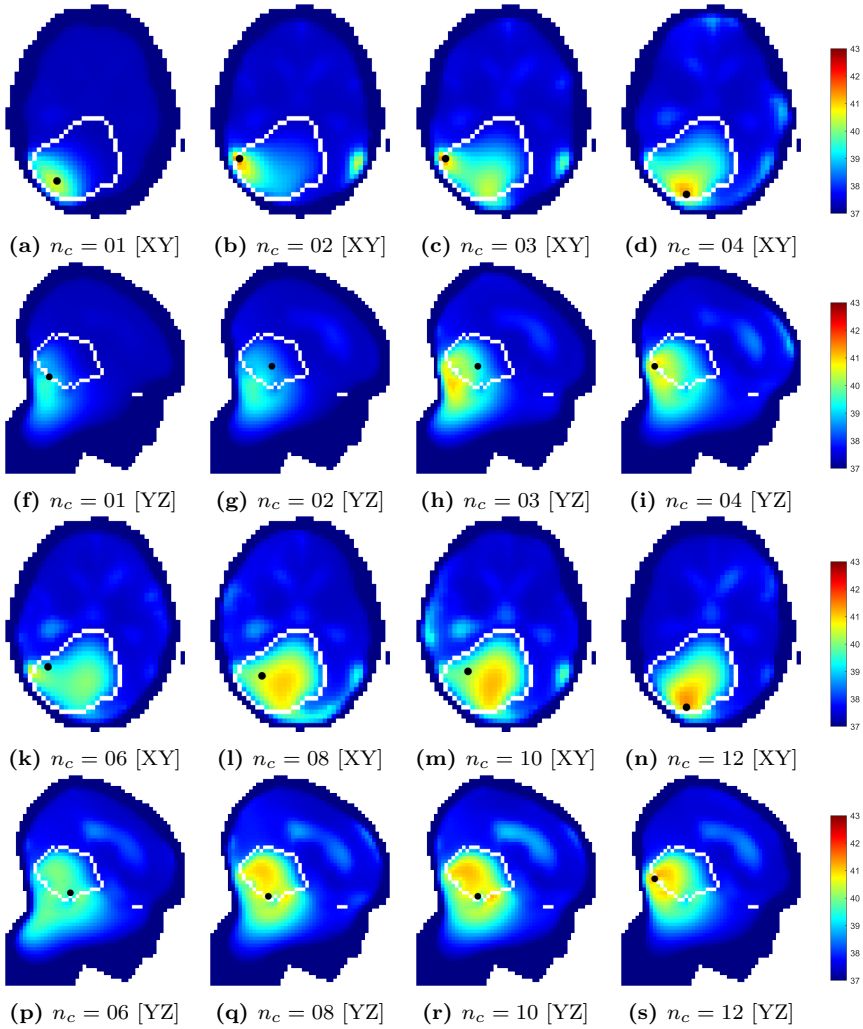

(a) $n_c = 01$ [XY] **(b)** $n_c = 02$ [XY] **(c)** $n_c = 03$ [XY] **(d)** $n_c = 04$ [XY]

(f) $n_c = 01$ [YZ] **(g)** $n_c = 02$ [YZ] **(h)** $n_c = 03$ [YZ] **(i)** $n_c = 04$ [YZ]

(k) $n_c = 06$ [XY] **(l)** $n_c = 08$ [XY] **(m)** $n_c = 10$ [XY] **(n)** $n_c = 12$ [XY]

(p) $n_c = 06$ [YZ] **(q)** $n_c = 08$ [YZ] **(r)** $n_c = 10$ [YZ] **(s)** $n_c = 12$ [YZ]

Figure 17: Temperature distributions relative to each optimized applicator design. Sections taken at target center. The views are flipped to show the side where the temperature peak in the healthy tissue is located, marked with a black dot. The white line delineates the target volume.

Table 1: Error indicators of the overall approximated SAR distributions with respect to the corresponding distributions obtained from full simulations. Both optimized (OPT) and canonical (CAN) array designs are reported. The last 4 rows report the same error indicators for the densest optimized array and increasing reflection order K for the coupling modeling.

	ϵ_{DIS} [%]	$\eta_{\text{H-S}}$ [%]	$\eta_{\text{C-S}}$ [%]
$n_c = 01$ (OPT)	08	98	99
$n_c = 02$ (OPT)	32	80	95
$n_c = 03$ (OPT)	36	79	96
$n_c = 04$ (OPT)	22	63	87
$n_c = 06$ (OPT)	28	54	84
$n_c = 08$ (OPT)	29	46	81
$n_c = 10$ (OPT)	32	46	82
$n_c = 12$ (OPT)	28	65	84
$n_c = 06$ (CAN)	26	46	88
$n_c = 08$ (CAN)	20	69	91
$n_c = 10$ (CAN)	58	41	84
$n_c = 12$ (CAN)	25	57	85
$n_c = 12$ (OPT) $[K = 1]$	42	62	86
$n_c = 12$ (OPT) $[K = 2]$	34	71	94
$n_c = 12$ (OPT) $[K = 3]$	28	65	84
$n_c = 12$ (OPT) $[K = 4]$	29	72	95
$n_c = 12$ (OPT) $[K = 5]$	28	44	78

in predicting the resulting temperature increase. In the first case, the error arises already in the SAR distribution, and the reasons for this are not entirely clear. A possible explanation could be a strong variation in the patient anatomy within the interpolation patch of one (or more) of the antenna elements, which is not adequately captured by the resolution of the interpolation grid. A detailed analysis of the individual antenna fields is necessary to unveil the cause behind this outlier. In the second case, however, the relative improvement in HCQ is correctly predicted, and the reason for the unrealized corresponding increase in the temperature indexes must be traced to the shift in location of the most prominent hot-spot. While in the treatment plans relative to the optimized dense arrays $n_c = [06, 08, 10]$ the limiting hot-spot is located in the pocket of cerebrospinal fluid caudal to the target volume, in the optimized $n_c = 12$ case the peak temperature is reached near the super-

ficial part of the tumor (Fig. 17n and 17s). We have previously shown that 1/HCQ correlates well with the target temperature increase T_{50} and T_{90} but the correlation quickly deteriorates for superficial targets where the water bolus directly affects the temperature distribution in the target volume [25], so this is an expected result. To improve on this aspect, one might apply a more aggressive water bolus cooling to suppress this superficial hot-spot. Alternatively, a thinner exclusion layer in the SAR evaluation mask might guide the optimizer towards solutions that deposit less power in this superficial zone. In this study, we applied a 20 mm exclusion, which is on the upper limit of typical cooling depths for clinical water boluses [14].

The comparison between optimized and canonical arrays reveals a moderate gain in temperature indexes ($\approx 0.2\ ^\circ C$ in T_{50}, $\approx 0.3\ ^\circ C$ in T_{90}). We expected this, as the canonical designs developed here are in fact already tailored to the patient in terms of antenna design and bolus shape. Nevertheless, these gains are still clinically relevant since the relative temperature increase after applicator steering has been shown to follow the predicted change with an accuracy of $0.1\ ^\circ C$ [41]. According to the CEM43T90 model [40], an increase of $\approx 0.3\ ^\circ C$ in T_{90} would correspond to an increase of ≈ 1.5 in thermal dose.

As a final note, we address the question on whether it is meaningful to consider applicator designs with such a degree of customization for a certain patient, especially when it is already a challenge to accurately model and position patients in much simpler applicator designs [42]. In our opinion, the rationale behind this contribution lies in addressing a particularly challenging anatomical region, the brain, and strive for a design that will eventually enable hyperthermia treatments in this organ. Such treatments might require a higher degree of customization than current clinical solutions. The method allows us to qualitatively sift through many potential array configurations and select the most suitable one for a certain tumor size, shape and location. Unfortunately, a direct comparison with current clinical applicators cannot be done right away as these, to the best of our knowledge, have not yet been used in the treatment of brain tumors. Furthermore, any comparison with the absolute temperatures reported in literature would be affected by the considerable uncertainties in thermal simulations [43] and their strong dependence on the specific patient modeling.

5 Conclusion

We proposed and validated a field approximation method for the fast evaluation of different antenna arrangements in a helmet applicator for microwave hyperthermia treatments, and used it in conjunction with a fast multi-frequency treatment plan optimization scheme to improve the design of an applicator for a specific paediatric brain cancer patient. The method is accurate enough to provide qualitative indications about the most suitable antenna arrangement for a given tumor shape and location. The technique can be particularly useful in the design of UWB applicators where the classical single-frequency array theory used for narrow band applicators might prove insufficient to achieve an optimal configuration. Further studies are required to assess the sensitivity of the proposed technique to the resolution of the interpolation grid, and future developments might involve the inclusion of the antenna polarization angles in the set of design parameters.

References

[1] P. B. Elming, B. S. Sørensen, A. L. Oei, *et al.*, "Hyperthermia: The optimal treatment to overcome radiation resistant hypoxia," *Cancers*, vol. 11, no. 1, p. 60, 2019.

[2] N. Datta, S. G. Ordóñez, U. Gaipl, *et al.*, "Local hyperthermia combined with radiotherapy and-/or chemotherapy: Recent advances and promises for the future," *Cancer treatment reviews*, vol. 41, no. 9, pp. 742–753, 2015.

[3] A. van der Horst, E. Versteijne, M. G. Besselink, *et al.*, "The clinical benefit of hyperthermia in pancreatic cancer: A systematic review," *International journal of hyperthermia*, vol. 34, no. 7, pp. 969–979, 2018.

[4] H. P. Kok, E. N. Cressman, W. Ceelen, *et al.*, "Heating technology for malignant tumors: A review," *International Journal of Hyperthermia*, vol. 37, no. 1, pp. 711–741, 2020.

[5] A. Bakker, J. van der Zee, G. van Tienhoven, H. P. Kok, C. R. Rasch, and H. Crezee, "Temperature and thermal dose during radiotherapy and hyperthermia for recurrent breast cancer are related to clinical out-

come and thermal toxicity: A systematic review," *International Journal of Hyperthermia*, vol. 36, no. 1, pp. 1023–1038, 2019.

[6] P. K. Sneed, P. H. Gutin, P. R. Stauffer, *et al.*, "Thermoradiotherapy of recurrent malignant brain tumors," *International Journal of Radiation Oncology* Biology* Physics*, vol. 23, no. 4, pp. 853–861, 1992.

[7] K. A. McNeill, "Epidemiology of brain tumors," *Neurologic clinics*, vol. 34, no. 4, pp. 981–998, 2016.

[8] M. T. Makale, C. R. McDonald, J. A. Hattangadi-Gluth, and S. Kesari, "Mechanisms of radiotherapy-associated cognitive disability in patients with brain tumours," *Nature Reviews Neurology*, vol. 13, no. 1, pp. 52–64, 2017.

[9] J. Haveman, P. Sminia, J. Wondergem, J. van der Zee, and M. Hulshof, "Effects of hyperthermia on the central nervous system: What was learnt from animal studies?" *International journal of hyperthermia*, vol. 21, no. 5, pp. 473–487, 2005.

[10] A. Cutz, "Effects of microwave radiation on the eye: The occupational health perspective.," *Lens and Eye Toxicity Research*, vol. 6, no. 1-2, pp. 379–386, 1989.

[11] P. Fessenden and J. W. Hand, "Hyperthermia therapy physics," in *Radiation Therapy Physics*, Springer, 1995, pp. 315–363.

[12] P. Hasgall, F. Di Gennaro, C. Baumgartner, *et al.*, *IT'IS Database for thermal and electromagnetic parameters of biological tissues*, version 4.0, May 2018.

[13] H. Shoji, M. Motegi, K. Osawa, *et al.*, "Output-limiting symptoms induced by radiofrequency hyperthermia. are they predictable?" *International Journal of Hyperthermia*, vol. 32, no. 2, pp. 199–203, 2016.

[14] M. Van der Gaag, M. De Bruijne, T. Samaras, J. Van Der Zee, and G. Van Rhoon, "Development of a guideline for the water bolus temperature in superficial hyperthermia," *International journal of hyperthermia*, vol. 22, no. 8, pp. 637–656, 2006.

[15] M. Seebass, R. Beck, J. Gellermann, J. Nadobny, and P. Wust, "Electromagnetic phased arrays for regional hyperthermia: Optimal frequency and antenna arrangement," *International Journal of Hyperthermia*, vol. 17, no. 4, pp. 321–336, 2001.

[16] M. M. Paulides, S. H. Vossen, A. P. Zwamborn, and G. C. van Rhoon, "Theoretical investigation into the feasibility to deposit rf energy centrally in the head-and-neck region," *International Journal of Radiation Oncology* Biology* Physics*, vol. 63, no. 2, pp. 634–642, 2005.

[17] J. Crezee, P. Van Haaren, H. Westendorp, *et al.*, "Improving locoregional hyperthermia delivery using the 3-d controlled amc-8 phased array hyperthermia system: A preclinical study," *International Journal of Hyperthermia*, vol. 25, no. 7, pp. 581–592, 2009.

[18] H. Kok, M. De Greef, P. Borsboom, A. Bel, and J. Crezee, "Improved power steering with double and triple ring waveguide systems: The impact of the operating frequency," *International Journal of Hyperthermia*, vol. 27, no. 3, pp. 224–239, 2011.

[19] P. Togni, Z. Rijnen, W. Numan, *et al.*, "Electromagnetic redesign of the hypercollar applicator: Toward improved deep local head-and-neck hyperthermia," *Physics in Medicine & Biology*, vol. 58, no. 17, p. 5997, 2013.

[20] G. P. Skandalakis, D. R. Rivera, C. D. Rizea, *et al.*, "Hyperthermia treatment advances for brain tumors," *International Journal of Hyperthermia*, vol. 37, no. 2, pp. 3–19, 2020.

[21] E. Oberacker, A. Kuehne, J. Nadobny, *et al.*, "Radiofrequency applicator concepts for simultaneous mr imaging and hyperthermia treatment of glioblastoma multiforme," *Current Directions in Biomedical Engineering*, vol. 3, no. 2, pp. 473–477, 2017.

[22] P. Takook, M. Persson, and H. D. Trefná, "Performance evaluation of hyperthermia applicators to heat deep-seated brain tumors," *IEEE Journal of Electromagnetics, RF and Microwaves in Medicine and Biology*, vol. 2, no. 1, pp. 18–24, 2018.

[23] E. Oberacker, C. Diesch, J. Nadobny, *et al.*, "Patient-specific planning for thermal magnetic resonance of glioblastoma multiforme," *Cancers*, vol. 13, no. 8, p. 1867, 2021.

[24] M. Zanoli and H. D. Trefná, "Combining target coverage and hot-spot suppression into one cost function: The hot-to-cold spot quotient," in *2021 15th European Conference on Antennas and Propagation (EuCAP)*, IEEE, 2021, pp. 1–4.

[25] M. Zanoli and H. D. Trefná, "The hot-to-cold spot quotient for sar-based treatment planning in deep microwave hyperthermia," *submitted to the International Journal of Hyperthermia*, 2022.

[26] P. Takook, M. Persson, J. Gellermann, and H. D. Trefná, "Compact self-grounded bow-tie antenna design for an uwb phased-array hyperthermia applicator," *International Journal of Hyperthermia*, vol. 33, no. 4, pp. 387–400, 2017.

[27] COMSOL AB, Stockholm, Sweden, *COMSOL Multiphysics® v. 5.6*, 2020.

[28] B. J. James and D. M. Sullivan, "Creation of three-dimensional patient models for hyperthermia treatment planning," *IEEE transactions on biomedical engineering*, vol. 39, no. 3, pp. 238–242, 1992.

[29] W. T. Joines, Y. Zhang, C. Li, and R. L. Jirtle, "The measured electrical properties of normal and malignant human tissues from 50 to 900 mhz," *Medical physics*, vol. 21, no. 4, pp. 547–550, 1994.

[30] M. M. Paulides, D. B. Rodrigues, G. G. Bellizzi, *et al.*, "Esho benchmarks for computational modeling and optimization in hyperthermia therapy," *International Journal of Hyperthermia*, vol. 38, no. 1, pp. 1425–1442, 2021.

[31] R. F. Verhaart, G. M. Verduijn, V. Fortunati, *et al.*, "Accurate 3d temperature dosimetry during hyperthermia therapy by combining invasive measurements and patient-specific simulations," *International Journal of Hyperthermia*, vol. 31, no. 6, pp. 686–692, 2015.

[32] H. H. Pennes, "Analysis of tissue and arterial blood temperatures in the resting human forearm," *Journal of applied physiology*, vol. 1, no. 2, pp. 93–122, 1948.

[33] G. Bruggmoser, S. Bauchowitz, R. Canters, *et al.*, "Quality assurance for clinical studies in regional deep hyperthermia," *Strahlentherapie und Onkologie*, vol. 187, no. 10, p. 605, 2011.

[34] The MathWorks Inc., Natick, Massachusetts, "MATLAB R2021a," 2021.

[35] M. Zanoli and H. D. Trefná, "Iterative time-reversal for multi-frequency hyperthermia," *Physics in Medicine & Biology*, vol. 66, no. 4, p. 045 027, 2021.

[36] J. Bakker, M. Paulides, E. Neufeld, A. Christ, N. Kuster, and G. Van Rhoon, "Children and adults exposed to electromagnetic fields at the icnirp reference levels: Theoretical assessment of the induced peak temperature increase," *Physics in Medicine & Biology*, vol. 56, no. 15, p. 4967, 2011.

[37] M. Ghaderi Aram, M. Zanoli, H. Nordström, I. Toma-Dasu, K. Blomgren, and H. D. Trefná, "Radiobiological evaluation of combined gamma knife radiosurgery and hyperthermia for pediatric neuro-oncology," *Cancers*, vol. 13, no. 13, p. 3277, 2021.

[38] H. E. Romeijn, "Random search methods," in *Encyclopedia of Optimization*, C. A. Floudas and P. M. Pardalos, Eds., Boston, MA: Springer US, 2009, pp. 3245–3251, ISBN: 978-0-387-74759-0.

[39] M. Kroesen, H. T. Mulder, J. M. van Holthe, *et al.*, "Confirmation of thermal dose as a predictor of local control in cervical carcinoma patients treated with state-of-the-art radiation therapy and hyperthermia," *Radiotherapy and oncology*, vol. 140, pp. 150–158, 2019.

[40] G. C. van Rhoon, "Is CEM43 still a relevant thermal dose parameter for hyperthermia treatment monitoring?" *International Journal of Hyperthermia*, vol. 32, no. 1, pp. 50–62, 2016.

[41] H. Kok, G. Schooneveldt, A. Bakker, *et al.*, "Predictive value of simulated sar and temperature for changes in measured temperature after phase-amplitude steering during locoregional hyperthermia treatments," *International Journal of Hyperthermia*, vol. 35, no. 1, pp. 330–339, 2018.

[42] B. Aklan, P. Gierse, J. Hartmann, O. J. Ott, R. Fietkau, and C. Bert, "Influence of patient mispositioning on sar distribution and simulated temperature in regional deep hyperthermia," *Physics in Medicine & Biology*, vol. 62, no. 12, p. 4929, 2017.

[43] B. Aklan, B. Zilles, P. Paprottka, *et al.*, "Regional deep hyperthermia: Quantitative evaluation of predicted and direct measured temperature distributions in patients with high-risk extremity soft-tissue sarcoma," *International Journal of Hyperthermia*, 2019.

PAPER E

Radiobiological Evaluation of Combined Gamma Knife Radiosurgery and Hyperthermia for Pediatric Neuro-Oncology

Morteza Ghaderi Aram, **Massimiliano Zanoli**, Håkan Nordström, Iuliana Toma-Dasu, Klas Blomgren, Hana Dobšíček Trefná

Cancers
30 June 2021

DOI: 10.3390/cancers13133277

The layout has been revised.

cancers

MDPI

Article

Radiobiological Evaluation of Combined Gamma Knife Radiosurgery and Hyperthermia for Pediatric Neuro-Oncology

Morteza Ghaderi Aram [1,*], Massimiliano Zanoli [1], Håkan Nordström [2], Iuliana Toma-Dasu [3,4], Klas Blomgren [5,6] and Hana Dobšíček Trefná [1]

1 Department of Electrical Engineering, Chalmers University of Technology, 412 96 Gothenburg, Sweden; zanoli@chalmers.se (M.Z.); hanatre@chalmers.se (H.D.T.)
2 Elekta Instrument AB 113 57, 103 93 Stockholm, Sweden; hakan.nordstrom@elekta.com
3 Department of Oncology-Pathology, Karolinska Institutet, 171 64 Stockholm, Sweden; iuliana.livia.dasu@ki.se
4 Department of Physics, Stockholm University, 106 91 Stockholm, Sweden
5 Department of Women's and Children's Health, Karolinska Institutet, 171 64 Stockholm, Sweden; klas.blomgren@ki.se
6 Pediatric Oncology, Karolinska University Hospital, 171 64 Stockholm, Sweden
* Correspondence: aramg@chalmers.se

Simple Summary: This study proposes a novel strategy in brain cancer management. Stereotactic radiosurgery delivered by the Gamma Knife was combined with hyperthermia. For the radiobiological modelling of this synergistic treatment modality, we used the linear-quadratic model with temperature-dependent parameters to assess the potential enhancement of the therapeutic outcome. The results indicate that focused intracranial heating can be used to boost the dose to the target. Alternatively, one can conclude that for the same therapeutic effect, hyperthermia can help to minimize the dose undesirably delivered to healthy tissues. This study is also the first to advocate a combination of stereotactic radiosurgery with focused heating and motivates the future development of hyperthermia systems for brain cancer treatment.

Abstract: Combining radiotherapy (RT) with hyperthermia (HT) has been proven effective in the treatment of a wide range of tumours, but the combination of externally delivered, focused heat and stereotactic radiosurgery has never been investigated. We explore the potential of such treatment enhancement via radiobiological modelling, specifically via the linear-quadratic (LQ) model adapted to thermoradiotherapy through modulating the radiosensitivity of temperature-dependent parameters. We extend this well-established model by incorporating oxygenation effects. To illustrate the methodology, we present a clinically relevant application in pediatric oncology, which is novel in two ways. First, it deals with medulloblastoma, the most common malignant brain tumour in children, a type of brain tumour not previously reported in the literature of thermoradiotherapy studies. Second, it makes use of the Gamma Knife for the radiotherapy part, thereby being the first of its kind in this context. Quantitative metrics like the biologically effective dose (BED) and the tumour control probability (TCP) are used to assess the efficacy of the combined plan.

Keywords: stereotactic radiotherapy; hyperthermia; CNS tumors; medulloblastoma; biological modelling; LQ model

check for updates

Citation: Aram, M.G.; Zanoli, M.; Nordström, H.; Toma-Dasu, I.; Blomgren, K.; Dobšíček Trefná, H. Radiobiological Evaluation of Combined Gamma Knife Radiosurgery and Hyperthermia for Pediatric Neuro-Oncolog. *Cancers* **2021**, *13*, 3277. https://doi.org/10.3390/cancers13133277

Academic Editor: Simon S. Lo

Received: 29 April 2021
Accepted: 25 June 2021
Published: 30 June 2021

Publisher's Note: MDPI stays neutral with regard to jurisdictional claims in published maps and institutional affiliations.

1. Introduction

Central nervous system (CNS) tumours constitute the second most common form of cancer in children [1]. Improved treatment protocols have increased survival rates to more than 80% [2]. However, the treatment may have multiple, debilitating side effects, so-called late effects or late complications. Radiotherapy (RT) is an essential treatment modality in the clinical management of brain tumours and vascular malformations, but it is also most prone to cause late complications. Long-term neurocognitive sequelae are often

severe in paediatric patients, where 50–96% of the treated individuals display intellectual impairments [3,4]. Methods such as proton therapy and stereotactic treatments with photons are becoming increasingly popular, especially in children, because of their potential to deliver a dose limited to the target and thus reduce RT-related toxicity.

Hyperthermia (HT) is defined as an induced temperature increase in tumours to about 40–44 °C for typically 60 min. It has been demonstrated that hyperthermia (HT) improves local control for a wide range of tumours and can increase overall survival rates in patients treated with radiotherapy (RT) [5–9] or chemotherapy [10,11]. For instance, despite the technically challenging delivery of HT to the head and neck (H&N) region, HT offers a valuable treatment option for patients with tumours in this region [12]. A meta-analysis study of H&N carcinomas, recently published in [7], shows that the complete response rate (CR) in patients treated with combined radiotherapy and hyperthermia (RTHT) appears to be significantly better than that of the patients treated with RT alone (RT alone: CR = 39.6% vs. RTHT: CR = 62.5%). At the same time, acute and late-grade 3/4 toxicities have not been reported to be significantly different between two arms [7]. Although most of the patients treated with hyperthermia have been adults, encouraging clinical results also exist for children and adolescents [13]. The combination of chemotherapy and hyperthermia has been successfully applied in children with refractory or recurrent non-testicular malignant germ cell tumours. The long-term prognosis for patients with poor response or after the first relapse is similar to the prognosis for those receiving first-line treatment [14].

The clinical experiences with HT applied for brain cancer treatment are limited to high-grade glioblastomas (GBM). The interstitial HT combined with radiotherapy has been demonstrated to be a safe [15–17] and promising modality to improve the survival of the patients. In a two-arm study, Sneed et al. [18] have shown a two-year survival rate of 31% in the arm with HT versus 15% in the arm without HT. Despite the promising results in terms of an improved treatment outcome, homogeneous tumour temperatures were difficult to achieve with the interstitial applicators used [15,18]. As an adjuvant for RT, intratumoral injection of magnetic nanoparticles in magnetic hyperthermia therapy has also been shown to improve survival rate in GBM, compared to the therapeutic outcomes achieved with RT alone [19]. More recently, a localised increase of tumour temperature has been achieved through magnetic fluid HT [20], in which injected iron oxide nanoparticles are excited by an externally applied AC magnetic field. Again, the higher overall survival of patients in the arms including HT was observed [21]. Another technology with promising results in moderate heating in small animal tumours is the high-intensity focused ultrasound (HIFU) [22]. The present HIFU technology has not yet been proven feasible for the heating of large volumes typical for childhood brain tumours.

Our work is based on microwave phased array technology [23,24] that has been the most widely applied technology for the treatment of deep-seated tumours in clinical settings. However, this technology has not been applied intracranially before due to several challenges. The high perfusion rates in the brain quickly normalise the temperature and thus require the application of strong electromagnetic (EM) fields to achieve adequate tumour temperatures. Moreover, the presence of electrically highly conductive cerebrospinal fluid (CSF) leads to considerable absorption of EM radiation, thereby making CSF more susceptible to the emergence of treatment-limiting hot spots. However, recently published numerical studies [25–29] suggest that the intracranial heating with those innovative approaches is feasible. A particularly unique approach is a helmet-like configuration that utilises UWB antennas, allowing for better focusing with fewer antennas than standard annular-phased-array applicators [30]. Using a thermodynamic fluid model of CSF, the study demonstrated that this type of applicator is capable of obtaining an adequate temperature in large brain tumours without inducing unacceptable hot spots [31].

In current clinical practice, HT is typically delivered in combination with external beam radiation therapy (EBRT), which strongly relies on the fact that normal tissues are generally better at sublethal DNA damage repair than tumour tissues. Therefore, numerous dose fractionation schemes, in the order of 30 fractions delivered over a period

of 5–10 weeks, have been exploited [32]. In comparison, stereotactic radiosurgery (SRS) aims to achieve a therapeutic effect by using a single or few fractions to deliver a highly conformal dose. Since its invention, the Leksell Gamma Knife® (Elekta AB, Stockholm, Sweden) models have been used to sculpt the dose to conform to the target. The dose gradient outside the target is sharp, with little impact on surrounding healthy tissues and organs at risk. The SRS delivery is often limited to small target volumes, since its application for medium-sized and large tumours eradication would lead to an unfeasible increase in the treatment time.

In this study, we propose a novel strategy in brain cancer management, combining hyperthermia with SRS delivered by the Gamma Knife. The hypothesis is that focused microwave heating of a tumour will boost the radiotherapeutic effect or alternatively allow for a reduced radiation dose without compromising the treatment outcome. The potential treatment enhancement is investigated via radiobiological modelling, specifically via the linear-quadratic (LQ) model adapted to thermoradiotherapy through modulating the radiosensitivity of temperature-dependent parameters [33,34]. The model is further extended with an oxygen modification factor (OMF) that includes the effect of the local oxygen tension, pO_2 [35]. The model is applied to evaluate the expected increase of the therapeutic window when hyperthermia is added to SRS. The combined effect is assessed on a medium-sized paediatric brain tumour. The methodology proposed in this work can be considered as a framework for the evaluation of the combined effect of thermal therapy and radiosurgery.

2. Materials and Methods

2.1. Patient Model

An MRI scan with a $1 \times 1 \times 1$ mm resolution was obtained from a 13-year old boy with medulloblastoma. The scan was manually segmented by a clinician into 10 tissue types, as visualized in Figure 1. Only a part of the head was segmented, and the section outside the treatment volume, that is, the part of the head below the tumour that was not covered by the applicator was modelled as muscle. Observe that the volume of the original tumour, as studied in [31], has been reduced to 34 mL by means of morphological operations (erosion). The volume no longer occupied by the tumour has been filled with a mirrored copy of the opposite healthy brain hemisphere to preserve the anatomical correctness. In the context of the current proof-of-concept study, this may be considered a valid model for various residual brain tumours, such as medulloblastomas or ependymomas.

Electromagnetic and thermal simulations are performed using tissue parameters from the IT'IS database [36] adjusted for hyperthermic conditions: muscle perfusion is increased by a factor of 4 due to the systemic response to heat [37], while the thermal conductivity of the cerebrospinal fluid is increased by a factor of 10 to emulate the convective transport of heat [31]. Tumour properties are obtained as an average of grey and white matter, and its blood perfusion is decreased by a factor of 0.7 to account for the chaotic vasculature [38]. Due to the frequency dependence of the dielectric properties and utilisation of multiple frequencies in the treatment planning phase, the properties are not listed here. Nevertheless, the tissue properties listed in [31] can be considered as an example for 450 MHz.

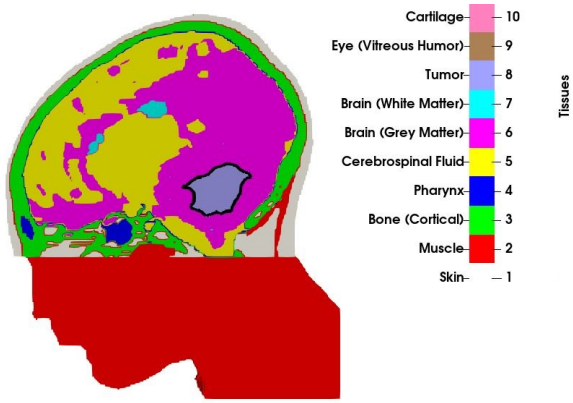

Figure 1. Cross-section of the patient model along with the tissue indices. Border of the tumour is shown with the solid black line.

2.2. Hyperthermia Treatment Planning with Novel Applicator

The hyperthermia applicator consists of eight self-grounded bow-tie antennas immersed into a separate water bolus [39] and arranged in a helmet-shaped array. A water bolus is inserted between the antennas and the patient for skin-cooling and impedance-matching. Four antennas operate across the frequency band of 400∼800 MHz, while the others are upscaled to operate at lower frequencies of 300∼600 MHz. The applicator is thus designed for multi-frequency treatments, and the set of operating frequencies considered for this study is 300, 400, 500, 600, 700, and 800 MHz. Each antenna is excited by a periodic signal resulting from the superposition of all the individual frequencies. Each frequency component is independently steered in phase and amplitude for each antenna.

The antenna arrangement within the applicator is obtained via a global optimization procedure based on a specific absorption rate (SAR) that, conjointly for each antenna, determines the location and polarization angle to minimize the hot-spot to target quotient (HTQ) [40]. The procedure has been introduced in [41] and subsequently extended for use with the non-linear cost function HTQ and for the multi-frequency ultra-wideband (UWB) range adopted in this study. The steering parameters, that is, the phase and amplitude of each antenna at each operating frequency, are obtained via particle swarm optimization [42], using the HTQ as the cost function. The final antenna arrangement is visualized in Figure 2. The temperature distribution is then obtained by scaling the power deposition until the threshold for thermal damage in healthy brain temperatures (42 °C) [43] is reached. The temperature of the water bolus is set to 10 °C. The quality and feasibility of the treatment plan are evaluated in terms of the indexed temperatures T_{10}, T_{50} and T_{90}, which represent the temperatures achieved in 10, 50, and 90% of the target volume, respectively.

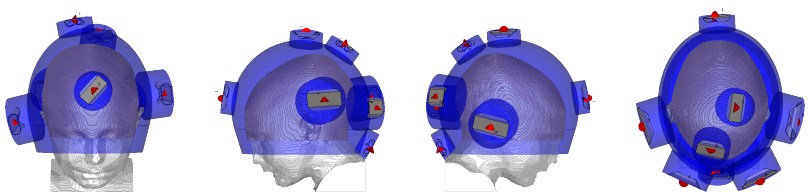

(**a**) Front (**b**) Left (**c**) Right (**d**) Top

Figure 2. Helmet applicator optimized for the thermal treatment of the tumour considered in this study. The red cones indicate the feed point and polarization direction of each antenna. The blue shade indicates water.

2.3. Stereotactic Radiosurgery Treatment Planning

The Gamma Knife models, Leksell Gamma Knife Icon® Icon™ and Leksell Gamma Knife® Perfexion™ (Icon, Perfexion), deliver dose from 192 Cobalt-60 sources that are collimated into narrow beams by a large tungsten body, see, for example, [44]. The beams converge in a small volume, called the isocenter, about 40 cm from the sources. The sources are housed within eight sectors with 24 sources in each sector. The sectors can slide over the collimator body, which in total has 576 collimator channels, in four different positions to produce beams of sizes of 4, 8 and 16 mm (The sizes refer to the cross-sectional diameters of single beams at the isocenter). The fourth position is beam-off when only a negligible amount of radiation leaks through the tungsten body. For each isocenter there are 65,535 different beam size combinations, colloquially called "shots". By shifting the position of the patient, a dose is delivered to several isocenters. The total dose can thus be sculpted to conform to the target with a sharp dose gradient outside the target, leading to a small dose to healthy tissue and organs at risk.

To create a dose plan, patient images are imported to the treatment-planning software Leksell GammaPlan® (LGP). In LGP, the target and organs at risks (OAR) are outlined, and the shots are placed in the target and weighted relative to each other to create an adequate dose distribution. The dose plan to the tumour described above was created by the new optimization tool, Leksell Gamma Knife® Lightning. By specifying the prescription dose to the target, max dose constraints on OARs, and optimization weights, a plan with a reasonable trade-off between quality and beam-on-time (BOT) is determined.

For this particular case no specific OAR is outlined, instead bringing down the dose to the tissue surrounding the target is promoted. Furthermore, achieving a plan with good-quality metrics was considered to be the most important objective, and hence less emphasis was put on bringing down the BOT. In Table 1 the quality metrics and beam-on-time are given for this plan. For definitions of radiosurgical metrics, see [45]. Note that achieving high target dose homogeneity is seldom an objective in Gamma Knife surgery. On the contrary, for most plans, the prescription dose at the periphery of the target corresponds to 40–60% of the max dose in the target. This is to ensure a sharp dose gradient at the target periphery leading to a rapid fall-off of the dose. In this particular case, the relative isodose of 60% was chosen by the optimizer.

Table 1. Metrics for the medulloblastoma plan.

Prescription Dose	Coverage	Selectivity	Gradient Index	Beam-on Time (min) @ 3 Gy/min	Number of Shots
15 Gy	0.994	0.850	2.63	54.8	110

2.4. Radiosensitivity Modelling

The overall cell survival of the combined therapy can be described by a generalised LQ model that includes both direct cytotoxicity and a radiosensitising effect of hyperthermia. The cell survival is expressed as a function of temperature (T) and radiation dose (D), as well as the time interval between the two therapies:

$$SF(D, T, t_{int}) = SF_{HT}(T) \times SF_{RT}(D, T, t_{int}), \quad (1)$$

where SF_{HT} is the term referring to cell-killing due to direct hyperthermic cytotoxicity, while SF_{RT} accounts for cell-killing due to radiation. t_{int} is the time interval between the end of radiotherapy and the start of hyperthermia treatment in the range of [0–4] h.

SF_{HT} can be modeled using the Arrhenius relationship [46]:

$$SF_{HT}(T) = exp[-K(T) \times t_H], \quad (2)$$

where t_H is the heating time (in this case 1 h) and K is the reaction rate as a function of temperature T (°C), given by [33]:

$$K(T) = 2.05 \times 10^{10} \times (T + 273.15) \times exp\left(\frac{\Delta S}{2} - \frac{\Delta H}{2(T + 273.15)}\right), \quad (3)$$

where ΔH (cal/mol) is the inactivation energy of the critical rate-limiting molecules which are responsible for cell death, and ΔS (cal/°C/mol) is the entropy of inactivation.

For the SF_{RT} part, the extended LQ model, which considers the radiosensitising effect of HT, is used to describe the cell killing due to radiotherapy, according to [33]

$$SF_{RT}(D, T, t_{int}) = exp\Big(- \alpha(T, t_{int}) \times D - G \times \beta(T, t_{int}) \times D^2\Big), \quad (4)$$

with G as the protraction factor as defined in Section 2.5 and

$$\alpha(T, t_{int}) = \alpha_{37} \times exp\left(\frac{T - 37}{41 - 37} \times ln(\frac{\alpha_{41}}{\alpha_{37}}) \times exp(-\mu.|t_{int}|)\right), \quad (5)$$

$$\beta(T, t_{int}) = \beta_{37} \times exp\left(\frac{T - 37}{41 - 37} \times ln(\frac{\beta_{41}}{\beta_{37}}) \times exp(-\mu \times |t_{int}|)\right), \quad (6)$$

where μ (h^{-1}) is the rate at which the radiosensitizing effect of hyperthermia disappears, $\alpha_{37} = \alpha(37, 0)$, $\alpha_{41} = \alpha(41, 0)$, $\beta_{37} = \beta(37, 0)$, and $\beta_{41} = \beta(41, 0)$.

In this study, we applied parameters for a generic head and neck (H&N) tumour [47], as reported in Table 2. The parameters for healthy tissues are same as tumour parameters with two distinctions: (a) at normothermic temperatures $\alpha_{37}/\beta_{37} = 3$ Gy, a ratio which is well-established, (b) $\mu = 1\ h^{-1}$ as the radiosensitising effect tends to disappear faster in normal tissue than in tumorous tissue [48]. The alpha and beta ratios at elevated temperatures, that is, α_{41}/α_{37} and β_{41}/β_{37}, are kept the same as for the tumour model since we could not find any experimental data for them in the literature.

Table 2. Parameters for the model in Equation (4).

Parameters	Tumour	Healthy Tissue
α_{37} (Gy^{-1})	0.35	0.35
α_{37}/β_{37} (Gy)	10	3
α_{41}/α_{37}	2.36	2.36
β_{41}/β_{37}	0.53	0.53
μ (h^{-1})	0.047	1
ΔS (cal/° C/mol)	423.14	423.14
ΔH (cal/mol)	157,312.3	157,312.3

The Oxygen Effect

The cell survival model, as described in the preceding section, considers that all the cells in the population are well-supplied with oxygen, hence a fully oxic cell population. To assess the effect of molecular oxygen on the irradiated tissue, the oxygen enhancement ratio (OER) is defined as the ratio of radiation dose in hypoxia to that of in well-oxygenated conditions. Based on OER, oxygen modification factors (OMF) being dependent on both the local oxygen tension (pO_2) and the duration of hypoxia (t_{hyp}) can be incorporated in the linear and quadratic parameters of the model, that is, α and β, as follows [49]:

$$\alpha_{hyp} = \frac{\alpha(T, t_{int})}{OMF(pO_2, t_{hyp})} \quad (7)$$

$$\beta_{hyp} = \frac{\beta(T, t_{int})}{OMF^2(pO_2, t_{hyp})}. \quad (8)$$

In this study, it was assumed that the cell oxygenation is not changing during the course of the treatment. Hence, only the pO_2 effect has been taken into account and the time factor is omitted by adopting the following OMF proposed by Alper and Howard-Flanders [35]:

$$OMF(pO_2) = OER_{max} \frac{k + pO_2(r)}{k + OER_{max}.pO_2(r)}, \quad (9)$$

where k is a reaction constant of 2.5–3 mmHg [50,51], while OER_{max} is the maximum protection achieved in the absence of oxygen which is considered to be 3 here.

The oxygenation of the tumour depends on its vasculature, which is chaotic and irregular [52]. Tumours are often characterized by a poorly oxygenated core due to the lack of blood vessels reaching the deeper layers that are surrounded by regions of progressively increased oxygenation towards the tumour periphery. To investigate the impact of oxygenation effect on the outcome of combined HT and SRS treatment, three cases have been considered: a well-oxygenated tumour, a moderately oxygenated tumour, and a poorly oxygenated tumour. The tumour was segmented into several iso-distance layers from the periphery inwards as shown in Figure 3a and a degree of oxygenation was allocated to each layer from a set of three distributions of oxygen partial pressure in tissue [53], Figure 3b. Figure 3c visualizes the resulting distributions of oxygen partial pressure in the considered models.

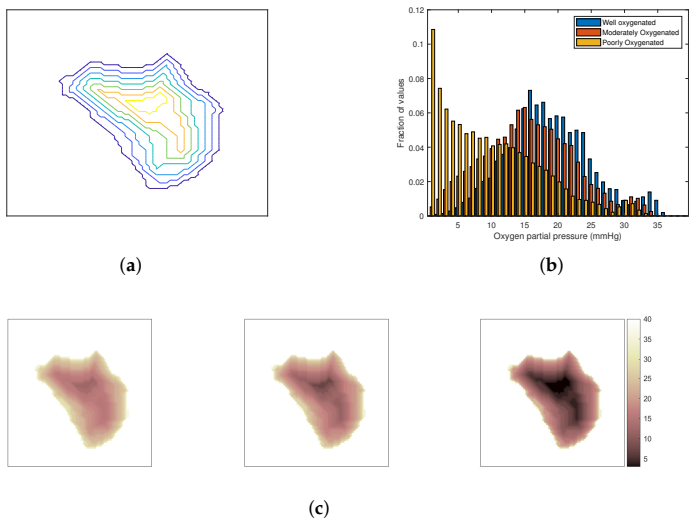

Figure 3. Modelling of the oxygenation level in the tumour. (**a**) A transverse cut of the iso-contour from the surface of the tumour. (**b**) Clinically representative histograms of pO_2 for a generic tumour under three different hypoxic conditions. (**c**) Mapped pO_2 distribution for those that are well-, moderately-, and poorly-oxygenated, respectively, from left to right.

2.5. Evaluation of Effect of the Combined Treatment

In order to quantify the impact of combined treatment, we consider two metrics: the equivalent normalized total dose (EQD) and biological effective dose (BED). Although these two metrics are related to each other, a clear distinction between them is necessary. Supposing an SRS schedule with n fractions of equal size, complete repair between fractions, and negligible repair during the fractions, the protraction factor is given by $G = 1/n$. The EQD can then be calculated by solving the following equation

$$SF(EQD) = SF(D, T, t_{int}), \quad (10)$$

which results in a second-order equation in terms of EQD and yields the following formula:

$$EQD = \frac{-\alpha_{37} + \sqrt{\alpha_{37}^2 + 4G\beta_{37} \times [\alpha(T, t_{int}) \times D + G \times \beta(T, t_{int}) \times D^2 + K(T) \times t_H]}}{2G\beta_{37}}, \quad (11)$$

where $\alpha(T, t_{int})$ and $\beta(T, t_{int})$ are given in Equations (7) and (8), respectively. The BED given for the fractionated plan with d_{frac} as the dose per fraction is then calculated using $BED = EQD \times RE$ where RE stands for relative effectiveness given by $RE = 1 + \frac{d_{frac}}{\alpha/\beta}$ [47].

In our analysis, we further considered tumour control probability (TCP), an additional metric that estimates the probability that a tumour will be eradicated or controlled by the thermoradiotherapy. In particular, the TCP describes the probability with which cancer cells will be killed by a given radiation treatment dose D and can be described by a Poisson-based function [54]:

$$\prod_{i=1}^{N_T} (1 - SF_i)^{n_i} \approx \prod_{i=1}^{N_T} exp(-n_i.SF_i), \quad (12)$$

where N_T is the total number of voxels in tumour and $n_i = n$ is the number of clonogenic cells.

The potential effect of the combined treatment on the normal brain tissue is evaluated by assessing the clinically relevant parameter V_{10} volume. The V_{10} volume is defined as the volume of the brain tissue outside the target that receives a BED $\geq 10\ \left(1 + \frac{10}{(\alpha/\beta)_{Healthy}}\right)$ Gy. Hence, in the forthcoming analysis, V_{10} is defined as a region with $BED \geq 43$ Gy, and its estimation is limited to the resolution of the voxel model, that is, 1 (mm^3).

3. Results

The hyperthermia treatment plan was obtained by using the SAR optimization procedures, which resulted in HTQ values of 1.5 and excellent tumour coverage $TC_{25} = 98\%$. The resulting steady-state temperature distribution, visualized in Figure 4a, was then obtained by scaling the power deposition with hard constrains for normal tissue temperature of 42 °C. The temperature distribution is visualized in the sagittal plane of the patient model, with the tumour delineated by a solid black line. Note that only temperatures above 37 °C are shown for better visualization. Temperatures below 37 °C are caused by the surface cooling water bolus and do not have any impact on the analysis of the combined RT + HT effect. The main hot-spot (i.e., the tissue temperature 42 °C) is located in the pocket of cerebrospinal fluid caudal to the target volume. The achieved $T_{90} = 39.0$ °C, $T_{50} = 39.8$ °C and $T_{10} = 40.4$ °C indicate adequate tumour coverage by the thermal dose.

The Gamma Knife treatment plan with the prescribed dose of 15 Gy resulted in 99.4% coverage, as reported in Table 1, and BED of 37.5 Gy when delivered in a single fraction. Given the size of the target, this treatment plan resulted in an unacceptably high V_{10} of 43 cm^3. In order to mitigate this issue, a five-fraction scheme is considered in the analysis. Observe that we used a simple, uncompensated scheme where the original treatment dose is maintained despite the fractionation. The compensation is considered later in this section. In all cases of the fractionated scheme, we assume that HT is delivered after each RT fraction, provided that the time between the RT fractions is long enough to allow for sublethal damage reparation and for prevention of development of the thermotolerance [55,56]. The BED distribution corresponding to the five-fraction scheme is visualized in Figure 4b. One can observe a sharp dose gradient around GTV that is characteristic of SRS treatments.

The boosting effect of adjuvant hyperthermia on the BED is illustrated on two cases: heat applied to fully oxic tumour directly after irradiation (Figure 4c) and heat applied to poorly oxygenated tumour four hours after radiation (Figure 4d). These cases represent the extreme values of the enhanced BED achieved for all considered cases shown in Figure 5. In both cases, the thermoradiotherapy plan resulted in a substantially higher BED to the GTV than the radiosurgery-only plan.

Figure 5 summarizes in detail the estimated biological effective radiation dose of the combined thermoradiotherapy treatment plan (RT + HT) achieved for different oxygenation conditions and sequential administration. The black lines represent the results for radiation only, while the coloured lines represent the combined treatment administered with time interval 0 (solid coloured lines) and 4 h after irradiation (dashed coloured lines). Although the results suggest a noticeable increase in the BED values for all levels of oxygenation, the administration of HT directly after RT, that is, $T_{int} = 0$, yields a bigger boost for each oxygenation level. Furthermore, the highest BED is observed for the oxic population, followed by the estimated BED for well-, moderately-, and poorly-oxygenated scenarios.

As a result of fractionation, the BED inevitably decreases. In order to achieve the same therapeutic outcome for the target, specified by the BED = 37.5 Gy, the radiation dose needs to be magnified by an appropriate scale factor, which increases with an increased number of fractions. To assess the effect of fractionation as well as to quantify the impact of the combined plan outside GTV, the V_{10} values for three fraction schemes and two RT + HT time intervals are reported in Figure 6. Observe that the reported fractionated plans are compensated by their respective scaling factors to give the same BED in the target as a single fraction scheme. The combined administration of HT with RT reduces the V_{10} volume, and this reduction is pronounced with an increased number of fractions. In a five-fraction scheme, the V_{10} volume is reduced from 30 cm^3 to approximately 17 cm^3 for both time intervals of 0 and 4 h.

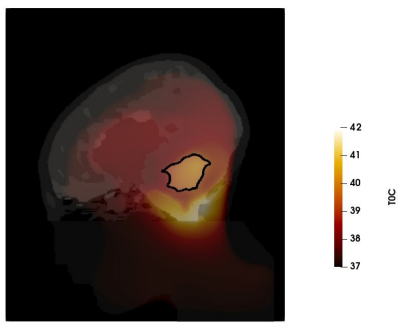

(**a**) Hyperthermia Temperature (°C)

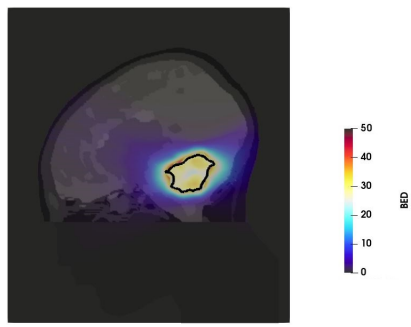

(**b**) BED, RT-alone, Oxic

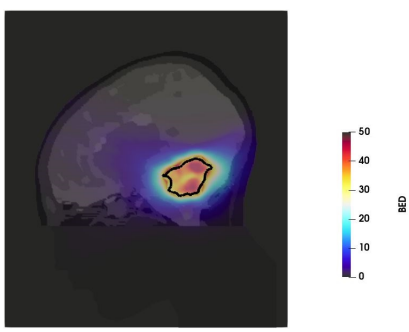

(**c**) BED, Oxic, $T_{int} = 0$

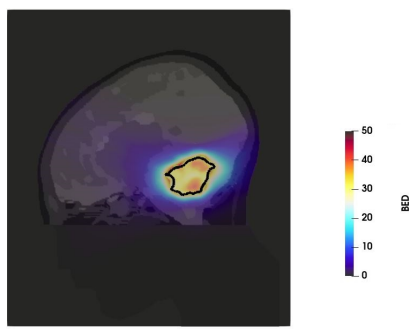

(**d**) BED, Poorly-oxygenated, $T_{int} = 4$

Figure 4. The thermal and BED distributions in the sagittal plane (**a**) Temperature distribution. (**b**) BED for RT plan with the total dose of 15 Gy delivered in five-fractions (**c**) BED of the combined plan for the well-oxygenated tumour and sequential administration with $T_{int} = 0$ (**d**) BED of the combined plan for the poorly oxygenated tumour and HT administration 4 h after RT.

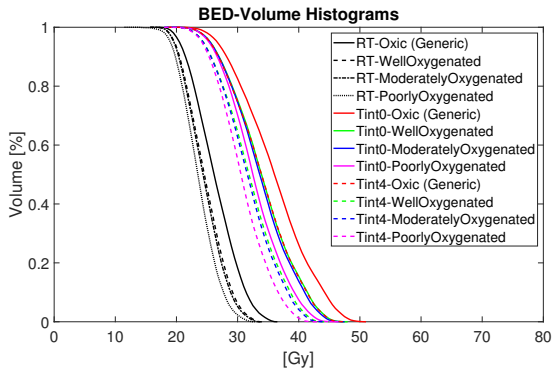

Figure 5. BED-Volume histograms for thermoradiotherapy plan with a total dose of 15 Gy given in five fractions.

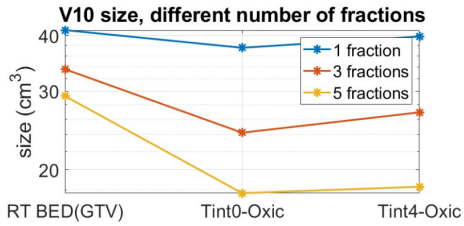

Figure 6. V_{10} for compensated plans so that even with fractionation, we can still achieve BED equal to 37.5 Gy for 99.4% of the voxels in the target.

Finally, the results in terms of TCP are shown in Figure 7. The TCP for the combined HT and RT is shown in comparison with the TCP for RT alone in the range of [0.5–0.8] and denoted by TCP_0. In particular, TCP_0 is based on the assumption that the radiosensitivity of all the cells in the tumour is described by the generic parameters derived in oxic conditions, as given in Table 2. The TCP is calculated for the RT + HT treatment through Equation (12) assuming an average clonogenic cell density determined from TCP_0. Again, the results are presented for different oxygenation conditions and for time intervals of 0 and 4, respectively (Figure 7a,b). The RT + HT combined plans, represented by dashed lines, exhibit substantially higher TCP than the corresponding RT alone curves. Furthermore, the enhanced effect of combined treatment is more pronounced for cells in hypoxic conditions. The impact of the time interval between the RT and HT is not prominent, as TCP values of the combined plans for both time intervals exhibit the TCP above 0.9 in all cases.

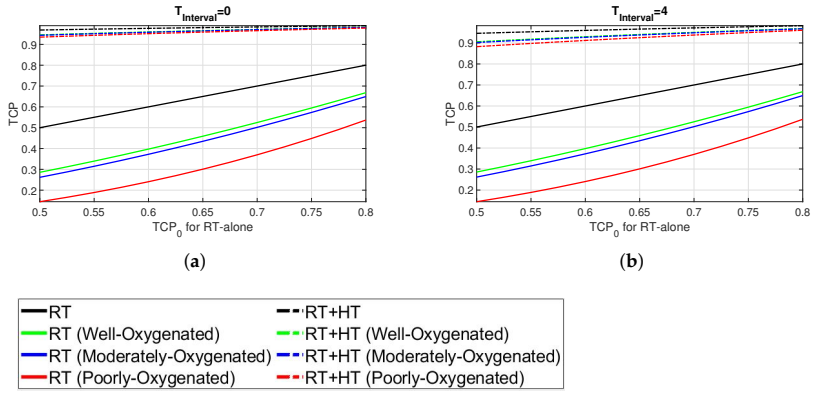

Figure 7. TCP at time intervals (**a**) 0 h and (**b**) 4 h.

4. Discussion

In this methodological study, we implemented the LQ model adapted for thermoradiotherapy [33] and determined clinically relevant parameters for assessing the combined effect of SRS and mild hyperthermia. We further extended the original model by oxygen modification factor [49]. That way, we could account for the well-known ability of hyperthermia to enhance tumour radiosensitivity.

Focused intracranial heating is challenging due to strict constrains on maximum temperatures of 42 °C [57,58]. The patient specific applicator design along with the multi-frequency treatment planning resulted in adequate tumour coverage represented by $T_{90} = 39.0$ °C, $T_{50} = 39.8$ °C and $T_{10} = 40.4$ °C. The size of the target, 34 cc, is considered to be a large volume for a Gamma Knife treatment, and therefore, many shots were required to reach high-quality metrics, such as coverage, selectivity, and gradient index. The new inverse planner for Gamma Knife treatments, Leksell Gamma Knife® Lightning, leads to plans with more shots than manual planning. Lightning often generates plans with more than one shot in a given isocenter to enhance the dose sculpting properties, which is reflected in Table 1. Note that although many shots are used, the beam-on-time for this large target is not particularly long.

The original, single fraction Gamma Knife treatment plan specified by the BED of 37.5 Gy, corresponding to a prescription dose of 15 Gy, gives a V_{10} of 43 cm^3. Since a large V_{10} volume has been found to correlate to adverse cognitive effects, see, for example, [59], we used a five-fraction scheme in the analysis of the boosting effect of thermal therapy. Furthermore, we could show that the combined administration of HT with RT can halve the V_{10} volume in a five-fraction scheme while maintaining the BED in the target. In certain cases, such as in multi-organ metastasis treatments, the size of the low dose volume V_{10} is a highly relevant parameter for treatment planning. In these cases, organs at risk (OAR) are often delineated and inspected specifically for the delivered dose levels.

A significant improvement of the examined parameters, that is, the BED and TCP, was achieved for the combined treatment, indicating a beneficial effect of elevated tumour temperatures. However, it must be stated that the calculated quantitative gains might be affected by the uncertainties in reported values of LQ parameters. Uncertainties in the values of α, β, and α/β, categorized typically by tumour sites, are generally large. In the absence of more specific values, we applied parameters for a generic, early reacting tumour [47]. This is a conservative approach which assumes that the cells are rapidly proliferating and hence have a higher sensitivity to fractionation. A similar strategy was used in previous modelling studies that assessed the trend of the investigated parameters related to the tumour response such as BED and TCP instead of actual quantitative estimates of these parameters [60]. The α_{41}/α_{37}, β_{41}/β_{37} were kept the same for both tumour and healthy

tissues, as those parameters are unknown for healthy tissue cells. Recently, the thermal dependence of cervical tumour cell lines SiHa and HeLa was experimentally determined by in vitro studies [33,34]. A difference between in vitro and in vivo for some parameters, α/β ratio in particular, is anticipated. Since the difference between the radiobiological parameters for brain tumour cell lines might be even larger than that of cervical cell lines, the results achieved in this study are illustrative.

Furthermore, these results can still be considered as a conservative assessment of the enhanced effect associated with hyperthermia. The LQ model and its extensions do not consider important features of hyperthermia, such as modulation of immunologic responses or changes in tumour microenvironment. In particular, an increased blood flow is expected to enhance the killing effect in hypoxic tumours.

The impact of the time interval between radiotherapy and hyperthermia delivery, in terms of both TCP and BED, appears less important than expected from reviews of radiobiological studies [61,62]. Nevertheless, the enhanced effect appears consistent for different hypoxic conditions. In the context of technological requirements for sequential administration, this is a positive observation that strengthens the combined therapy's feasibility.

The main impact of this study, apart from demonstrating the potential application of thermoradiotherapy in brain tumour management, is the guidance for evaluation and quantification of the common biological effect of both therapies. Kok et al. [63] suggested the use of equivalent radiation dose (EQD) instead of the cell survival model. We propose to direct the analysis towards the BED, which provides a more straightforward clinical insight and is often used for clinical decisions [64]. Furthermore, for the SRS, we recommend applying the second-order equation to calculate the EQD instead of the first-order solution proposed by [33,65]. Given that dose distributions of SRS are typically more inhomogeneous than that of EBRT, our approach avoids any approximation and thus yields more precise results.

In this study, the combined treatment is demonstrated on a paediatric tumour. However, the use of the Gamma Knife stereotactic radiosurgery (SRS) is not limited by the age of the patients. Rather, the Gamma Knife SRS is widely used in the treatment of both children and adults, primarily when the number of tumours is limited and their volumes small (ideally < 2 cubic centimetres). In pediatric patients, it is important to minimize the dose to the surrounding healthy tissue and thus to reduce the risk of late complications. In adult patients, the Gamma Knife SRS, potentially in combination with hyperthermia, can be particularly useful in the treatment of tumour residues, meningiomas, or metastases.

5. Conclusions

This study is the first to propose a methodological concept that evaluates a treatment plan combining stereotactic radiosurgery with microwave hyperthermia. Radiosensitisation has been modelled using an extended version of the LQ model with temperature-dependent radiosensitivity parameters and an oxygen modification factor. The results presented in terms of clinically relevant parameters, BED, V_{10} and TCP, indicate that the focused intracranial heating can be used either to boost the dose to the GTV area or to minimize the dose given to healthy tissues while maintaining the therapeutic effect described by BED. The estimated tumour control can be significantly improved by adjuvant hyperthermia. However, the results should not be seen in terms of absolute gain as they are achieved for this particular and generic case of radiosensitivity parameters.

This study is also the first to advocate a combination of stereotactic radiosurgery with focused heating. It motivates the future development of hyperthermia systems for brain cancer treatment to facilitate clinical trials and validate the effects of the combined treatment. Moreover, the methodological concept proposed here is independent of the form of RT or HT delivery. Therefore, a similar assessment can be performed for virtually any treatment; both EBRT and SRS plans can be applied, as well as heating by other focused delivery modalities, such as ultrasound.

Author Contributions: Conceptualization, H.D.T., H.N., I.T.-D.; methodology, H.D.T., H.N., I.T.-D., K.B., M.G.A., M.Z.; software, M.G.A., M.Z., H.N.; formal analysis, M.G.A.; investigation, all; data curation, M.G.A., M.Z.; writing—original draft preparation, all; visualization, M.G.A., M.Z.; supervision, H.D.T., H.N., I.T.-D., K.B.; funding acquisition, H.D.T. All authors have read and agreed to the published version of the manuscript.

Funding: This work was financially supported by the VINN EXcellence Center of ChaseOn (Chalmers Antenna Systems), The Swedish Childhood Cancer Fund and Hasselblad foundation.

Institutional Review Board Statement: Not applicable.

Informed Consent Statement: The model of the patient was derived from a MRI scan of a patient treated at Sahlgrenska University Hospital. All patients and their custodians were asked by the institute to sign a general consent that blood samples and test results (including radiology exams) can be used for research purposes in an anonymous form.

Data Availability Statement: Data available on request due to restrictions eg privacy or ethical. The data presented in this study are stored on secure servers and available on request from the corresponding author.

Conflicts of Interest: Håkan Nordström is senior research leader at Elekta AB. The other authors declare no conflict of interest. Elekta AB had no role in the design of the study, in the collection, analyses, or interpretation of data or in the decision to publish the results.

Abbreviations

The following abbreviations are used in this manuscript:

HTP	Hyperthermia Treatment Planning
PLD	Power Loss Density
SAR	Specific Absorption Rate
GTV	Gross tumour Volume
DVH	Dose Volume Histogram
EQD	EQuivalent radiation Dose
BED	Biologically Effective Dose
TCP	tumour Control Probability

References

1. Rosychuk, R.J.; Witol, A.; Wilson, B.; Stobart, K. Central nervous system (CNS) tumor trends in children in a western Canadian province: A population-based 22-year retrospective study. *J. Neurol.* **2012**, *259*, 1131–1136. [CrossRef]
2. Prigorowsky, M. *Cancerfondsrapporten 2009*; Cancerfonden: Stockholm, Sweden, 2009 .
3. Han, J.; Kwon, S.; Won, S.; Shin, Y.; Ko, J.; Lyu, C. Comprehensive clinical follow-up of late effects in childhood cancer survivors shows the need for early and well-timed intervention. *Ann. Oncol.* **2009**, *20*, 1170–1177. [CrossRef] [PubMed]
4. Makale, M.T.; McDonald, C.R.; Hattangadi-Gluth, J.; Kesari, S. Brain irradiation and long-term cognitive disability: Current concepts. *Nat. Rev. Neurol.* **2017**, *13*, 52. [CrossRef]
5. Overgaard, J.; Bentzen, S.; Gonzalez, D.G.; Hulshof, M.; Arcangeli, G.; Dahl, O.; Mella, O. Randomised trial of hyperthermia as adjuvant to radiotherapy for recurrent or metastatic malignant melanoma. *Lancet* **1995**, *345*, 540–543. [CrossRef]
6. van der Zee, J.; González, D.; van Rhoon, G.C.; van Dijk, J.D.; van Putten, W.L.; Hart, A.A. Comparison of radiotherapy alone with radiotherapy plus hyperthermia in locally advanced pelvic tumours: A prospective, randomised, multicentre trial. *Lancet* **2000**, *355*, 1119–1125. [CrossRef]
7. Datta, N.R.; Rogers, S.; Ordóñez, S.G.; Puric, E.; Bodis, S. Hyperthermia and radiotherapy in the management of head and neck cancers: A systematic review and meta-analysis. *Int. J. Hyperth.* **2016**, *32*, 31–40. [CrossRef] [PubMed]
8. Datta, N.R.; Rogers, S.; Klingbiel, D.; Gómez, S.; Puric, E.; Bodis, S. Hyperthermia and radiotherapy with or without chemotherapy in locally advanced cervical cancer: A systematic review with conventional and network meta-analyses. *Int. J. Hyperth.* **2016**, *32*, 809–821. [CrossRef]
9. Datta, N.R.; Puric, E.; Klingbiel, D.; Gomez, S.; Bodis, S. Hyperthermia and radiation therapy in locoregional recurrent breast cancers: A systematic review and meta-analysis. *Int. J. Radiat. Oncol. Biol. Phys.* **2016**, *94*, 1073–1087. [CrossRef]
10. Issels, R.D.; Lindner, L.H.; Verweij, J.; Wust, P.; Reichardt, P.; Schem, B.C.; Abdel-Rahman, S.; Daugaard, S.; Salat, C.; Wendtner, C.M.; et al. Neo-adjuvant chemotherapy alone or with regional hyperthermia for localised high-risk soft-tissue sarcoma: A randomised phase 3 multicentre study. *Lancet Oncol.* **2010**, *11*, 561–570. [CrossRef]
11. Issels, R.D.; Lindner, L.H.; Verweij, J.; Wessalowski, R.; Reichardt, P.; Wust, P.; Ghadjar, P.; Hohenberger, P.; Angele, M.; Salat, C.; et al. Effect of neoadjuvant chemotherapy plus regional hyperthermia on long-term outcomes among patients with localized

high-risk soft tissue sarcoma: The EORTC 62961-ESHO 95 randomized clinical trial. *JAMA Oncol.* **2018**, *4*, 483–492. [CrossRef] [PubMed]
12. Peeken, J.C.; Vaupel, P.; Combs, S.E. Integrating hyperthermia into modern radiation oncology: What evidence is necessary? *Front. Oncol.* **2017**, *7*, 132. [CrossRef]
13. Ott, O.J. *Hyperthermia in Oncology: Principles and Therapeutic Outlook*; UNI-MED Verlag: Bremen, Germany, 2010.
14. Wessalowski, R.; Schneider, D.T.; Mils, O.; Friemann, V.; Kyrillopoulou, O.; Schaper, J.; Matuschek, C.; Rothe, K.; Leuschner, I.; Willers, R.; et al. Regional deep hyperthermia for salvage treatment of children and adolescents with refractory or recurrent non-testicular malignant germ-cell tumours: An open-label, non-randomised, single-institution, phase 2 study. *Lancet Oncol.* **2013**, *14*, 843–852. [CrossRef]
15. Hulshof, M.; Raaymakers, B.; Lagendijk, J.; Koot, R.; Crezee, H.; Stalpers, L.; Gonzalez Gonzalez, D. A feasibility study of interstitial hyperthermia plus external beam radiotherapy in glioblastoma multiforme using the multi electrode current source (MECS) system. *Int. J. Hyperth.* **2004**, *20*, 451–463. [CrossRef] [PubMed]
16. Salcman, M.; Samaras, G.M. Interstitial microwave hyperthermia for brain tumors. *J. Neuro-Oncol.* **1983**, *1*, 225–236. [CrossRef] [PubMed]
17. Winter, A.; Laing, J.; Paglione, R.; Sterzer, F. Microwave hyperthermia for brain tumors. *Neurosurgery* **1985**, *17*, 387–399. [CrossRef] [PubMed]
18. Sneed, P.K.; Stauffer, P.R.; McDermott, M.W.; Diederich, C.J.; Lamborn, K.R.; Prados, M.D.; Chang, S.; Weaver, K.A.; Spry, L.; Malec, M.K.; et al. Survival benefit of hyperthermia in a prospective randomized trial of brachytherapy boost ± hyperthermia for glioblastoma multiforme. *Int. J. Radiat. Oncol. Biol. Phys.* **1998**, *40*, 287–295. [CrossRef]
19. Shirvalilou, S.; Khoei, S.; Esfahani, A.J.; Kamali, M.; Shirvaliloo, M.; Sheervalilou, R.; Mirzaghavami, P. Magnetic Hyperthermia as an adjuvant cancer therapy in combination with radiotherapy versus radiotherapy alone for recurrent/progressive glioblastoma: A systematic review. *J. Neuro-Oncol.* **2021**, *152*, 419–428 . [CrossRef]
20. Jordan, A.; Maier-Hauff, K. Magnetic nanoparticles for intracranial thermotherapy. *J. Nanosci. Nanotechnol.* **2007**, *7*, 4604–4606. [CrossRef] [PubMed]
21. Wankhede, M.; Bouras, A.; Kaluzova, M.; Hadjipanayis, C.G. Magnetic nanoparticles: An emerging technology for malignant brain tumor imaging and therapy. *Expert Rev. Clin. Pharmacol.* **2012**, *5*, 173–186. [CrossRef]
22. Giammalva, G.R.; Gagliardo, C.; Marrone, S.; Paolini, F.; Gerardi, R.M.; Umana, G.E.; Yağmurlu, K.; Chaurasia, B.; Scalia, G.; Midiri, F.; et al. Focused Ultrasound in Neuroscience. State of the Art and Future Perspectives. *Brain Sci.* **2021**, *11*, 84. [CrossRef]
23. Turner, P.; Tumeh, A.; Schaefermeyer, T. BSD-2000 approach for deep local and regional hyperthermia: Physics and technology. *Strahlenther. Onkol.* **1989**, *165*, 738–741.
24. Paulides, M.; Bakker, J.; Neufeld, E.; Zee, J.v.d.; Jansen, P.; Levendag, P.; Van Rhoon, G. The HYPERcollar: A novel applicator for hyperthermia in the head and neck. *Int. J. Hyperth.* **2007**, *23*, 567–576. [CrossRef] [PubMed]
25. Takook, P.; Persson, M.; Trefná, H.D. Performance evaluation of hyperthermia applicators to heat deep-seated brain tumors. *IEEE J. Electromagn. RF Microwaves Med. Biol.* **2018**, *2*, 18–24. [CrossRef]
26. Rodrigues, D.; Ellsworth, J.; Turner, P. Feasibility of heating brain tumors using a 915 MHz annular phased array. *IEEE Antennas Wirel. Propag. Lett.* **2021**, in press. [CrossRef]
27. Winter, L.; Özerdem, C.; Hoffmann, W.; Santoro, D.; Müller, A.; Waiczies, H.; Seemann, R.; Graessl, A.; Wust, P.; Niendorf, T. Design and evaluation of a hybrid radiofrequency applicator for magnetic resonance imaging and RF induced hyperthermia: Electromagnetic field simulations up to 14.0 Tesla and proof-of-concept at 7.0 Tesla. *PLoS ONE* **2013**, *8*, e61661. [CrossRef]
28. Zanoli, M.; Trefna, H.D. Iterative time-reversal for multi-frequency hyperthermia. *Phys. Med. Biol.* **2021**, *66*, 045027 . [CrossRef] [PubMed]
29. Oberacker, E.; Kuehne, A.; Oezerdem, C.; Nadobny, J.; Weihrauch, M.; Beck, M.; Zschaeck, S.; Diesch, C.; Eigentler, T.W.; Waiczies, H.; et al. Radiofrequency applicator concepts for thermal magnetic resonance of brain tumors at 297 MHz (7.0 Tesla). *Int. J. Hyperth.* **2020**, *37*, 549–563. [CrossRef] [PubMed]
30. Trefná, H.D.; Martinsson, B.; Petersson, T.; Renström, N.; Torstensson, M.; Ravanis, J.; Kok, P.; Persson, M. Multifrequency approach in hyperthermia treatment planning: Impact of frequency on SAR distribution in head and neck. In Proceedings of the 2017 11th European Conference on Antennas and Propagation (EUCAP), Paris, France, 19–24 March 2017; pp. 3710–3712.
31. Schooneveldt, G.; Trefná, H.D.; Persson, M.; De Reijke, T.M.; Blomgren, K.; Kok, H.P.; Crezee, H. Hyperthermia treatment planning including convective flow in cerebrospinal fluid for brain tumour hyperthermia treatment using a novel dedicated paediatric brain applicator. *Cancers* **2019**, *11*, 1183. [CrossRef] [PubMed]
32. Pollock, B.E. Complications After Stereotactic Radiosurgery. In *Complications in Neurosurgery*; Elsevier: Amsterdam, The Netherlands, 2019; pp. 203–206.
33. Van Leeuwen, C.; Oei, A.; Ten Cate, R.; Franken, N.; Bel, A.; Stalpers, L.; Crezee, J.; Kok, H. Measurement and analysis of the impact of time-interval, temperature and radiation dose on tumour cell survival and its application in thermoradiotherapy plan evaluation. *Int. J. Hyperth.* **2018**, *34*, 30–38. [CrossRef]
34. van Leeuwen, C.; Crezee, J.; Oei, A.; Franken, N.; Stalpers, L.; Bel, A.; Kok, H. The effect of time interval between radiotherapy and hyperthermia on planned equivalent radiation dose. *Int. J. Hyperth.* **2018**, *34*, 901–909. [CrossRef]
35. Alper, T.; Howard-Flanders, P. Role of oxygen in modifying the radiosensitivity of *E. coli* B. *Nature* **1956**, *178*, 978–979. [CrossRef]

36. Tissue Properties Database. V3.1. 2016. Available online: http://itis.swiss/virtual-population/tissue-properties/downloads-v3-1/ (accessed on 29 January 2021).
37. Rossmann, C.; Haemmerich, D. Review of temperature dependence of thermal properties, dielectric properties, and perfusion of biological tissues at hyperthermic and ablation temperatures. *Crit. Rev. Biomed. Eng.* **2014**, *42*, 467–492. [CrossRef] [PubMed]
38. Lang, J.; Erdmann, B.; Seebass, M. Impact of nonlinear heat transfer on temperature control in regional hyperthermia. *IEEE Trans. Biomed. Eng.* **1999**, *46*, 1129–1138. [CrossRef] [PubMed]
39. Takook, P.; Persson, M.; Gellermann, J.; Trefná, H.D. Compact self-grounded Bow-Tie antenna design for an UWB phased-array hyperthermia applicator. *Int. J. Hyperth.* **2017**, *33*, 387–400. [CrossRef]
40. Canters, R.; Franckena, M.; van der Zee, J.; Van Rhoon, G. Optimizing deep hyperthermia treatments: Are locations of patient pain complaints correlated with modelled SAR peak locations? *Phys. Med. Biol.* **2010**, *56*, 439. [CrossRef] [PubMed]
41. Zanoli, M.; Trefná, H.D. Optimization of microwave hyperthermia array applicators using field interpolation. In Proceedings of the 2019 IEEE International Symposium on Antennas and Propagation and USNC-URSI Radio Science Meeting, Atlanta, GA, USA, 7–12 July 2019; pp. 537–538.
42. Kennedy, J.; Eberhart, R. Particle swarm optimization. In Proceedings of the ICNN'95-International Conference on Neural Networks, Perth, WA, Australia, 27 November–1 December 1995; Volume 4, pp. 1942–1948.
43. Yarmolenko, P.S.; Moon, E.J.; Landon, C.; Manzoor, A.; Hochman, D.W.; Viglianti, B.L.; Dewhirst, M.W. Thresholds for thermal damage to normal tissues: An update. *Int. J. Hyperth.* **2011**, *27*, 320–343. [CrossRef] [PubMed]
44. Lindquist, C.; Paddick, I. The Leksell Gamma Knife Perfexion and comparisons with its predecessors. *Oper. Neurosurg.* **2007**, *61*, ONS-130–ONS-140. [CrossRef]
45. Torrens, M.; Chung, C.; Chung, H.T.; Hanssens, P.; Jaffray, D.; Kemeny, A.; Larson, D.; Levivier, M.; Lindquist, C.; Lippitz, B.; et al. Standardization of terminology in stereotactic radiosurgery: Report from the Standardization Committee of the International Leksell Gamma Knife Society: Special topic. *J. Neurosurg.* **2014**, *121*, 2–15. [CrossRef]
46. Dewey, W.; Hopwood, L.; Sapareto, S.; Gerweck, L. Cellular responses to combinations of hyperthermia and radiation. *Radiology* **1977**, *123*, 463–474. [CrossRef]
47. Fowler, J.F. Sensitivity analysis of parameters in linear-quadratic radiobiologic modeling. *Int. J. Radiat. Oncol. Biol. Phys.* **2009**, *73*, 1532–1537. [CrossRef]
48. Overgaard, J. Simultaneous and sequential hyperthermia and radiation treatment of an experimental tumor and its surrounding normal tissue in vivo. *Int. J. Radiat. Oncol. Biol. Phys.* **1980**, *6*, 1507–1517. [CrossRef]
49. Toma-Dasu, I.; Dasu, A. Modelling tumour oxygenation, reoxygenation and implications on treatment outcome. *Comput. Math. Methods Med.* **2013**, *2013*, 141087. [CrossRef] [PubMed]
50. Alper, T. *Cellular Radiobiology*; CUP Archive: Cambridge, UK, 1979.
51. Hall, E.J.; Giaccia, A.J. *Radiobiology for the Radiologist*; Wolters Kluwer Health: Philadelphia, PA, USA, 2006 ; Volume 6.
52. Vaupel, P.; Multhoff, G. Accomplices of the hypoxic tumor microenvironment compromising antitumor immunity: Adenosine, lactate, acidosis, vascular endothelial growth factor, potassium ions, and phosphatidylserine. *Front. Immunol.* **2017**, *8*, 1887. [CrossRef] [PubMed]
53. Daşu, A.; Toma-Daşu, I. Treatment modelling: The influence of micro-environmental conditions. *Acta Oncol.* **2008**, *47*, 896–905. [CrossRef]
54. Brahme, A. Optimized radiation therapy based on radiobiological objectives. In *Seminars in Radiation Oncology*; Elsevier: Amsterdam, The Netherlands, 1999; Volume 9, pp. 35–47.
55. Dewey, W.C. Arrhenius relationships from the molecule and cell to the clinic. *Int. J. Hyperth.* **1994**, *10*, 457–483. [CrossRef] [PubMed]
56. van Rhoon, G.C. Is CEM43 still a relevant thermal dose parameter for hyperthermia treatment monitoring? *Int. J. Hyperth.* **2016**, *32*, 50–62. [CrossRef] [PubMed]
57. van der Zee, J.; Vujaskovic, Z.; Kondo, M.; Sugahara, T. The Kadota fund international forum 2004–Clinical group consensus. *Int. J. Hyperth.* **2008**, *24*, 111–122. [CrossRef]
58. Haveman, J.; Sminia, P.; Wondergem, J.; van der Zee, J.; Hulshof, M. Effects of hyperthermia on the central nervous system: What was learnt from animal studies? *Int. J. Hyperth.* **2005**, *21*, 473–487. [CrossRef] [PubMed]
59. Minniti, G.; Clarke, E.; Lanzetta, G.; Osti, M.F.; Trasimeni, G.; Bozzao, A.; Romano, A.; Enrici, R.M. Stereotactic radiosurgery for brain metastases: Analysis of outcome and risk of brain radionecrosis. *Radiat. Oncol.* **2011**, *6*, 1–9. [CrossRef]
60. Lindblom, E.; Toma-Dasu, I.; Dasu, A. Accounting for two forms of hypoxia for predicting tumour control probability in radiotherapy: An in silico study. In *Oxygen Transport to Tissue XL*; Springer: Berlin, Germany, 2018; pp. 183–187.
61. Horsman, M.; Overgaard, J. Hyperthermia: A potent enhancer of radiotherapy. *Clin. Oncol.* **2007**, *19*, 418–426. [CrossRef]
62. Oei, A.; Kok, H.; Oei, S.; Horsman, M.; Stalpers, L.; Franken, N.; Crezee, J. Molecular and biological rationale of hyperthermia as radio-and chemosensitizer. *Adv. Drug Deliv. Rev.* **2020**, *163*, 84–97. [CrossRef]
63. Kok, H.P.; Crezee, J.; Franken, N.A.; Stalpers, L.J.; Barendsen, G.W.; Bel, A. Quantifying the combined effect of radiation therapy and hyperthermia in terms of equivalent dose distributions. *Int. J. Radiat. Oncol. Biol. Phys.* **2014**, *88*, 739–745. [CrossRef] [PubMed]

64. Fowler, J.F. 21 years of biologically effective dose. *Br. J. Radiol.* **2010**, *83*, 554–568. [CrossRef] [PubMed]
65. Van Leeuwen, C.; Crezee, J.; Oei, A.; Franken, N.; Stalpers, L.; Bel, A.; Kok, H. 3D radiobiological evaluation of combined radiotherapy and hyperthermia treatments. *Int. J. Hyperth.* **2017**, *33*, 160–169. [CrossRef] [PubMed]